UNIVERSITÀ DEGLI STUDI DI NAPOLI FEDERICO II

Dottorato di Ricerca in Ingegneria Industriale
XXXIII Ciclo

Aero-thermo-dynamic Study on Thermal Protection Systems and Rocket Nozzles in Innovative Ceramic Materials

Coordinatore:
Prof. Michele Grassi

Tutor:
Prof. Raffaele Savino

Candidato:
Ing. Stefano Mungiguerra

Ad ogni istante
in cui ho dubitato

ABSTRACT

New-generation hypersonic and reusable re-entry vehicles set increasingly demanding requirements for the development of high-performance Thermal Protection Systems (TPS), due to the challenges of extremely harsh aero-thermo-dynamic conditions characteristic of atmospheric re-entry, including hypersonic Mach numbers, temperatures above 2000°C, the activation of gas dissociation/recombination reactions at extremely low oxygen partial pressures, which can substantially enhance the heat flux on the exposed surface of the spacecraft.

On the other hand, challenges for solid and hybrid rocket technologies include the design and fabrication of non-eroding firing thrusters able to survive severe thermal-structural and thermal-chemical combustion environments without cooling systems. The inner surface of the exhaust nozzle, through which the propellant flow is accelerated to supersonic conditions, is very critical in this sense, as it is subjected to the highest shear stresses, pressures and heat fluxes in a chemically aggressive environment. These severe conditions usually lead to removal of surface material (ablation) due to heterogeneous reactions between oxidizing species in the hot gas and the solid wall. Because of the material erosion, there is an enlargement of the nozzle throat section and a consequent decrease of the rocket thrust, with detrimental effects over the motor operation. Thus, the requirement that dimensional stability of the nozzle throat should be maintained makes the selection of suitable rocket nozzle materials extremely hard.

Over the last decades, research identified Ultra-High-Temperature Ceramic (UHTC) materials, based on transition metals carbides and diborides, as potentially promising candidates for these applications, especially in light of their high melting temperatures, strength and ablation resistance at temperatures over 2000°C. Nevertheless, some issues related to poor oxidative behaviour and mechanical properties (damage tolerance, fracture toughness, thermal shock resistance) of single and multi-phase UHTCs at high temperatures limit the applicability of these materials. The introduction of SiC or other silicon based ceramics as minority phase, in the form

of particles, short/long fibres or whiskers, in the main refractory ceramic has been often proposed to improve damage tolerance and oxidation resistance at intermediate temperature, essentially thanks to the formation of a low-viscosity borosilicate glass protective scale. The most recent frontiers in a research oriented to high Technology Readiness Level (TRL) applications of the UHTC technology to aerospace involve the enhancement of mechanical properties by introducing short and continuous carbon fibre reinforcements in a UHTC matrix, leading to the definition of the Ultra-High-Temperature Ceramic Matrix Composites (UHTCMCs). The overall objective is developing large ultra-refractory aerospace transportation systems components with outstanding ablation resistance and enhanced mechanical properties and reliability. To achieve this goal, testing in a relevant environment is required to properly characterize the ceramic materials in conditions representative of the real flight applications.

In this framework, the European Horizon 2020 C^{3}HARME Project (Next Generation Ceramic Composites for Combustion Harsh Environments and Space), involving several research institutions and private companies all over Europe, has been focused on the development of a new class of UHTCMC materials, based on an UHTC matrix and reinforcing carbon fibres. The aim was to develop near-zero ablation Thermal Protection Systems and near-zero erosion hybrid and solid rocket nozzles. The University of Naples "Federico II" has been involved in the experimental campaigns aimed at the characterization of the new materials in relevant environments, in the definition of the geometries of the samples to be tested, and in numerical modelling of the aero-thermo-chemical conditions around the test articles and the material thermal response.

Most of the activities described in the present thesis have been carried out in the framework of the C^{3}HARME project. Specifically, the objectives of this work include: i) a characterization, as comprehensive as possible, of the aero-thermo-dynamic behaviour of ceramic materials, with different formulations, sizes and shapes, in lab-reproduced representative environments, and ii) the definition and employment of numerical models for the simulation of the thermo-fluid-dynamic conditions and material thermal response.

After a general introduction to the topic and the description of experimental facilities and computational models, results obtained in the framework of materials characterization for hypersonic TPS are presented. Relevant tests were performed in an arc-jet supersonic wind tunnel, where the typical aero-thermodynamic and chemical conditions of atmospheric re-entry are reproduced at supersonic Mach numbers, temperatures above 5000 K and a consistent amount of dissociated oxygen and nitrogen. Non-intrusive diagnostic techniques (two-colour pyrometers and infrared thermo-cameras) were used to continuously monitor samples surface temperatures during testing. The main activities included: an extensive experimental campaign for the characterization of UHTCMC materials with almost zero ablation properties at ultra-high temperature; a series of dedicated test campaigns carried out in order to understand the effect of SiC content on the ultra-high-temperature oxidation and material behaviour under simulated re-entry conditions; specific experiments to compare the material response in different chemical atmospheres (simulated air and pure nitrogen flows); large scale tests on UHTCMC samples carried out in the arc-jet wind tunnel available at the premises of the German Aerospace Centre (DLR) in Cologne (Germany). The outcomes of all these experimental activities are presented and discussed, also in light of the post-test characterizations carried out, in collaboration with project partners, to investigate the features of the materials microstructures after the exposure to the atmospheric re-entry environment. Moreover, the experimental results were complemented by Computational Fluid Dynamics (CFD) simulations, employed to allow accurate prediction not only of the thermo-fluid-dynamic flow field around the test articles, but also of the thermal behaviour of the materials samples, including an investigation of the effect of material properties, such as thermal conductivity, emissivity and catalycity. A great interest has been paid to the interpretation of a phenomenon observed in several tests, consisting in a rapid temperature increment at constant flow conditions (known as *temperature jump* in the relevant literature regarding UHTCs and SiC-based ceramics). This thesis intends to propose a thorough and detailed analysis of the materials aero-thermo-dynamic behaviour at ultra-high temperatures in a representative re-entry environment, aiming to provide a comprehensive interpretation of the *temperature jump*, correlating the

outcomes of infrared temperature measurements, post-test microstructural analyses and numerical simulations to highlight the parameters which mainly affect the heat transfer from the flow to the ceramic.

The second part of results is focused on characterization of the same class of materials, for near-zero erosion rocket nozzles. The experimental activities were carried out with a 200 N-class hybrid rocket engine in different test configurations. The first tests have been performed with a novel, dedicated test set-up exposing UHTCMC samples to the supersonic exhaust jet of the hybrid rocket operated with gaseous oxygen burning cylindrical port High-Density PolyEthylene (HDPE) grains. Also in this case, non-intrusive diagnostic equipment has been employed to monitor the surface temperature of the samples. The combination of combustion temperature over 3000 K, supersonic Mach number and stagnation pressures allowed reproducing realistic rocket nozzles operating conditions, in order to demonstrate the ability of the specimens to preserve their functional integrity in a relevant environment. The second set-up ("Chamber insert test") was meant to assess the capability of the test article (in the shape and size of an annular combustion chamber element) to withstand high thermo-mechanical stress at high pressures in relevant aero-thermo-chemical combustion environment. As a third step, UHTCMC nozzle throat inserts have been manufactured and experimentally tested to verify the erosion resistance and evaluate the effects on the rocket performance by comparison with those obtained in similar operating conditions employing a graphite nozzle. Finally, complete subscale nozzles, made by different processing routes, matrix formulations, fibres architectures and having different properties (such as fibre volume content and porosity), were repeatedly tested in order to select the most promising technology for reusable non-eroding rocket nozzles. Also in this case, CFD models were exploited to characterise the flow field in the different test configurations, evaluate the aero-thermo-dynamic loads on the prototypes during tests and to rebuild the thermal response of the materials. Combining experimental and numerical results, general conclusions were drawn about the effect of different parameters, such as matrix composition, fibre architecture and volume content, densification process and final material porosity.

TABLE OF CONTENTS

LIST OF ABBREVIATIONS

ARV	Advanced Re-entry Vehicle
BSG	BoroSilicate Glass
C^3HARME	Next Generation Ceramic Composites for Combustion Harsh Environments and Space
CCD	Charge-Coupled Device
CEA	Chemical Equilibrium with Applications software
CFD	Computational Fluid Dynamics
CMC	Ceramic Matrix Composite
CNR	National Research Council
CRT	Central Research Technology
DLR	German Aerospace Centre
EDS	Energy Dispersive x-ray Spectroscopy
EBC	Environmental Barrier Coating
FC	Fully catalytic
FEM	Finite Element Method
FVC	Fibre Volume Content
HDPE	High-Density PolyEthylene
HP	Hot Pressing
HPPC	High Performance Plasma Coating
HRM	Hybrid Rocket Motor
HTPB	Hydroxyl-Terminated PolyButadiene
IR	Infrared
ISTEC	Institute of Science and Technology for Ceramics
LBK	*LichtbogenBeheizter WindKanal* (German for "Arc-heated wind tunnel")
LEO	Low Earth Orbit
NC	Non-catalytic
NIR	Near Infrared

PAN	Polyacrylonitrile
PIP	Polymer Infiltration and Pyrolysis
PDF	Probability Density Function
RF-CVI	Radio-Frequency Chemical Vapour Infiltration
RMI	Reactive Melt Infiltration
SEM	Scanning Electron Microscope
SPES	Small Planetary Entry Simulator
SPS	Spark Plasma Sintering
SRM	Solid Rocket Motor
TC	Thermo-camera
TJ	Temperature Jump
TPS	Thermal Protection System
TRL	Technology Readiness Level
UD	UniDirectional
UHTC	Ultra-High-Temperature Ceramic
UHTCMC	Ultra-High-Temperature Ceramic Matrix Composite
UNINA	University of Naples “Federico II”
UoB	University of Birmingham
XRD	X-ray Diffraction

CHAPTER 1. CHALLENGES OF AEROSPACE EXTREME ENVIRONMENTS

1.1 Atmospheric re-entry

Atmospheric re-entry is the terminal portion of the flight mission of spacecraft returning on Earth. Since it involves re-entering into the Earth's atmosphere at very high speeds, this is certainly one of the most critical phases because the vehicle structure is exposed to strong inertial (due to the deceleration it undergoes) and thermal stresses (due to the hypersonic flow regime). It is therefore necessary to provide the spacecraft with a suitable Thermal Protection System (TPS) for the external structure and in order to keep the inner (cabin) temperatures within acceptable values. Indeed, if the atmosphere acts as an aerobrake on the high-speed vehicle, allowing to approach safely and gradually decelerating the spacecraft before final landing, on the other hand, viscous effects in hypersonic flow lead to substantial aerodynamic heating [1].

The kinetic energy associated to hypersonic flows, in fact, is very high and due to the viscous boundary layer around the vehicle, it is partly converted into internal energy of the gases. Increasing the internal energy, the gas temperature may be higher than 3000 K leading to excitation of the vibrational degrees of freedom of the molecules, to molecules dissociation or even atoms ionization.

The viscous boundary layer, however, is not the only region where a remarkable increase in temperature is possible. In fact, it is well known that when a relatively blunt vehicle is exposed to hypersonic flow conditions, a bow shockwave behind the spacecraft provides a strong jump of the flow pressure and temperature, followed by a "chemical relaxation zone" where the gas mixture modifies its composition due to the high temperature downstream of the shockwave (Fig. 1.1). This layer is therefore characterized by strong chemical concentration gradients and the chemical species approach equilibrium compositions only if the shock "stand-off distance" is thick

enough. Fig. 1.2 shows typical values of temperature and chemical composition in the post-shock region as a function of velocity (or equivalently of Mach number).

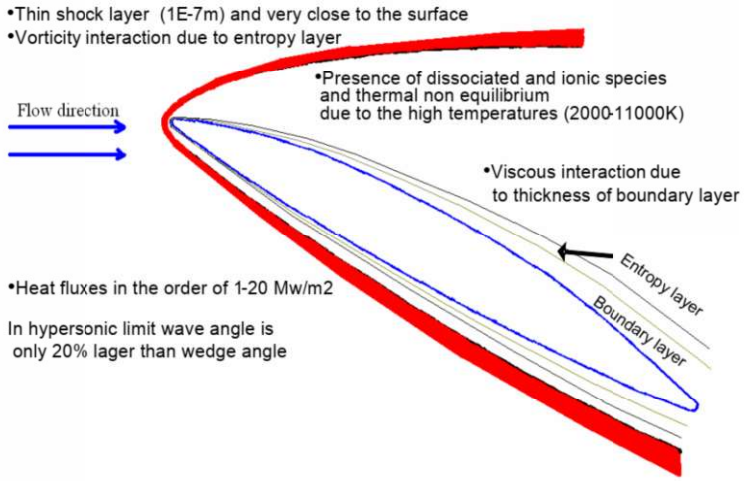

Fig. 1.1. Schematics of a hypersonic flow field around an aerodynamic profile, showing the bow shockwave structure and the main field features [2].

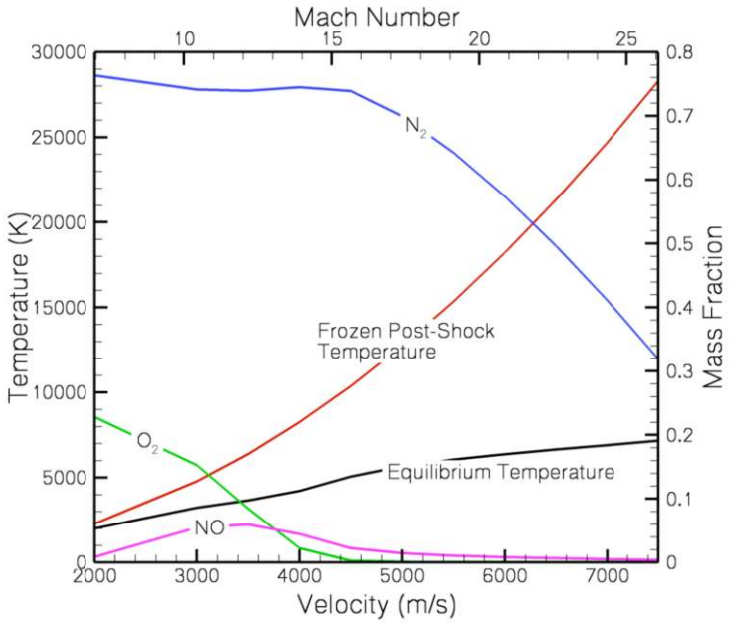

Fig. 1.2. Post-shock conditions as a function of flow velocity (or Mach number). The mass fractions of the main chemical species are shown. Two temperatures are plotted, in the hypothesis of chemical equilibrium (black line) and of frozen chemical composition (red line) [3].

If the Reynolds number is not large enough due to rarefaction effects at relatively high altitudes, hypersonic boundary layer /shockwave interactions become important.

It can be easily understood, therefore, how the combined effect of the two mentioned phenomena (viscous dissipation and detached normal shockwave) has a substantial impact on the temperature increase on the body surface, triggering complex chemical reactions. The molecular oxygen (O_2), for example, dissociates to form atomic oxygen above 2000 K; the molecular nitrogen (N_2), on the other hand, begins to dissociate above 4000 K, when molecular oxygen is completely dissociated, and is completely dissociated when the temperature is about 9000 K. Exceeding 9000 K ions would form (thanks to the following reactions: $N \rightarrow N^+ + e^-$, $O \rightarrow O^+ + e^-$), and the gas becomes a partially ionized plasma.

It is also necessary to point out another critical and interesting aspect related to aerothermal heating: when oxygen or nitrogen atoms come into contact with the spacecraft walls, exothermic molecular recombination reactions may be triggered. Consequentially, a significant additional energy can be released increasing the heat flux. The parameter regulating this phenomenon is called catalycity of the wall, the higher its value is the greater will be the additional energy the recombination reactions will provide [4,5].

A further contribution to surface chemical reactions is related to the possible presence of ablative coating materials, which, degrading during the exposure to the considerable thermal flux, will react chemically with the dissociated atmospheric gases.

In any event, the most important consequence of the exposure of a spacecraft to hypersonic high-enthalpy flows is certainly represented by the considerable convective heat exchange that is triggered between the thermal boundary layer and the cold body surface. It should also be considered that in case of extremely high temperatures in the shock layer, the energy radiated by the gas can be dangerously significant, giving rise to an additional radiative heat flux towards the body walls.

It is interesting to provide quantitative estimations of the actual gas temperature increase during of atmospheric re-entry. Let us consider a vehicle in Low Earth Orbit (LEO) at the extreme limit of the atmosphere. In our analysis the potential energy

contribution is neglected compared to the kinetic energy, because the atmosphere thickness is negligible compared to the Earth's radius. A realistic value of the orbital velocity is 7.7 km/s, corresponding to a kinetic energy in the order of 30 MJ/kg, while it would reach 11.2 km/s (escape velocity), resulting in kinetic energy of about 63 MJ/kg, if we consider an interplanetary probe. Under such conditions, if all the kinetic energy, due to the viscous dissipation (friction) action in the hypersonic boundary layer around the vehicle, was converted into internal energy, the wall temperature would be unaffordable for any existing material. In particular, if a total enthalpy of 30 MJ/kg was completely converted into specific thermal energy in the body, even materials with relatively high specific heat, in the order of 1000 J/(kg K), should reach temperatures in the order of 30000 K. In practice, metallic materials would melt at much lower temperatures, while insulating materials (e.g. refractory ceramics) could reach very high equilibrium temperatures only re-radiating a considerable amount of this energy towards the outer space.

1.1.1 Thermal protection systems

It is therefore evident that in order to solve or at least minimize the heat flux associated to the atmospheric re-entry, only a limited part of the kinetic energy dissipated by friction can be converted into internal energy.

Nowadays different concepts of thermal protection systems are widely used in aerospace [6]. Although deeply different, they share the common objective of thermally insulating the internal structures of the aircraft. This task is pursued to avoid degradation of the mechanical properties as well as consequent deformations or failures.

Thermal protection systems based on radiative heat exchange only are typically defined as passive; in this case no other mechanisms, e.g. active cooling or boiling or evaporation, are possible. Another simple passive thermal protection system is the so-called *Heat-Sink* that is capable of absorbing the incident heat and store it in its structure. Its applicability is however limited by the fact that the energies involved in aerospace applications are significant. It is difficult, in fact, at the current state of the art, to apply this solution in atmospheric re-entry as it would require to large mass to

absorb the energy exchanged between the flow and the vehicle during re-entry operations.

Another solution, to this day the most widely used in hypersonic aerospace applications, is represented by the so-called *Insulated Structures*, involving the superposition to the primary structure of the vehicle of materials or multilayers able to quickly reach radiative equilibrium conditions, and then radiatively re-emit much of the incident heat. The last solution, that will be widely discussed in this dissertation is the *Hot Structure,* consisting in the use of materials with remarkable mechanical and thermal performances in high enthalpy motion regimes [1].

An intermediate thermal protection strategy is the so-called semi-passive thermal protection system, based on materials able to absorb energy during ablation, i.e. in the transition from the solid to the vapour phase. Always extensively used as TPS since the beginning of the space age for re-entering capsules, they are not viable solutions for future reusable transportation systems. This is the reason why the research is actually focused on the development of near zero-ablation and near zero-erosion ultra-high temperature materials whose ability to withstand the critical conditions of high-enthalpy hypersonic flows is a requirement of increasing importance.

1.2 Rocket propulsion

The issue of extreme heat fluxes and aero-thermo-chemical loads on aerospace vehicles is not limited to atmospheric re-entry. In fact, the combination of extremely harsh thermo-fluid-dynamic and chemical conditions achieved inside the combustion chamber and through the exhaust nozzle of rocket engines sets demanding requirements for advanced materials, resistant to chemical attack and to erosion at high temperatures. The typical propulsion environment contains oxidizing chemical species, such as O_2, O, CO_2, H_2O [7], resulting from the combustion reactions occurring in the chamber, which are accelerated to supersonic Mach number through the nozzle, whose inner surface experiences the aero-thermo-chemical loads deriving from the tangential flow of the combusting mixture. Particularly, the throat section, where a sonic Mach number is achieved, is the most solicited region, being subjected

to the highest heat fluxes and shear stresses. The combusting gas expansion through the nozzle, with consequent quick decrease of pressure and temperature along the nozzle profile, generates asymmetric pressure loads and up to 3000 K flame temperature in the boundary layer above the internal nozzle surface. This leads to strong thermal gradient and thermal shock in the radial direction (especially if material thermal conductivity is low [8]) and high tensile stresses in the longitudinal direction.

Solid propellant rockets usually are used in first stages due to their capacity to provide thrust high enough to overwhelm the launcher and payload overall weight [8]. High levels of thrust (> 1.5 MN) can be achieved by increasing both motors pressure (> 50 bar) and minimum nozzle area (minimum diameter > 150 mm), leading to necessity to use materials able to withstand thermo-structural strength and thermal shock in thick components. In fact, nozzles for this kind of rockets does not foresee any active cooling system, and the components have to withstand relatively long operation times (on the order of several minutes).

Hybrid rocket motors, instead, are often characterized by lower operative pressure. It must be observed that the wall heat flux that the nozzle can withstand may be higher because, as in liquid rockets, nozzle cooling systems may be used, exploiting the same liquid oxidizer, in order to remove heat from the most critical regions, e.g. the nozzle throat. Therefore hybrid rockets offer the advantage to reduce throat ablation and to increase the life and operating range of the nozzles with active or innovative regenerative cooling mechanisms [9]. However, in general, conventional uncooled nozzles are preferred for their simplicity but similarly to solid rockets often severe ablation occurs, the nozzle throat area increases and the thrust performance degrades continuously even throughout 10-20 seconds operations. Moreover, the requirement of multiple operations is often set, so that hybrid rocket engines must be operative for at least 2/3 cycle of burning, inducing the need for reusability of their components.

Besides the intensity of heat fluxes and mechanical loads, nozzles for rocket applications typically operate in chemically aggressive environments. For instance, Fig. 1.3 shows the typical chemical compositions of the combustion chamber of hybrid and solid rockets in representative operating conditions.

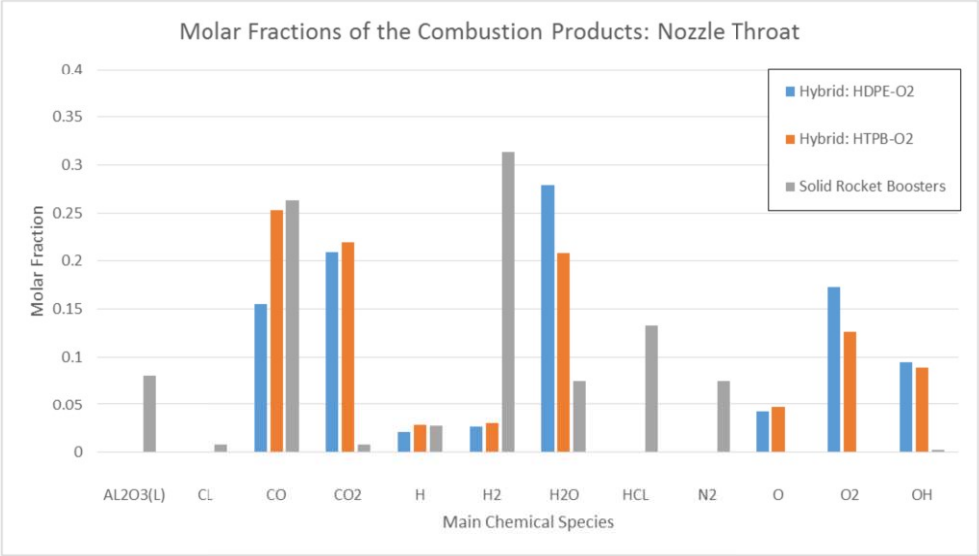

Fig. 1.3. Molar fractions of the combustion products in rockets with different propellants.

In particular, for the hybrid rockets, two cases have been analysed, considering oxygen as oxidizer and a High-Density PolyEthylene (HDPE) fuel grain in one case and a Hydroxyl-Terminated PolyButadiene (HTPB) fuel grain in the other one. In the first case, the average Oxidizer to Fuel ratio (OF) considered is equal to 4, while in the second case the average OF considered is equal to 3.2: these values are well representative of the operating condition of the 200N-class Hybrid Rocket Motor available at the Aerospace Propulsion Laboratory of the University of Naples "Federico II", that will be used for the experiments presented in this thesis. From the figure it can be noticed that in these cases the chemical environment is characterized by the presence of significant concentration of oxygen and other oxidizing species. On the other side, for solid rockets, the typical propellant composition used for the boosters of the launcher Ariane V has been analysed. In this case, although the oxidizing species are present in smaller concentrations, they are enough to induce thermochemical erosion of nozzle throat materials. Moreover, the environment is characterized by the presence of condensed phase, such as liquid particles of Al_2O_3, which can lead to a further mechanical erosion of the inner nozzle surface.

These severe conditions usually lead to removal of surface material, due to heterogeneous reactions between oxidizing species in the hot gas and the solid wall

[10], which could be significant also in relatively short single operation determining detrimental effects on the rocket performance. In fact, for rocket converging-diverging nozzle the mass balance equation leads to the following relationship

$$\dot{m}_{ox}\left(1+\frac{1}{OF}\right)=\frac{p_c A_t}{\eta c^*} \tag{1.1}$$

in which $\dot{m}_{ox}$ is the oxidizer mass flow rate, p_c is the chamber pressure, A_t is the nozzle throat area, c^* is the theoretical characteristic exhaust velocity (that primarily depends on the mixture ratio and, to a minor degree, on pressure) and η is the combustion efficiency. Therefore, for a fixed propellant mass flow rate and mixture ratio, the chamber pressure inversely depends on the nozzle throat area. Consequently, throat erosion causes a decrease in the combustion chamber pressure, which in the end results in a reduction of the thrust.

Thus, the requirement that dimensional stability of the nozzle throat should be maintained guaranteeing a stable engine operation makes the selection of rocket nozzle materials extremely challenging.

1.3 Ultra-High-Temperature Ceramic Matrix Composites

At the current state of art, the best structural materials for use in aerospace environments characterized by high temperature and chemical oxidation are limited to silicon-based ceramics, e.g. SiC, C/SiC, SiC/SiC, and protected C/C composites that, unfortunately, boast service temperatures not higher than 2000 K [11–14]. Typical applications include not only components of atmospheric re-entry vehicles but also critical subsystems of propulsion system such as engine intakes, combustion chambers or rocket nozzles. The classical materials used for the latter applications include refractory metals, refractory metal carbides, graphite, ceramics and fibre-reinforced plastics [15–17]. Certain classes of materials demonstrated superior performances

under specific operating conditions but the choice depends on the specific application. For instance, fully densified refractory-metal nozzles generally are more resistant to erosion and thermal-stress cracking than the other materials. Graphite performs well with the least oxidizing propellant but is generally eroded severely [18–20].

To extend the temperature range and develop materials able to withstand larger aero-thermo-chemical loads, Ultra-High-Temperature Ceramic (UHTC) materials have been progressively introduced and are increasingly gaining importance thanks to some relevant characteristics, including melting point above 3250 K, high temperature strength and capability to manage and conduct heat when the service temperature exceeds 2250 K [21–23]. These characteristics allow UHTCs to work in thermo-chemically aggressive environments encountered in the most demanding space applications [24,25]. These materials generally include IV-V transition metal diborides and carbides (i.e. ZrB_2, HfB_2, ZrC, HfC, TaC). Diborides, in particular, although showed lower melting point than carbides, are characterized by substantial thermal conductivity, therefore, they, by uniformly redistributing energy into the material, succeed in relieving temperature gradients and minimizing peak of temperatures nearby stagnation region.

However, at the same time, it was demonstrated that pure UHTCs are excessively vulnerable to oxidation attack, so that there is no way to use them without the addition of a secondary metallic or ceramic phase. Results obtained by intense experimental campaigns realized in suitable supersonic and hypersonic wind tunnels underlined, ultimately, that the use of UHTCs composites added to SiC or other silicon based ceramic in form of particles, short fibres and whiskers have facilitated a considerable improvement of their properties (only at modest temperatures, e.g. below 2000°C), in particular their oxidation resistance [26,27]. It has been found that this solution led to a marked improvement in damage tolerance and better thermal shock resistance in chemically extreme reactive environments, characterized by the presence of dissociated oxygen. The addition of SiC to ZrB_2 made it possible to exploit the formation, following oxidation, of a surface layer of silica, silicon dioxide, which would be able to preserve the composite material from erosion phenomena at relatively high temperatures (up to about 2000°C).

Anyway, the majority of UHTC-made components, despite the very good oxidation resistance, unfortunately, turned out to be fragile, characterized by low fracture toughness, low thermal shock resistance and lack of damage tolerance and exhibited poor reliability, particularly in large scales components often subjected to critical failures in high enthalpy flows.

For instance, TPS systems such as nosecones and leading edges entirely based on bulk, unreinforced UHTC ceramics produced at CNR-ISTEC (the Institute of Science and Technology for Ceramics, of the Italian National Research Council) were successfully tested in lab scale arc jet experiments [28] at the University of Naples "Federico II" (UNINA). Successive experiments in ground simulated re-entry conditions of prototypes with more realistic sizes, however, suffered premature aborting of the test due to a lack of thermal shock resistance and insufficient damage tolerance (Fig. 1.4) [29].

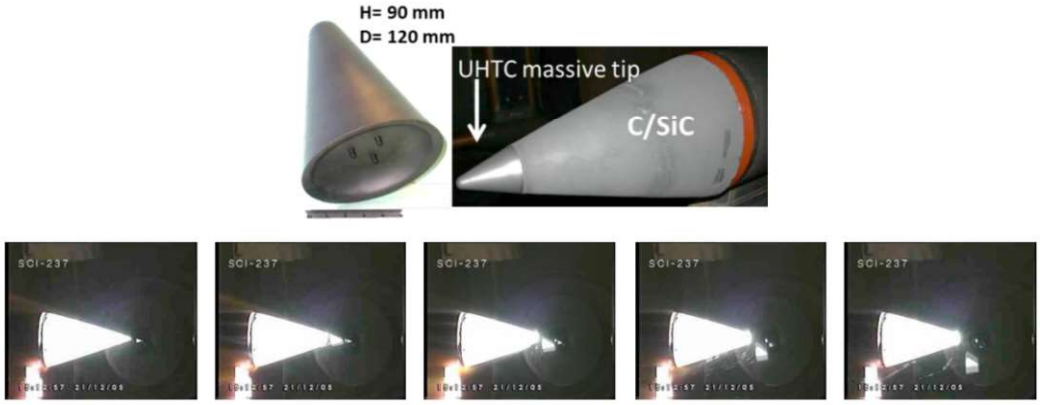

Fig. 1.4. Test of large-scale massive UHTC/C-SiC nosecone in the CIRA SCIROCCO plasma wind tunnel, failing during plasma exposure [29].

On the other hand, in Ref. [10] a tantalum carbide (TaC)-based nozzle throat insert was manufactured and tested in the lab scaled hybrid rocket at the UNINA Aerospace Propulsion Laboratory. Although no erosion occurred in the throat, the outer surface remained unchanged after the test and no visible chemical alteration was observed, radial cracks were detected, as shown in Fig. 1.5, which demonstrated the fragility of this UHTC material.

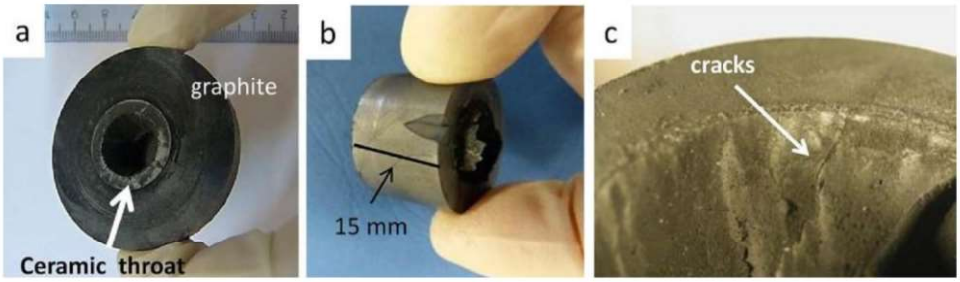

Fig. 1.5. (a) Segmented nozzle (after removal of the converging outer element), (b) ceramic throat, (c) details of the ceramic throat showing radial cracks [10].

Therefore, the current research in aerospace field is oriented to the experimentation of Ultra-High-Temperature Ceramic Matrix Composites (UHTCMC) materials [25,30–33], consisting of a matrix of UHTC reinforced by carbon or SiC fibres that represent, to this day, the best candidates to develop thermal protection systems of new generation hypersonic vehicles, or high-temperature components for rocket engines [34–36].

1.4 Aero-thermo-dynamic characterization of Ultra-High-Temperature Ceramic materials

Based on these considerations, it appears clear that development of materials able to perform properly in such conditions is a topic of major interest. In particular, the ability of surviving exposure to harsh environments without significant oxidation/ablation is one of the key requirements of ceramic materials and relevant experimental characterization is needed. Initial evaluations of high-temperature ablation resistance are often performed relatively inexpensively utilizing high power lasers [37,38], shock tubes [39] and plasma [28,40,41] or oxyacetylene torches [42–45], which can produce significant heat fluxes and ultra-high temperatures. However, as suggested in [46], testing the material performance in an environment representative of hypersonic flight conditions requires a realistic combination of heat flux, gas composition, surface pressure, and flow velocity. An air plasma may exhibit very high temperatures (in excess of 5000 K) and Mach number in excess of 3 with highly

dissociated gas species (oxygen and nitrogen), while a flame in a rocket nozzle reaches supersonic Mach numbers at high pressures (order of 10 bar) in presence of highly reacting chemical species (including in some cases solid metallic particles). On the other hand, oxyacetylene torch produces a confined jet of combustion products (carbon mono/dioxide, water vapor, OH and active hydrocarbon species) at lower (subsonic) Mach number and temperatures in the order of 3000 K. The specific total enthalpies are relatively lower than in typical atmospheric re-entry conditions or in a supersonic combusting flow in a propulsion application. The flame torch operates at subsonic flow conditions and atmospheric pressure. Therefore, the ablation is generally induced by oxidation and vaporization with weak effects of surface shear stresses. Whereas, in hypersonic re-entry flow or in supersonic flows in nozzles of rockets, ablation is additionally enhanced by high-velocity-induced mechanical erosion.

The above-mentioned facilities are thus convenient especially for preliminary, qualitative evaluation of the thermal shock and ablation resistance properties of different materials. Instead, a hypersonic wind tunnel is the only facility able to provide the real gas flow conditions and aerodynamic loads at the realistic static and dynamic pressures to simulate real flight environments and related fluid-solid surface interactions for characterization of materials for aerospace Thermal Protection Systems [47,48]. Also, materials for rocket components can be tested by means of similar low-cost techniques but the most relevant thermo-fluid-chemical environment can only be reproduced in dedicated rocket propulsion facilities [49].

Another important difference is related to the different surface modifications occurring in different gas environments, even if heat fluxes and temperatures are comparable, as demonstrated by previous activities carried out in UNINA facilities. Specifically, in [28], ZrB_2-SiC ceramic samples were exposed to a subsonic plasma jet, at atmospheric pressure. Total enthalpies higher than 10 MJ/kg were reached, for a maximum wall heat flux of 7 MW/m^2, corresponding to a maximum temperature of 2200 K. Scanning Electron Microscope (SEM) analyses performed after the test showed the formation of a glassy layer, protecting the external surface directly facing the oxidizing environment (Fig. 1.6a). On the other hand, the characterization of samples with the same composition in arc-jet facility, with supersonic flow and low

partial pressure (in the order of some kPa) conditions resulted in a different material surface behaviour [50]. In this case, although lower heat fluxes (3.5 MW/m^2) and maximum temperatures (2000 K) were reached (but with a specific total enthalpy of 18 MJ/kg), the coating was wiped away and the oxidation proceeded faster, leaving a more catalytic oxide scale (Fig. 1.6b). This demonstrates once more that, even reproducing the same chemical environment, the material response is significantly influenced by the operating conditions.

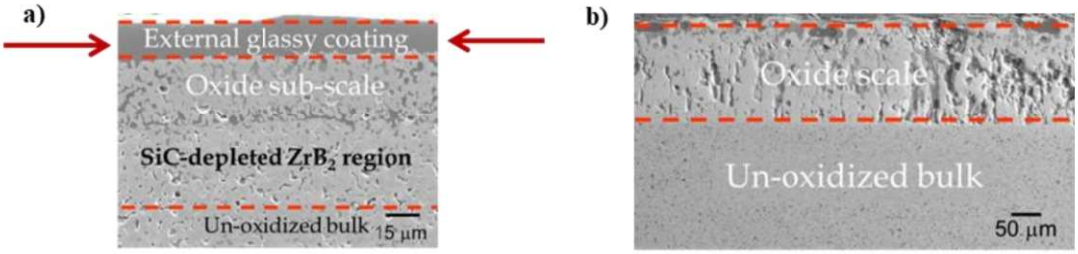

Fig. 1.6. Cross-section of a ZrB2–15SiC material (a) after subsonic plasma torch testing (at atmospheric pressure) [28] and (b) after supersonic arc-jet testing (at low pressure) [50].

It is also known that the worst environment for UHTC and UHTCMC ablation should be at the maximum heat flux and at the lowest possible pressure. In fact, under well-known values of the temperature-pressure domain, SiC suffers an active oxidation with significant mass losses (Fig. 1.7) [51]. Therefore, the transition from passive to active oxidation of UHTCMCs materials based on SiC fibres takes place at the lowest pressures. Furthermore, also for Si-free ZrB_2-based ceramic composites (e.g. with carbon fibres) low partial pressure conditions are critical in terms of ablation behaviour, since the glassy phase formed by boron oxides is actively removed at high temperatures and low pressures. At reduced pressures significant mass losses (ablation) may occur, making this phenomenon interesting to be investigated.

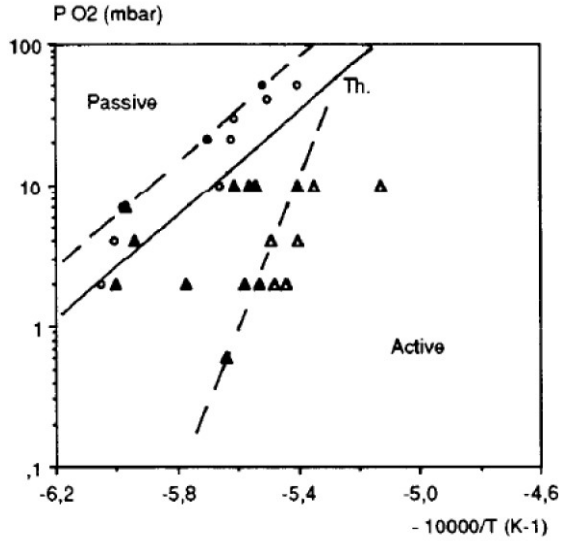

Fig. 1.7. Oxygen partial pressure versus temperature for the active to passive transition of SiC under molecular (o) and (Δ) dissociated air [51].

Another important example of the effect of peculiar test conditions on material surface modifications is the *spontaneous temperature jump phenomenon* first reported by Marschall [52] and then found also by other authors [47,50,53–59]. When a sample of material in presence of SiC-containing MeB_2 ceramics or C_f-SiC based CMC is exposed to a flow of constant total enthalpy for some minutes, the surface temperature, after having reached an apparent steady state, exhibits an abrupt jump of several hundreds of degrees under the same free stream conditions. A number of interpretations were proposed: - the loss of protective silica glass which substantially increases the chemical component of heat flux delivered to the surface [52]; - a transition from passive to active oxidation of SiC [47,53,54]; - an enhanced catalytic recombination of N_2 due to the presence of Si(g) [55]; - an accelerated oxygen diffusion rate through new formed cracks which promotes exothermic reactions of oxidation and nitridation [54,56]; - a surface chemical modification which alters emissivity and catalycity [50,57]. Despite the variety of interpretation, a sound consensus on one of them has not been reached yet, making this topic extremely interesting to be investigated in order to achieve a global comprehension of UHTCs and UHTCMCs behaviour in the most demanding (and relevant) conditions.

1.4.1 Role of numerical simulations

Due to the complexity of the flow conditions generated in high-enthalpy plasma wind tunnels and lab-scaled rocket engines [60,61], computational tools play an important role as support to the design of arc-jet and rocket tests, making possible an accurate prediction of the aero-thermo-chemical flow field in different operating conditions and also to rebuild the thermal field inside the samples [62,63]. For example, the most interesting parameters, such as heat flux to material samples, can be somehow measured by means of dedicated devices. Unfortunately, not all the realistic experimental conditions can be reliably reproduced. For instance, only cold-wall heat fluxes can be directly measured, but information about the thermal loads on samples heated at ultra-high temperatures cannot be obtained by conventional measurement techniques. In general, some of the critical parameters, such as flow temperature or chemical species mass fractions, are measurable only by expensive and complex techniques, thus these parameters need to be rebuilt *a posteriori* by means of appropriate computational models, and by a combination of numerical and experimental results.

In the framework of this topic, it is extremely interesting to evaluate the effect of material properties, such as thermal conductivity, or surface emissivity and catalycity, which can substantially alter the material response to ultra-high-temperature heating. For instance, a significant interest has been shown in recent studies for numerical/experimental determination of surface catalytic efficiency [64–68]. Numerical simulations offer the possibility to perform parametric analyses of the individual effect of each property, providing a step-by-step improvement of the understanding of experimental results.

1.5 The C^{3}HARME European Project

In the framework of the European Union's Horizon2020 research and innovation program, University of Naples "Federico II" has been involved in the C^{3}HARME (Next Generation Ceramic Composites for Combustion Harsh Environments and Space) research project, whose main purpose is the design, development, manufacturing and testing of a new class of UHTCMCs suitable for application in severe aerospace environments. The project was meant to bring the Proof-of-Concept of these new materials into two main applications:

- Near zero-ablation thermal protection systems (tiles) able to resist the very high heat fluxes in strongly reactive gases and thermo-mechanical stresses found at launch and re-entry into Earth's atmosphere.
- Near zero-erosion nozzle inserts that can maintain dimensional stability during firing in combustion chambers of high-performance rockets for civil aerospace propulsion.

The project was structured in a 4-year plan of research activities, aimed at introducing innovative material solutions with high performances and optimizing standard processing techniques in order to manufacture final products suitable for space applications. The research and development activities relied on the integration of extensive existing experience with both UHTCs (ultra-high temperature ceramics) and CMCs (ceramic matrix composites). Well-established techniques for CMC production were integrated with state-of-art methods for the hot consolidation of ultra-refractory ceramics.

The University of Naples "Federico II" has contributed to the definition of the requirements and has been responsible for the prototypes design and the identification of the corresponding testing conditions. An incremental approach was proposed, aiming to start the experimental campaign with simple material samples and increasing the complexity up to a Technology Readiness Level (TRL) 6. The experimental activities were performed also in collaboration with the German Aerospace Centre (DLR) and the large Italian company AVIO S.p.a., in order to characterize the

materials in different experimental conditions, with incremental scale up. The University of Naples "Federico II" performed tests on samples for both applications.

Arc-jet testing included experimentation on small specimens (dimensions in the order of 1.5 cm), with TRL up to 4, in a relevant atmospheric re-entry environment, Fig. 1.8. Characterizations allow identifying the most promising material compositions and manufacturing processes, before starting experimental activities on larger and more complex geometries, that were carried out at DLR facilities, until a complete TPS assembly test, which allowed achieving a TRL 5.

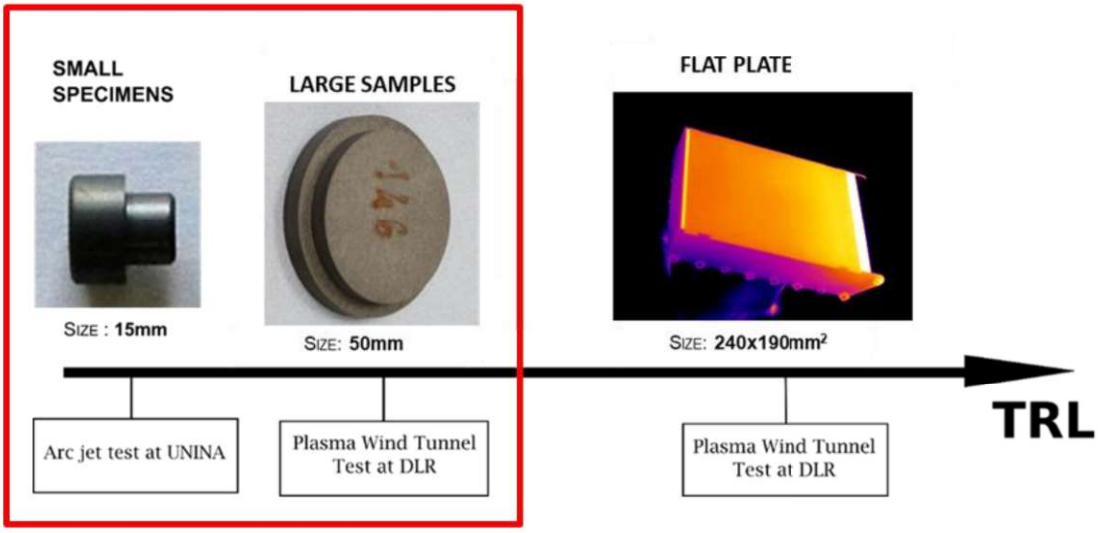

Fig. 1.8. Design of prototypes tested in arc jet facilities at the University of Naples "Federico II" and DLR in C³HARME Project. The red square highlights the test configurations included in this thesis.

The reference mission for the UHTCMC thermal protection systems in the C³HARME project, defined by ARIANEGroup, is the re-entry from Low Earth Orbit (LEO) of Advanced Re-entry Vehicle (ARV) re-entry module spacecraft. The complete set of aero-thermo-dynamic requirements, has been deduced from nominal and abort trajectories of the reference mission, as shown in Table 1.1. Table 1.2 shows the main environmental requirements for the materials for this application.

Table 1.1. Aero-thermo dynamic parameters for critical points on front shield of the ARV capsule.

Re-Entry type	Max heat flux [MW/m^2]	Max Pressure [kPa]	Heat load [MJ/m^2]	Remarks
Guided	0.684	13	211	Guided, highest heat load
Abort	1.988	45	98	Abort, highest heat flux
Abort	0.749	65	42	Abort, highest pressure

Table 1.2. Aero-thermo-dynamic requirements for TPS characterization.

Parameter	Specification	Remarks
Maximum stagnation pressure	64.79 kPa	From abort trajectory
Peak Heat Flux	1.988 MW/m^2	From abort trajectory
Integrated Heat Load	211.2 MJ/m^2	From nominal trajectory

The arc-jet facilities considered in this thesis (whose details are presented in next section) are not able to guarantee the maximum heat flux requirement (2 MW/m^2) and the maximum required pressure (more than 60 kPa) simultaneously. However, from Table 1.1 it can be noticed the critical conditions for both heat flux and pressure requirements, corresponding to the abort (ballistic) re-entry scenario, are obtained in different points of the TPS and different moments of the trajectory, so the materials shall not withstand simultaneously the maximum heat flux at the maximum pressure and for the maximum integrated heat load. Moreover, as highlighted in the previous section, the most demanding condition for SiC-containing UHTCs ablation corresponds to high temperature and low pressure, because of passive/active SiC oxidation transition, so that the tests that will be presented will be somehow even more demanding than the requirements in terms of ablation resistance.

Also referring to the second application, near-zero erosion rocket nozzles, an incremental approach has been used for prototype design, proposing to start the experimental campaign with simple material samples and increasing the complexity up to a TRL 6, as shown in Fig. 1.9. The experimental activities for this application were carried out in UNINA test facilities, the AVIO laboratory and DLR facilities.

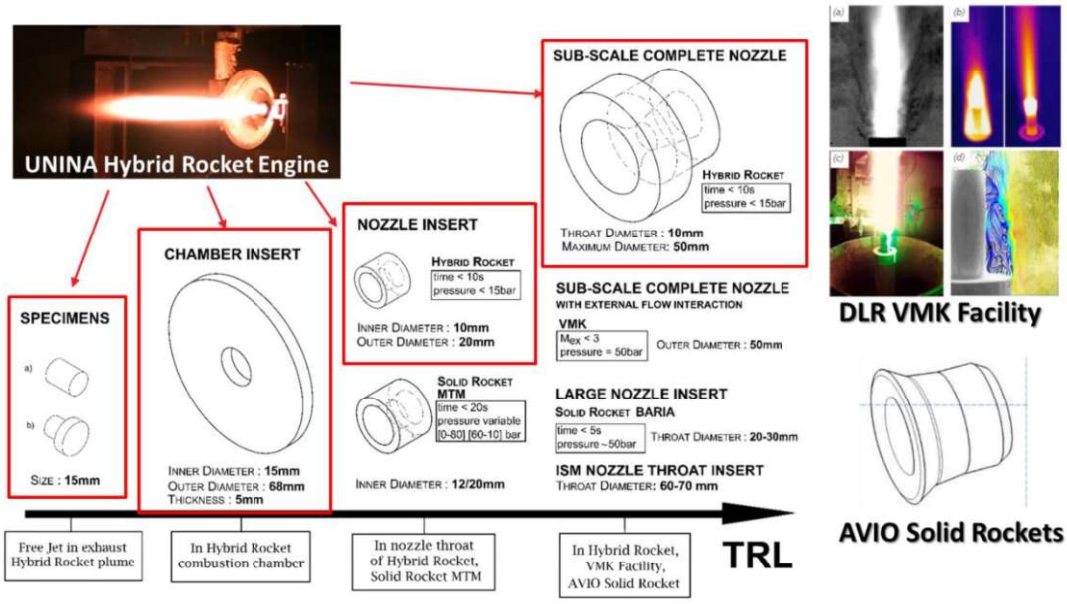

Fig. 1.9. Design of the test articles for C^{3}HARME experimental campaign for characterization of UHTCMCs in propulsion application. The red squares highlight the test configurations included in this thesis.

Requirements for solid and hybrid rocket applications have been set in collaboration with AVIO. Table 1.3 summarizes typical operating conditions and design ranges encountered in solid (SRM) and hybrid rocket (HRM) chamber and nozzle.

Table 1.3. Solid and hybrid rocket nozzle operating conditions.

	Range SRM	**Range HRM**
Pressure [bar]	50-100	5-25
Combustion time [s]	70-150	>10
Throat diameter [K]	0.1-1	0.1-0.2
Throat flame temperature [K]	≈3000 K	≈3000 K
Throat heat flux [MW/m^2]	5 - 30	5 - 15

1.6 Summary of original contributions of the present dissertation

The research goals of this thesis work are the characterization of the aero-thermo-dynamic response of innovative ceramic materials for high-temperature space applications, with different formulations, sizes and shapes, in lab-reproduced representative environments, and the definition and employment of numerical models for the simulation of the thermo-fluid-dynamic conditions and material thermal behaviour.

Regarding research for hypersonic TPS materials, an extensive experimental campaign has been first carried out, in the framework of the C^3HARME project, for the characterization of UHTCMC materials with almost zero erosion properties at ultra-high temperature, comparing materials with different formulations, fibre/matrix architecture, and manufacturing process. Relevant tests were performed in an arc-jet supersonic wind tunnel, where the typical aero-thermodynamic and chemical conditions of atmospheric re-entry are reproduced at supersonic Mach numbers, temperatures above 5000 K and a consistent amount of dissociated oxygen and nitrogen. Non-intrusive diagnostic techniques (two-colour pyrometers and infrared thermo-cameras) were used to continuously monitor samples surface temperatures during testing. Based on interesting results achieved with material samples based on ZrB_2-SiC, both in terms of ablation resistance and of a series of phenomena observed at ultra-high-temperatures, further experiments were carried out for a more detailed investigation of these materials aero-thermal response. Specifically, a series of dedicated test campaigns has been carried out in order to understand the effect of SiC content on the ultra-high-temperature oxidation and material behaviour under simulated re-entry conditions. Moreover, a further test campaign allowed comparing the material response in different chemical atmospheres (simulated air and pure nitrogen flows). Finally, a part of the PhD activities has been spent at the premises of DLR Institute of Aerodynamics and Flow Technology, in Cologne (Germany), where tests were carried out in a larger scale arc-jet supersonic plasma wind tunnel for the second step of UHTCMCs characterization in stagnation point configuration.

The outcomes of all these experimental activities are presented and discussed, also in light of the post-test characterizations carried out, in collaboration with project partners, to investigate the features of the materials microstructures after the exposure to the atmospheric re-entry environment. Moreover, the experimental results are complemented by Computational Fluid Dynamics (CFD) simulations, employed to allow accurate prediction not only of the thermo-fluid-dynamic flow field around the test articles, but also of the thermal behaviour of the materials samples, including an investigation of the effect of material properties, such as thermal conductivity and catalycity.

Specifically, a rapid temperature increment during the highest-enthalpy steps (the phenomenon known as *temperature jump* in the relevant literature regarding UHTCs and SiC-based ceramics, as discussed above) has been observed. This thesis intends to propose a thorough and detailed analysis of the materials aero-thermo-dynamic behaviour at ultra-high temperatures in a representative re-entry environment, aiming to provide a comprehensive interpretation of the *temperature jump*, correlating the outcomes of infrared temperature measurements, post-test microstructural analyses and numerical simulations to highlight the parameters which mainly affect the heat transfer from the flow to the ceramic. A deep understanding of the materials response is indeed an important step in the path towards a reliable engineering application of these novel TPS technologies.

The other research topic is characterization of the same class of materials, developed within the framework of C^3HARME, for near-zero erosion rocket nozzles. The experimental activities were carried out with the hybrid rocket test bench available at the aerospace propulsion laboratory of the UNINA Department of Industrial Engineering, in different test configurations, according to the scheme of Fig. 1.9. In particular, the first tests have been performed with a novel, dedicated test set-up exposing UHTCMC samples to the supersonic exhaust jet of a 200 N-class hybrid rocket operated with gaseous oxygen burning cylindrical port HDPE grains. Non-intrusive diagnostic equipment, including two-colour pyrometers and an infrared thermo-camera, has been employed to monitor the surface temperature of the samples. The combination of combustion temperature over 3000 K, supersonic Mach number

and stagnation pressures allowed reproducing realistic rocket nozzles operating conditions, in order to demonstrate the ability of the specimens to preserve their functional integrity in a relevant environment. The second set-up ("Chamber insert test") was meant to assess the capability of the test article (in the shape and size of an annular combustion chamber element) to withstand high thermo-mechanical stress at high pressures in relevant aero-thermo-chemical combustion environment. As a third step, UHTCMC nozzle throat inserts have been manufactured and experimentally tested to verify the erosion resistance and evaluate the effects on the rocket performance by comparison with those obtained in similar operating conditions employing a graphite nozzle. Finally, complete subscale nozzles, made by different processing routes, matrix formulations, fibres architectures and having different properties (such as fibre volume content and porosity), were repeatedly tested in order to select the most promising technology for reusable non-eroding rocket nozzles.

Also in this case, CFD models were proposed and used to characterise the flow field in the different test configurations, evaluate the test conditions experienced by the prototypes, and in some cases to analyse the steady or unsteady thermal response of the materials. Combining experimental and numerical results, general conclusions were drawn about the effect of different parameters, such as matrix composition, fibre architecture and volume content, densification process and final material porosity.

1.7 List of publications

Part of the results presented in this PhD thesis have been published in the following journal articles and conference proceedings.

Journal articles

- **Mungiguerra S.**, Cecere A., Savino R., Saraga F., Monteverde F., Sciti D., Improved aero-thermal resistance capabilities of ZrB2-based ceramics in hypersonic environment for increasing SiC content, *Corrosion Science*, Vol. 178, January 2021, 109067, ISSN: 0010938X, doi: https://doi.org/10.1016/j.corsci.2020.109067

- **Mungiguerra S.**, Di Martino G.D., Savino R., Zoli L., Silvestroni L., Sciti D., Characterization of novel ceramic composites for rocket nozzles in high-temperature harsh environments, *International Journal of Heat and Mass Transfer*, Vol. 163, December 2020, 120492, ISSN: 00179310, doi: doi.org/10.1016/j.ijheatmasstransfer.2020.120492
- **Mungiguerra S.**, Di Martino G.D., Cecere A., Savino R., Zoli L., Silvestroni L., Sciti D., Ultra-High-Temperature Testing of Sintered ZrB_2-based Ceramic Composites in Atmospheric Re-entry Environment, *International Journal of Heat and Mass Transfer*, Vol. 156, August 2020, 119910, ISSN: 00179310, doi: doi.org/10.1016/j.ijheatmasstransfer.2020.119910
- Sciti D., Zoli L., Vinci A., Silvestroni L., **Mungiguerra S.**, Galizia P., Effect of PAN-based and Pitch-based carbon fibres on microstructure and properties of continuous Cf/ZrB2-SiC UHTCMCs, *Journal of the European Ceramic Society*, In Press, ISSN: 09552219, doi: doi.org/10.1016/j.jeurceramsoc.2020.05.032
- **Mungiguerra S.**, Di Martino G.D., Zuppardi G., Computational Evaluation of Aero-Thermo-Dynamic Loads and Effect of Catalyticity in an Arc-Jet Wind Tunnel, *Journal of Aerospace Engineering*, Vol. 33, Issue 3, May 2020, ISSN: 08931321, doi: 10.1061/(ASCE)AS.1943-5525.0001114
- Silvestroni L., **Mungiguerra S.**, Sciti D, Di Martino G.D., Savino R., Effect of hypersonic flow chemical composition on the oxidation behavior of a super-strong UHTC, *Corrosion Science*, Vol. 159, October 2019, Article n. 108125, ISSN: 0010938X, doi: 10.1016/j.corsci.2019.108125
- **Mungiguerra S.**, Di Martino G.D., Cecere A., Savino R., Silvestroni L., Vinci A., Zoli L., Sciti D., Arc-jet wind tunnel characterization of Ultra-High-Temperature Ceramic Matrix Composites, *Corrosion Science,* Vol. 149, April 2019, Pages 18-28, ISSN: 0010938X, doi: 10.1016/j.corsci.2018.12.039
- Savino R., **Mungiguerra S.**, Di Martino G.D., Testing ultra-high temperature ceramics for thermal protection and rocket applications, *Advances in Applied Ceramics: Structural, Functional and Bioceramics,* Vol. 117, sup. 1, 2018, Pages s9-s18, ISSN: 17436753, doi: 10.1080/17436753.2018.1509175

- Savino R., Criscuolo L., Di Martino G.D., **Mungiguerra S.**, Aero-thermo-chemical characterization of Ultra-High-Temperature Ceramics for aerospace applications, *Journal of the European Ceramic Society,* Vol. 38, No. 8, July 2018, Pages 2937-2953, ISSN: 09552219, doi: https://doi.org/10.1016/j.jeurceramsoc.2017.12.043

Conference proceedings

- **Mungiguerra S.**, Esser B., Savino R., Sciti D., Binner J., Lagos M. A., Schoberth A., Gottschalk N., Aero-thermo-dynamic Characterization of Large-scale Near-zero Ablation Thermal Protection Systems in Ultra-High-Temperature Ceramic Matrix Composites, *71st International Astronautical Congress (IAC)*, IAC-20.C2.4.x58731, Virtual conference, October 2020
- **Mungiguerra S.**, Di Martino G. D., Cecere A., Savino R., Monteverde F., Effect of SiC concentration on aero-thermal behavior of ZrB_2-based ceramics in hypersonic environment, *70th International Astronautical Congress (IAC)*, IAC-19-C2.4.4.x50232, Washington D.C., USA, October 2019
- Di Martino G. D., **Mungiguerra S.**, Cecere A., Savino R., Vinci A., Zoli L., Sciti D., Ultra-High-Temperature Ceramic Matrix Composites for Hybrid Rocket Nozzles, *70th International Astronautical Congress (IAC)*, IAC-19.C4.5.7.x50235, Washington D.C., USA, October 2019
- **Mungiguerra S.**, Di Martino G. D., Cecere A., Savino R., Zoli L., Silvestroni L., Sciti D., Experimental investigation on sintered UHT-CMC composites for Combustion Harsh Environments and Space, *10th International Conference on High Temperature Ceramic Matrix Composites (HT-CMC10)*, Bordeaux, France, September 2019
- **Mungiguerra S.**, Di Martino G. D., Cecere A., Savino R., Zoli L., Silvestroni L., Sciti D., Characterization of Carbon-fiber reinforced Ultra-High-Temperature Ceramic Matrix Composites in arc-jet environment. *69th International Astronautical Congress (IAC)*, IAC-18.C2.4.4.x47335, Bremen, Germany, October 2018

- Di Martino G. D., **Mungiguerra S.**, Cecere A., Savino R., Vinci A., Zoli L., Sciti D., Hybrid rockets with nozzles in Ultra-High-Temperature Ceramic Composites. *69th International Astronautical Congress (IAC)*, IAC-18.C4.3.6.x47333, Bremen, Germany, October 2018
- **Mungiguerra S.**, Di Martino G.D., Savino R., Zoli L., Sciti D., Lagos M.A., Ultra-High-Temperature Ceramic Matrix Composites in Hybrid Rocket Propulsion Environment, *2018 International Energy Conversion Engineering Conference, AIAA Propulsion and Energy Forum,* Cincinnati, OH, July 2018 (AIAA 2018-4694), doi: https://doi.org/10.2514/6.2018-4694, ISBN: 978-1-62410-571-5

CHAPTER 2. EXPERIMENTAL FACILITIES

This chapter describes the experimental facilities used in this thesis for the characterization of ceramic materials in relevant harsh environments. Section 2.1 presents the small-scale arc-jet wind tunnel SPES, available at the University of Naples "Federico II". Section 2.2 describes the plasma wind tunnel L3K, available at DLR. Section 2.3 presents the hybrid rocket test bench available at UNINA, while its subsections describe the different set-ups used for materials characterization.

2.1 SPES arc-jet wind tunnel

SPES (Small Planetary Entry Simulator, Fig. 2.1) is a continuous, open-circuit, blow-down arc-jet wind tunnel, provided with a torch (Perkin-Elmer 9MB-M) with maximum power of 80 kW, able to operate with inert gas (He, N_2, Ar and their mixtures), which is connected, downstream, to a mixing chamber and then to a conical convergent/divergent nozzle exhausting into the test chamber where pressure is lowered by two vacuum pumps in series, a mechanical booster (EH4200) and radial pump (E2M275). This vacuum system is able to achieve a static pressure of 10 Pa in the test chamber. The torch, the mix-chamber and the nozzle are cooled by water flowing in a double wall.

A nitrogen plasma is generated by the industrial torch at mass flow rates up to 5 g/s. In order to simulate the air composition, the mixer downstream the torch is used to supply a secondary gas (e.g. O_2) to the primary plasma. Specific total enthalpies above 20 MJ/kg are achieved at gas mass flow rate of 1g/s. The convergent-divergent conical nozzle is characterized by a throat diameter of 11 mm, and an outlet diameter of 22 mm and is able to accelerate the flow up to a nominal Mach number about 3. A schematics of the facility is shown in Fig. 2.2.

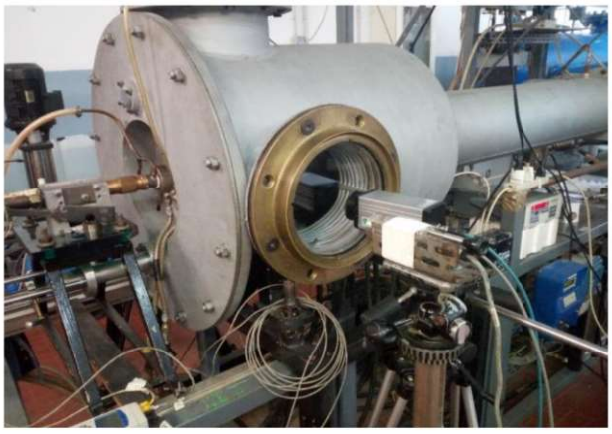

Fig. 2.1. SPES Arc-heated facility available at the University of Naples.

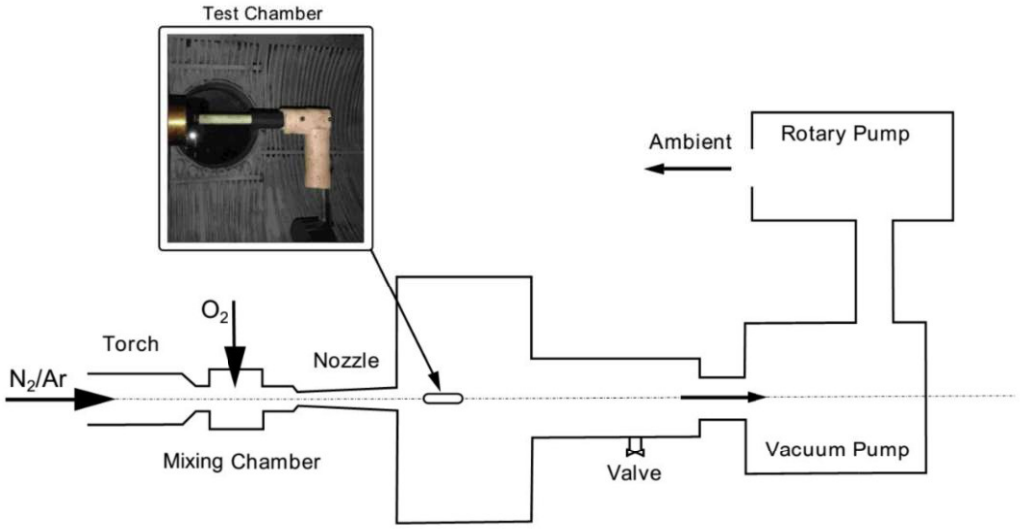

Fig. 2.2. Schematics of UNINA SPES laboratory.

The test articles (nominal design in Fig. 2.3a,b) were accommodated inside the test chamber of the plasma wind tunnel, at the exit of the supersonic nozzle, by using a dedicated set-up with thermally protected mechanical supports (Fig. 2.3c). The position was regulated to place the sample at the desired distance from the nozzle. In the current test campaigns, the samples were placed at a distance of 1 cm from the nozzle.

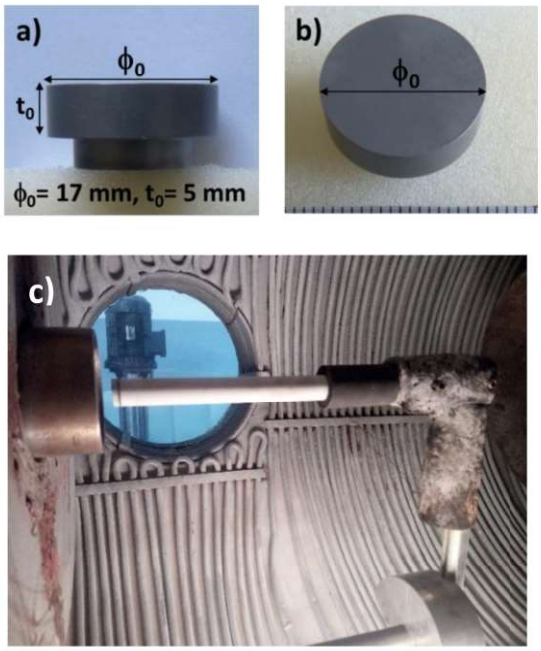

Fig. 2.3. (a-b) Design of UHTCMC sample to test in UNINA SPES facility, (c) a picture of the mechanical support for the test article mounted inside the test chamber.

In the test campaigns discussed in this thesis, samples were exposed to a supersonic flow generated by the expansion of a high enthalpy gas mixture of nitrogen (0.8 g/s) and oxygen (0.2 g/s). During the test, the arc power of the plasma torch and consequently the total enthalpy of the flow are gradually increased through successive increments, leading correspondingly to an increase of pressure and temperature. A quasi-stationary condition generally occurs when the maximum value of temperature is reached during the last steps of the test. In the tests discussed in the present report, the nominal duration of each step was 30 seconds, except for the last step of 120 seconds. As shown below, some tests had a different duration. The total specific enthalpy is obtained through an energy balance at the exit of the plasma torch, based on measurement of temperature and flow rate of cooling water, according to the following formula:

$$H_0 = \frac{VI + c_{g1}\dot{m}_{g1}T_{g1}^i + c_{pg2}\dot{m}_{g2}T_{g2}^i - c_{pw}\dot{m}_w\Delta T_w}{\dot{m}} \tag{2.1}$$

in which H_0 is the Mean Total Specific Enthalpy at the nozzle exit, VI the power provided by the arc heater to the gas, $\dot{m}_{g1}$ and $\dot{m}_{g2}$ represent the mass flow rates of the gas in the primary line and in the secondary line respectively, T_{g1}^{i} and T_{g2}^{i} the initial temperatures of the gases, $\dot{m}_w$ the mass flow rate of the water in the cooling line of the torch and the nozzle and ΔT_w the delta temperature of the water at the end of the cooling line, $\dot{m}$ the total gas mass flow rate, c_{pg1}, c_{pg2} and c_{pw} the specific heat values at constant pressure of the gases and the water.

In Table 2.1, the typical values of the physical quantities of interest for each torch arc power step are reported. Specific total enthalpy values are averaged over different test, with an uncertainty around ±1 MJ/kg. Heat fluxes were measured by a copper slug calorimeter. The pressure in the test chamber was approximately equal to 2 mbar. At the end of the most stressful enthalpy step, the torch power was decreased gradually until facility shutdown, resulting in a stepwise cooling of the buttons.

Table 2.1. Test conditions in SPES facility.

Step	H_0 [MJ/kg]	Heat Flux - Slug Calorimeter [MW/m^2]	Stagnation Point Pressure [mbar]
0	5.5	0.8	62
1	7.0	0.95	64
2	8.5	1.1	67
3	10	1.5	70
4	12	2.0	73
5	14	2.5	76
6	16	3.0	79
7	18	3.6	82
8	20	4.2	85

The surface temperature of the samples was continuously measured (±1% instrumental accuracy) by digital two-colour pyrometers (Infratherm ISQ5 and IGAR6, Impac Electronic GmbH, Germany) at an acquisition rate of 100 Hz. In addition, the infrared response of the specimen during the arc-jet testing was obtained by means of an infrared (IR) thermo-camera (TC, Pyroview 512N, DIAS Infrared GmbH, Germany). The two-colour ISQ5 pyrometer exploits two overlapping infrared wavelength bands at 0.7–1.15 μm and 0.97–1.15 μm to measure the temperature from

1273 K up to 3273 K. The IGAR6 pyrometer operates in the bands 1.5-1.6 μm and 2.0-2.5 μm to return the sample temperature in the range 523-2273 K. The measurement area of the ISQ5 pyrometer is approximately a round spot 3.3 mm in diameter. The pyrometers mode can be set in order to give back the peak value of the temperature field detected inside the focused area. In addition, the so-called "two-colour mode" provides an output value independent on the (directional) spectral emittance (ε_λ). It is generally assumed that the observed surface behaves as a grey body over the operating temperature range. Surface chemical reactions occurring during testing can have been responsible for changes in ε_λ versus testing time. On one hand, the two-colour pyrometers overcome this problem measuring the true temperature. On the other hand, the IR-TC detects the spectral radiance coming out from the heated sample along the infrared band wavelength of 0.8-1.1 μm. The surface temperature distribution can be calculated assuming constant emissivity along the monitored surfaces of the samples and taking into account the axial symmetry of the specimens. Once the local temperature was measured thanks to the pyrometers at the measurement spot, that value was input to determine the spectral emittance in the range of the IR-TC, and finally the surface temperature distribution was evaluated. The operating wavelength is that in which most of the radiative power is emitted at ultra-high temperatures [69], which reduces the error in temperature estimation due to spectral emittance uncertainty (an error of 10% in emissivity leads to an error of about 1% in temperature). High-Definition videos of the tests were recorded by means of a Camera Flea3 1.3 MP Color USB3 Vision with a resolution of 1328x1048 and a frame rate equal to 25 fps. A picture of the optical and infrared setup in shown in Fig. 2.4.

A balance (1 mg accuracy) and a precision calliper (0.01 mm accuracy) were used to measure mass and thickness losses of the specimen. In the post-processing analyses, two erosion rates were calculated: one based on the loss of mass (assuming uniform consumption of the sample in the axial direction) and the other evaluated by the thickness measurement made by the calliper.

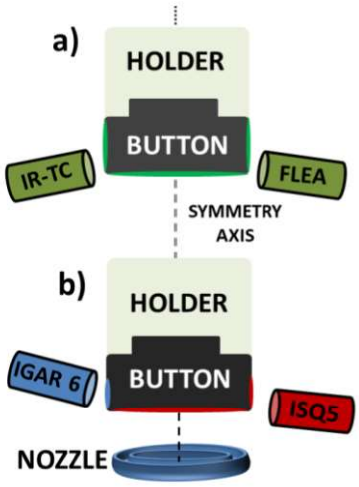

Fig. 2.4. Arrangement of pyrometers ISQ5 and IGAR6 (a), and infrared (IR) thermo-camera (TC) with video recorder FLEA (b): the coloured portions of the button surface match diagnostics and their field of view.

2.2 L3K hypersonic plasma wind tunnel

As described in section 1.5, the qualification tests of the UHTCMCs in the framework of the C^{3}HARME project were designed according to an incremental approach, with a progressive increase in the size of the samples. Based on this, a part of the PhD was spent in the premises of DLR (German Aerospace Centre) in Cologne, Germany, where tests on larger-sized samples in stagnation point configuration were carried out. The qualification tests were performed in DLR's arc-heated facility L3K, which is part of DLR's arc-heated facilities LBK (LichtbogenBeheizter WindKanal) in Cologne. A picture of L3K is shown in Fig. 2.5. L3K is setup very similar to a conventional hypersonic blow-down wind tunnel, complemented by a segmented arc-heater with a maximum electrical power of 6 MW, which allows for energising the working gas to high enthalpy conditions.

For thermal testing, samples and models were placed in the homogeneous hypersonic free stream, which was generated by a convergent-divergent nozzle. The nozzle is modular, its expansion part is conical with a half angle of 12°. Different throat diameters from 14 mm to 29 mm are available and can be combined with nozzle exit diameters of 50 mm, 100 mm, 200 mm, and 300 mm. So, the facility setup can

effectively be adapted to specific requirements. With this facility setup, thermal protection materials and structures can be tested for atmospheric entry conditions at flight-relevant heat fluxes and pressures. The test conditions provide a realistic chemical environment. Accordingly, the effects of surface catalycity and surface reactions are properly included in the specimens thermal response.

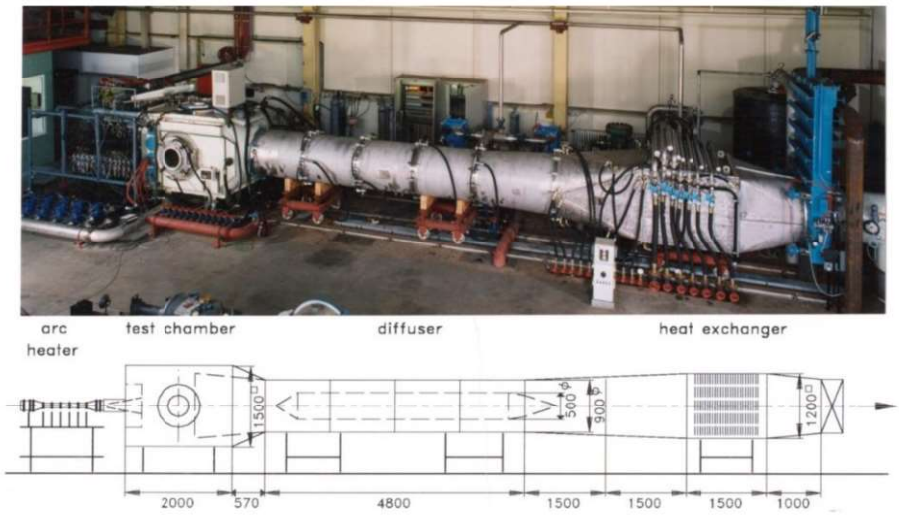

Fig. 2.5. The L3K facility. Dimensions in mm.

In L3K cold wall heat flux rates of more than 12 MW/m^2 can be achieved on a 50 mm flat-faced cylinder sample at stagnation pressures up to 1500 hPa. In general, stagnation point models with a diameter up to 150 mm can be tested in L3K. For flat plate models, the size is limited to a width of 280 mm, a length of 350 mm and a height of 70 mm. A detailed description of the LBK facility is given in [70,71].

In compliance with the reference C^{3}HARME mission (section 1.5), all tests in L3K were performed with air as working gas. The stagnation tests were performed on circular samples with a diameter of 50 mm. The nominal sample geometry is illustrated in Fig. 2.6. The baseline samples (Fig. 2.6a,b) had a mushroom shape with an overall thickness of 10 mm. In the bottom half, the diameter was reduced to 42.5 mm in order to fit into the ceramic shell of the model holder. The mushroom-type geometry could not be realized with one of the tested processing routes, since sample thickness was restricted to a maximum value of 4 mm for this process. Therefore, those samples were prepared as conical disks (Fig. 2.6a,c).

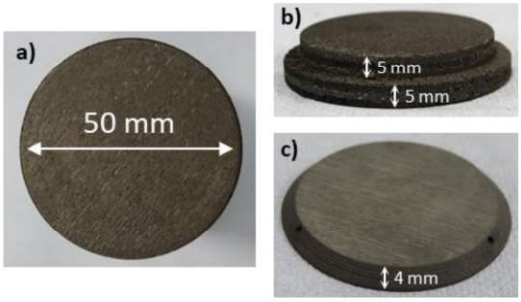

Fig. 2.6. Pictures and main dimensions of stagnation samples: a) front view, b) rear view (mushroom type), c) rear view (disk type).

The complete test assembly for the mushroom samples is shown in Fig. 2.7a. Its overall geometry was a sharp-edged flat-faced cylinder. The head of the sample was forming the front part. Three ceramic pins were used to fix the sample to the ceramic shell. At the bottom, the sample was in touch with a large block of insulation material. Due to the insulation, the thermal response of the sample was not being influenced by the water-cooling of the model holder. For the conical disk samples, also the ceramic shell was modified to a corresponding cone at its front part (Fig. 2.7b). As in the nominal setup, sample fixation was realized by three ceramic pins, and a block of insulation material was installed at the samples rear end.

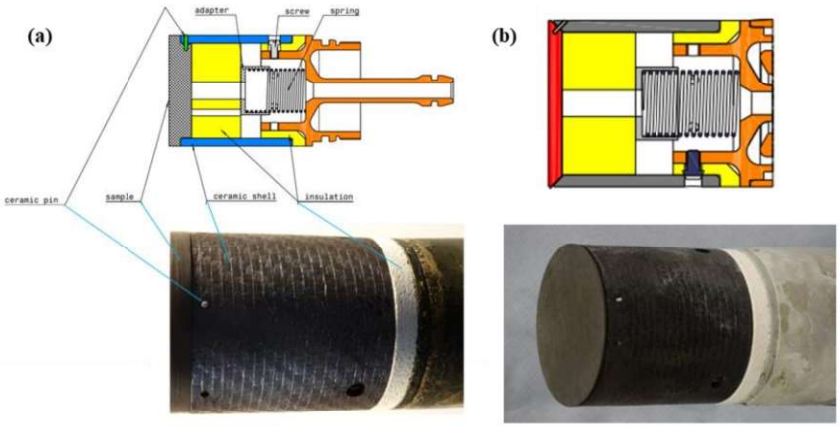

Fig. 2.7. Test assembly used (a) for mushroom-type and (b) for disk-type stagnation samples.

The materials were provided baseline qualification by sustaining the specified values for heat flux rate and integral heat load. In order to make the qualification more representative, three samples of each UHTCMC variant were foreseen. By that,

additional information was achieved on sample-to-sample repeatability and particular influences of a single sample properties on the measured data could be reduced.

Details of the test conditions are listed in Table 2.2. The measured cold wall heat flux rate of 2.39 MW/m^2 matches quite well to the specified heat flux rate of 1.99 MW/m^2. L3K was setup with a 29 mm nozzle throat and a 200 mm nozzle exit for these tests. Based on the specified heat flux rate, a test duration of 106 seconds was defined in order to meet the specified integral heat load.

Table 2.2 Operating and test conditions for the stagnation tests in L3K.

Reservoir conditions	L3K-Q1
Mass flow rate [g/s]	101
Specific enthalpy [MJ/kg]	15.9
Pressure [hPa]	3750
Temperature [K]	6450
N_2 mass fraction	0.645
O_2 mass fraction	$< 10^{-3}$
NO mass fraction	0.016
N mass fraction	0.113
O mass fraction	0.225
Nozzle throat diameter [mm]	29
Nozzle exit diameter [mm]	200
Test location wrt to nozzle exit [mm]	200
Heat flux rate [MW/m^2]	2.39
Stagnation pressure [hPa]	85
Test duration [s]	106

Non-intrusive temperature measurements were performed to record the samples surface temperature. Two different pyrometers, i.e. a spectral pyrometer (Dr. Maurer KTR 1485, temperature range 973-3773 K, wavelength 1µm) and a two-colour pyrometer (Dr. Maurer QKTRD 1485-1, temperature range 1273-3573 K, wavelength 1µm), were adjusted to the stagnation point in the centre of the front surface. The simultaneous measurement of both instruments at the same spot principally allowed to extract additional information on potential changes in the materials emissivity from

the temperature data. In addition to the pyrometer measurements, infrared camera systems (InfraTec VarioCAM HD head 980 HT, temperature range 773-2273 K, wavelength 7.5-14 μm; and Optris PI 1M, temperature range 723-2073 K, wavelength 1 μm) were used for monitoring the thermal response and to obtain information on the homogeneity of heating to the front surface. A principal sketch of the optical setup is given in Fig. 2.8.

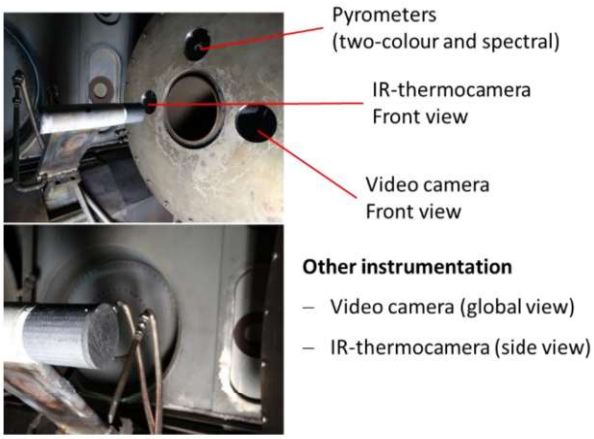

Fig. 2.8. Optical setup for L3K stagnation tests.

In addition to the thermal response data, erosion measurements were taken before and after the tests. Weight and thickness were measured to evaluate the sample mass loss and recession as well as the corresponding time-based rates. All thickness measurements were taken at the centre of the front surface.

During all tests in L3K, the samples and models were exposed to constant flow conditions. This was achieved by applying the following principal test procedure:

- The model assembly with the specimen was mounted to the facility's model support.
- The test chamber was closed and evacuated.
- The arc heater was ignited and the set parameters were gradually changed until the desired operating conditions were reached (during this period the model with the specimen is placed at its park position where it is not exposed to the flow).
- After achieving steady flow conditions, the model was moved to the test position.
- After the specified test duration, the model was moved out of the flow.

- The arc heater was shut down.
- The test chamber was pressurized and opened.

2.3 The Aerospace Propulsion Laboratory

The experimental activities described in this work for the characterization of rocket nozzle materials were carried out at the Aerospace Propulsion Laboratory of University of Naples "Federico II", located in the Military Airport "F. Baracca" of Grazzanise (CE, Italy). The test rig is a versatile set up primarily designed for testing hybrid rocket engines of several sizes [72]. It is equipped with a test bench and a general-purpose acquisition system, which allow evaluating propellant performance and combustion stability [73], testing of sub-components and/or complete power systems, nozzles [10,74], air intakes, catalytic devices [75,76], burners, ignition and cooling systems [77]. For the purposes of the C^3HARME project, the experimental set-up was adjusted for testing materials in harsh combusting environment for propulsion applications.

Several rocket demonstrators of different scales are available for testing at the Laboratory. The experimental firings presented in this thesis were performed with a 200 N-class hybrid rocket whose schematic is depicted in Fig. 2.9.

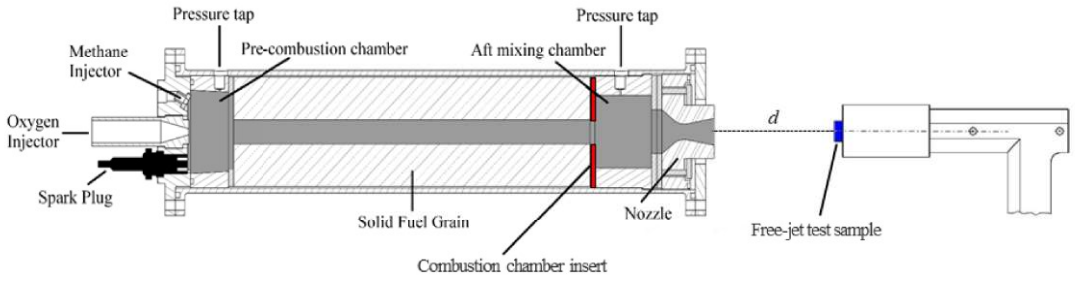

Fig. 2.9. Layout of 200 N-class hybrid rocket engine, including the set-up for UHTCMC testing.

The lab rocket engine has an axisymmetric combustion chamber, with 350 mm length and 69 mm case inner diameter.

The motor forward closure can accommodate different injectors; the tests presented in the following sections were performed with a converging nozzle injector, whose exit section diameter is 6 mm, which delivered oxygen in single-port cylindrical fuel grains.

Upstream and downstream of the solid grain a dump plenum and an aft-mixing chamber were set up. The pre-chamber, which is 25 mm long with a 46 mm inner diameter, shifts the broad oxidizer recirculation towards the fore end of the grain, in order to increase the overall regression rate. The post-chamber is usually required in hybrids to promote gas mixing at the exit of the fuel port, thereby improving combustion efficiency. Aft-mixing chamber with either 38 mm or 58 mm length can be employed with the aim of testing fuel grains of either 240 mm or 220 mm length, respectively. The engine has two pressure taps for static pressure measurements in the pre- and in the post-chamber.

A graphite converging-diverging exhaust nozzle was usually employed. The modular design of the engine allows the use of nozzles with different throat diameter and area ratio. As will be discussed in detail in the following subsections, the graphite nozzle can be easily replaced by segmented nozzles with throat insert or by complete nozzles made of new high performance materials to test their erosion behaviour and structural and thermal resistance for this kind of applications.

A spark plug powered by a Honeywell solid-state igniter spark generator is arranged in the pre-chamber where methane gas is injected for 3 seconds simultaneously with the oxygen to ignite the motor. This system ensures repeatable ignition conditions as well as motor re-ignition.

A schematic of the oxidizer feeding line is depicted in Fig. 2.10. Gaseous oxygen was supplied by a reservoir of 4-6 pressurized tanks connected to the motor feed line. The feeding pressure was then set by means of the TESCOM ER3000 electronically controlled pressure valve, which regulated an electro-pneumatic valve in order to reduce the pressure to the desired set point. The control was performed on the basis of the pressure signal measured by a transducer located downstream the regulator. The presence of a chocked Venturi tube before the injector ensured that the set feeding pressure was directly proportional to the desired oxygen mass flow rate. The same

device allowed the evaluation of the latter parameter through gas temperature and pressure measurements upstream of the throat section. An additional line was present for nitrogen purging into the chamber for the burn out and in case of an accident.

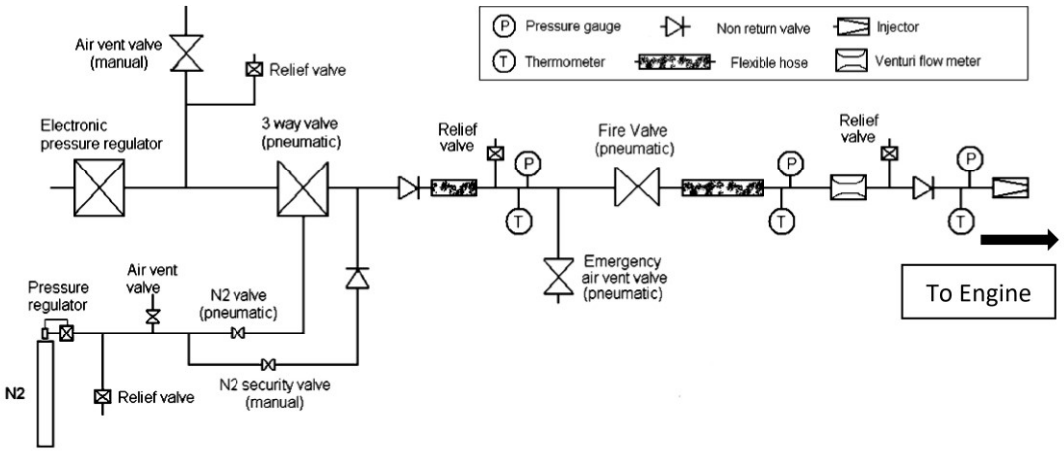

Fig. 2.10. Test feeding lines schematic.

Several sensors were present for the measurement of significant quantities during experimental test, which are listed in the following.

- Three capacitive pressure transducers and three thermocouples were located along the feeding line and at the section upstream of the oxidizer injector for the measurement (and monitoring for safety reasons) of the feeding pressure and of the temperature.
- As above mentioned, a choked Venturi tube was located upstream the oxidizer injector; a pressure transducer and a thermocouple allowed the measurement of the pressure and the temperature upstream its throat section for the evaluation of the oxidizer mass flow rate.
- Two pressure transducers were assembled on proper pressure taps present on the rocket for the measurement of the pressure in the pre-chamber and in the aft-mixing chamber during engine operation.
- Four load cells assembled on the test bench allowed evaluating the motor thrust by computing the sum of the loads measured with each cell.

The analogue signals generated by thermocouples, pressure transducers and load cells were sampled at 5 kHz, digitally converted, processed and recorded on the hard disk by a National Instruments (NI) PXI Express standard system interconnected with the computer by means of optic fibre connections. With this equipment and using a software developed in LabView, the motor was ignited and the firing test was completely automated. All the signals were stored in a binary format and, after downsampling the data to 100 Hz with a boxcar average, in text format for post-processing.

Finally, digital two-colour pyrometers and an infrared thermo-camera were available for non-intrusive monitoring of surface temperature in the case of characterization testing on materials for propulsion applications, as it will be described in more detail in section 2.3.1.

The main parameters directly measured in the firing tests were the oxidizer mass flow rate $\dot{m}_{ox}$, the chamber pressure p_c, the motor thrust Th, the fuel grain mass consumption ΔM and the burning time t_b. The remaining quantities of interest were derived from the measured ones, according to the procedure described in [78,79].

For material testing purposes, four experimental configurations were conceived, according to the incremental approach defined in section 1.5:

- Free-jet tests
- Combustion chamber insert tests
- Nozzle throat insert tests
- Complete subscale nozzle tests

The following subsections describe in detail the corresponding test set-ups.

2.3.1 Free-jet test

The Free-jet test configuration was conceived to expose different UHTCMC samples to the supersonic exhaust jet of the 200 N-class hybrid rocket nozzle. The specimens were small, button-like samples, with maximum diameter of 17 mm, as for tests carried out in the SPES arc-jet facility (Fig. 2.11).

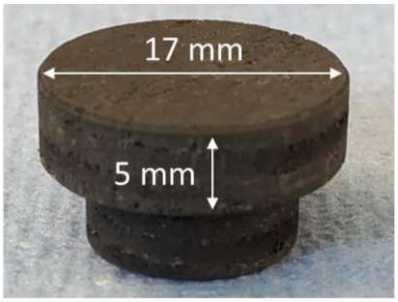

Fig. 2.11. Nominal design of UHTCMC samples for free jet tests.

Each specimen was placed downstream the hybrid rocket engine, in order to be reached by the exhaust plume coming from the nozzle (see Fig. 2.9). The size of the specimen, chosen accordingly to the available mechanical interfaces, was such that the front surface diameter was comparable to the nozzle exit section, allowing the sample to be thoroughly hit by the supersonic jet. The experimental set-up consisted in a mechanical system connected to the test bench in order to support and keep the specimen aligned with the motor axis. This system was designed to place the test article at the desired distance to the nozzle exit, *d*. In the present test campaign, a distance of 15 cm was selected, compatibly with the mechanical requirements for the fixation to the test bench, in order to provide realistic conditions to test the materials, in terms of heat fluxes, temperatures, pressures and gas composition. In fact, it is expected that, for this kind of applications, throat heat fluxes in hybrid rockets are on the order of 15 MW/m^2, throat pressures are on the order of a few bars, temperatures can be higher than 3000 K, as highlighted in section 1.2, while the reacting gas products are the same, as in free-jet test the flow comes directly from nozzle exit. These conditions were well reproduced by the present configuration, as will be shown in detail in section 5.1.1. The described configuration was in some way similar to that adopted to test materials in the arc-jet wind tunnel simulating the re-entry conditions, simplifying manufacturing; but while in this latter case the environment was characterized by near-vacuum conditions (stagnation pressure on the sample of the order of 10 kPa), in the free-jet tests the stagnation pressure was on the order of 2-5 bar. Therefore, the material was subjected also to significant structural stresses due to the relatively high pressure.

Fig. 2.12 shows pictures of the experimental set-up, including the non-intrusive diagnostic equipment employed for the real-time evaluation of the sample surface temperature. In particular, the surface temperature of the samples was continuously measured by the digital two-colour pyrometers Infratherm ISQ5 and IGAR6 described in section 2.1. In addition, the infrared response of the specimen during the free-jet testing was obtained by means of the IR-TC Pyroview 512N. The two pyrometers, both pointing at the central area of the samples front surface, gave perfectly equivalent responses, so only the temperature profiles measured by ISQ5 are herein reported. The measurement area consists in a round spot of roughly 5 mm in diameter. The spectral emittance of the surfaces in the range of the IR-TC was estimated as described in section 2.1.

Fig. 2.12. Set-up for free-jet test. The area within the red circle in the left picture is zoomed in the right picture.

2.3.2 Combustion chamber insert test

The second UHTCMC sample was designed as a simple flat disk. Fig. 2.13 shows the prototype design, characterized by a simple shape: an external diameter of 68 mm, an internal diameter of 15 mm and a thickness of 5 mm. Referring to Fig. 2.9, the new-class material insert was able to replace one of the thermal protections usually placed between the fuel grain and the post-chamber.

This chamber insert was conceived to combine simple shape and low manufacturing cost, allowing to evaluate the response of the materials to be tested in typical operating conditions in the combustion chamber of a hybrid rocket, where high temperatures and pressures are expected, in presence of a combustion flame, with relevant chemical composition. Although a relevant environment for nozzle applications was not fully reproduced (gas velocities are low in the combustion chamber), this kind of sample can be considered a breadboard validating the main structural functionalities of the final component in a laboratory-reproduced representative environment.

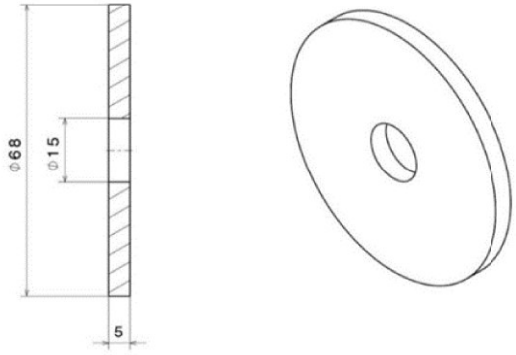

Fig. 2.13. Nominal design of UHTCMC combustion chamber inserts. Dimensions are in mm.

2.3.3 Nozzle throat insert

The third kind of prototype was a segmented nozzle with UHTCMC throat insert, having the same shape and size of the graphite nozzle typically used in the hybrid rocket engine to expand and accelerate the combustion gases produced by burning propellants. Before manufacturing a subscale complete UHTCMC nozzle to be tested on the test bench of the rocket motor, the prototype was segmented in order to assemble the converging and diverging parts together with a new-class material throat (Fig. 2.14). The converging and diverging elements were manufactured in graphite. This prototype was characterized by small dimensions: overall dimensions about 15x20mm and a nozzle throat section of 9.6 mm of diameter. This configuration allowed to manufacture relatively small prototypes, gradually increasing the geometric

complexity, and to test them to most severe conditions in terms of shear stresses and heat fluxes, which are encountered right in the nozzle throat region.

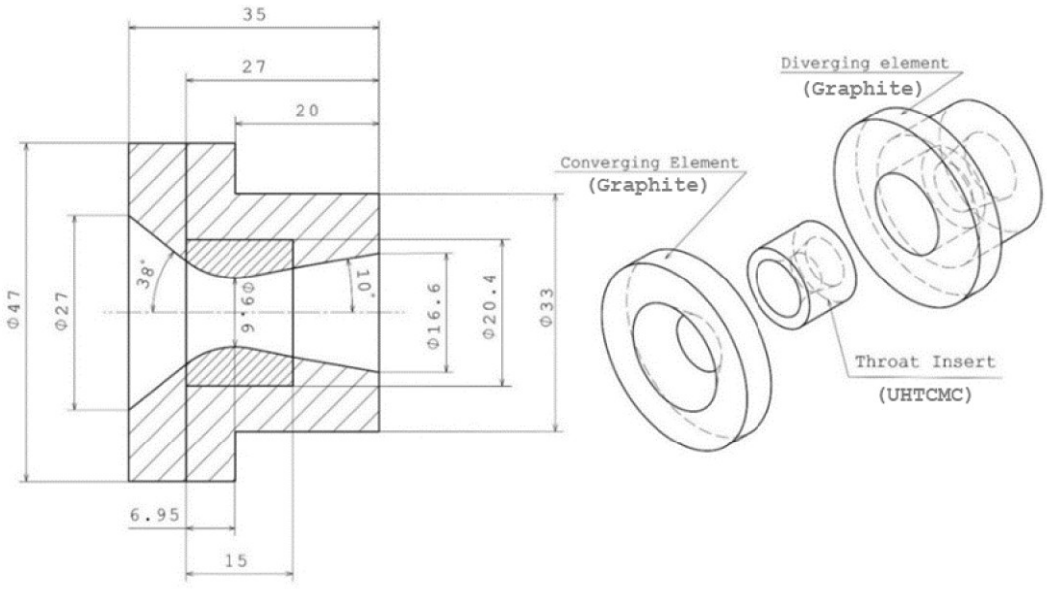

Fig. 2.14. Design of subscale segmented nozzle with UHTCMC nozzle throat insert for hybrid rocket engine. Dimensions are in mm.

2.3.4 Complete subscale nozzle

In the final step of the characterization activities, the sample was an entire nozzle completely manufactured in the UHTCMC material. The design was the same of the previous section, without segmentations (Fig. 2.15): overall dimensions of 47 mm of diameter and 35 mm length, nozzle inlet of 27 mm of diameter and converging inclination about 38°, nozzle throat section of 9.6 mm diameter with 11.6 mm of curvature radius, nozzle exit diameter of 16.6 mm and 10° of diverging angle. This configuration, besides allowing a further validation of critical functionalities in TRL 5, could also provide an approach to a TRL 6. In fact, a complete nozzle of such dimensions could be considered a full-scale component for specific applications, such as attitude control hybrid rocket motors for mini- or micro-satellites.

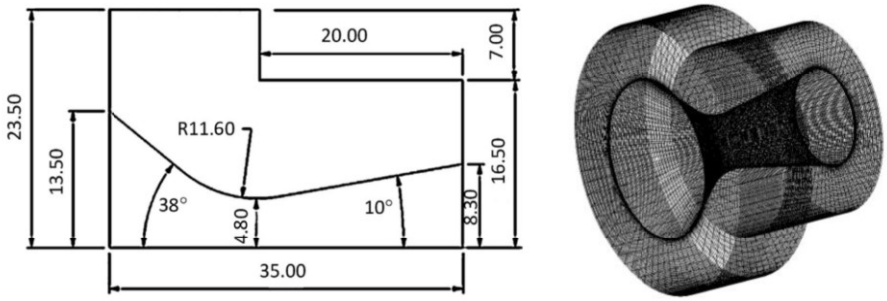

Fig. 2.15. Design of complete subscale UHTCMC nozzle, for UNINA hybrid rocket testing. Dimensions are in mm.

Nozzle surface temperatures were measured by an infrared thermo-camera (FLIR ThermaCam P40, spectral range 8-14 μm).

Samples and nozzle throat section surfaces were observed before and after the test by a Digital Microscope KH-8700 (HIROX-USA, Inc., United States), employing a MX(G) 5040SZ optical lens with 50-400x magnification factor. The throat diameters were also measured by a digital calliper (0.01 mm accuracy), for each test, before and after the experiment.

CHAPTER 3. NUMERICAL MODELS

This chapter describes the numerical models and computational domains used for the simulation of the flow field in the different test configurations and the analysis of the materials thermal behaviour. Section 3.1 presents the CFD models for the simulation of supersonic plasma flow in arc-jet wind tunnels, including the description of the chemical model and the catalytic reactions. Section 3.2 describes the different models used for the simulation of rocket propulsion environment, in the various test configurations. Section 3.3 describes the models used for the simulation of materials thermal response.

3.1 CFD models for arc-jet testing

For the simulation of the aero-thermo-dynamic flow field around test articles in arc-jet environment and the evaluation of loads on the samples, Computational Fluid-Dynamic simulations were carried out by means of a commercial Navier-Stokes equations solver.

The Reynolds-Averaged Navier-Stokes equations, in the Favre-averaged formulation [80], were solved for a turbulent multi-reacting gas mixture with a control-volume-based technique and a density-based algorithm [81]. The equation for total energy was solved taking into account energy transfer due to conduction, species diffusion, and viscous dissipation, including also the heat of chemical reaction.

The system of equations was closed by the Standard k-ε turbulence model [82], in which the turbulent kinetic energy, k, and its rate of dissipation, ε, were obtained taking into account the generation of turbulence kinetic energy due to the mean velocity gradients [82] and the contribution of the fluctuating dilatation in compressible turbulence to the overall dissipation rate [83], with a turbulent Prandtl number $Pr_t = 0.85$.

As tests were carried out considering air, gas was considered made of five species (O, O_2, NO, N and N_2), in chemical non-equilibrium. Viscosity, thermal conductivity

and mass diffusivity of the gas species were derived from the kinetic theory of gases. For the calculation of density, mixture was modelled as an ideal gas and a mass-weighted mixing law was considered for the mixture transport properties.

A simplified 2D-axi-symmetric computation domain was employed to perform steady-state simulations of the high-enthalpy flow field in the SPES mixing chamber, supersonic nozzle and test chamber. The computations were carried out dividing the domain into two separate parts: i) mixing chamber and nozzle (Fig. 3.1a); ii) test chamber (Fig. 3.1b). The two computational grids were made up of 3900 and 18300 quadrilateral cells respectively. Cells were clustered towards the specimen front wall in order to ensure that the maximum value of the dimensionless wall distance y^+ (which may be interpreted as a local Reynolds number, which means that its magnitude can be expected to determine the relative importance of viscous and turbulent processes), which should be smaller than 5 to guarantee an appropriate treatment of the boundary layer [84], was in the range 0.1÷2 at the wall-adjacent cell all along the surface.

Concerning the grid related to mixing chamber and nozzle (Fig. 3.1a), the specified mass flow rate of the hot nitrogen coming from the torch was injected into the computation domain throughout a mass flow inlet boundary condition simulating the exit section of the torch. The gas total temperature and chemical composition (i.e. mass fraction of N_2 and N) were evaluated by the NASA Chemical Equilibrium with Applications software (CEA) [85] in order to match the total specific enthalpy corresponding to the input value of the arc power (see Table 2.1). Furthermore, a radial mass flow inlet was used to simulate the injection of the cold gas (i.e. O_2) in the mixing chamber. The top surface of the domain was treated as a no-slip stationary wall (using the Enhanced Wall Treatment model), at temperature T = 400 K (in order to simulate water-cooling of the nozzle). The nozzle exit section was modelled as a supersonic pressure outlet.

Concerning the grid related to the test chamber (Fig. 3.1b), the thermo-fluid-dynamic conditions at the nozzle exit section were used as input to study the aero-thermo-dynamic flow field around the specimens. Here, the nozzle exit section was described as a velocity inlet. The surfaces of the specimen were treated as cold walls (T = 300 K). The treatment of the chemical boundary conditions for such walls is

described in section 3.1.1. A pressure-outlet condition, corresponding to the experimental vacuum environment, was set on the top and rear boundaries of the domain. The computational domain of Fig. 3.1b includes both the fluid region of the test chamber and the solid components. Details about material samples thermal analyses are reported in section 3.3.

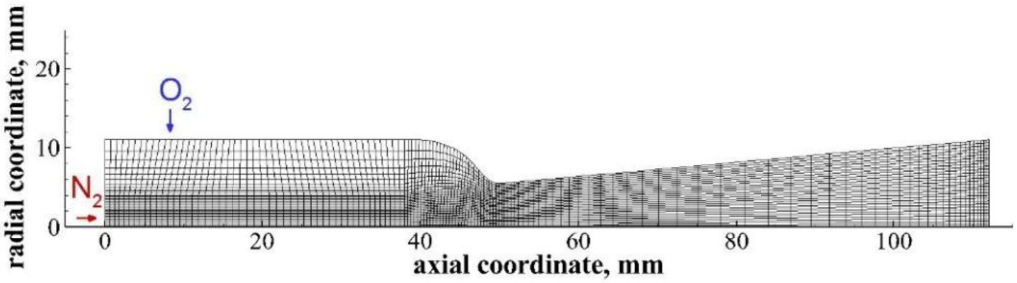

(a)

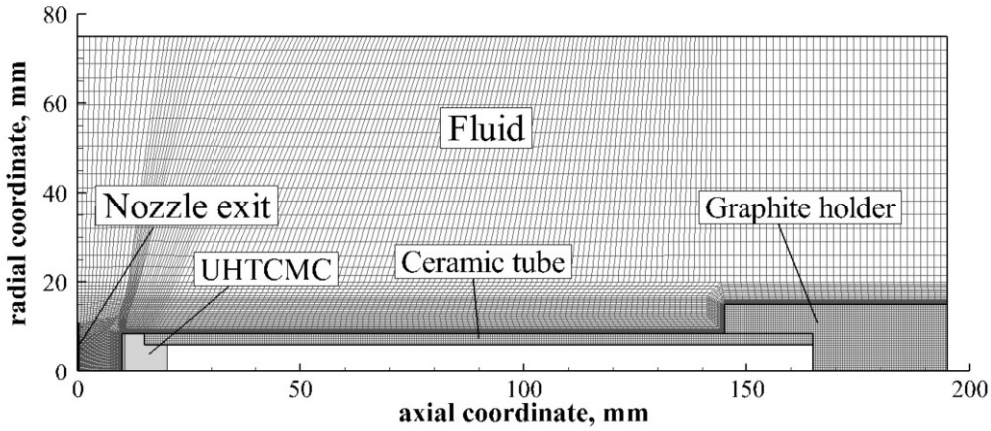

(b)

Fig. 3.1. Mesh for the CFD simulations: a) mixing chamber and nozzle; b) test chamber, including test sample and solid supporting system.

The same fluid-dynamic model was used to simulate the flow field in the L3K arc-jet facility of DLR. Also in this case, 2D-axisymmetric steady-state simulations were carried out. Fig. 3.2a shows the computational grid used for the simulation of the flow in the reservoir upstream the nozzle, the nozzle itself, and a portion of the test chamber. The flow entered the domain through a pressure inlet boundary, at the far left, in which the (uniform) conditions of total pressure, temperature and mass fraction of the chemical species (corresponding to an equilibrium composition at the specified

pressure and temperature) were set according to the values reported in Table 2.2. Nozzle wall cooling was taken into account by specifying a boundary temperature T = 500 K.

The conditions achieved at the nozzle exit were then used as input for the simulation of the flow inside the test chamber (Fig. 3.3b), setting a velocity inlet boundary condition (identified by a blue line in the Figure). This allowed estimating the aero-thermo-dynamic loads acting on the samples during test.

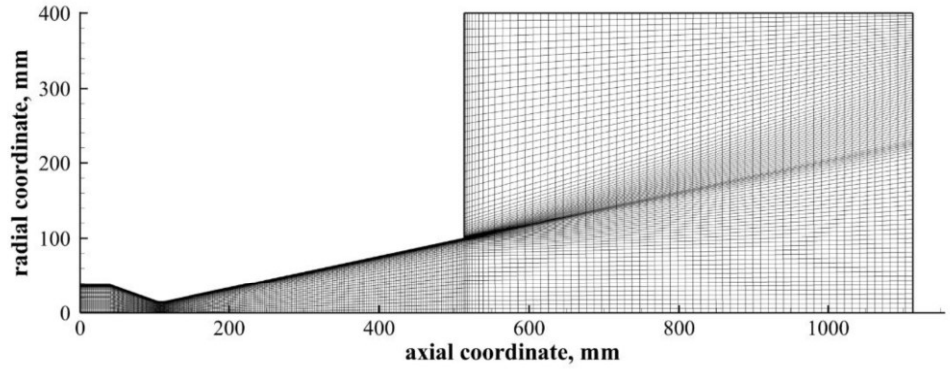

(a)

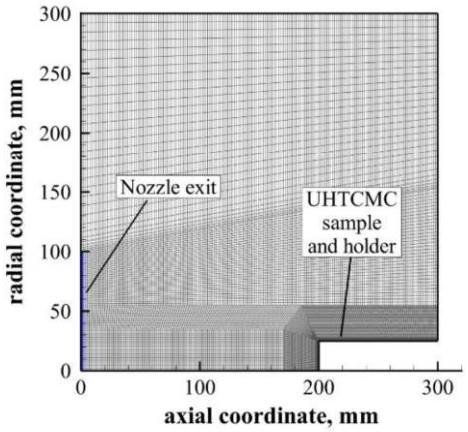

(b)

Fig. 3.2. Mesh for the CFD simulation of L3K flow field: a) reservoir, nozzle and test chamber without samples; b) test chamber, with shape of the actual UHTCMC sample and its holder.

3.1.1 Chemical model and catalytic reactions

The CFD simulations implemented the chemical models by Dunn-Kang [86]. Reaction rates were calculated according to an Arrhenius law:

$$K = A_K T^{\beta} \exp\left(-\frac{E_a}{R_0 T}\right) \tag{3.1}$$

where A_K is a pre-exponential factor, T is temperature, β is a temperature exponent, which allows taking into account reaction rate dependence on temperature, E_a is the activation energy and R_0 is the universal gas constant. The details on the chemical model are reported in Table 3.1. In the present application, ionization was not considered. In fact, previous studies [87] verified that the degree of ionization, evaluated by the Saha equation [88] at conditions pretty close to the present ones, was almost negligible.

Table 3.1. Chemical model for arc-jet flow simulation. The M symbol refers to a generic third body for the reaction.

#	Reaction	A_K (m^3/kgmol·s)	β	E_a (J/kgmol)	Third body efficiency
1	$O_2 + M \rightleftarrows 2O + M$	$3.61 \cdot 10^{15}$	-1	$4.94 \cdot 10^{8}$	O_2=9, N_2=2, O=25, N=NO=1
2	$N_2 + M \rightleftarrows 2N + M$	$1.92 \cdot 10^{14}$	-0.5	$9.41 \cdot 10^{8}$	O_2=1, N_2=2.5, O=N=NO=1
3	$N_2 + N \rightleftarrows 3N$	$4.15 \cdot 10^{19}$	-1.5	$9.40 \cdot 10^{8}$	-
4	$NO \rightleftarrows N + O$	$3.97 \cdot 10^{17}$	-1.5	$6.29 \cdot 10^{8}$	O_2=N_2=1, O=N=NO=20
5	$NO + O \rightleftarrows O_2 + N$	$3.18 \cdot 10^{6}$	1	$1.64 \cdot 10^{8}$	-
6	$N_2 + O \rightleftarrows NO + N$	$6.75 \cdot 10^{10}$	1	$3.12 \cdot 10^{8}$	-

Surface catalycity is defined as the ability of the material surface to promote exothermic recombination reactions at the wall. The diffusive flux of atomic species at the wall, part of which recombines into molecules, results in an increased heat flux (as will be shown in Eq. (3.10) in section 3.3). According to [89], the diffusive flux at the wall for the i-th atomic species can be written as:

$$\frac{\partial Y_i}{\partial n} = \frac{Y_i K_w}{D_i} \tag{3.2}$$

where Y_i is the species concentration, D_i the corresponding diffusivity and K_w is the material catalytic recombination rate constant, which is both function of the wall material and of the considered chemical species. K_w can be expressed as function of the catalytic recombination coefficient γ_w:

$$K_w = \gamma_w \sqrt{\frac{R_0 T_w}{2\pi m_i}} \tag{3.3}$$

where R_0 is the universal gas constant, T_w is the wall temperature and m_i is the molar mass of the i-th species. γ_w is the ratio between the number of atomic collisions effective in recombination and the total number of atomic collisions occurring at the wall [90]. It can assume values between 0 and 1, being $\gamma_w = 0$ the case of not-catalytic wall (zero species diffusive flux) and $\gamma_w = 1$ the case of fully catalytic wall (zero atomic species concentration at the wall).

In the CFD simulation, the non-catalytic (NC) condition was specified by assigning, for each species, a zero diffusive flux in the direction normal to the specimen surface. The fully-catalytic condition (FC) was set by assigning, on the specimen surface, the species mass fractions corresponding to a complete recombination of atoms into molecules. Intermediate catalytic recombination levels were set by assigning a specified value for the species concentration at wall. Extracting, from the fluid field solution, the quantities appearing in Eqs. (3.2)-(3.3), the values of K_w and γ_w were calculated. In the present thesis, to reduce the number of unknown quantities, it was assumed that the catalytic recombination coefficients were the same for the two atomic species, nitrogen and oxygen.

3.2 CFD models for rocket propulsion

In this section the models for the numerical simulations of the thermo-fluid dynamic flow field inside the combustion chamber and through the nozzle of hybrid rocket engines and for the evaluation of the operating conditions around the test article are described. The presented numerical models were employed as a relatively low-computational-cost support to the experimental tests in order to get additional information, that are difficult to collect experimentally, about the operating conditions corresponding to the different selected test conditions. The 1D model presented in section 3.2.1, based on simplified chemical equilibrium calculations, was used for a rapid estimation of the average conditions in the combustion chamber and at the rocket nozzle exit section. These were then provided to the CFD model described in section 3.2.2, as inlet boundary conditions for the simulation of the flow field in the nozzle and in free-reacting jets, respectively. To have a detailed description of the thermo-fluid-chemical flow field inside the rocket combustion chamber, useful to estimate the test conditions for chamber insert tests, stand-alone CFD simulations were carried out by means of the model presented in section 3.2.3.

3.2.1 One-dimensional model for chamber and nozzle conditions simulation

A one-dimensional model based on NASA CEA software was used to rapidly evaluate the evolution of the operating conditions in the combustion chamber, in particular the chamber pressure, and through the nozzle during the time. In this case, the inputs of the model were the oxidizer mass flow rate, the geometrical dimensions of the fuel grain and the operating time. The 1D approach provides a sensitive reduction of the computational cost for a preliminary estimation of the above-mentioned conditions.

As the instantaneous regression rate is an unknown parameter and the oxidizer mass flux and chamber pressure depend on the regression rate itself, the expected data were estimated assuming the classical regression rate law

$$\dot{r} = aG_{ox}^{n} \tag{3.4}$$

where the coefficient a and n were selected from the values available in literature relevant to the combustion of gaseous oxygen with HDPE fuel grains [91]. Integrating Eq. (3.4) in time, the instantaneous port diameter $D(t)$ was calculated. Then, considering the prescribed oxidizer mass flow rate, the corresponding mass flux $G_{ox}(t)$ and regression rate $\dot{r}(t)$ were estimated. Then the fuel mass flow rate was easily calculated as

$$\dot{m}_f(t) = \rho_f \pi D(t) L \dot{r}(t) \tag{3.5}$$

where ρ_f is the solid fuel density and L is the length of the grain, and correspondingly the average mixture ratio $OF(t) = \frac{\dot{m}_{ox}}{\dot{m}_f(t)}$ was derived. From these calculations, the estimation of the aft-chamber pressure p_c was performed by means of an iterative procedure to solve the steady-state mass balance equation

$$\frac{\dot{m}_{ox}}{A_t}\left(1 + \frac{1}{OF}\right) = \frac{p_c}{\eta C^*} \tag{3.6}$$

in which A_t is the nozzle throat area, C^* is the theoretical characteristic exhaust velocity (that primarily depends on the mixture ratio and, to a minor degree, on pressure) and the combustion efficiency, η, has been assumed equal to unity. For the dependence of the C^* on pressure, Eq. (3.6) is implicit and an iterative calculation technique was needed. A combustion pressure was first assumed, then the CEA code [85] was run to calculate the equilibrium composition and the theoretical exhaust velocity, assuming frozen flow through the nozzle, at the given *OF* ratio in input. Finally, combustion pressure was adjusted repeatedly until convergence.

3.2.2 CFD model for simulation of flow and heat transfer in free-jet test and throughout rocket nozzles

In order to provide a better understanding of test conditions around the material samples and prototypes, CFD simulation of the flow through the rocket nozzle and of the external plume of the exhaust gases were performed, employing as boundary conditions the time-averaged results of the numerical tool described in the previous section.

To this purpose the RANS equations for single-phase multicomponent turbulent reacting flows were solved with a control-volume-based technique and a density-based algorithm [81], employing the SST k–ω model as turbulence closure [92]. A detailed analysis of thermo-chemical evolution of gas mixture was performed, in order to have an accurate prediction of heat transfer at solid walls. The transport equations for the main combustion products (O_2, C_2H_4, H_2O, CO_2, CO, H_2, H, O, OH were the species considered in the current model, together with the non-reacting N_2) were solved, and the Eddy Dissipation Concept (EDC) model [93] was employed for the combustion mechanism, which accounts for detailed chemical reaction rates in turbulent flows. Consequently, the Arrhenius rate K for each reaction was calculated as

$$K = A_K T^{\beta} \exp\left(-\frac{E_a}{RT}\right) \tag{3.7}$$

where A_K is a pre-exponential factor, T is temperature, β is a temperature exponent, which allows taking into account reaction rate dependence on temperature, E_a is the activation energy and R is the universal gas constant. The constants were taken from Ref. [94] and are reported in
Table 3.2.

The Discrete Ordinates model [95] for the radiation was included in the numerical modelling.

The computational grid used for the simulation of the free reacting jet exiting from the nozzle is shown in Fig. 3.3. A supersonic inflow boundary condition was set on the surface representative of the nozzle exit section, imposing the total pressure and

the total temperature corresponding to the operating chamber pressure and temperature in the rocket and the static pressure and the chemical composition at the exit of the nozzle. The ambient pressure was set on the other external boundaries of the computational domain.

Table 3.2. C_2H_4 – O_2 reaction system. The symbol M refers to a generic third body for the reaction.

No.	Reaction[a]	A_K[b]	β	E_a[b]
1	$C_2H_4 + O_2 \rightleftarrows 2CO + 2H_2$	1.80e+14	0.0	35500
2	$CO + O \rightleftarrows CO_2 + M$	5.30e+13	0.0	-4540
3	$CO + OH \rightleftarrows CO_2 + M$	4.40e+06	1.5	-740
4	$H_2 + O_2 \rightleftarrows OH + OH$	1.70e+13	0.0	48000
5	$H + O_2 \rightleftarrows OH + O$	2.60e+14	0.0	16800
6	$OH + H_2 \rightleftarrows H_2O + H$	2.20e+13	0.0	5150
7	$O + H_2 \rightleftarrows OH + H$	1.80e+10	1.0	8900
8	$OH + OH \rightleftarrows H_2O + O$	6.30e+13	0.0	1090
9	$H + H \rightleftarrows H_2 + M$	6.40e+17	-1.0	0
10	$H + OH \rightleftarrows H_2O + M$	2.2e+22	-2.0	0

[a]Third-body efficiencies for all thermolecular reactions are 2.5 for $M = H_2$, 16 for $M = H_2O$, and 1 for all other M.
[b]Units are in seconds, moles, cubic centimeters, calories and Kelvin.

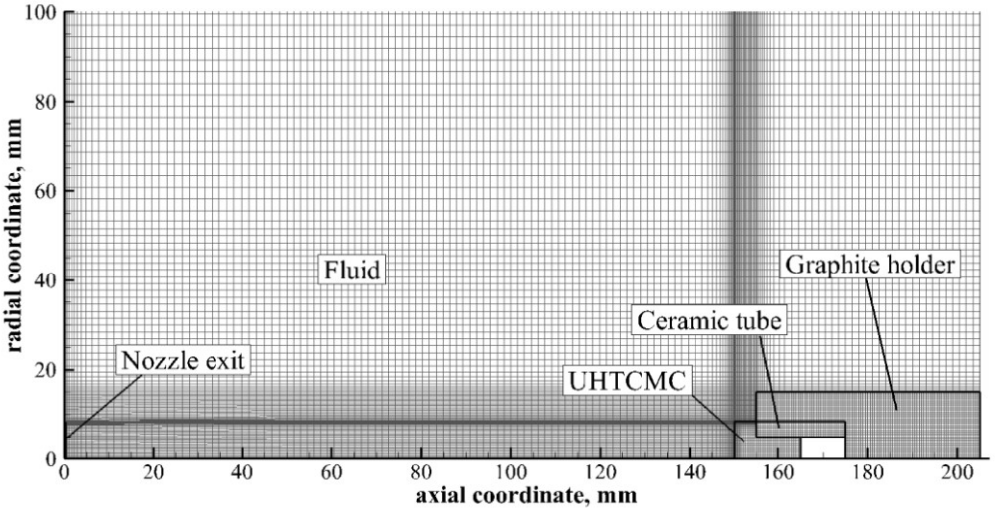

Fig. 3.3. Computational grid for the simulation of the free reacting jet exiting from the rocket nozzle, including solid components for material thermal analysis.

The typical computational grid for the simulation of the flow field through the exhaust nozzle of the hybrid rocket is shown in Fig. 3.4. Similarly to what described above, a pressure inlet boundary condition was set on the inlet section of the nozzle imposing the time-averaged values of the total pressure, the total temperature and the chemical composition estimated by means of the model described in the previous section. A supersonic outlet condition was set at the exit section.

For the simulation of the material thermal behaviour, also the solid components were meshed. Details about the models used for this analysis are reported in section 3.3.

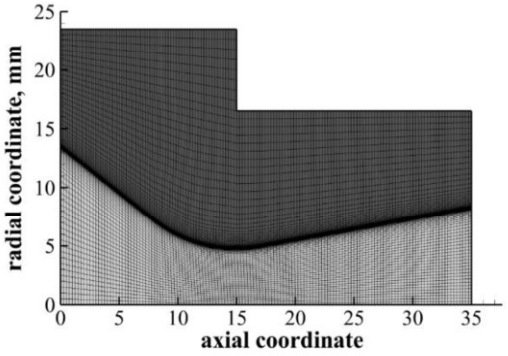

Fig. 3.4. Computational grid for the simulation of the flow through the rocket nozzle, and material thermal behaviour.

3.2.3 CFD model for the simulation of flow and heat transfer in chamber insert test

The application of suitable numerical model assumes even a higher importance for having a deep insight on the operating conditions for the test of chamber inserts, which were located inside the combustion chamber of the rocket and therefore could not be monitored by means of optical diagnostic instruments used in the case of free-jet tests.

Also in this case CFD simulation were carried out applying a numerical model specifically defined at the University of Naples "Federico II" for the detailed simulation of hybrid rockets internal ballistics [96–98], in which the correct estimation of the wall heat fluxes, which was the main objective of the present simulations, was

a key factor to correctly predict the fuel regression rate, and the achieved agreement between simulation and experiment was highly satisfactory in a range of test cases.

Again, the model provided the resolution of the RANS equation considering the SST k–ω model as turbulence closure. In this case, considering that the diffusion processes typically occurring in hybrid rocket motors are slow with respect to the chemical kinetics, the non-premixed combustion of oxygen and gaseous fuel injected from the wall was modelled by means of the Probability Density Function (PDF) approach coupled to chemical equilibrium [99]. Accordingly, combustion was simplified to a mixing problem, and the difficulties associated with closing non-linear mean reaction rates were avoided. The turbulence-chemistry interactions were described by means of the average mixture fraction, f, and its variance, f''^2. The shape of the assumed PDF was described by the β-function of these two quantities. Once f and f''^2 were calculated at each point in the flow field, the known PDF was used to compute the time-averaged values of individual species mole fractions, density, and temperature with simple thermochemistry calculations based on the minimization of Gibbs free energy [85]. Although the actual products of solid fuel pyrolysis are numerous and their composition depends on both the wall temperature and heating rate, the practice common in the literature is to consider the gaseous monomer alone; here, thus, gaseous ethylene was considered as the fuel injected from the grain surface.

Fig. 3.5 shows a typical axisymmetric computational grid employed for the CFD simulation of the flow field inside the subscale hybrid rocket, constituted by the internal volume of the pre-chamber, of the fuel grain port, of the aft-mixing chamber and of the nozzle.

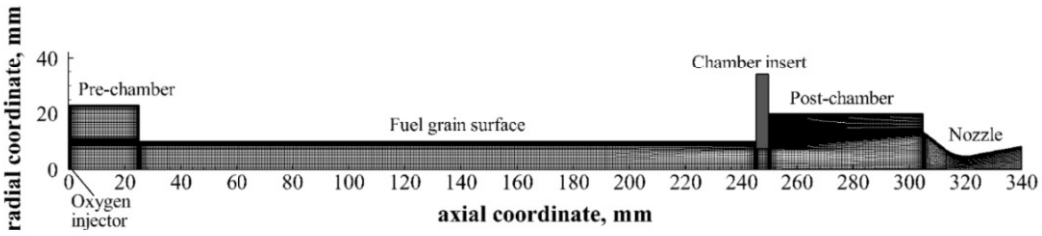

Fig. 3.5. Typical computational grid for the simulation of hybrid rocket internal ballistic

The model included a specific treatment for the boundary conditions at the interface between the gaseous flow region and the solid fuel wall, based on the mass, energy and species balance and an Arrhenius-type equation for the fuel pyrolysis, in order to allow calculation of the local fuel regression rate, which governs the fuel mass flow rate and in the last instance the oxidizer-to-fuel ratio. Details on this aspect can be found in the cited literature [96].

3.3 Thermal analysis of materials samples

For the thermal analysis of the solid samples in both applications, the time-dependent temperature field inside the sample and its supporting elements was computed solving the energy equation

$$(\rho C)_s \frac{\partial T}{\partial t} = k_s \nabla^2 T \tag{3.8}$$

where ρ_s, C_s and k_s are the solid density, specific heat and thermal conductivity, respectively.

The distribution of the thermo-fluid dynamic quantities and the chemical compositions in the fluid area near the solid material, and subsequently the convective heat flux, are influenced by the temperature on the exposed surface of the sample. For these reasons, an accurate approach is the one considering the interaction between the fluid and the materials. The thermal coupling condition wass set on the interfaces between fluid and solid domains, that is temperature and heat flux continuities:

$$T_{f,int} = T_{s,int} \tag{3.9}$$

$$k_f \left.\frac{\partial T}{\partial n}\right|_{f,int} + \dot{q}_{rad,in} + \dot{q}_{chem} = k_s \left.\frac{\partial T}{\partial n}\right|_{s,int} + \dot{q}_{rad,out} \tag{3.10}$$

where n is the normal direction of the interface, the subscripts f and s represent fluid and solid, respectively, $\dot{q}_{rad,in}$ is the radiative heat flux entering the solid domain, $\dot{q}_{chem}$ is the chemical contribution to the heat transfer (due to the dissociation/recombination reactions occurring at the solid/fluid interface) and $\dot{q}_{rad,out} = \varepsilon\sigma T^4$ is the radiative heat flux emitted by the solid surface, being ε the total hemispherical emissivity of the surface and σ the Stefan-Boltzmann constant.

CHAPTER 4. RESULTS IN ARC-JET ENVIRONMENT

This chapter presents and discusses all the results obtained regarding the characterization of innovative ceramic materials for TPS applications. Tests on UHTC and UHTCMC samples were carried out by the two arc-jet wind tunnels (SPES and L3K) described in CHAPTER 2, and a combined experimental/numerical effort allowed proposing interpretations for the wide range of observed phenomena occurring during plasma exposure of the materials.

The content is structured as follows. Section 4.1 describes the results of numerical simulations for the characterization of the flow field in SPES and L3K. Section 4.2 presents the results obtained in SPES on different UHTCMC small-scale samples, comparing their performance in terms of ablation resistance and focusing on the ultra-high-temperature behaviour of ZrB_2-SiC-based samples. In section 4.3, the outcomes of a series of test campaigns for the investigation of the effect of SiC content on ZrB_2-based UHTCs aero-thermal response are described. Section 4.4 presents the results of a test campaign aimed at the analysis of the effect of flow composition (simulated air and pure nitrogen) on UHTCs ultra-high-temperature behaviour. Tests carried out on larger-scale UHTCMC samples in L3K are reported in section 4.5. Finally, section 4.6 presents a comprehensive discussion of the most interesting observed phenomena, including a *spontaneous temperature jump*, combining experimental and numerical results to correlate the UHTC and UHTCMC response with their high-temperature oxidation process.

4.1 Numerical simulations and flow characterization

Numerical simulations offer the possibility to model the aero-thermo-dynamic conditions experienced by the samples in the test chamber and to characterize the unknown thermal and chemical properties of the material. In particular, it could be

interesting to investigate the effects of thermal conductivity and surface catalycity on the radiative equilibrium temperatures at different specific total enthalpy levels, as will be discussed in detail in next sections. To achieve these objectives, some of the conditions of the experimental tests have been simulated by means of the CFD models presented in section 3.1.

4.1.1 Simulation of the flow field in SPES

First, the flow field in SPES has been simulated, considering different values of the torch arc power (see Table 2.1). As an example, the Mach number distribution calculated inside the mixing chamber and nozzle of the arc-jet facility, for the case of step #5 (H_0 = 14 MJ/kg), is depicted in Fig. 4.1. As expected, a strong expansion occurs to the flow up to a Mach number value of almost 3 at nozzle exit. It resulted that higher values of the torch arc power lead not only to an increase in velocity, pressure and temperature at nozzle exit, but most of the specific total enthalpy is used to increase the mass fractions of the dissociated species (N and O). As discussed in next section, this is one of the reasons why surface catalycity becomes increasingly important at higher enthalpy levels.

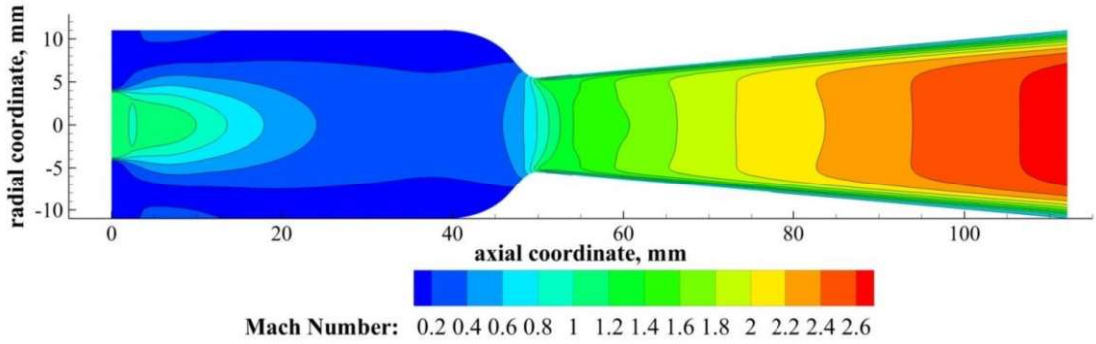

Fig. 4.1. Mach Number distribution inside the mixing chamber and nozzle of the arc-jet facility. Conditions corresponding to step #5 (H_0 = 14 MJ/kg).

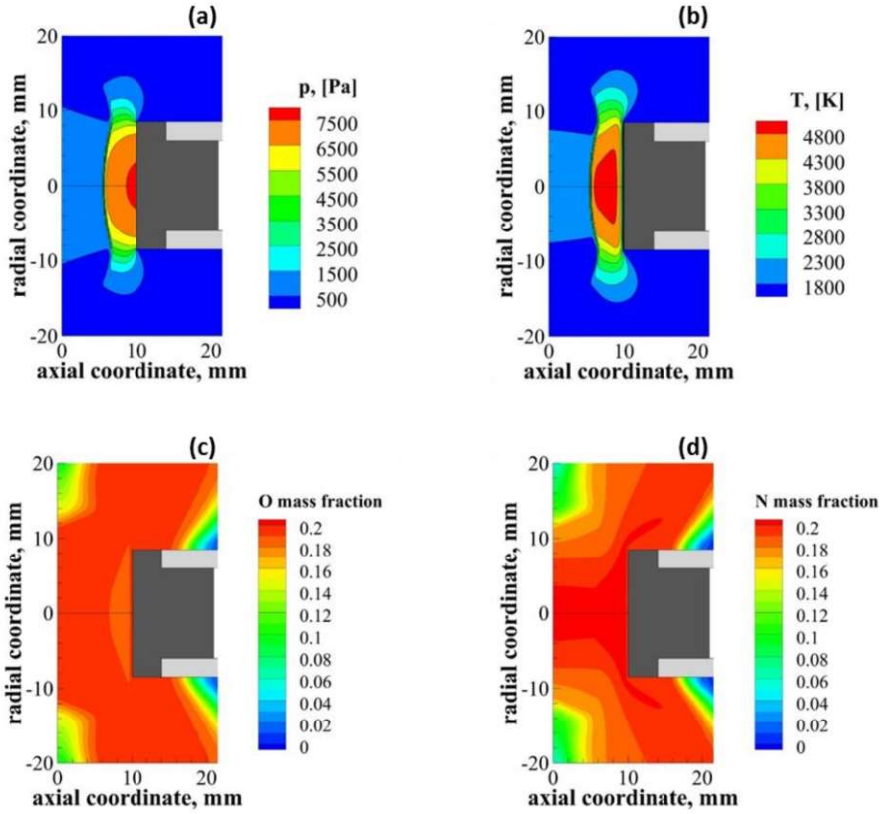

Fig. 4.2. Distribution of a) static pressure, b) static temperature, c) O mass fraction and d) N mass fraction around the test sample. Conditions corresponding to step #5 (H_0 = 14 MJ/kg).

The profiles of the thermo-fluid-dynamic quantities and of the species concentrations, obtained at nozzle exit, are used as inputs for the CFD simulation of the flow field inside the test chamber. As an example, Fig. 4.2 shows the distributions of pressure, temperature and atomic oxygen and nitrogen mass fractions around the sample obtained in correspondence of the enthalpy level of step #5. It is clear that, even at intermediate enthalpies, there is a considerable amount of dissociated species, resulting in a non-negligible effect of surface catalycity on sample equilibrium temperature. It is also interesting to notice that the λ-structure of the shock-wave that, according to CFD solution, forms in front of the sample, is clearly visible also in a picture taken by a CCD (Charge-Coupled Device) camera during a test (Fig. 4.3).

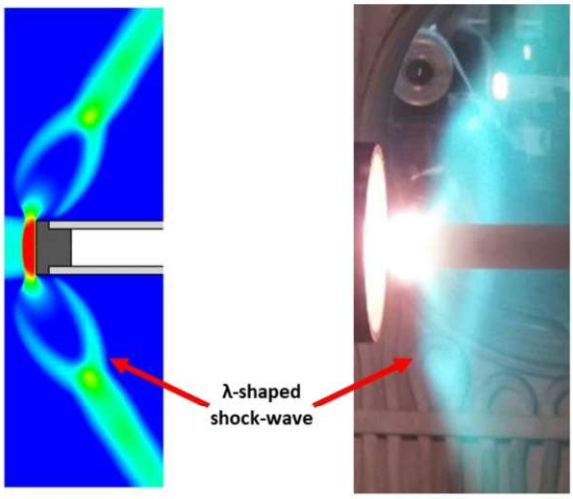

Fig. 4.3. Comparison between numerical distribution of temperature (left) and a CCD picture of the test (right), which shows the λ-structure of the shockwave in front of the specimen.

Table 4.1 summarizes the average and maximum values of the surface heat flux obtained on the sample front surface at cold wall with the assumption of non-catalycity at different enthalpy steps. As discussed above, the increase in the enthalpy level only causes a slight rise in the flow static temperature at nozzle exit, whereas most of the energy is spent in the endothermic dissociation reactions of oxygen and nitrogen. Therefore, as reported in the Table, the heat flux only increases by less than 50% from Step 1 to 8, being in the order of 1-2 MW/m^2. In order to match the sample equilibrium temperature in different cases, it was necessary to suppose that the sample surface promotes a partial catalytic recombination of oxygen and nitrogen dissociated atoms into molecules.

A detailed analysis of the effect of surface catalycity on aero-thermal loads was carried out for the conditions corresponding to step #5. As shown in Table 4.2, in presence of a complete recombination of both the atomic species at the wall, the average heat flux at those conditions increased from 1.62 MW/m^2 up to 3.59 MW/m^2, whereas the maximum heat flux rose from 1.83 MW/m^2 to 4.50 MW/m^2. The actual value of surface heat flux, depending on the effective catalytic recombination efficiency, is expected for this reason to attain values in the interval defined by the two limit cases (non-catalytic and fully-catalytic).

Table 4.1. Average and maximum heat flux on the sample front surface at cold, non-catalytic wall, for the four analysed enthalpy steps.

Step	Average Surface Heat Flux [MW/m^2]	Maximum Surface Heat Flux [MW/m^2]
1	1.04	1.22
3	1.47	1.71
5	1.62	1.83
8	1.98	2.15

Table 4.2. Average and maximum heat flux on the sample front surface at step #5, comparison between non-catalytic and fully catalytic wall.

	Average Surface Heat Flux [MW/m^2]	Maximum Surface Heat Flux [MW/m^2]
Non-catalytic	1.62	1.83
Fully catalytic	3.59	4.50

As also test in pure nitrogen flow have been performed, one related test condition (corresponding to an enthalpy of 18 MJ/kg) has been simulated, and compared to step #8 on a conventional test in air. The mass fraction of dissociated nitrogen was comparable in the two conditions (Fig. 4.5 and 4.4c). The absence of oxygen, whose endothermic dissociation reaction lowered the amount of sensitive enthalpy in the air flow, caused the static temperature to be slightly higher in the case of nitrogen flow.

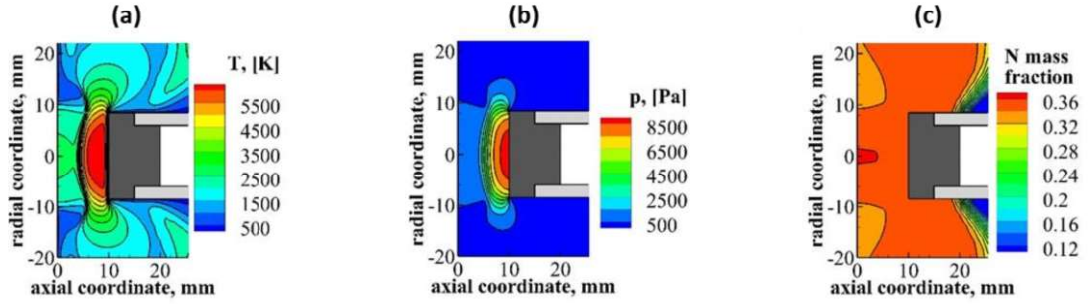

Fig. 4.4. (a) Temperature, (b) Pressure and (c) N mass fraction distributions around the test article, nitrogen flow, H_0 = 18 MJ/kg.

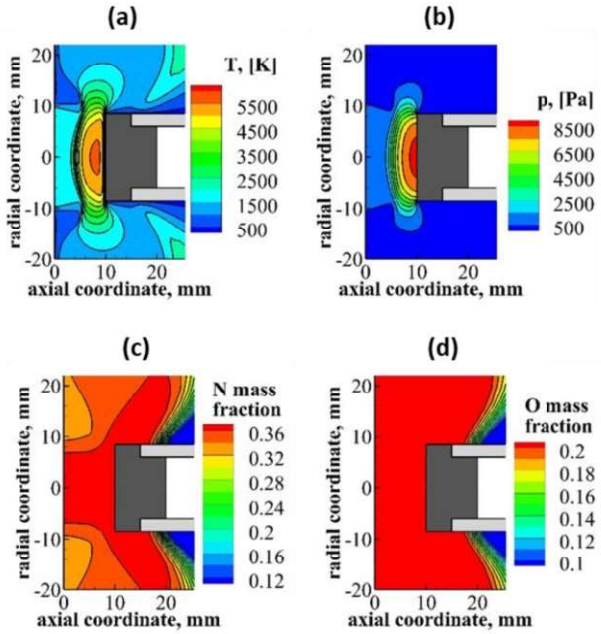

Fig. 4.5. (a) Temperature, (b) Pressure, (c) N mass fraction and (d) O mass fraction distributions around the test article, air flow, step #8.

4.1.2 Simulation of the flow field in L3K

CFD simulations have been carried out also to describe the flow field in L3K. As an example, Fig. 4.6 shows the distribution of Mach number in the reservoir, the converging-diverging nozzle and the test chamber. It can be seen that, as expected, the flow reached hypersonic conditions, achieving a Mach number around 5 at nozzle exit. The flow would have continued its expansion through the test chamber in absence of a sample. Fig. 4.7a-d shows instead the distribution of temperature, pressure and mass fractions of atomic nitrogen and oxygen, in close proximity of the test article. As in SPES, the pressure contour highlights the formation of a normal shockwave in front of the sample. Temperatures in excess of 7000 K were reached close to the stagnation point. Also in this case, oxygen was completely dissociated, while the mass fraction of atomic nitrogen was relatively lower than in SPES.

These flow conditions generated, on the front surface of the sample, an average cold-wall heat flux of 1.29 MW/m^2 in the case of non-catalytic surface, and of 2.38 MW/m^2 in the case of fully catalytic surface. It is worth noticing that the FC value was perfectly in line with the measured heat flux reported in section 2.2.

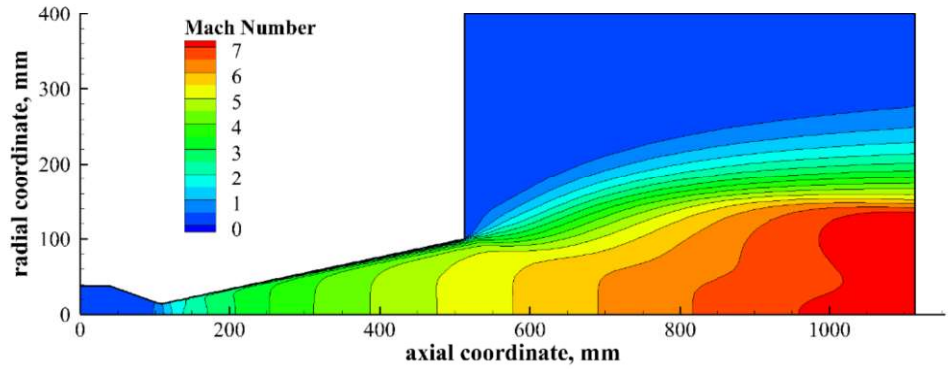

Fig. 4.6. Mach number distribution from the reservoir to the test chamber of L3K.

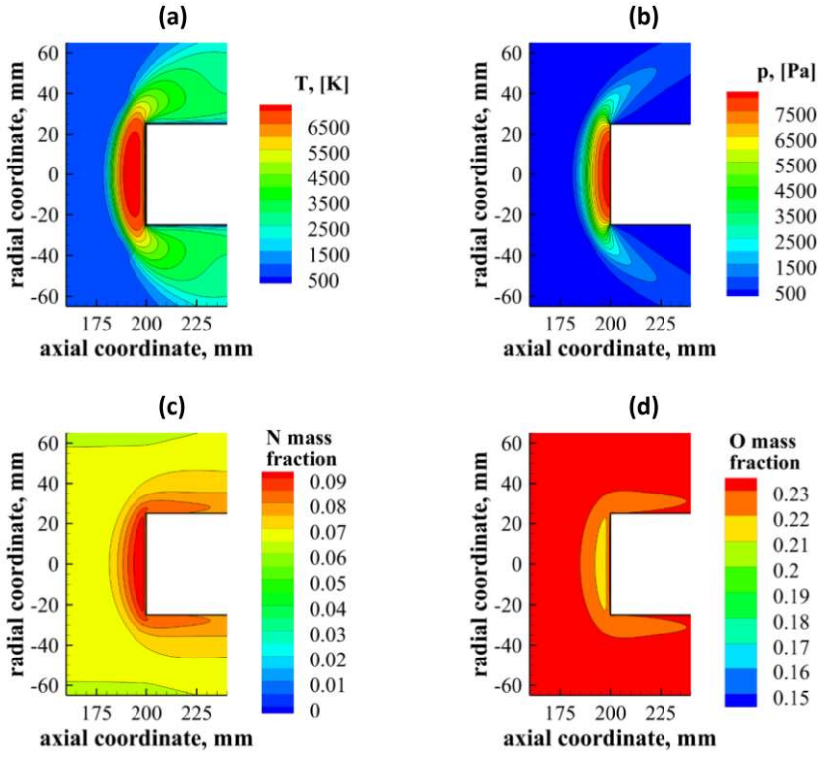

Fig. 4.7. (a) Temperature, (b) Pressure, (c) N mass fraction and (d) O mass fraction distributions around the test article in L3K.

4.2 Comparison of different UHTCMC formulations

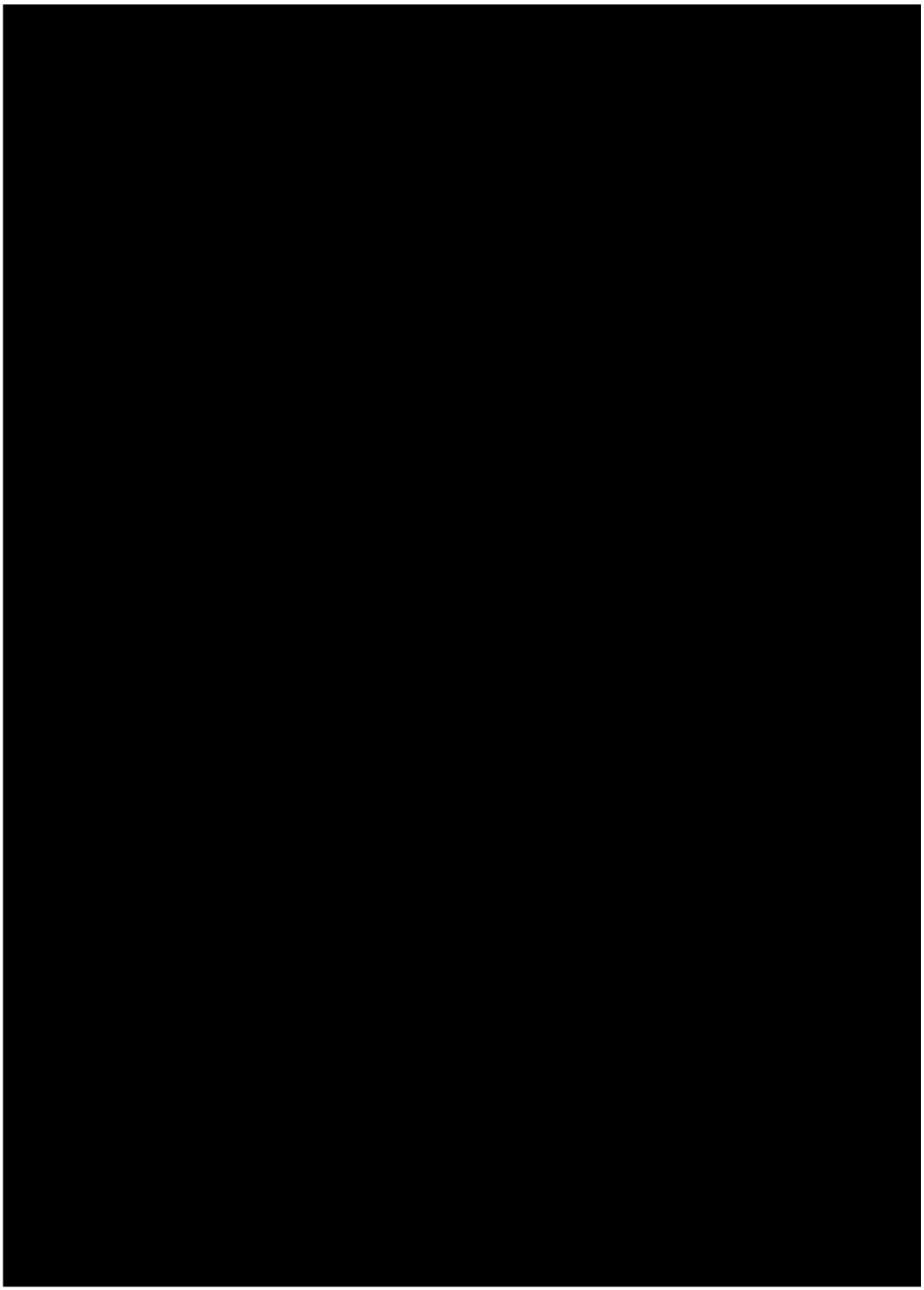

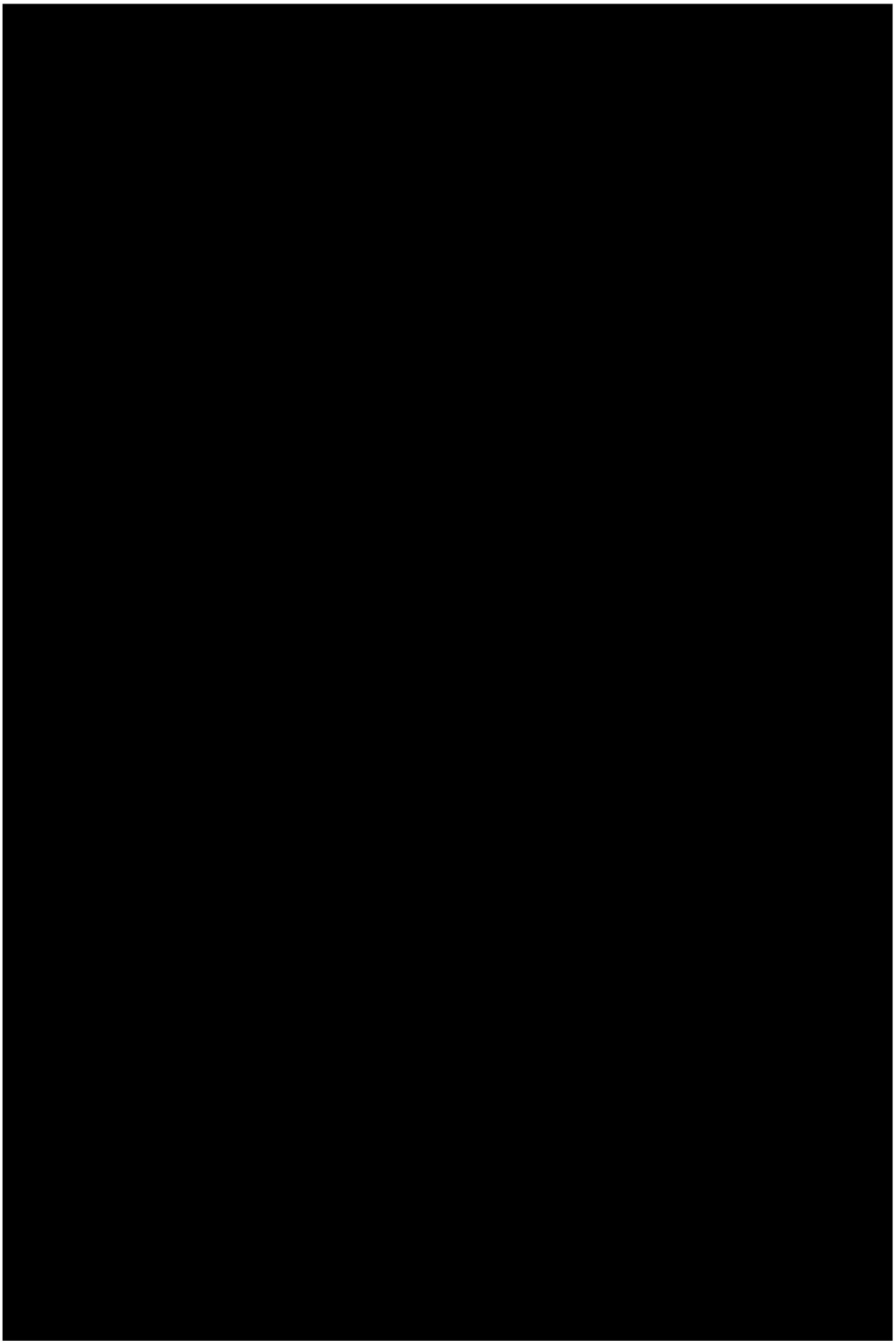

thermo-camera (dotted lines) are compared, allowing an estimation of the surface spectral emissivity of the sample. Test 1 was a preliminary test, carried out a relatively low enthalpies (step #0 of Table 2.1), to assess the capability of the material to withstand exposure to supersonic plasma flow without significant damages. In Test 2, higher enthalpy levels were reached, achieving temperatures up to 2020 K. The spectral emissivity appears to be decreasing with temperature, possibly also because of the surface modification occurring during the exposure to plasma jet. The temperature measured by the thermo-camera is in fact shown in the assumption of a constant spectral emissivity ε_λ of 0.75 [101] but it does not perfectly overlap the actual surface temperature measured by the pyrometer, in the two-colour mode. Employing the procedure outlined in section 2.1, it was possible to estimate that the spectral emissivity of the sample decreased from a value of 0.85 during the first two steps (specimen temperatures up to 1600 K), to 0.75 at the third step (temperature around 1700 K), to 0.6 during the fourth step and 0.5 for the fifth step, when the temperature exceeded 2000 K. This behaviour is in line with literature data [102,103] and the value of 0.5 is typical for zirconium oxide/silicon oxide outer scale [104]. The surface modifications are highlighted by the white colour assumed by the sample head due to the oxidation, as clearly visible in Fig. 4.9a-c, showing the specimen before and after the tests. After the exposure to the first two heating cycles, however, the sample exhibited neither structural damages, nor significant mass losses.

Hence, it was possible to expose it to the arc-jet during a third test, reaching, as anticipated, a specific total enthalpy of the flow of 20 MJ/kg and temperatures higher than 2400 K. Once again, the decrease in spectral emissivity with temperature is noticeable, since the thermo-camera (dotted) curve is plotted in the assumption of ε_λ = 0.75. It is interesting to notice the appearance of a high-temperature spot on the front surface of the sample, highlighted in Fig. 4.8b, which shows the infrared thermal images detected by the thermo-camera during steps #5 and #8. The sample temperature in step #5 was rather uniform, around 2000 K, except for the zone where the sample appears red, corresponding to a temperature of more than 2100 K. The hot spot was clearly visible until the end of the test, as demonstrated by the second thermal image of Fig. 4.8b, where the presence of a thin layer relatively hotter than the rest of the

sample surface is observable. This behaviour could be related to the formation of a zirconium oxide layer, leading to a dramatic reduction of the material thermal conductivity, which however preserved the rear part of the sample at sustainable temperatures. From Fig. 4.9d, which depicts the sample after Test 3, it is possible to observe the tendency of the oxide to spall off, since a structural crack is evidently noticeable. This could justify the presence of the localized hot spot discussed above. However, an almost negligible erosion rate was detected, as reported in Table 4.5.

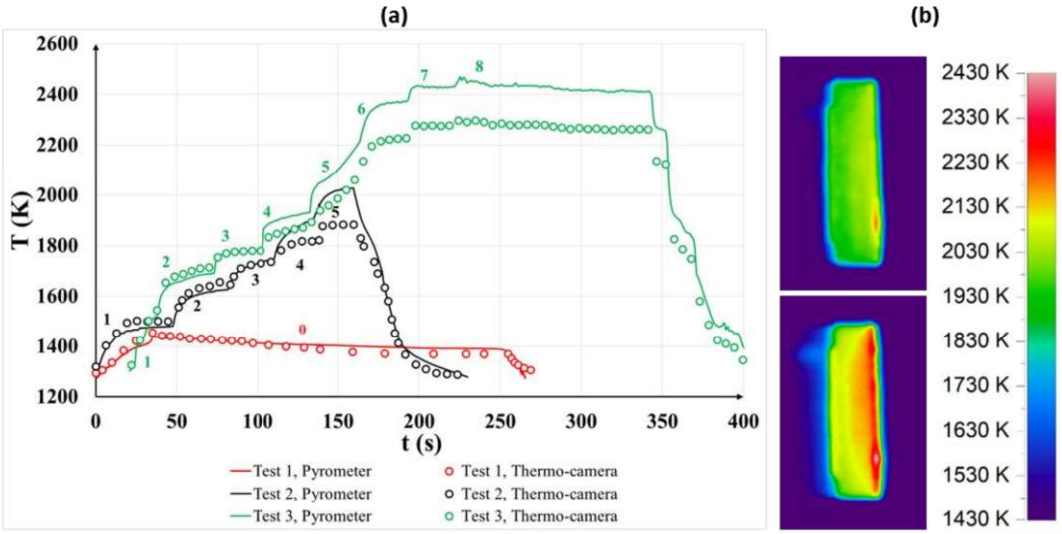

Fig. 4.8. a) Time histories of the maximum surface temperature of Sample n.1 during the three arc-jet tests, comparison between pyrometer and thermo-camera measurements. The specific total enthalpy levels corresponding to each step are listed in Table 2.1. b) IR thermal images of ZS-LF-1 at step #5 (top) and step #8 (bottom) of Test 3.

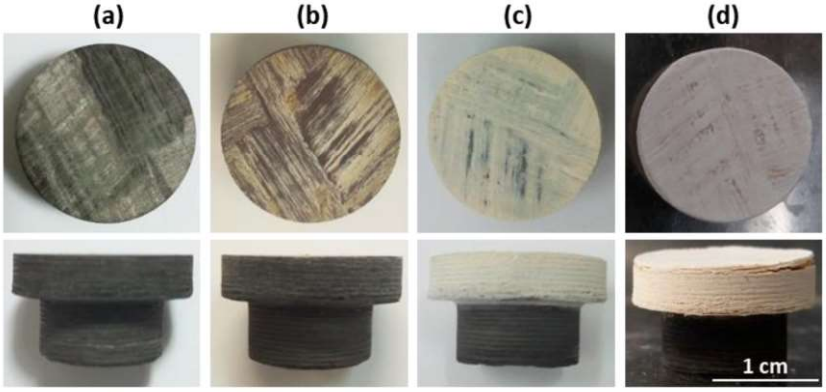

Fig. 4.9. Pictures of ZS-LF-1 (a) before the tests, (b) after Test 1, (c) after Test 2, (d) after Test 3, showing surface oxidation and oxide delamination (Fig. d).

Table 4.5. Ablation data for the three tests on sample ZS-LF-1.

Test #	Initial mass	Final mass	Average erosion rate (mass)
1	4.781 g	4.777 g	$2.5 \cdot 10^{-5}$ mm/s
2	4.777 g	4.763 g	$3.5 \cdot 10^{-4}$ mm/s
3	4.763 g	4.669 g	$4.9 \cdot 10^{-4}$ mm/s

Sample ZS-LF-2 was tested once, reaching the enthalpy levels corresponding to steps from #1 to #8, listed in Table 2.1. The last step ($H_0 = 20$ MJ/kg) lasted about 120 s. The thermal history of the specimen is plotted in Fig. 4.10, comparing the real temperature measurement performed by the pyrometer and the thermo-camera output, obtained assuming a constant spectral emissivity of 0.5. A slightly different positioning of the thermo-camera allowed in this case to observe also the front surface of the sample.

An interesting phenomenon was detected during the last step, when the thermo-camera signal presented a sudden discontinuity in the measured temperature (in Fig. 4.10, it is highlighted by a red circle), similar to those detected during arc-jet characterization of ZrB_2-SiC UHTCs [50] and C-SiC composites [55]. This "*jump-of-radiance*" was associated to the appearance of some surface instabilities on the front face of the sample. Fig. 4.10 also shows two thermal images of the sample, just before and just after the jump in the measured temperature. In the second picture, higher values of the irradiated power are noticeable in a bubble forming on the surface, due either to an increase in spectral emissivity or to an increase in temperature. In the second case, since the two-colour pyrometer did not detect significant temperature jumps during the test, a possible explanation of this might be that the instrument, facing the opposite side of the sample, did not point directly on the instabilities. The formation of bubbles evolved unsteadily during the last enthalpy step, until a thin hot layer was formed also in this case in the front part of the sample, as shown in Fig. 4.11. In the picture on the right, in particular, the front surface of the sample, relatively hotter than the rear region, is clearly distinguishable. According to the thermo-camera measurements, the highest temperature reached on the sample was almost 2550 K.

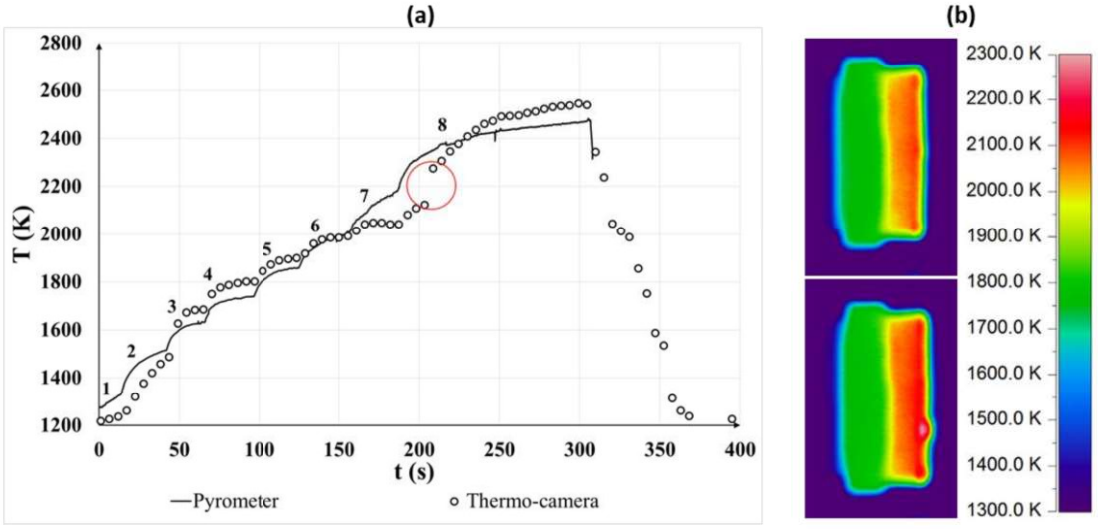

Fig. 4.10. a) Time history of the temperature of ZS-LF-2 with comparison between pyrometer and thermo-camera data. The temperature profile of the thermo-camera is obtained under the hypothesis of a spectral emissivity of 0.5. The red circle highlights a "jump-of-radiance" detected by the thermo-camera during the final step. b) IR thermal images of the sample just before (above) and just after (below) the appearance of the jump-of-radiance.

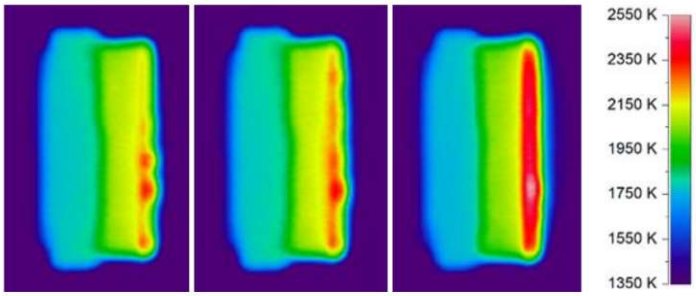

Fig. 4.11. Thermal images of the evolution of surface instabilities on ZS-LF-2 during step #8, showing bubble bursting on the front surface (right in the frames).

Bubble nucleation might be explained with extrusion of volatile products (e.g. CO, SiO, produced at high temperatures after transition from passive to active oxidation of SiC) through the liquid film of SiO_2 covering the surface, until almost total removal of the glassy phase, which left exposed a zirconium dioxide layer, according to the typical oxidation mechanism of ZrB_2-SiC ceramics [27], as will be discussed in detail in the next sections. The ZrO_2 scale, as discussed for ZS-LF-1, exhibits significant

insulating properties resulting in the temperature distribution observed by the IR thermal images, with the front, oxidized, area hotter than the rear bulk material.

To provide a deeper insight in the material behaviour and also to validate the numerical models, coupled to the fluid field (see section 4.1), the thermal behaviour of the material has been studied, performing steady-state simulations. The results of the simulations corresponding to the enthalpy levels of steps #1, #3 and #5 were compared to the data measured during Test 2 on sample ZS-LF-1. The density of the sample was derived from mass and volume measurements, and was equal to 3000 kg/m^3. The thermal conductivity was estimated by means of a sensitivity analysis comparing the CFD and experimental axial temperature profiles. The material surface emissivity, as discussed above, changed during the different steps of Tests 2 and 3. Different values have for this reason been used in the different simulations. The values of the overall surface emissivity have been estimated based on the spectral emissivities derived from the IR-TC measurements, in the assumption that, at the high temperatures reached during the tests, most of the power is irradiated in the wavelength band around 1μm, where the value of ε_λ was calculated [69]: it is therefore reasonable to assume that the estimated value of spectral emissivity is representative of the total emissivity along the whole wavelength spectrum.

To evaluate the thermal conductivity of the sample, a sensitivity analysis was performed. Assuming a surface emissivity $\varepsilon = 0.9$ and non-catalytic behaviour, different CFD simulations were carried out to match the temperature axial profile obtained by means of the thermo-camera measurements, in the case of step #1. As shown in Fig. 4.12a, the value of k = 20 W/(m K) allows matching the experimental surface temperature slope along the axial direction. Hence, this value was used also for the simulations of steps #3 and #5. At these enthalpy levels, the formation of zirconia on the surface appeared not to play a significant role in the determination of thermal conductivity, which was uniform all along the sample surface. Fig. 4.12b and c show also a comparison between the numerical and experimental distributions of temperature inside the sample.

To match the experimental values of maximum temperature at higher enthalpy levels at the steady state, both the conditions on surface emissivity and catalycity

needed to be changed. In particular, based on the analysis of the spectral emissivity reported above, values of 0.75 and 0.5 were set for the total emissivity of the specimen, respectively for step #3 and #5 of Test 2. However, the reduction in the irradiated power was not enough to justify the rise in temperature. To match the experimental value of the surface temperature, the catalycity also needed to be taken into account.

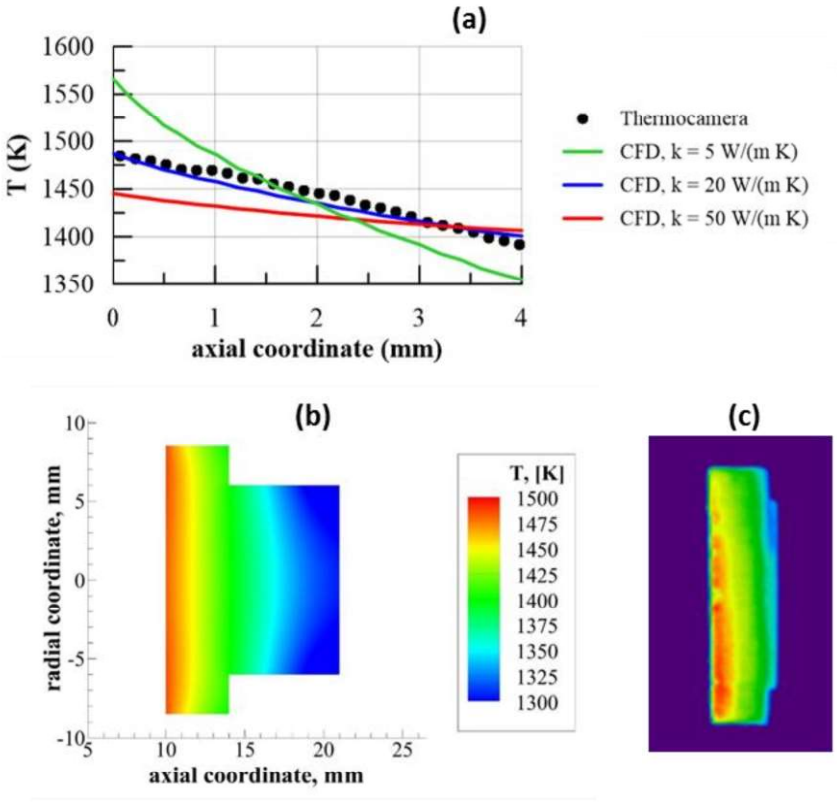

Fig. 4.12. a) Experimental and numerical temperature axial profiles at steady state, for different values of the thermal conductivity. Conditions corresponding to step #1 of Test 2 on ZS-LF-1 (H_0 = 7 MJ/kg). b) Temperature distribution inside the UHTCMC specimen: comparison between b) CFD steady-state solution and c) experimental measurement by IR thermo-camera.

Therefore, based on the models described in section 3.1.1 and 3.3, a detailed parametric analysis on the effect of the catalytic recombination occurring at wall was performed for step #5. For different values of the catalytic recombination coefficient, ranging from zero- to fully-catalytic condition, steady state simulations were carried out. The resulting maximum sample temperature is reported versus γ_w in Fig. 4.13.

The diagram shows the typical s-shape also reported in [105,106]. Comparing the results of the simulations with the experimental data, it was possible to estimate the value of γ_w allowing to match the pyrometer measurement. In particular, the catalytic recombination coefficient γ_w was set to $5.5 \cdot 10^{-3}$ and $8.5 \cdot 10^{-3}$, respectively for steps #3 and #5.

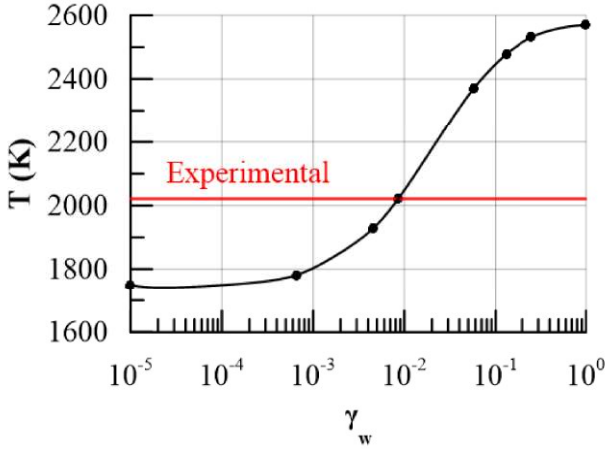

Fig. 4.13. Maximum sample front surface temperature versus catalytic recombination efficiency, for step #5 of Test 2 on ZS-LF-1 (H_0 = 14 MJ/kg, ε = 0.5). A good numerical-experimental agreement was found for $\gamma_w = 8.5 \cdot 10^{-3}$.

Fig. 4.14 shows a comparison between the numerical and experimental temperature axial profiles along the specimen for the three analysed steps of Test 2. The curves confirm that there is a good agreement not only in the maximum value, but also in the slope along the axis, justifying again the choice of a thermal conductivity of 20 W/(m K).

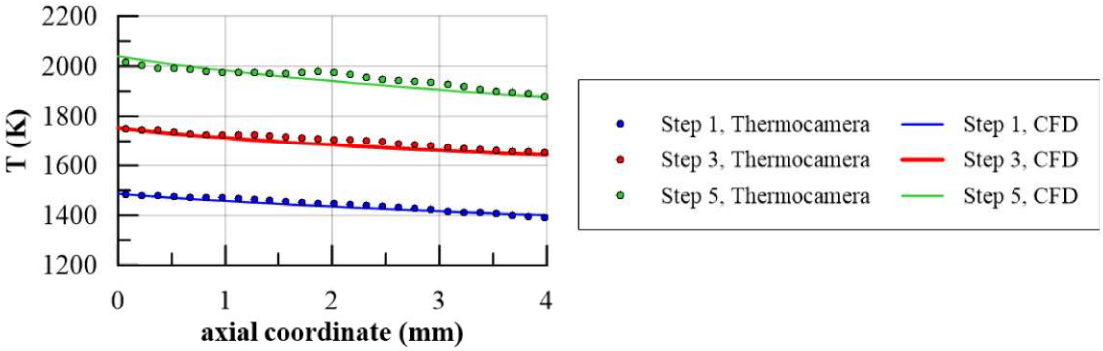

Fig. 4.14. Comparison between experimental and numerical temperature axial profiles for the three analysed steps of Test 2 on ZS-LF-1.

4.2.2 Further test on sintered ZrB_2-SiC-based UHTCMCs

Based on the promising results of the early test campaign on ZrB_2-SiC-based samples, further test were performed on materials provided by CNR-ISTEC, with the same matrix components (plus the inclusion, in some cases, of stabilizing Y_2O_3) and either short or long fibres. Samples are labelled ZS-SF, ZSY-SF and ZSY-LF. Two samples of each formulation were tested. Samples ZS-SF (densified by Spark Plasma Sintering, SPS) contained 10vol% SiC in the matrix. Sample ZSY-SF-1 (densified by HP) contained 5 vol% SiC and 5vol% Y_2O_3. Samples ZSY-SF-2 and ZSY-LF (densified by HP) contained 10 vol% SiC and 5 vol% Y_2O_3.

The thermal histories of the different samples, measured by the ISQ5 pyrometer, are plotted in Fig. 4.15. The stepwise increase in temperature is associated to the power increase procedure. At the maximum enthalpy level, the temperatures of all the samples reached values close to 2700 K and even overpassed 2800 K for one of the samples tested at the highest power condition, ZSY-SF-2. In particular, it was clear that a sudden rise in temperature (herein defined as *spontaneous temperature jump* because it occurs rapidly and at constant H_0, and labelled *TJ*) of several hundred degrees occurred during the highest-enthalpy steps, even at a constant arc power, after a steady state condition had apparently been reached. The jump happened for all the samples when the flow specific total enthalpy was 18 MJ/kg. For samples ZS-SF-1 and 2, the *jump* occurred around t = 160 s, when the temperature had reached an apparent stable value of 2200 K. For sample ZSY-SF-1 the *jump* occurred around t = 150 s, few seconds after the surface temperature reached a stable value over 2250 K, while for samples ZSY-SF-2 and ZSY-LF-1 and 2, the momentary equilibrium temperature was around 2150 K (achieved a t = 160 s and 180 s, respectively). For samples ZS-SF-1 and ZSY-SF-2 the torch arc power was further increased to the maximum value (H_0 = 20 MJ/kg) at t = 180 s, when the *jump* had already been triggered and the surface temperature was 2270 K, resulting in an increased slope of the temperature time profile and a surface temperature exceeding 2800 K at the end of the heating phase. The *temperature jump phenomenon* is typically observed for UHTC- and SiC-based composites [107,108] and can be associated to a drastic change in surface chemistry, as will be widely discussed in section 4.6.

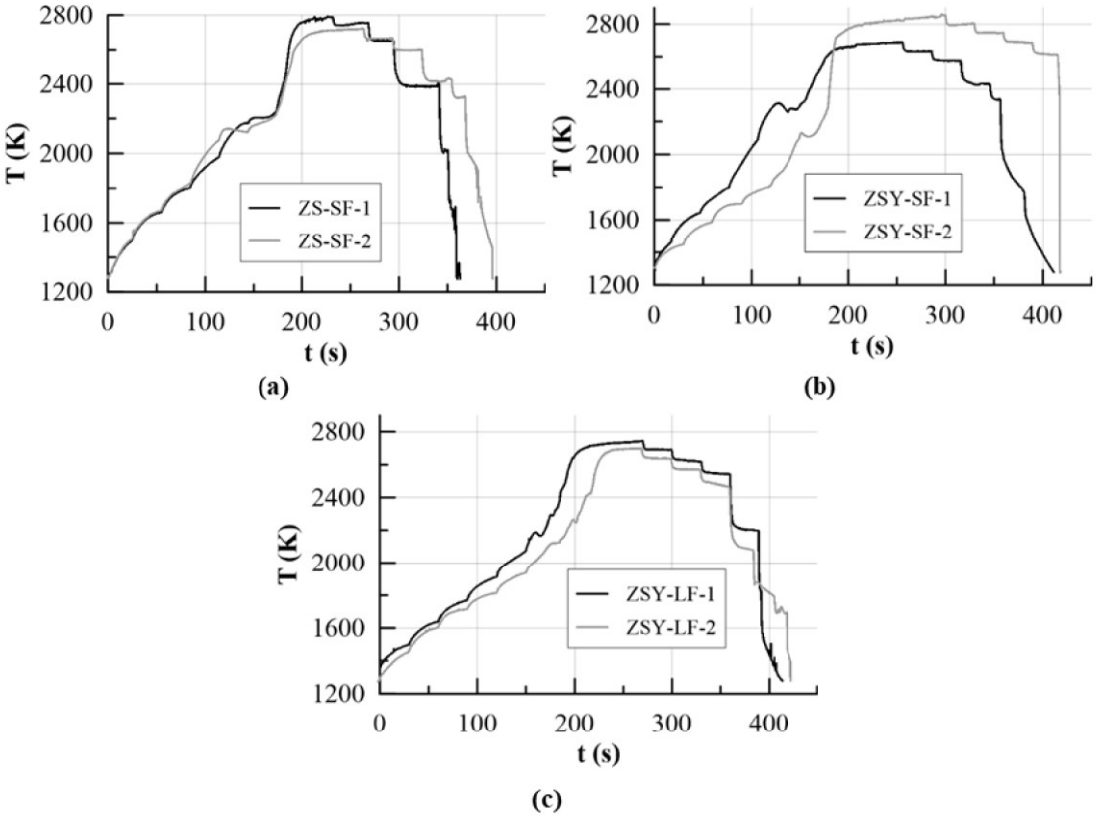

Fig. 4.15. Temperature histories of the samples, measured by the ISQ5 pyrometer.

After the tests, all samples heads appeared completely oxidized, with a white layer, mainly composed of ZrO_2, as discussed below, covering the surface. For samples described in the previous section, this layer had been found to be porous, fragile and with tendency to spall off. The outer oxide layer of samples ZS-SF-1 and 2 demonstrated a poor adherence to the lower substrate, from which it detached (Fig. 4.16a). The thickness of this layer was about 0.45 mm and this phenomenon clearly affected the estimation of erosion rate. All the other samples preserved instead the original shape and a perfect structural integrity, despite the clearly noticeable signs of surface oxidation (see Fig. 4.16b and c). The long-fibre layered architecture of samples ZS-LF is still observable (see Fig. 4.16c).

The average mass- and thickness-based erosion rates are reported in Table 4.6 and all of them are on the order of 10^{-3}-10^{-4} mm/s. Balance between oxygen inclusion and C, Si and B volatilization upon sample oxidation resulted in a net, although limited, mass loss. It is interesting to observe that, on the other hand, oxidation led to a

thickening of samples heads, resulting in a negative ablation rate based on thickness measurement. Since no other samples dimensions had significant variations with respect to the nominal values, only thickness data are here reported. Based on these measurements, it can be concluded that all the samples experienced a slight volume increase despite the net mass loss.

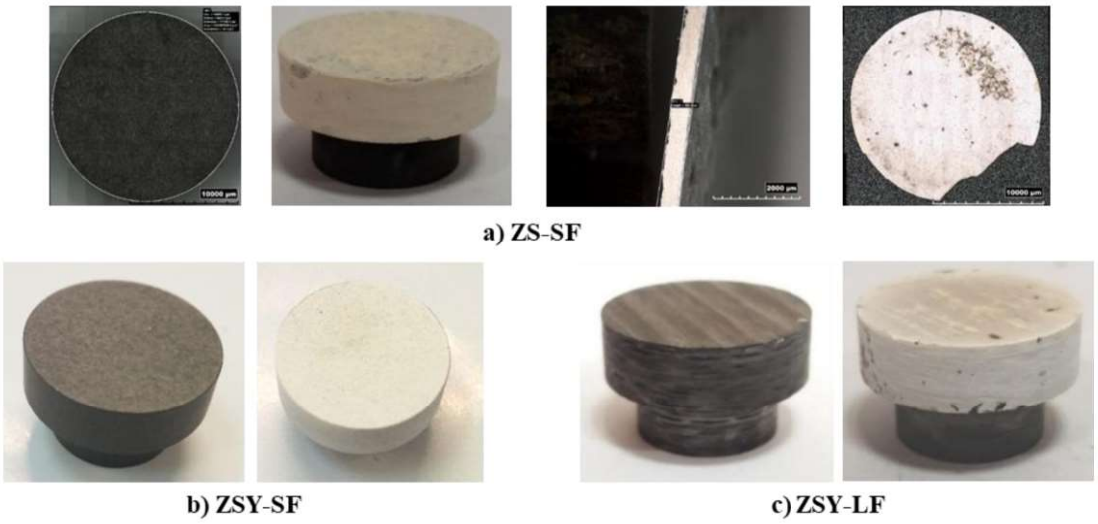

Fig. 4.16. Pictures of some samples before (left) and after (right) test. For sample ZS-SF-1 (a), pictures of the detached zirconia layer are also shown (the two pictures on the right).

During test on sample ZS-SF-1, at the last enthalpy step (H_0 = 20 MJ/kg), after the *temperature jump*, some instability phenomena were observed, in the form of bubbles nucleation (Fig. 4.17). These phenomena have also been detected by the ISQ5 pyrometer, which observes oscillations of the temperature profile at the maximum power condition (see Fig. 4.15a). As stated in the previous section, the appearance of bubbles on the exposed face had already been observed on the earliest samples, associated to a sudden increase by over 200 K in the temperature measured by the thermo-camera.

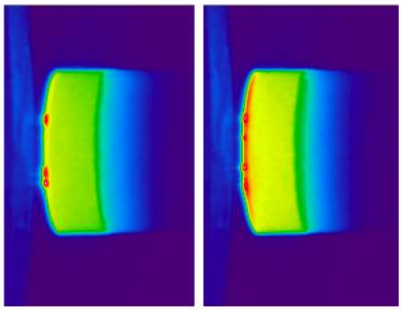

Fig. 4.17. IR pictures of sample ZS-SF-1 showing bubble bursting on the exposed surface.

The IR video of test on sample ZSY-SF-1 showed that, few seconds before the *temperature jump*, an unsteady evolution of the irradiated power appeared on the side surface, resulting in a wavy oscillation of the surface temperature. Specifically, the colour of the surface in the IR images displayed an unsteady variation, taking the form of a train of vertical waves of a liquid phase convectively moving downstream along the axial direction. A comparable phenomenon has been already reported by Monteverde et al. [50], who defined it as *waves of radiance* and correlated it to the transport of a liquid glassy oxide phase from the front surface along the side of the sample by the shear stresses induced by the supersonic flow. Evidence of the *waves of radiance* is provided in Fig. 4.18, which is referred, as examples, to samples ZSY-SF-1 and ZSY-LF-2, respectively. The diagrams on the left (Fig. 4.18a) show the temperature axial profiles measured by the TC on the side surface of the samples, each curve representing a specific time instant at the earliest stages of the temperature jump. The diagrams on the right (Fig. 4.18b) report instead the time evolution of the

temperature at different locations along the surface. The curves have been obtained assuming a constant spectral emissivity along the whole surface, so they should be more correctly interpreted as surface radiance profiles, rather than actual temperature diagrams. Two features can be remarked. First, the axial profiles of Fig. 4.18a are not straight, but temperature oscillations can be noticed, up to around 20 K. The same behaviour was observed in [50]. Moreover, it is possible to see that, as time advances, the radiation temperature does not change uniformly along the samples length, but the distance between two curves corresponding to consecutive instants is variable, and in some case the lines even cross each other. This phenomenon is evidenced also in the pictures on the right (Fig. 4.18b). The curves display an oscillatory trend and tend to get closer and farther as time advances, testifying an unsteady evolution of the radiated power which is different at each axial location.

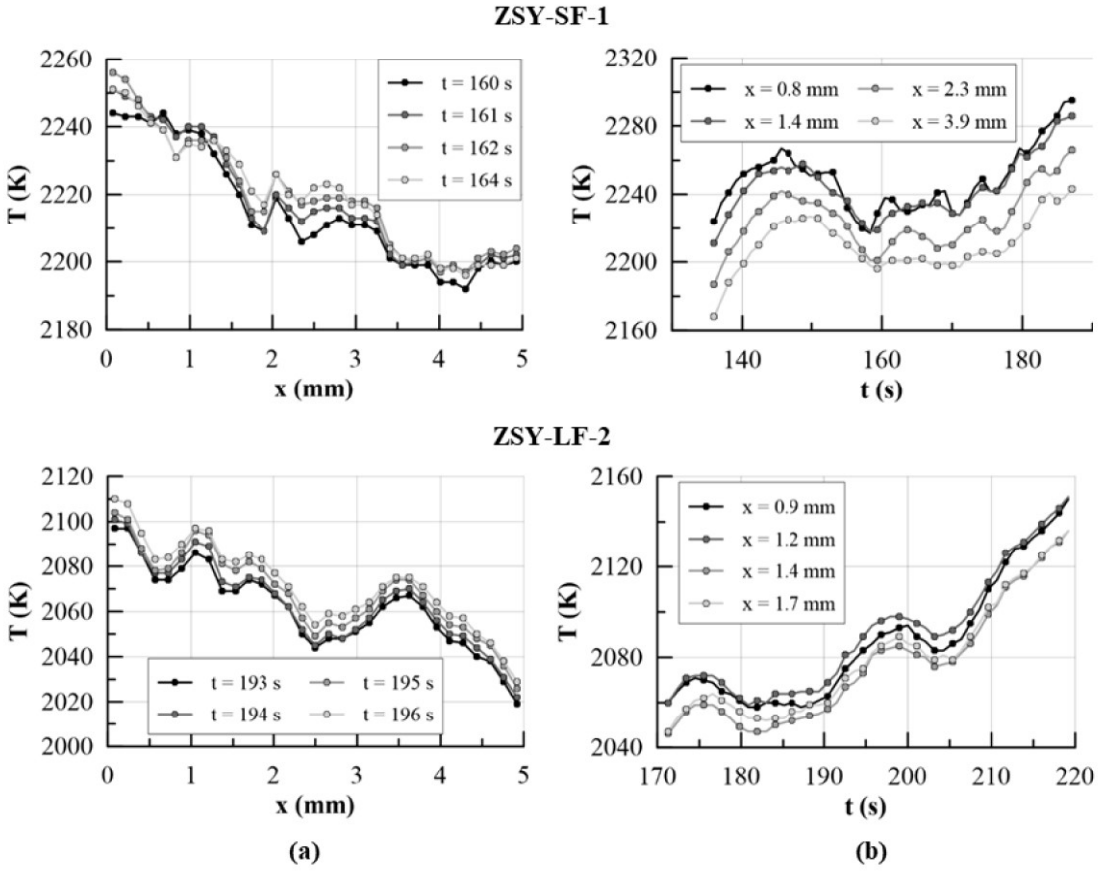

Fig. 4.18. For samples ZSY-SF-1 and ZSY-LF-2: a) Temperature axial profiles, measured by IR-TC before temperature jump; b) Time evolution of the IR-measured temperature at different points along the sample side surface.

For a sound analysis of the material thermal behaviour during arc-jet testing, infrared measurements on sample ZSY-LF-2 were taken as reference. During the tests, the ISQ5 pyrometer was pointed towards the sample front face, whereas the IGAR6 pyrometer looked at the side surface. Moreover, the IR thermo-camera positioning allowed to analyse both the front and the side surfaces facilitating the visualization and characterization of the temperature jump phenomenon. Fig. 4.19a and b show the thermal distribution on the sample respectively just before and just after the jump, during the maximum enthalpy step (H_0 = 18 MJ/kg). It is evident that only the front part of the sample experienced a dramatic increase in temperature, whereas the rear body appeared to be almost unaffected by the thermal rise. The same trend is visible in Fig. 4.19c, where the thermal histories recorded by the two pyrometers for the two surfaces of the sample are shown. It is evident that the measurements matched well in the earliest phases of the test, whereas, at temperatures over 2100 K, they started diverging, and the front face reached a steady-state temperature around 500 K higher than the side.

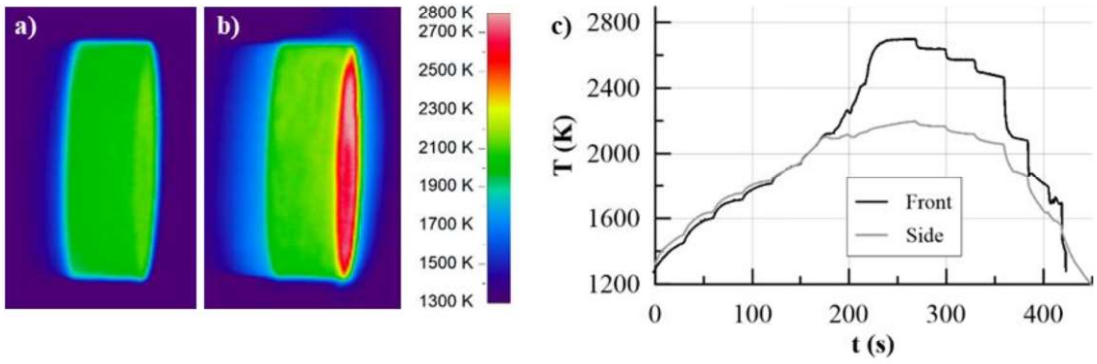

Fig. 4.19. Sample ZSY-LF-2: Thermal images (a) before and (b) after the temperature jump, and (c) Comparison of temperature measured by ISQ5 pyrometer (front surface) and IGAR6 pyrometer (side surface).

Thermo-camera and pyrometers measurements were compared to provide an estimation of the spectral emissivity in the near infrared wavelength band, which is common to all instruments. Fig. 4.20 shows the temperature curves collected by pyrometers and thermo-camera, on front (a) and on side (b) surfaces of sample ZSY-LF-2, assuming a spectral emissivity $\varepsilon_\lambda = 0.7$. The non-perfect overlapping suggests a

change in emissivity during heating. This trend is quantified in Fig. 4.21, where the value of ε_λ, evaluated by matching the pyrometer and thermo-camera measurements as described in section 2.1, is plotted versus test time (a) for both the front (black line) and side (grey line) surfaces of sample ZSY-LF-2, and also versus temperature (b) only for the front surface. Spectral emissivity appeared to increase in the earliest phases of the test, from a value below 0.4 after 30 s (end of first enthalpy step) up to over 0.7, after roughly 60 s (end of second enthalpy step). Then, ε_λ gradually decreased during heating on both surfaces, attaining a minimum value between 0.5 and 0.6 and then rapidly increasing again after the temperature jump up to almost 0.8. Finally, it appears that, during the cooling phase, the emissivity rapidly decreased on the front surface, while it is almost constant on the side.

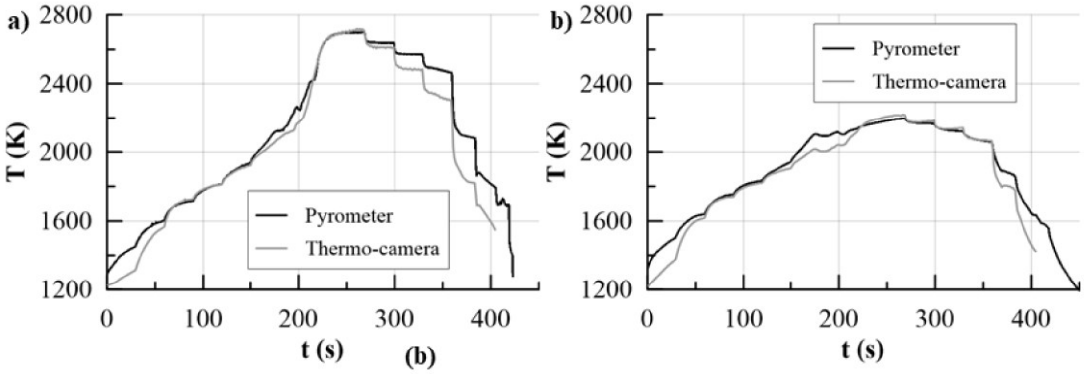

Fig. 4.20. Comparison between temperature measured by pyrometers and thermo-camera (ε_λ = 0.7) (a) on the front surface and (b) on the side surface, of sample ZSY-LF-2.

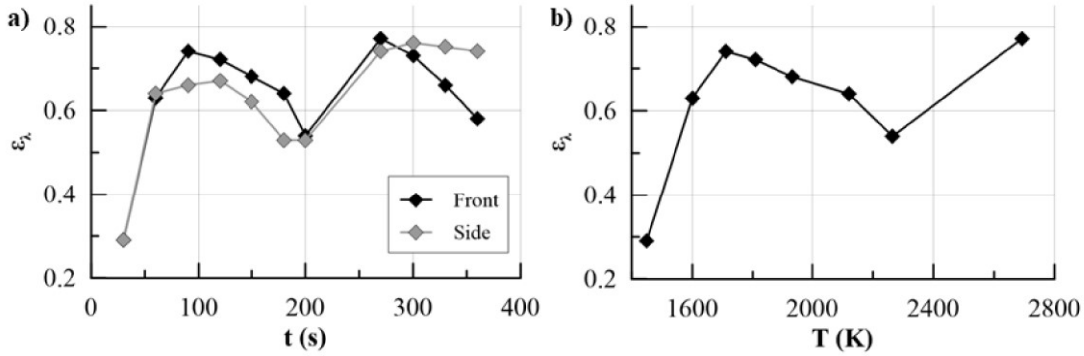

Fig. 4.21. Samples ZSY-LF-2: Spectral emissivity in the near-infrared wavelength band (a) on front and side surface, versus test time, (b) on the front surface, versus temperature.

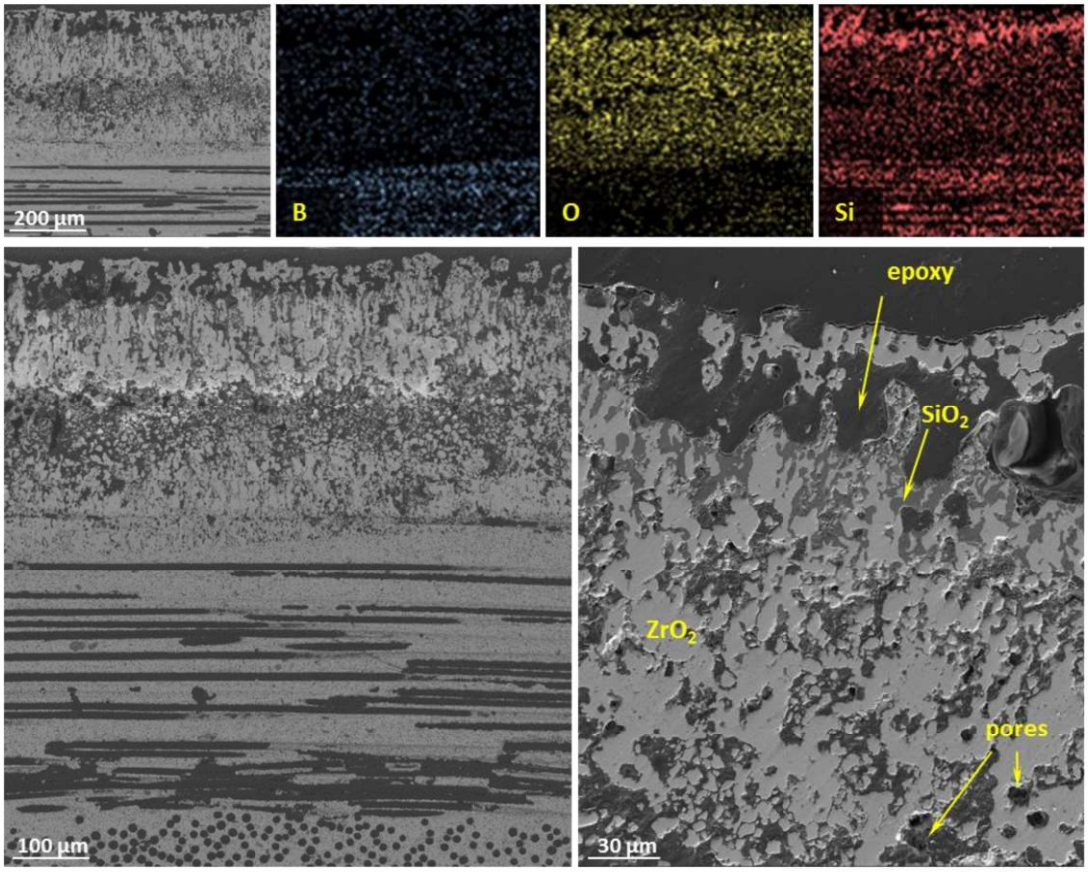

Fig. 4.22. SEM image of the cross section of the ZSY-LF-2 sample after the arc-jet test with corresponding EDS elemental maps showing boron, oxygen and silicon distribution across the profile. Bottom pictures show the outermost oxide layer at higher magnification.

In order to implement the numerical calculation (whose details will be reported in the overall discussion in section 4.6) and gain an insight into the samples aerothermal behaviour during arc-jet testing, post-test microstructures were analysed at CNR-ISTEC by SEM and energy dispersive x-ray spectroscopy (EDS, INCA Energy 300, Oxford instruments, UK). As an example, the long-fibre UHTCMC ZSY-LF-2 is considered. The outer surface presented discontinuous zones of silica-based rich glass and a sort of ZrO_2 sheath of the carbon fibre which were ablated away. Fig. 4.22 shows SEM pictures of the ZSY-LF-2 sample cross-section after exposure to the supersonic plasma flow with EDS mapping of the main components and a zoom on the outermost oxide layer. The overall oxide layer had a thickness of around 360 µm, which

approximately corresponds to the thickness of one fabric scale. The oxide appeared more damaged and brittle in the centre as compared to the periphery where it was rather compact smooth. Below this layer, the pristine microstructure appeared unaffected, with evidence of the 0°/90° architecture of the fibres. EDS revealed complete boron removal in the region of oxygen penetration, whilst silicon was slightly depleted in the subscale and accumulated close to the surface. At higher magnification, the outermost layer comprised a roughly 50μm-thick pure ZrO2 region, which displayed an irregular and highly porous structure. Below this, a silica-rich layer was present, which covered a SiC-depleted region, where voids were left by Si outwards diffusion. There was no evidence of carbon fibres survival to the exposure to the arc-jet flow, all along the oxide thickness (360 μm).

4.2.3 Other material formulations

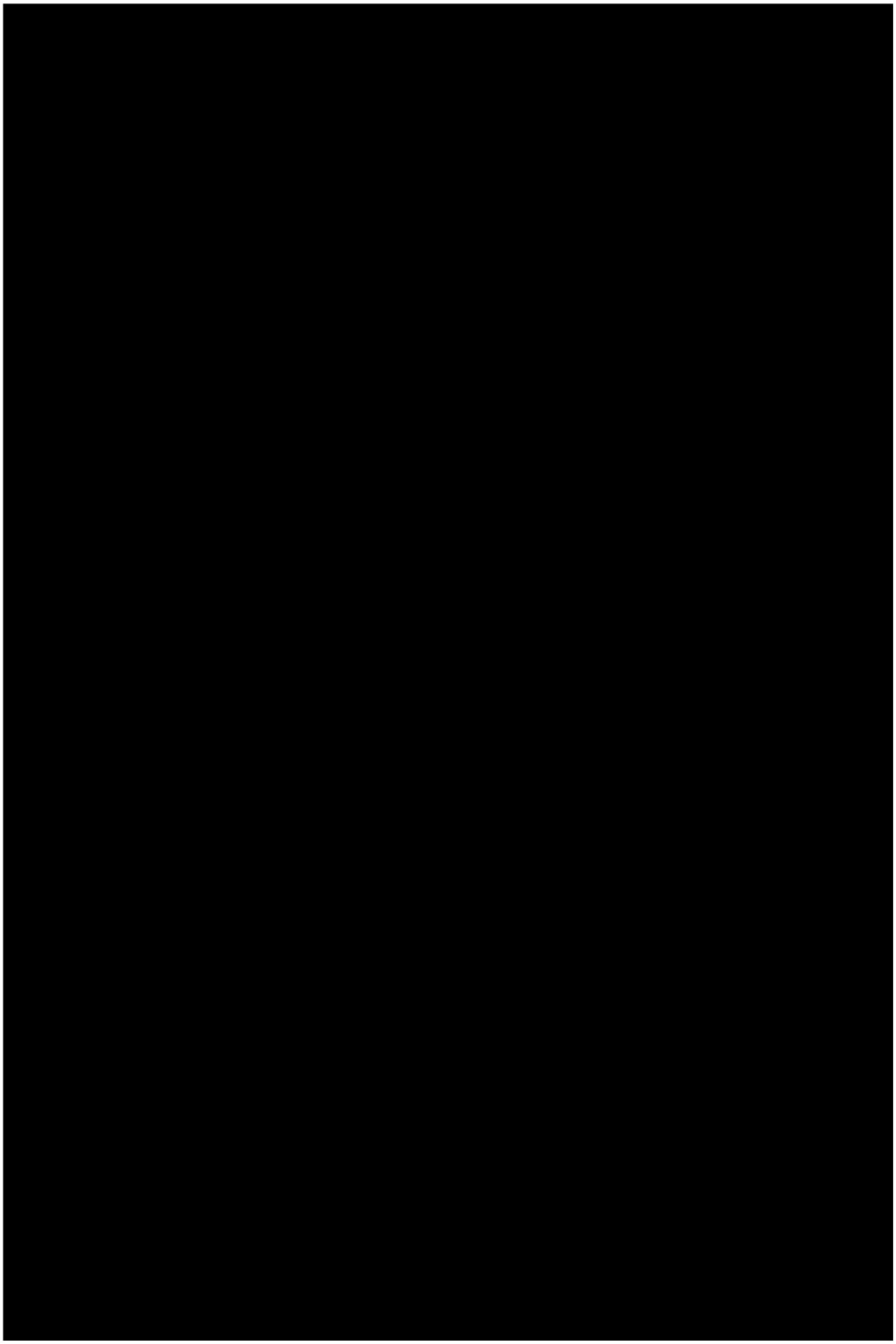

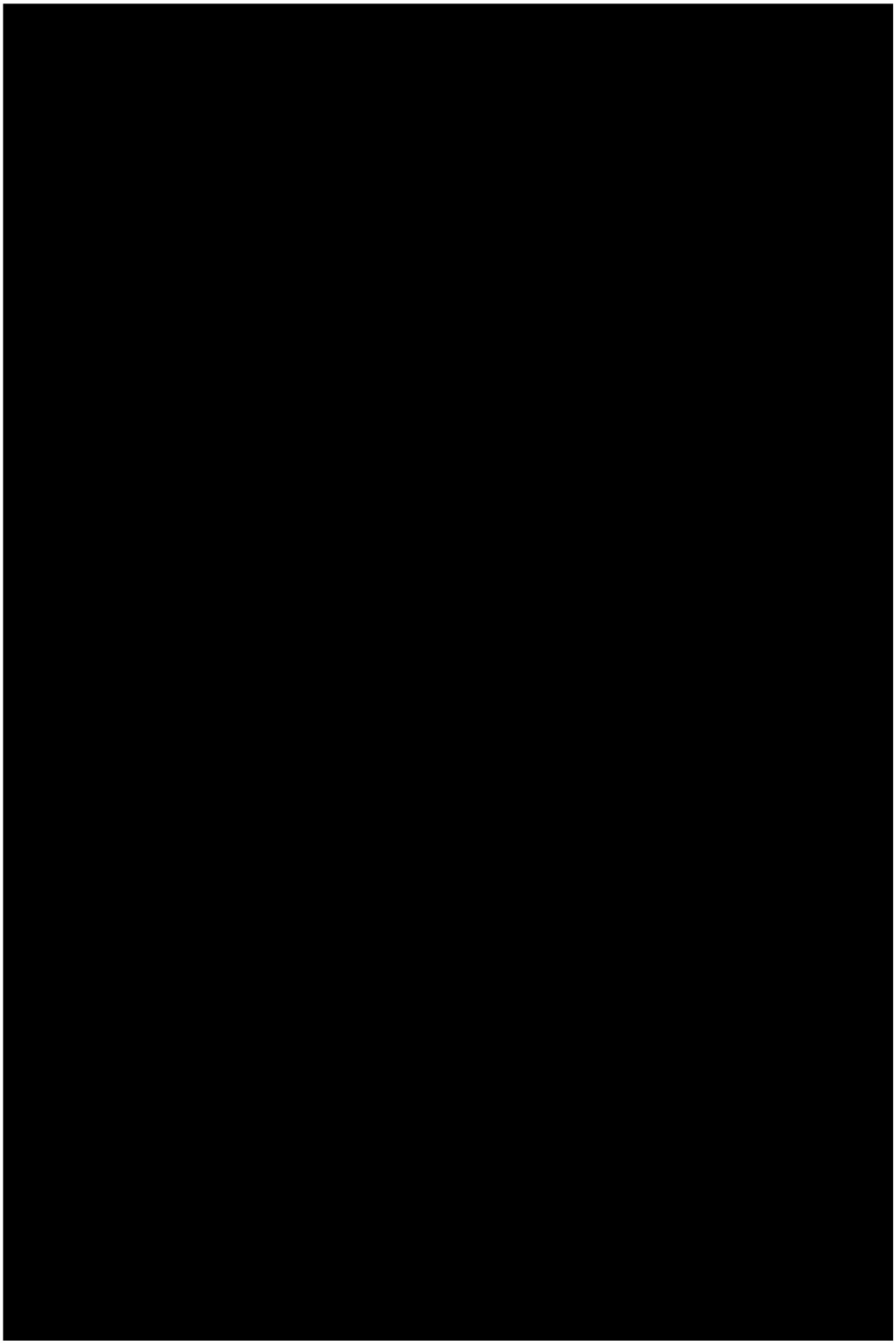

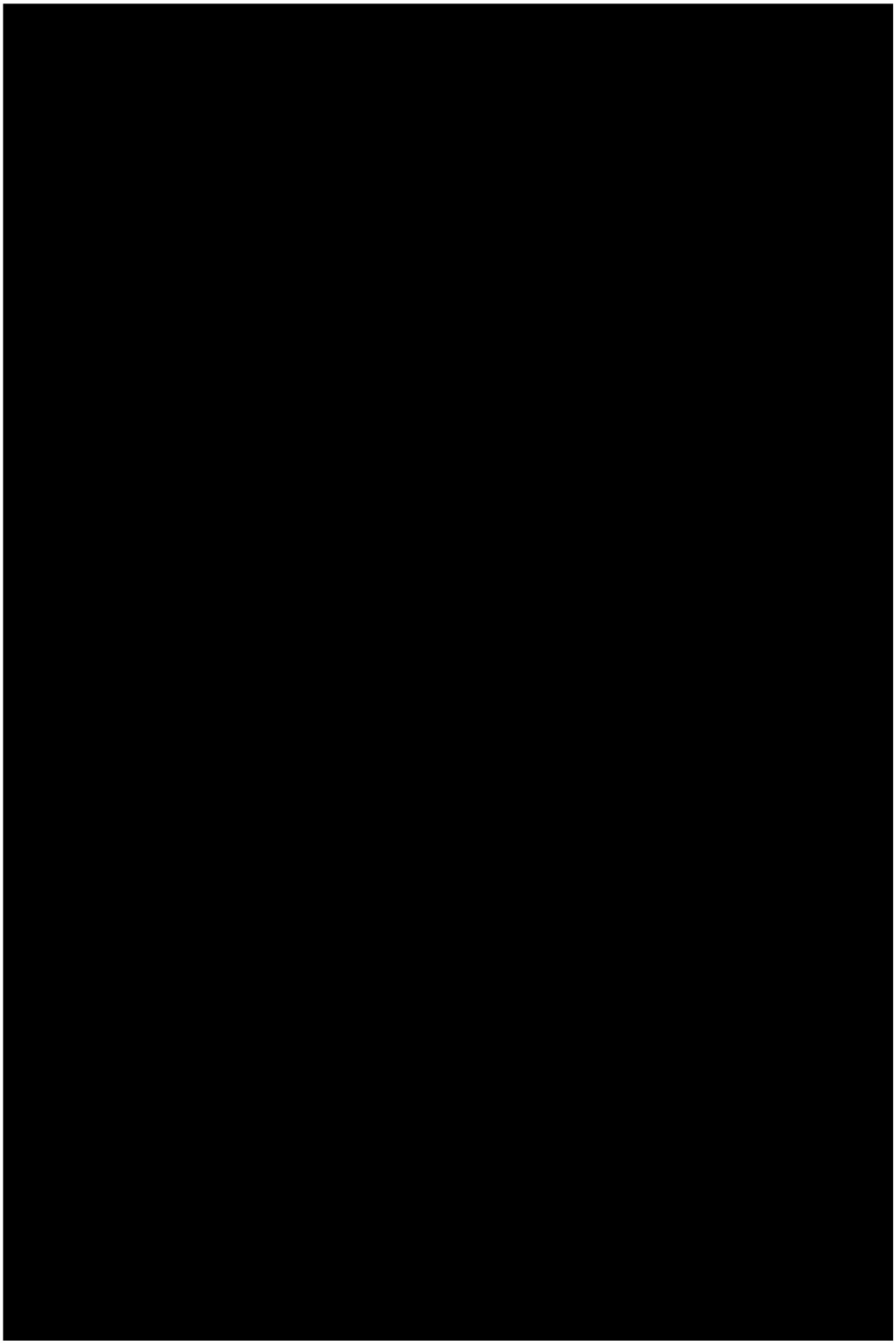

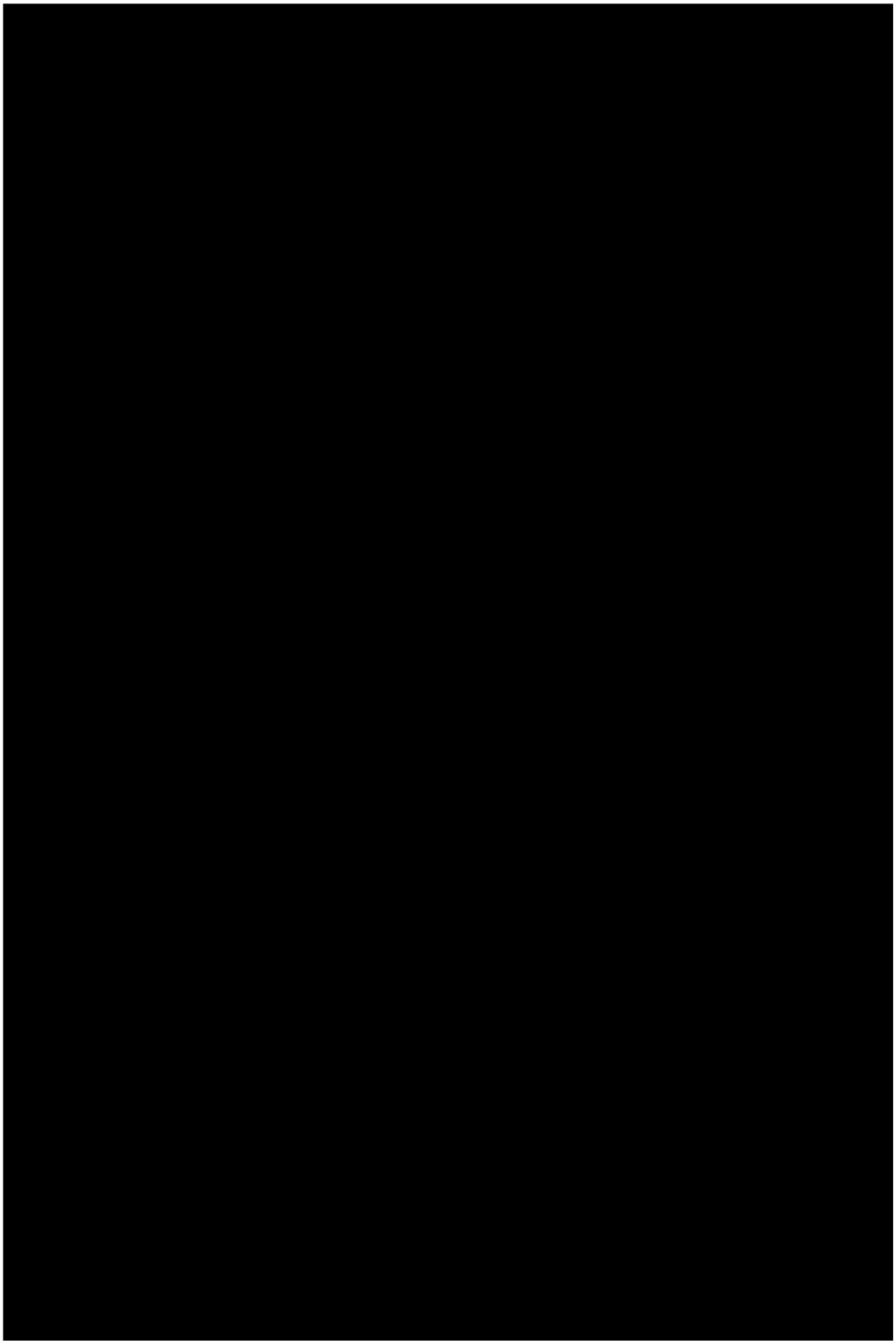

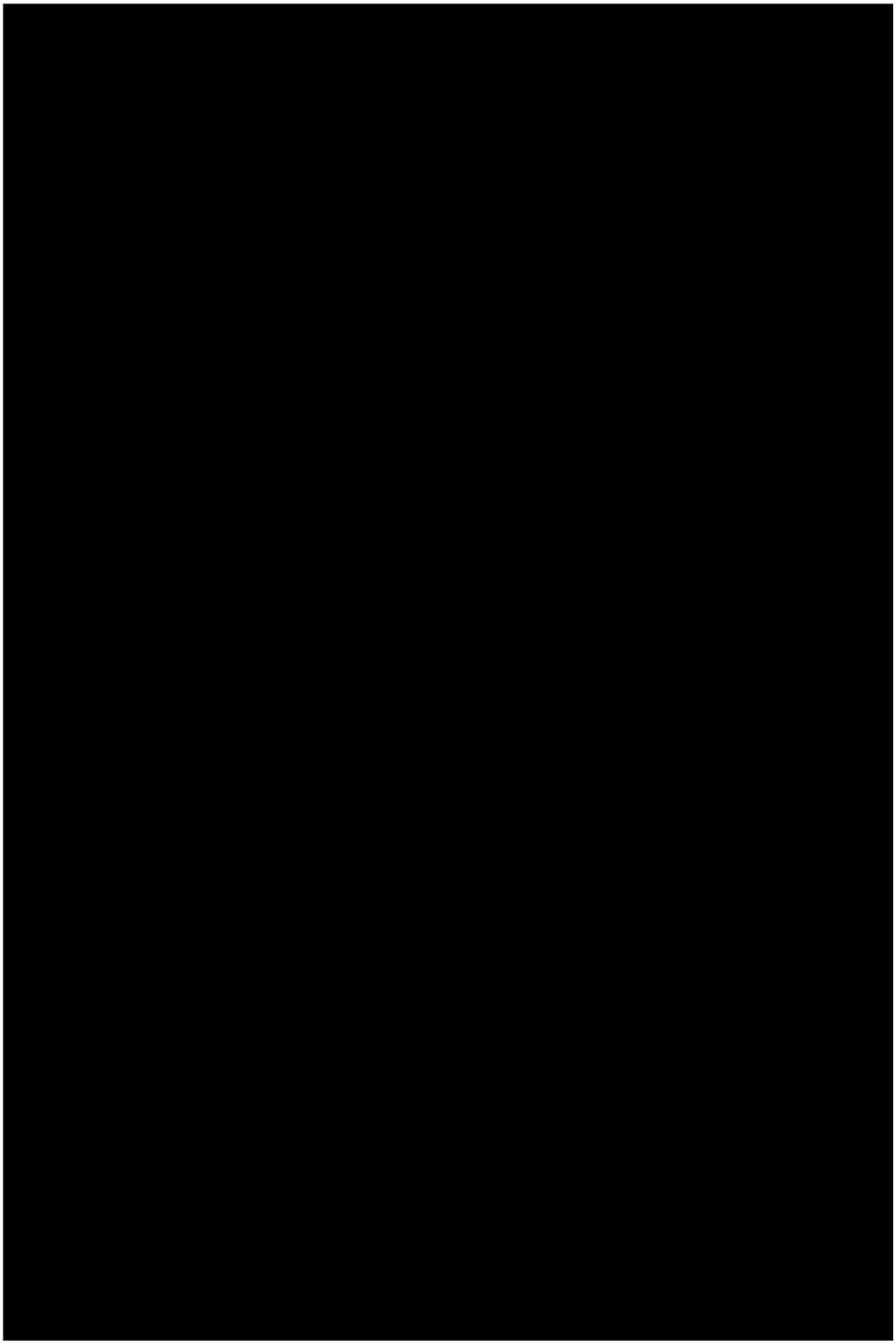

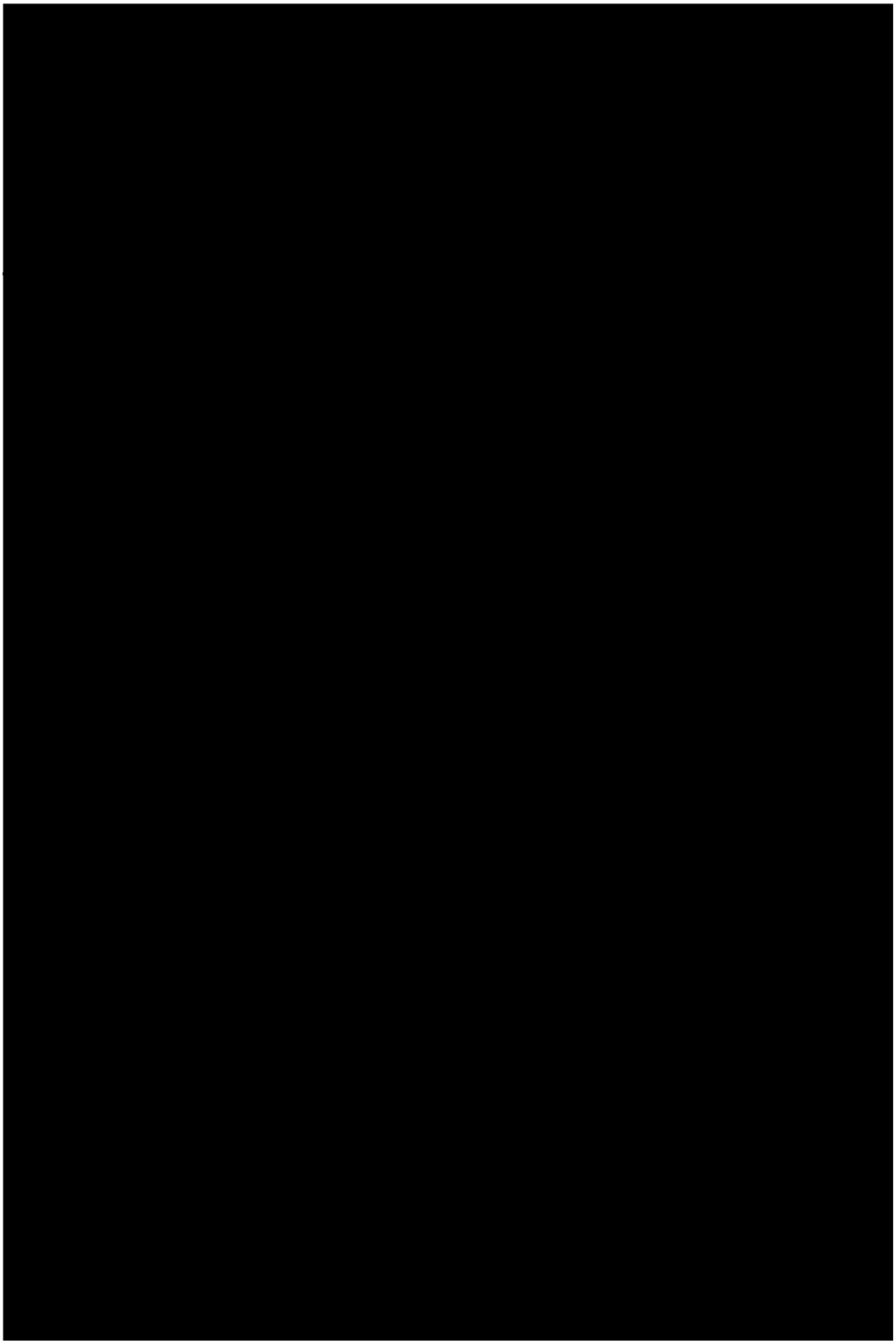

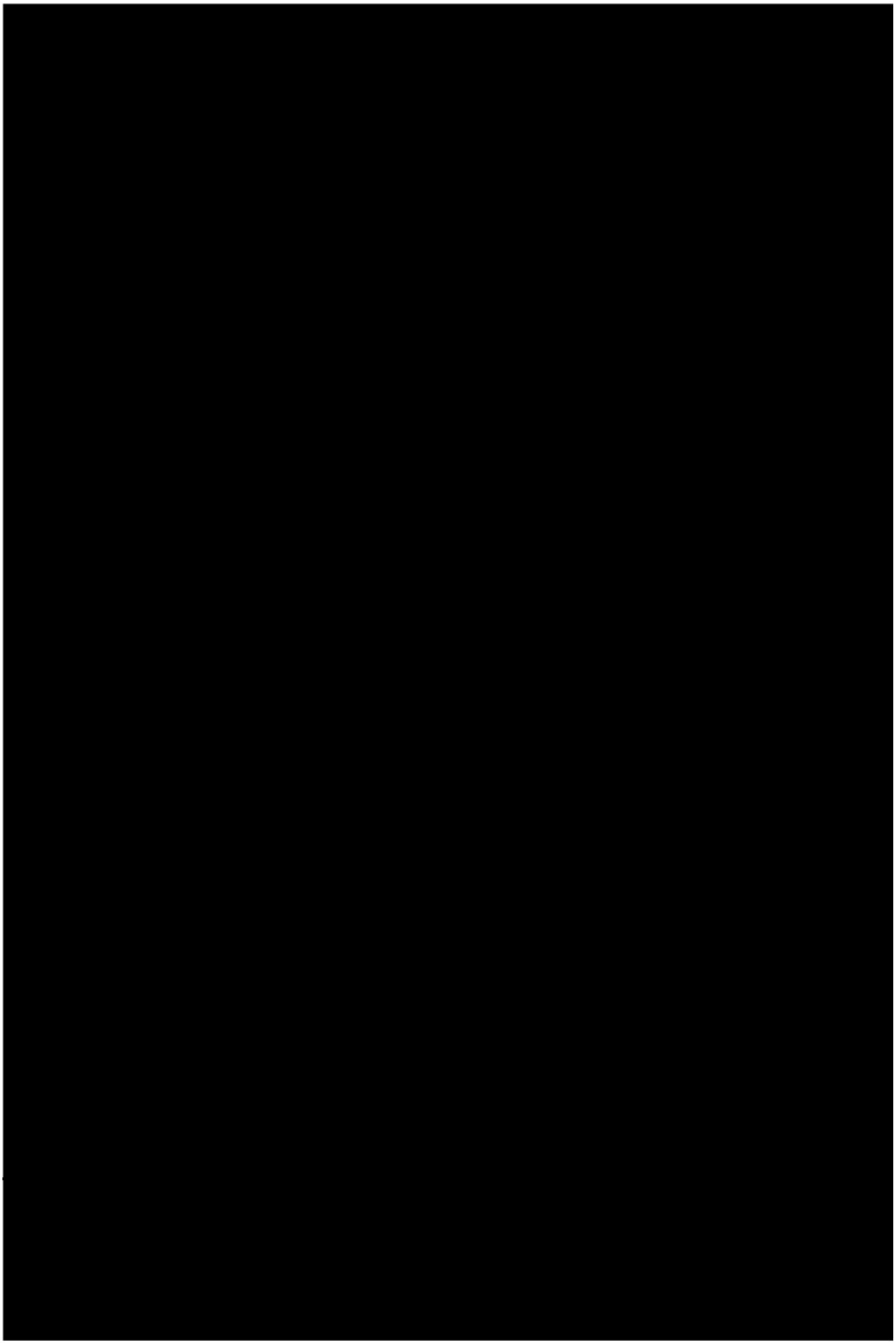

4.2.4 Conclusions of small-scale UHTCMC tests

The arc-jet tests described in this section allowed comparing the behaviour of different UHTCMC formulations. Fig. 4.30 shows a comparison among the ablation rates (based on mass loss) of the samples. Four tests on graphite (not reported in detail) are shown as a reference. Samples Graphite_1 and Graphite_3 were tested at conditions corresponding to step #0 (H_0 = 5.5 MJ/kg). Samples Graphite_2 and Graphite_4 were tested at conditions corresponding to steps #1-3 (at H_0 up to 10 MJ/kg).

ZrB_2-based samples showed an outstanding ablation resistance, although experiencing a sudden rise in temperature (*temperature jump*) of several hundred degrees, reaching temperatures up to 2700-2800 K. These samples develop a ZrO_2 solid coating preventing consistent sample erosion, especially at ultra-high temperature, when the oxide melts and form a dense scale; however, after exposure to plasma flow and *temperature jump*, the thin oxide layer is characterized by poor mechanical properties, rather compact but in some cases partially detached from the underneath boride matrix. Moreover, even in presence of a *temperature jump*, the low thermal conductivity of oxide phases appears to shelter the rear bulk material, which is kept at much lower temperatures, about 4-500 K lower. It is interesting to notice that ZrB_2-based samples not containing SiC (such as ZS0-LF and the two ZC-LF samples) did not show a sudden *temperature jump*, but rather a rapid increase in temperature already in the earliest stages of the test. These features, including the poorer mechanical performance of ZS0-LF and ZC-LF samples, will be addressed in detail in section 4.6, dedicated to the discussion of the possible mechanisms triggering the *TJ*.

On the other hand, materials used as reference, i.e. graphite and C/SiC composites, together with Ti_3SiC_2-based samples demonstrated a considerable ablation rate, which made not possible reaching the most demanding conditions achievable with the UHTCMCs.

Due to promising performance of the sintered ZrB_2-SiC based samples, and to further investigate their ultra-high-temperature response, including the occurrence of *temperature jump*, further activities were carried out on bulk materials with the same constituents, that will be presented in the next two sections.

4.3 Effect of SiC content

In order to further investigate the effect of SiC content in ZrB_2-based UHTCs, dedicated test campaigns were carried out, in collaboration with CNR-ISTEC. Four ultra-high temperature ceramics, all based on a ZrB_2 matrix and densified by Hot Pressing, were manufactured varying the ZrB_2 to SiC volume ratio. The compositions (amount in vol. %) are labelled as

- ZSY-05: ZrB_2 + 5 SiC + 5 Y_2O_3
- ZSY-10: ZrB_2 + 10 SiC + 5 Y_2O_3
- ZSY-15: ZrB_2 + 15 SiC + 5 Y_2O_3
- ZSY-18: ZrB_2 + 18.5 SiC + 5 Y_2O_3.

Three test sequences were performed. During the first test sequence (test sequence 1), all the samples were exposed to the supersonic plasma flow at stepwise increasing

enthalpy steps (from #1 to #8 of Table 2.1): the same test sequence was executed on the four different buttons. After the test, 1.5mm of oxidized material was removed from the top surface and the test repeated, up to step #6 (test sequence 2a). Finally, some samples were subjected to a third sequence, up to the most stressful step, #8, (test sequence 2b), without any further surface "refreshing". Further details and the rationale behind the test conditions selection will be given in next sections.

Upon cooling, an analytical balance (±0.1 mg instrumental accuracy) and a micrometric calliper (± 1 μm) were used to determine, respectively, mass and size variation of the button after testing. Prior to sectioning, the as-exposed front surface of the samples was analysed by X-ray Diffraction (XRD) and SEM-EDS at CNR-ISTEC.

4.3.1 Test sequence 1

During the first test sequence, the four buttons were subjected to all of the eight enthalpy steps of Table 2.1. Steps from #1 to #7 had a duration of 30 s, while the number #8 lasted 120 s. The surface temperature vs time (thermal) histories, measured by ISQ5 pyrometer, are plotted in Fig. 4.31. The visual appearance of the four samples after test is presented in Fig. 4.32. All the specimens gained a net mass, and increased the initial dimensions (see Table 4.11).

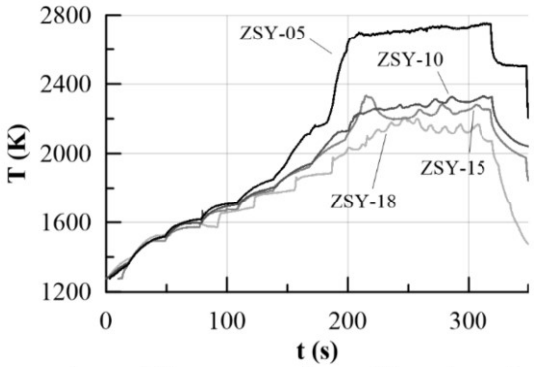

Fig. 4.31. Surface temperature (T) versus time (t) using the ISQ5 pyrometer during test sequence 1.

Some interesting preliminary deductions can be argued. First, it is clear that, whereas in the earliest segments of the power sequence the surface temperatures do not vary appreciably, they tend to differ for increasing enthalpy steps, until the maximum radiative equilibrium temperatures, which appear be higher for decreasing

SiC content, are reached. Worth of mention is the behaviour of specimen ZSY-05, which experienced an extremely rapid temperature rise (a *temperature jump*, recorded by ISQ5 pyrometer and IR-TC) when the surface temperature was approaching 2150 K, during step #7 (H_0 = 18 MJ/kg). After reaching an almost steady state, the temperature suddenly increased by more than 400 K. The steady state equilibrium temperature would have probably exceeded 2600 K, but the power was increased to the last step before the equilibrium was reached. The final peak temperature of the front surface was around 2750 K. Another interesting feature was that, at the maximum applied enthalpy H_0, the surface temperature oscillates, with more pronounced amplitude variations for larger SiC contents in the starting specimen. The observed correlation of SiC concentration vs the steady-state temperature is in agreement with what found by Hu et al. [110], who tested ZrB_2-based specimens with a SiC amount ranging from 10 to 30 vol. % in a high-enthalpy subsonic wind tunnel. They also found a reduction in the equilibrium temperature for increasing SiC content, associated with an increasing amount of glass retained in the sample after testing.

The post-test visual inspection of the buttons assessed they have a different appearance (Fig. 4.32). In particular, more SiC in the as-sintered material led to get smoother front surfaces. In addition, a loss of homogeneity is apparent in the ZSY-05 button, just that affected by the steep temperature rise (see Fig. 4.31 and 4.32).

In Fig. 4.33, the overall cross-sections of the exposed specimens are presented. It is apparent that the ZSY-05 button generated *in-situ* an external oxide scale whose partial compactness (left half in Fig. 4.33a) was severely altered (right half in Fig. 4.33a). The *TJ* is a direct manifestation, not the trigger, that a substantial change in the former thermal status took place and a new one was equilibrated. More in specific, the ZSY-05 button presents irregular macro-granules which protrude for 50 up to 100 μm and, very likely, an oxide scale/un-oxidized bulk detachment (right end in Fig. 4.33a). Some macro-granular structures on the front surface of the ZSY-05 button are discernible also in Fig. 4.32. Another important feature is the virtual absence of residual glass just on the outermost front surface which directly faced the dissociated hot plasma.

Table 4.11. Absolute and relative mass gain (Δm) and thickness increase (Δτ) of the button after test, and thickness of the oxide scale after test sequence 1 (Δs).

Sample ID	Δm, mg	$\Delta m/m_0$, %	Δτ, μm	$\Delta\tau/\tau_0$, %	Δs, μm
ZSY-05	43.6	0.51	250	5.0	305
ZSY-10	34.9	0.41	85	1.7	250
ZSY-15	20.7	0.25	70	1.4	215
ZSY-18	24.5	0.32	105	2.1	150

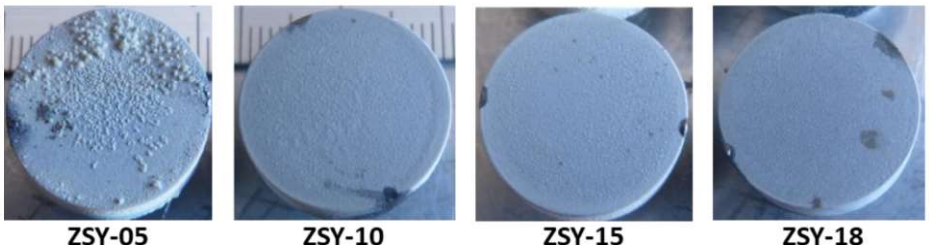

Fig. 4.32. Final post-test appearance of the four buttons.

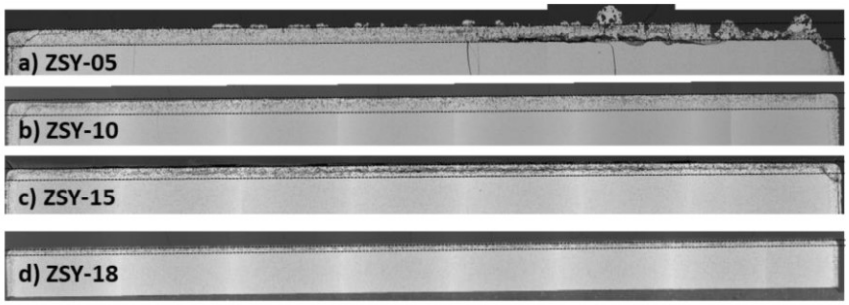

Fig. 4.33. Polished cross-sections, about 17 mm wide, by SEM of the tested buttons: upper and lower margins of the oxide scale (whose thickness is reported in Table 4.11) are plotted.

Fig. 4.34 shows some thermographic frames taken during step #7 and #8 of the test on sample ZSY-05, from the instant in which the *TJ* took place until the end of the step #8. The frames are identified by numbers 1-8 and the corresponding instants are indicated on the diagram presented on the right of Fig. 4.34. This shows again the temperature history of the sample as measured by pyrometer ISQ5, compared with two measurements made by the IR-TC, setting a directional spectral emissivity equal to 0.75. The first, labelled as “centre”, is the maximum temperature detected on a round

area in the central part of the sample front surface, matching as close as possible the measurement spot of the ISQ5 pyrometer; the second, labelled as "max", is the maximum temperature detected on the entire front surface. Several observations can be made. First, before the onset of the *TJ* (frame 1 of Fig. 4.34), the surface temperature was rather uniform, then a localized temperature increase occurred on the front surface, spreading to the whole surface (but not to the rear part of the material, as already observed for samples with fibres in section 4.2 – this behaviour will be attributed to a dramatic reduction of thermal conductivity throughout the oxide layer, in the discussion of section 4.6) when the new equilibrium temperature was reached, at the beginning of the harshest step (frame 4). During the first half of step #8 the three curves almost overlap, then for the remaining time ranges (frames 6-8), the only "max" curve started deviating and tended to reach values up to 3000 K. Such a temperature drift was linked to the appearance of the protrusions on the top part of the surface, with localized ultra-high-temperature spots.

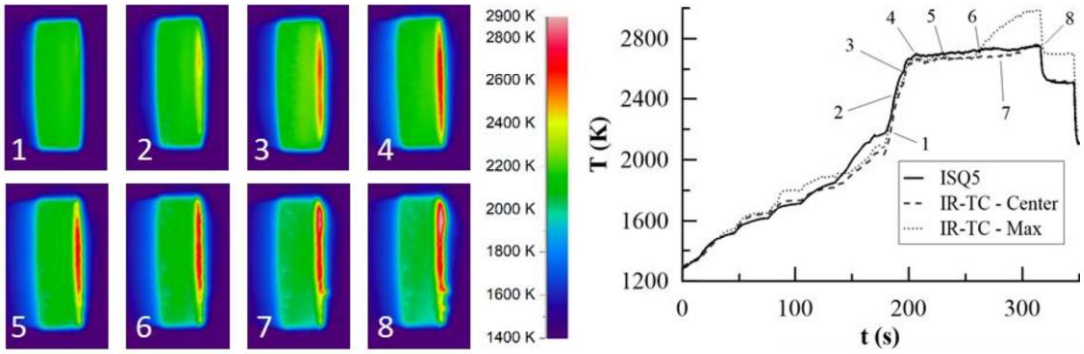

Fig. 4.34. Left: thermographic frames of button ZSY-05 during the most stressful enthalpy steps. Right: temperature history measured by ISQ5 pyrometer and IR-TC (ε_λ = 0.75). For IR-TC two curves are shown: the maximum temperature on the centre of the front surface (Centre), in an area corresponding to the measurement spot of the ISQ5 pyrometer; and the maximum temperature on the whole front surface (Max). The time instants corresponding to the TC frames are identified by numbers 1-8 on the temperature history diagram.

Fig. 4.35 shows a sequence of IR-TC frames taken during step #8 of test on the ZSY-15 button, in a time range characterized by oscillations in the temperature history.

It is possible to notice, on the lateral wall, an unsteady evolution of the irradiated power, resulting in a change of the surface colour. This is particularly evident in the bottom area, where an orange spot, highlighted by an arrow in each frame, appears to move downstream (from right to left, in the pictures). An analogous behaviour was observed also for the remaining buttons. This phenomenon is similar to the *waves of radiance* observed on fibre-reinforced UHTCs (see section 4.2.2), already reported by Monteverde et al. [50].

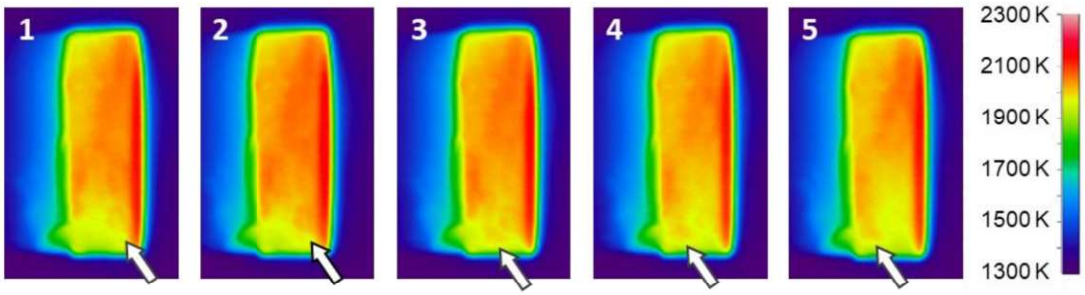

Fig. 4.35. IR-TC frames grabbed during step #8 showing *waves of radiance* along the lateral wall of ZSY-15 button. The arrow in each frame shows the position of a darker spot moving downstream (from right to left in the pictures), presumably attributed to the transport of a liquid phase along the surface.

Fig. 4.36a shows the (directional) spectral emissivity (ε_λ) of the four specimens versus surface temperature, obtained by matching the measurement of the ISQ5 pyrometer and IR thermo-camera, in the near infrared (NIR) wavelength band. For all samples, the ε_λ values tend to increase at the beginning of the test, reach a maximum that ranges between 0.8 and 0.9, at temperatures between 1600 and 1700 K, then they begin to decrease converging to higher values for the compositions richer in SiC. After *TJ*, ε_λ of the ZSY-05 button (the only that exceeded 2400 K) increases again up to 0.75 at the maximum temperature of 2750 K. One could argue that the temperature and emissivity measurements after *TJ* are less reliable due to the presence of protrusions, leading to inhomogeneity in temperature distribution on the sample front surface. However, a spectral emissivity trend comparable with that of the ZSY-05 button has already been observed during test in similar conditions on the fibre-reinforced UHTCs

based on ZrB_2-SiC-Y_2O_3, also experiencing a *TJ*, whose details are reported in section 4.2.2. In that case, no significant protrusions were observed on the samples front surface, which appeared homogeneous and compact. This is a first reason to infer that also the present temperature and emissivity measurements may not be affected by the specific presence of large protrusions. Moreover, looking at Fig. 4.34, it can be seen that in the first half of step #8, when the final equilibrium temperature of 2750 K had already been reached, the front surface temperature was uniform and the measurements of pyrometer and thermo-camera almost perfectly overlapped. This suggests that the set value of $\varepsilon_\lambda = 0.75$ was already representative of the actual (spectral) emissivity of the surface even before the catastrophic bursting of large protrusions and defects in the second half of the step (frames 6-8).

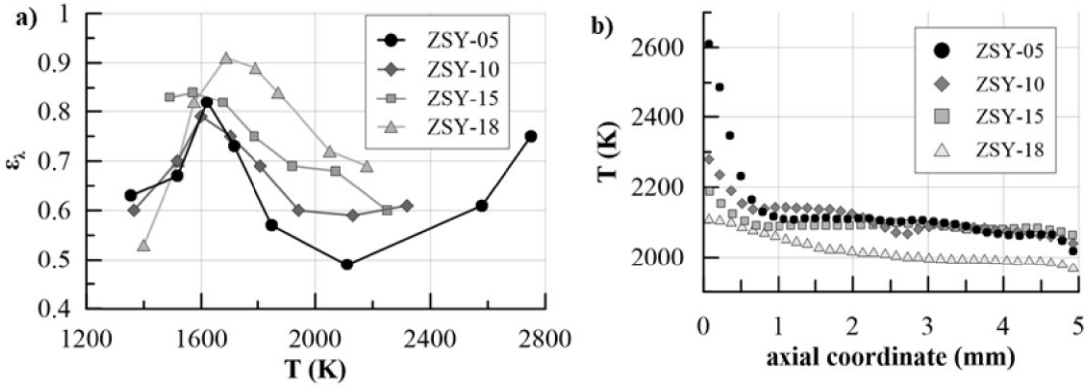

Fig. 4.36. (a) Directional spectral emissivity (ε_λ) versus maximum surface temperature (T), (b) Temperature axial profiles of the four buttons at the same instant (t = 300 s) during step #8, measured by the IR-TC (the correct value of ε_λ was set according to the diagram of Fig. a)

Fig. 4.36b shows the surface temperature profiles along the axis of the button, measured at the same time instant by the IR-TC during step #8. As already highlighted above, the substantial temperature rise related to the *TJ* appears to be confined on the front surface of specimen ZSY-05, with a steep temperature drop alongside the axial coordinate of the button. A similar, but less obvious trend, can be observed for the remaining buttons and the magnitude of the temperature drop decreases for increasing SiC content, suggesting a progressive increase in the ability of the oxide scale to conduct heat to the bulk material. The formation of oxidized areas on the side surfaces,

which is actually confirmed also by SEM analyses (see Fig. 4.33-4.34), can of course have some impact on the thermal conductivity-driven heat transfer to the rear part of the samples. However, the temperature profiles reported in Fig. 4.36b are the only directly available data to study the thermal axial distribution. Regardless of the accuracy of those profiles for a precise reconstruction of the heat transfer to the material, the variation, with SiC content, in their slope in the front area provides a clear, although only semi-quantitative, insight on the reduction of the thermal conductivity in that region of the sample, supporting the discussion that will be presented in section 4.6.

The resulting thickness of the oxide scale (see Fig. 4.33) is visibly affected by the starting SiC content. Larger SiC amounts favoured the creation of thinner and more compact oxide scale: if the oxide scale of the ZSY-05 button is thicker (i.e. about 300 μm) and partially detached, in the ZSY-18 button it remained much more compact and thinner (i.e. about 150 μm), and adherent to the un-oxidized substrate.

The FESEM-EDS analyses of the *in-situ* generated external oxide scale provided an additional insight into the internal zones affected by a severe oxidation attack. Two important shared features, often observed by other authors, were the lack of a SiC-depleted region underlying the oxide scale and the prevailing columnar shape of the zirconia grains grown during exposure [111]. If the columnar shape of the zirconia grains is apparent along the lateral walls of the exposed button, the elongated shape (of the zirconia grains) turns into a more regular one especially close to the outermost part of the oxide layer where temperature reached the hottest values. The other gaseous oxidation by-products originated at the oxide/inner bulk interface such as SiO(g), CO(g) and volatile boron oxides counter-diffuse due to concentration gradient exploiting the cited channels to reach the exterior.

Such a fluid glassy oxide finds origin from the oxidation products of the passively oxidized ZrB_2 and SiC, according to the well-known exothermic reactions

$$ZrB_2(s) + 5/2\ O_2(g) = ZrO_2(s) + B_2O_3(l,g) \quad (1)$$

$$SiC(s) + 3/2\ O_2(g) = SiO_2(s,l) + CO(g) \quad (2)$$

Fed also by the residual Y borate glassy pockets, an only oxidation product tends to form, up-taking Si, Zr, B and Y in only one oxide matrix: such an oxide matrix is

generally defined borosilicate glass (BSG). The BSG, depending on the pressure and temperature it actually encounters during the exposure, can vary its own composition substantially. To mention the most evident change, it begins losing the boron oxide component when the massive volatilization of the silica component has not started yet. The channels grown inside the oxide scale acted as getaway for the outflowing glass and other gaseous species and as an access gate for the incoming oxygen.

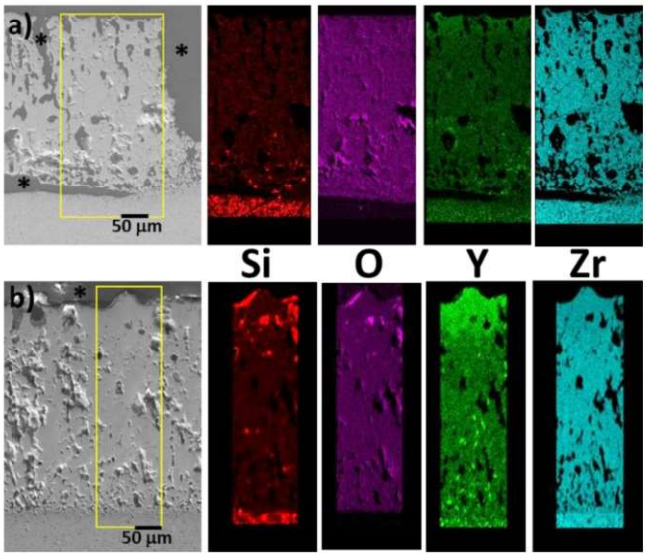

Fig. 4.37. SEM micrographs from front areas detached (a), or not (b) by the un-oxidized substrate of the ZSY-05 button: residual resin (*) is indicated. Elemental maps of Si, O, Y and Zr derive from the selected boxes.

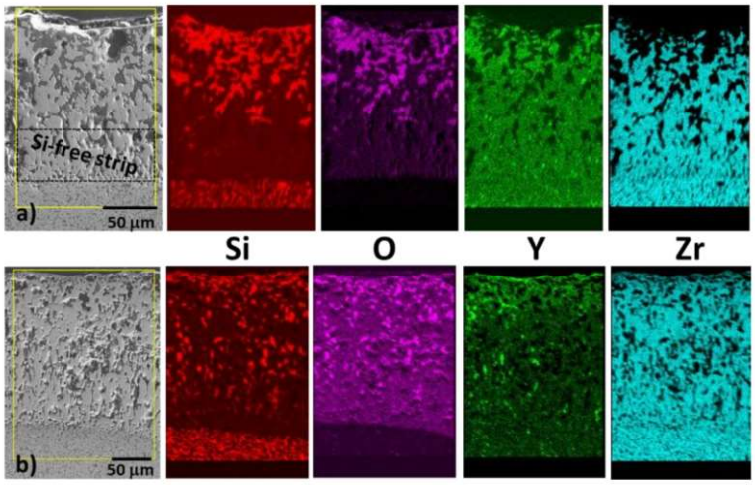

Fig. 4.38. SEM micrographs from the front surface (a) or the lateral wall (b) of the ZSY-18 button: elemental maps of Si, O, Y and Zr derive from selected boxes.

The elemental mapping of Si as well as other key species such as Y, Zr and O throughout the oxide scale is very important (Fig. 4.37-4.38) because it discloses how the BSG glass was transported outward, providing or not protection to the specimen. The response to aero-thermal heating was different. During the exposure of the ZSY-05 button, the entire oxide scale was virtually depleted of Si (Fig. 4.37). However, in the case of the ZSY-18 button, residual Si remained inside the oxide scale localized in small glassy pools, whose presence and distribution are discernible in Fig. 4.38. The maps of Fig. 4.37-4.38 depict the elemental distribution of the button poorest (Fig. 4.37) or richest in SiC (Fig. 4.38). Analogous elemental analyses were carried out in the button ZSY-10 and ZSY-15, and intermediate distributions (not shown) were similarly found.

In the ZSY-05 button, a Si-free strip of several tenths of micron survived, sandwiched between the oxide/substrate interface and the zone rich of residual glassy pools. Such an inner strip was interested by the diffusion of Si transported via SiO(g). As for the lack of SiC-depleted region underlying the bottom of the oxide scale, this can be explained in terms of the oxygen partial pressure vs temperature at the oxide/bulk interface which did not reach the threshold to switch into the active oxidation domain. The reasoning over the SiO(g) outward diffusion and its re-condensation will be reclaimed in section 4.6.

4.3.2 Test sequence 2a

To better investigate the physics behind the phenomenon of the *spontaneous temperature jump*, additional test sequences were performed. The same buttons were refreshed, by removal of a 1.5 mm thick surface layer, and then exposed to the plasma wind tunnel flow. Fig. 4.39 shows the appearance of the refreshed ZSY-05 before the test. The front surface is polished and resembles that of the as-sintered materials, whereas the lateral surface is whitened due to the residues of test sequence 1.

Fig. 4.39. Appearance of refreshed ZSY-05 before test sequence 2a.

In the test sequence 1, ZSY-05 experienced the *temperature jump*, when the specific total enthalpy was about 18 MJ/kg. The test sequence 2a was intended to assess whether the *jump* could occur also for samples with a higher SiC content, even at lower enthalpy conditions, if the exposure time was sufficiently long. Therefore, in the three tests, the specific total enthalpy corresponding to step #6 (H_0 = 16 MJ/kg) was reached stepwise, so that the sample temperature could exceed, at steady state, at least 2000 K. The duration of the last step was 300 s. For sample ZSY-15, the power was slightly increased during this step (by 2 kW), to achieve a higher temperature. The corresponding thermal histories, detected by pyrometer ISQ5, are shown in Fig. 4.40, whereas Fig. 4.41 shows IR-thermographic and CCD images taken during the tests, together with the visual appearance of the three samples after test.

As can be seen from Fig. 4.40, no measurable *temperature jump* was observed in this test sequence 2a. Once again, the steady-state temperature increased for decreasing SiC content, with sample ZSY-05 reaching the highest equilibrium temperature. In this case, the temperature profile of sample ZSY-15 did not exhibit any oscillations, whereas they became more evident for decreasing SiC content. The temperature oscillations find correlations with the oscillation of the surface brightness, as observable in the CCD pictures of Fig. 4.42. Fig. 4.42 also highlights the formation of an unstable phase on the front surface, which appears brighter than the side surface and unsteadily changes its shape, with nucleation and bursting of small bubbles.

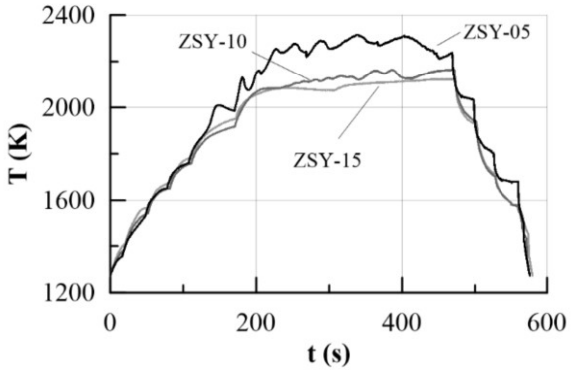

Fig. 4.40. Temperature histories of the samples during Test sequence 2a, measured by ISQ5 pyrometer.

Looking at the photographs of Fig. 4.41, none of the samples shows protruding zirconia grains, with only some irregular structures on the outer edge of sample ZSY-05. Relative mass changes were measured in the order of 0.4%. *Waves of radiance* were observed also during this test sequence. Fig. 4.43 shows the NIR spectral emissivity for the three samples versus surface temperature. The qualitative trend is the same as in test sequence 1, confirming that the amount of SiC influences ε_λ.

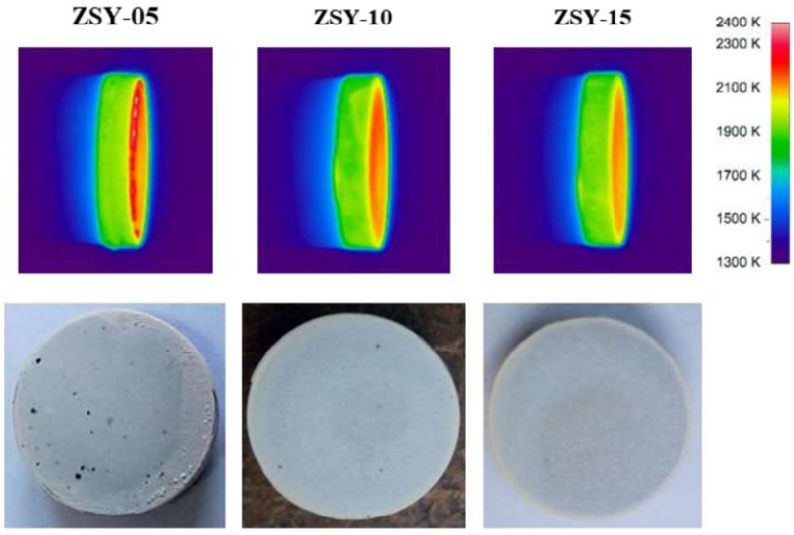

Fig. 4.41. For the three samples subjected to Test sequence 2a: top) IR thermographic image during last enthalpy step (H_0 = 16 MJ/kg), bottom) appearance of the sample after test.

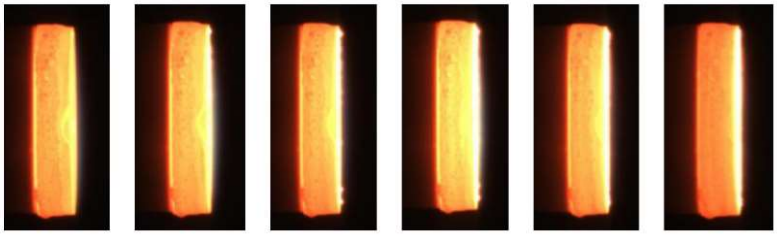

Fig. 4.42. Video frames of the last enthalpy step of Test 2a for sample ZSY-05.

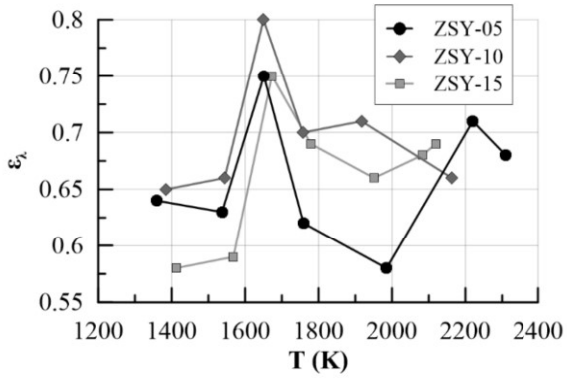

Fig. 4.43. Samples spectral emissivity ε_λ.versus surface temperature (T), for test sequence 2a.

4.3.3 Test sequence 2b

Because of the absence of *temperature jumps* during test sequence 2a, the two samples ZSY-10 and ZSY-15 were subjected to another arc-jet cycle as they came up the test sequence 2a. In this case, the maximum enthalpy (20 MJ/kg) was reached, but with different steps duration. The temperature histories detected by pyrometer ISQ5 are presented in Fig. 4.44, whereas Fig. 4.45 shows IR-thermographic images taken during the tests, together with the visual appearance of the two samples after test.

The thermal histories are different with respect to the previous test sequences. When the temperature of sample ZSY-10 reached 2200 K (step #6, H_0 = 16 MJ/kg), it started to rapidly increase, reached a maximum around 2300 K and then started decreasing. After a further enthalpy increase (H_0 = 18 MJ/kg), a similar temperature trend is observable, but still no *jump* was detected. A final increase to the maximum enthalpy level caused the surface temperature to progressively increase until exceeding 2800 K at the end of the step, without even reaching a steady state (after 120 s in those conditions).

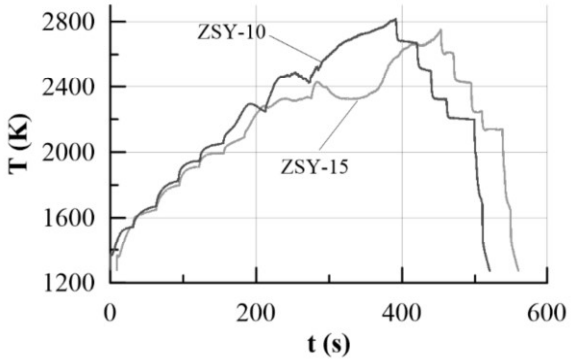

Fig. 4.44. Temperature histories of the samples during test sequence 2b, measured by ISQ5 pyrometer.

Sample ZSY-15 had a more stable surface temperature history until step #7 (H_0 = 18 MJ/kg), then, when the last enthalpy step was reached, the temperature had a slight increase, then it decreased, reached a plateau around 2320 K and finally started increasing up to 2750 K, with a monotonically increasing trend, without reaching a steady state. The whole duration of the last enthalpy step was 180 s.

After test, the appearance of both samples front surfaces changed, with the formation of a white irregular surface layer, which covered almost all of the surface of sample ZSY-10, whereas had a C-shape for sample ZSY-15. The C-shape can be compared to the shape of the hot region observable in the corresponding IR-TC image (Fig. 4.45). Relative mass changes were measured in the order of 0.2%.

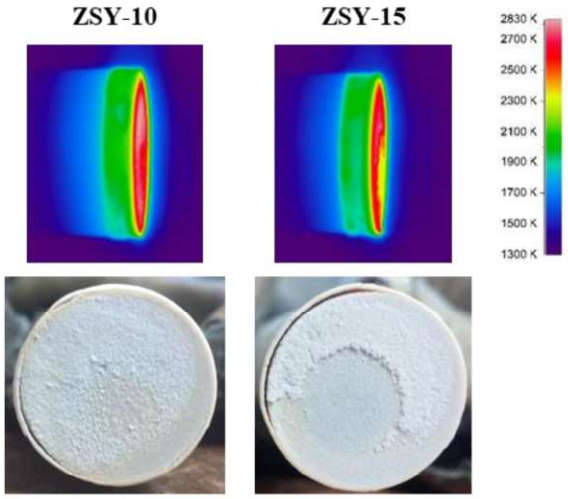

Fig. 4.45. For the two samples subjected to test sequence 2b: top) IR thermographic image during last enthalpy step (H_0 = 20 MJ/kg), bottom) appearance of the sample after test.

Fig. 4.46 shows some CCD pictures taken during the heating stage of sample ZSY-10. Also in this case, an unstable brighter zone was observed on the front surface. Liquid droplets were wiped off by the surface (second picture), while small bubbles appear and disappear during the test. It is also interesting to notice that the brightness of the side surface unsteadily changes while the surface temperature increases. IR thermography confirmed also in this test sequence the presence of the *waves of radiance* phenomenon.

Fig. 4.47 shows the NIR spectral emissivity ε_λ of the samples during the test sequence 2b, versus their surface temperature. Differently from the first two test campaigns, in this case the ε_λ has an almost monotonic increasing trend, starting for both samples from values above 0.3, reaching a plateau between 2000 and 2350 K, and then increasing to maximum values even over 0.9 when the temperature starts increasing at the end of the test.

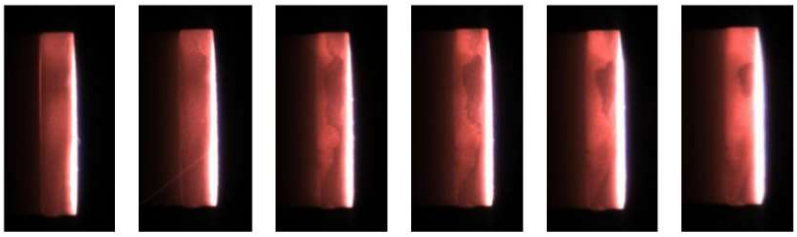

Fig. 4.46. CCD pictures taken during Test 2b on sample ZSY-10.

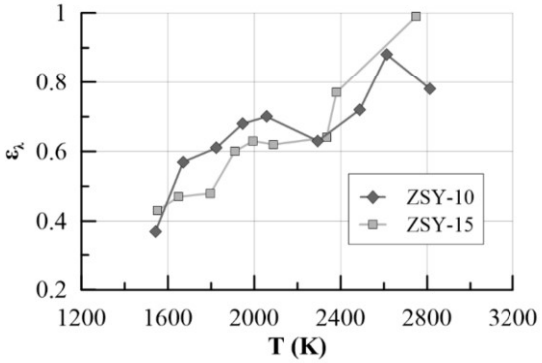

Fig. 4.47. Spectral emissivity versus surface temperature, for test sequence 2b.

4.3.4 Conclusions of tests for varying SiC content

Several experiments were carried out to study the effect of SiC concentration on the aero-thermal behaviour of ZrB_2-based Ultra-High-Temperature Ceramic materials in an arc-jet supersonic wind tunnel environment. It was found that, as SiC content increases (from 5 to 18 vol% in the present study), the maximum steady-state temperature reached on sample surface decreases, whereas the NIR spectral emissivity value is higher. Also, samples with lower SiC content had an almost null residual BSG in the oxide. Moreover, the experiments were focused on the observation of the *temperature jump*, a sudden and spontaneous increase in temperature in the order of 400-500 K characteristic of UHTCs, which is related to the appearance of a zirconia layer on the front surface of the sample after complete liquid silica oxide removal. The occurrence of the *jump* (which appears only on the front surface of the samples, while the rear part reaches much lower temperatures), is favoured by a low SiC amount, but can happen also for SiC concentrations up to at least 15%. However, it was observed that the flow total enthalpy should be on the order of at least 18 MJ/kg and the exposure time needs to be higher when the SiC amount is higher. For further discussion on this point, the reader is referred to section 4.6.

4.4 Effect of atmospheric composition

A further effort was dedicated to investigating the aero-thermo-dynamic and oxidative behaviour of ZrB_2-SiC-based materials in different flow atmospheres. Specifically, the investigated composition was ZrB_2 - 5 vol% SiC - 5 vol% WC.

Although it is well known that the oxidation behaviour of ultra-high-temperature ceramic material is crucial for their application in high-temperature harsh environments, only limited data are available in reduced oxygen partial pressure environments and supersonic flows, which are the most relevant conditions for the application of these materials as leading edges for hypersonic vehicles, subject to extreme heating in the upper atmosphere during re-entry. When the oxygen partial pressure is high enough and a considerable surface layer of protective borosilicate

glass is formed, this can provide a reduction of the oxidation rate, preventing, as a barrier, oxygen diffusion towards the bulk material. On the other hand, when oxygen partial pressure is ultra-low, different mechanisms may occur.

The objective of this study was thus to investigate the oxidation behaviour of the very high strength ZrB_2-based ceramic under high-enthalpy hypersonic flow with two different chemical compositions. Therefore, two ZrB_2-SiC-WC coupons were exposed to an arc-jet flow composed of simulated air (with oxygen partial pressure in the order of thousands of Pa) or pure nitrogen (with oxygen residual partial pressure two orders of magnitude lower.

A ceramic pellet was sintered to full density according to the methodology described in [112]. From the sintered disc, two flat button-shaped coupons (ZSW-A is the sample tested in air and ZSW-N is the sample tested in nitrogen atmosphere) were machined according to the nominal design shown in Fig. 2.3 (with a 5 mm-thick head, 17 mm diameter and an overall length of 10 mm including the cylindrical rear pin).

Tests were carried out considering two different atmospheric compositions: simulated air, composed by 80% nitrogen and 20% oxygen, and pure nitrogen. The estimated oxygen partial pressure for the first case is in the order of 1000-2000 Pa (about 20% of the total stagnation point pressure calculated by numerical simulations, see also Fig. 4.5), whereas, when the arc-jet flow is of pure nitrogen, considering the vacuum level in the test chamber, oxygen partial pressure is two orders of magnitude lower. In both cases, the total gas mass flow rate was 1 g/s. The torch arc power, and consequently the flow specific total enthalpy, were increased stepwise. The enthalpy level and the duration of each step for the two tests is reported in Table 4.12 and 4.13, respectively. After the maximum enthalpy step, the power was decreased gradually until facility shutdown.

Fig. 4.48 shows the temperature histories of the two samples, as detected by the ISQ5 pyrometer. It can be noticed that the thermal histories are comparable at relatively low enthalpies, then they tend to diverge. Both samples experienced a rapid rise in temperature at constant flow enthalpy (the *temperature jump* already discussed in the previous sections). The behaviour of the two samples is different though. In particular, the sample tested in nitrogen atmosphere experienced a sudden jump at

constant enthalpy (about 18 MJ/kg, step 5n) when the temperature approached 2000 K, and its final temperature exceeded 2800 K. The sample tested in air had instead a more gradual jump, during the last step (enthalpy of around 20 MJ/kg, step 7a), and reached temperatures over 2600 K only at the end of the test, which was stopped about 30 seconds after the occurrence of the jump. This *jump* is much more similar to what experienced by the ZrB_2-SiC-based samples whose tests are reported in sections 4.2.2 and 4.3.

Table 4.12. Test conditions in simulated air flow-

Step #	H_0 (MJ/kg)	Step Duration (s)
1a	8.5	30
2a	10.0	30
3a	12.0	30
4a	13.5	30
5a	15.5	30
6a	18.0	60
7a	20.0	105

Table 4.13. Test conditions in nitrogen flow.

Step #	H_0 (MJ/kg)	Step Duration (s)
1n	8.0	30
2n	10.5	30
3n	13.0	30
4n	15.5	30
5n	18.0	60
6n	21.0	120

The surface spectral emissivity at the wavelengths around 1 μm was estimated by comparison between pyrometer and thermo-camera measurements, and it was observed to be about 0.85 at all temperatures.

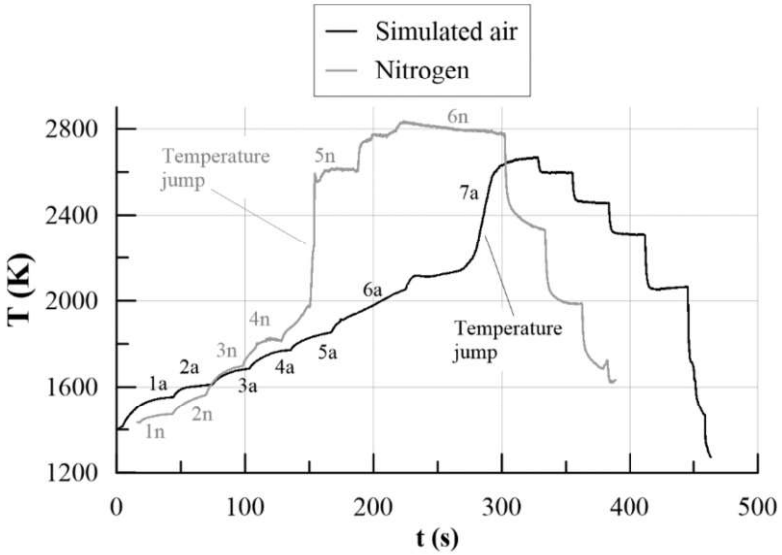

Fig. 4.48. Surface temperatures measured by pyrometer ISQ5 on the two samples ZSW-A (black line) and ZSW-N (grey line), tested in air and in nitrogen flows, respectively. Each enthalpy step is identified by labels on the plot, as well as the occurrence of a *TJ* for both samples.

Fig. 4.49 shows some thermal images of the two samples taken by the DIAS Pyroview 512N thermo-camera at different time instants, during test. Fig. 4.49a refers to sample ZSW-A. The picture on the left shows the sample during step 7a, before the occurrence of the temperature jump. In this phase, the temperature of the sample is rather uniform, around 2100-2200 K. The temperature jump appears then to be a dynamic process, leading to the formation of an ultra-hot region in the periphery of the exposed surface of the sample, which extends its size in time, as observable by comparison between the central and the right picture, while the rest of the sample keeps a much lower temperature. Fig. 4.49b shows instead the thermal evolution of the sample tested in pure nitrogen, ZSW-N. Just before the temperature jump (picture on the left), the temperature is uniform, around 2000 K, and bubbling is observable on the front surface of the sample. During and after the sudden jump, bursting of localized bubbles occurs, resulting in hot spots dispersed all over the surface (central picture). At the end of the heating phase, the surface reaches a uniform ultra-high temperature, whereas the rear region is kept at lower temperatures.

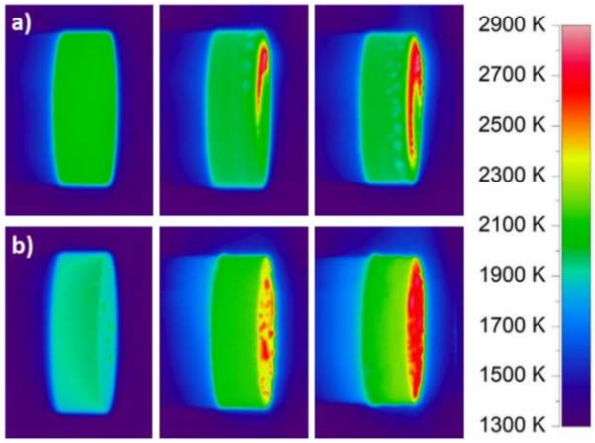

Fig. 4.49. Thermal images of a) sample ZSW-A and b) sample ZSW-N, just before temperature jump (left), just after temperature jump (centre) and at the end of heating phase (right). The temperature jump occurs at H_0 = 20 MJ/kg in air (a) and 18 MJ/kg in nitrogen (b).

The observed phenomena occurring during exposure to arc-jet supersonic flow are also highlighted by captions of the video recorded during test by the Flea3 optical camera, shown in Fig. 4.50. We can observe that when the impinging flux includes oxygen, Fig. 4.50a, initial outgassing of vapour fumes occurs. The blueish colour suggests it to be based mainly on W-O [113]. Then asymmetric heating on the button crown occurs and, as soon as the circle is completed, formation of borosilicate glassy-based drops/bubbles at the side edges is visible and remains with a dark contrast during cooling. As for the test in nitrogen, Fig. 4.50b, the formation of hot tiny bubbles is limited to isolated spots homogeneously spread on the surface, then they coalesce, the lateral sides are heated until the bottom starts to bubble as well. The last two pictures of Fig. 4.50b correspond to instants of advanced sample cooling, and therefore only very thin oxide scale is still visible because it is the only hot region. However, it can be appreciated that the largest bubble on the top surface breaks upon cooling, owing to tensile stresses rising in the oxide scale.

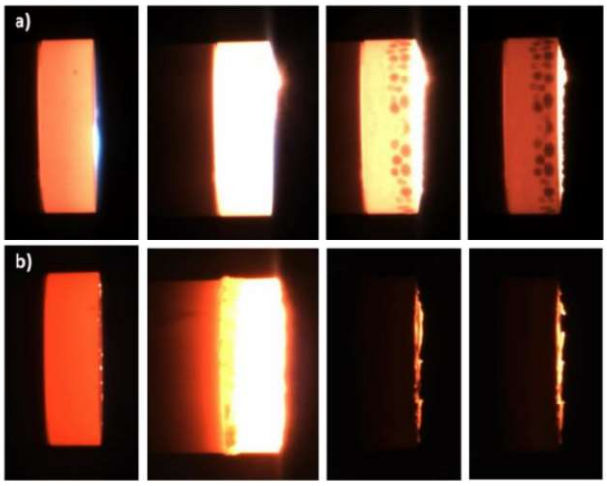

Fig. 4.50. Frame shots of the video recorded by the Flea3 Camera during a) test in simulated air and b) in nitrogen.

The microstructure modifications occurred after the tests are highlighted by the white colour assumed by the samples head, Fig. 4.51. It is visible that the oxide formed was not smooth and compact, but rather tended to spall off after both tests. Particularly, notable bubbles formation and oxide uplifting are visible in the periphery of sample ZSW-A, whilst evidence of bursting phenomena is visible on all the surface of sample ZSW-N.

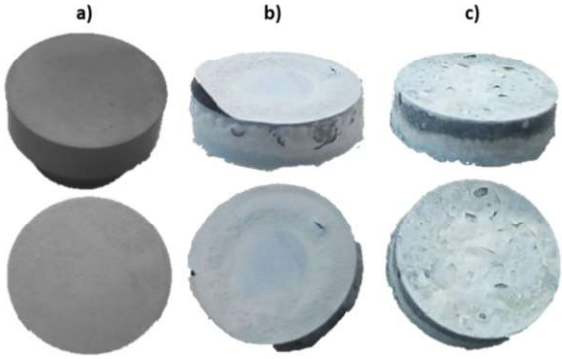

Fig. 4.51. Pictures of the samples (a) before the tests, (b) after test in simulated air, (c) after test in nitrogen.

Some more details are shown in the cross-sections of the two samples reported in Fig. 4.52 and 4.53, for ZSW-A and ZSW-N respectively. The oxide uplift occurred at the edges of samples ZSW-A was quantified in 330 μm. It could explain why the centre

of the button still displays a silica glass coverage on its surface, when normally this is compressed out towards the sample periphery by the gas impact at the stagnation point. The outermost scale, partially detached from the sample, is a dense ZrO_2 layer about 100 μm thick with few scattered WO_3 aggregates. The cross-section analysis of ZSW-N revealed also substantial oxide lifting with multiple delamination and formation of bubbles at various depth. The maximum height of the bubbles was in this case about 250 μm, whilst the modified scale in the least damaged zones was around 130 μm. The structure of the modified scale was analogous to that described for sample ZSW-A. Among the main differences with respect to the sample tested in simulated air, there is the composition of the outermost scale of the central area, which was mostly crystalline and based on ZrO_2/W, i.e. without silica-based glass.

The presence of the voids and oxide-bulk detachment, which resembles that experienced by sample ZSY-05 in the test campaign on the effect of SiC content (see section 4.3.1), which also underwent a *temperature jump*, can justify some localized dramatic decrease in thermal conductivity, with subsequent overheating of the exposed surfaces. This, together with the other microstructural features of the oxide phases, will also be taken into account in the discussion reported in section 4.6.

Despite the evident damages subsequent to the exposure to high-enthalpy flow, the mass is substantially unaltered after test, with a slight increase, possibly due to oxide formation (Table 4.14).

Table 4.14. Mass of samples tested in air and nitrogen before and after test.

Sample ID	Initial mass	Final mass
ZSW-A	10.592 g	10.616 g
ZSW-N	10.679 g	10.697 g

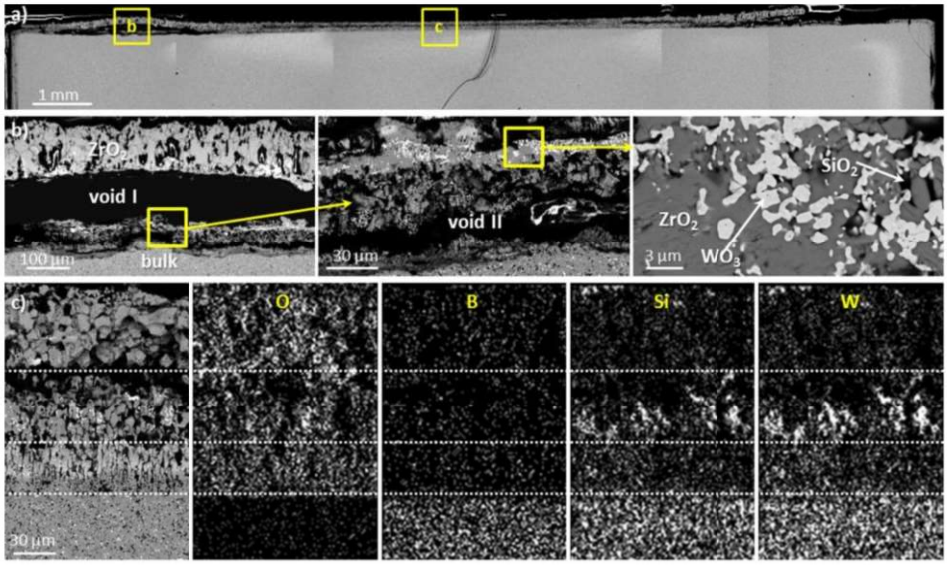

Fig. 4.52. SEM images of the cross section of sample ZSW-A. a) Whole button section showing oxide uplift at the edges, b)-c) magnifications of the microstructure as tagged, c) elemental mapping of the central zone.

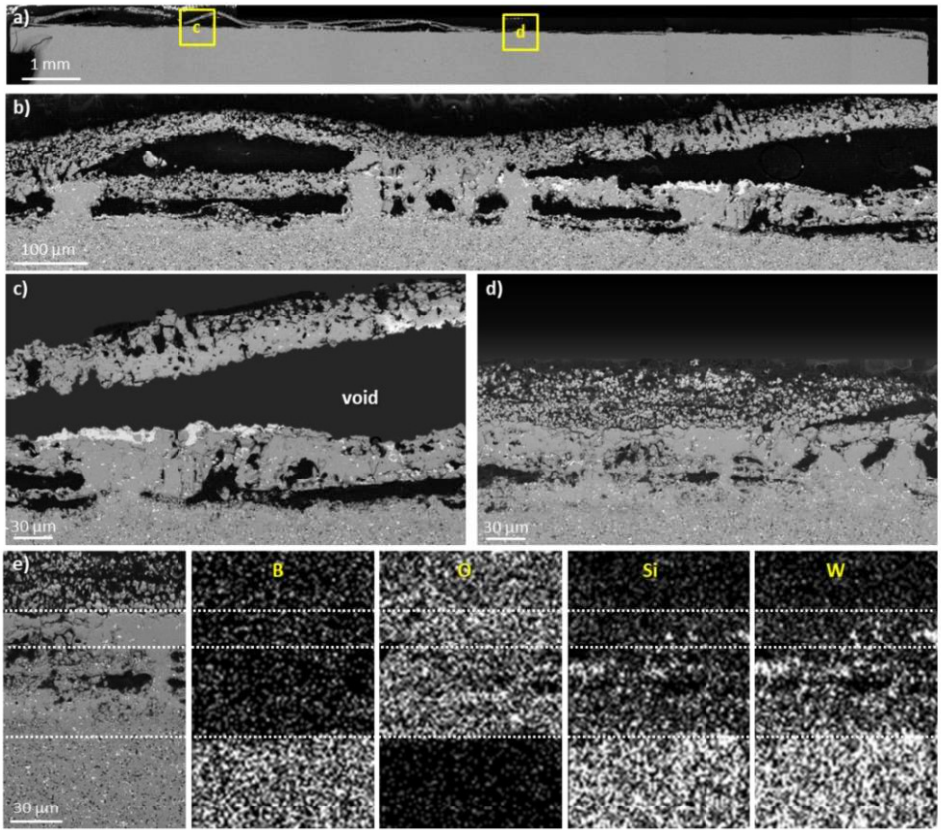

Fig. 4.53. SEM images of the cross section of sample ZSW-N. a) Whole button section showing oxide uplift and b) multiple delamination, c)-d) magnifications of the microstructure with and without bubbles, e) elemental mapping of zone d).

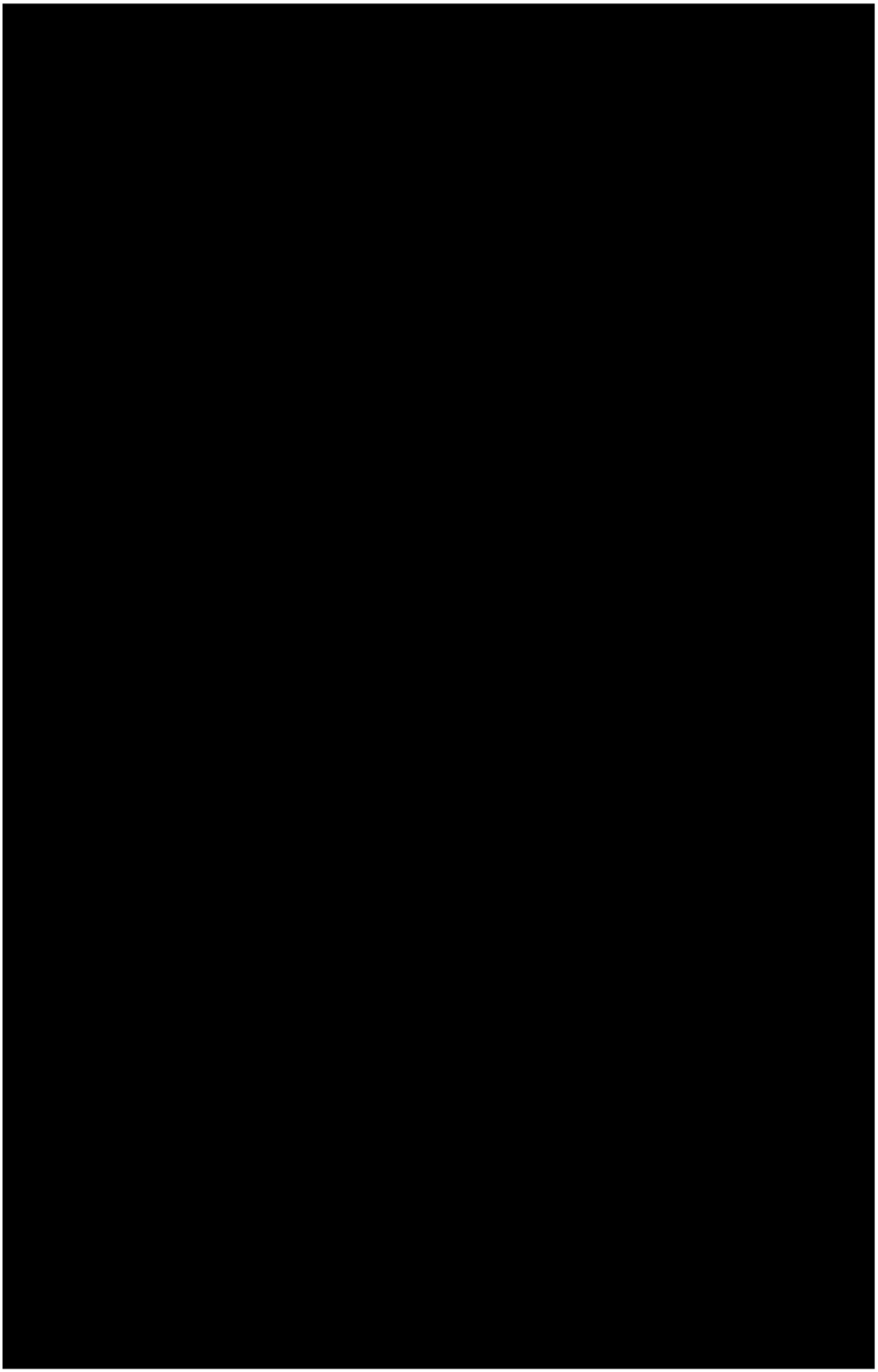

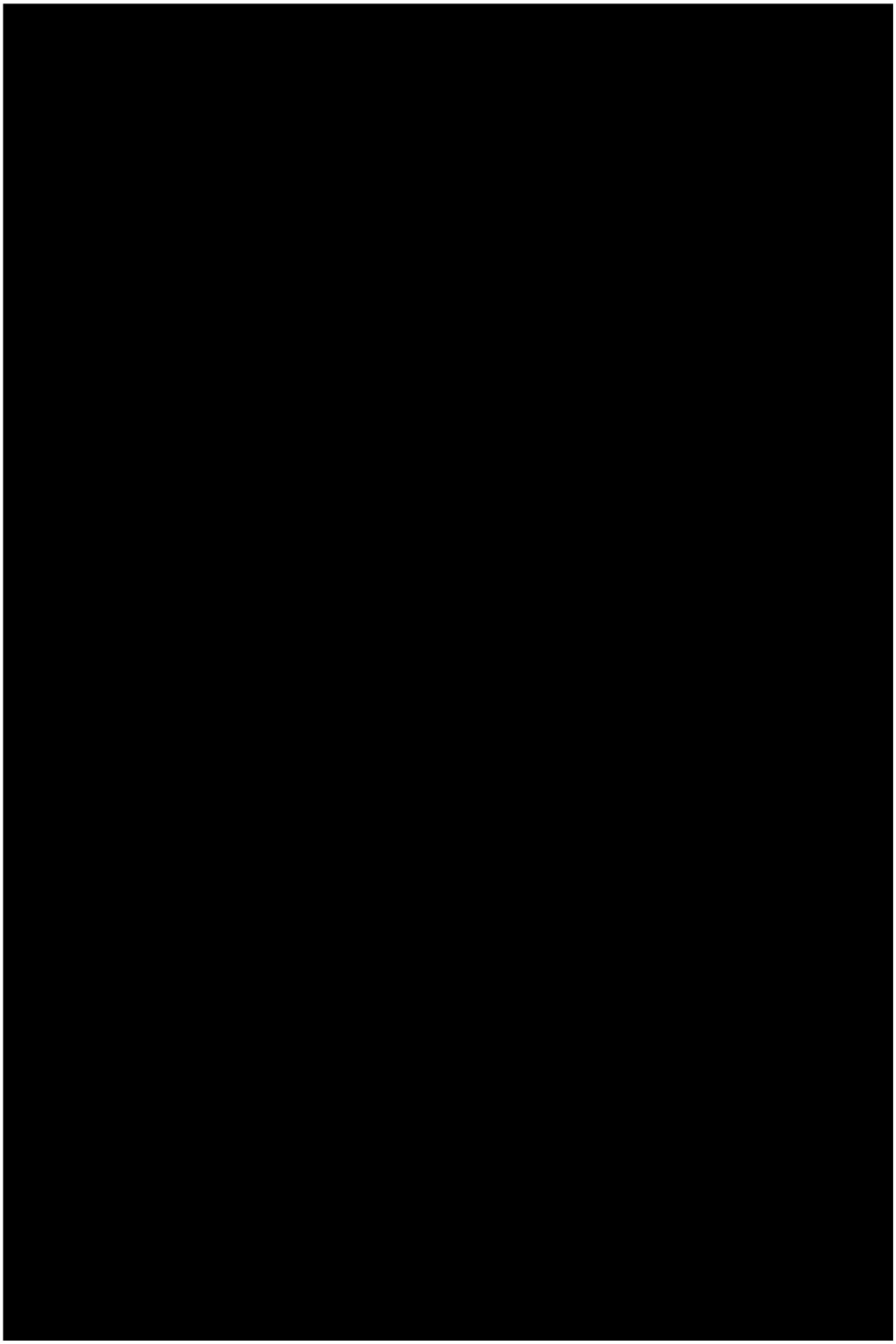

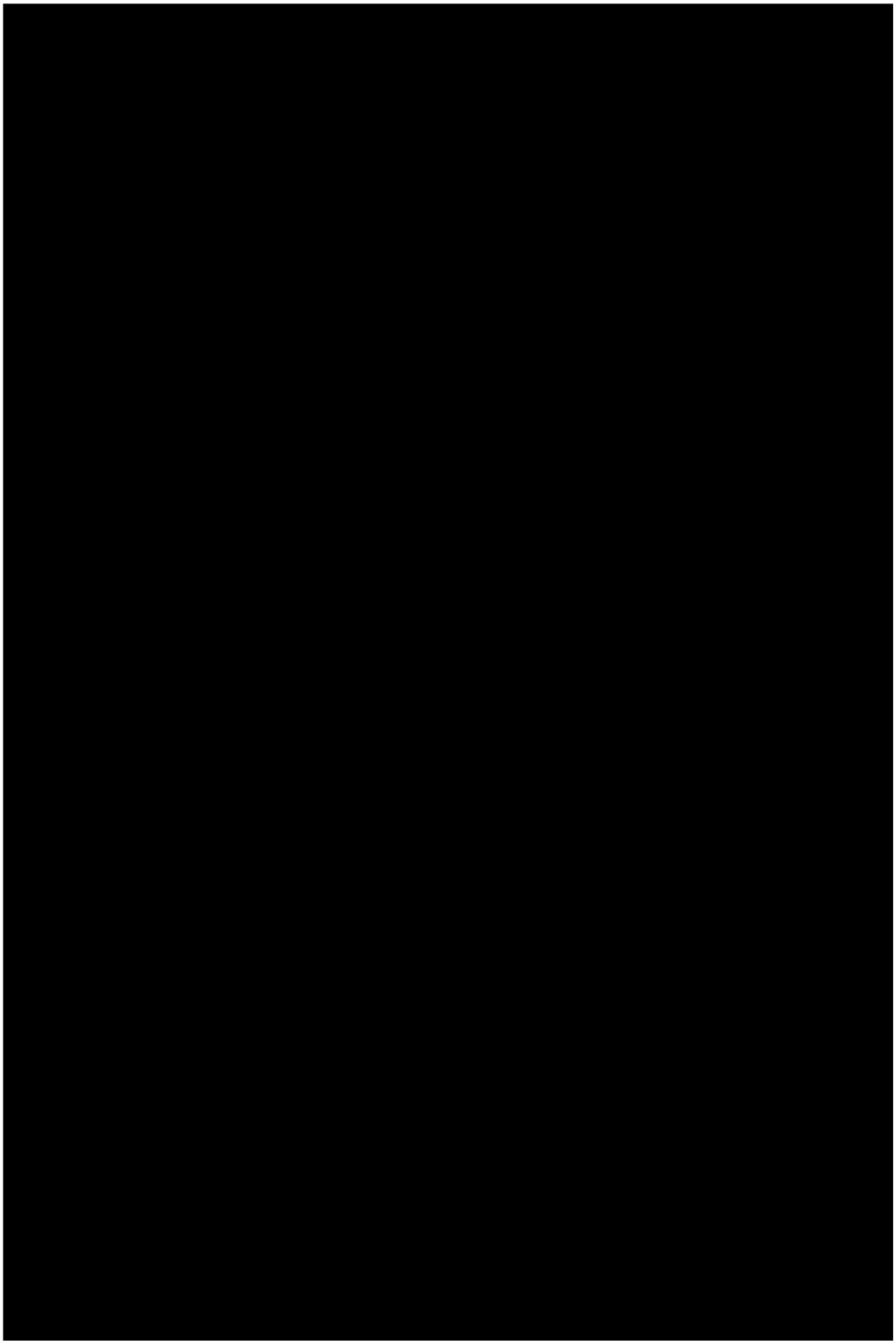

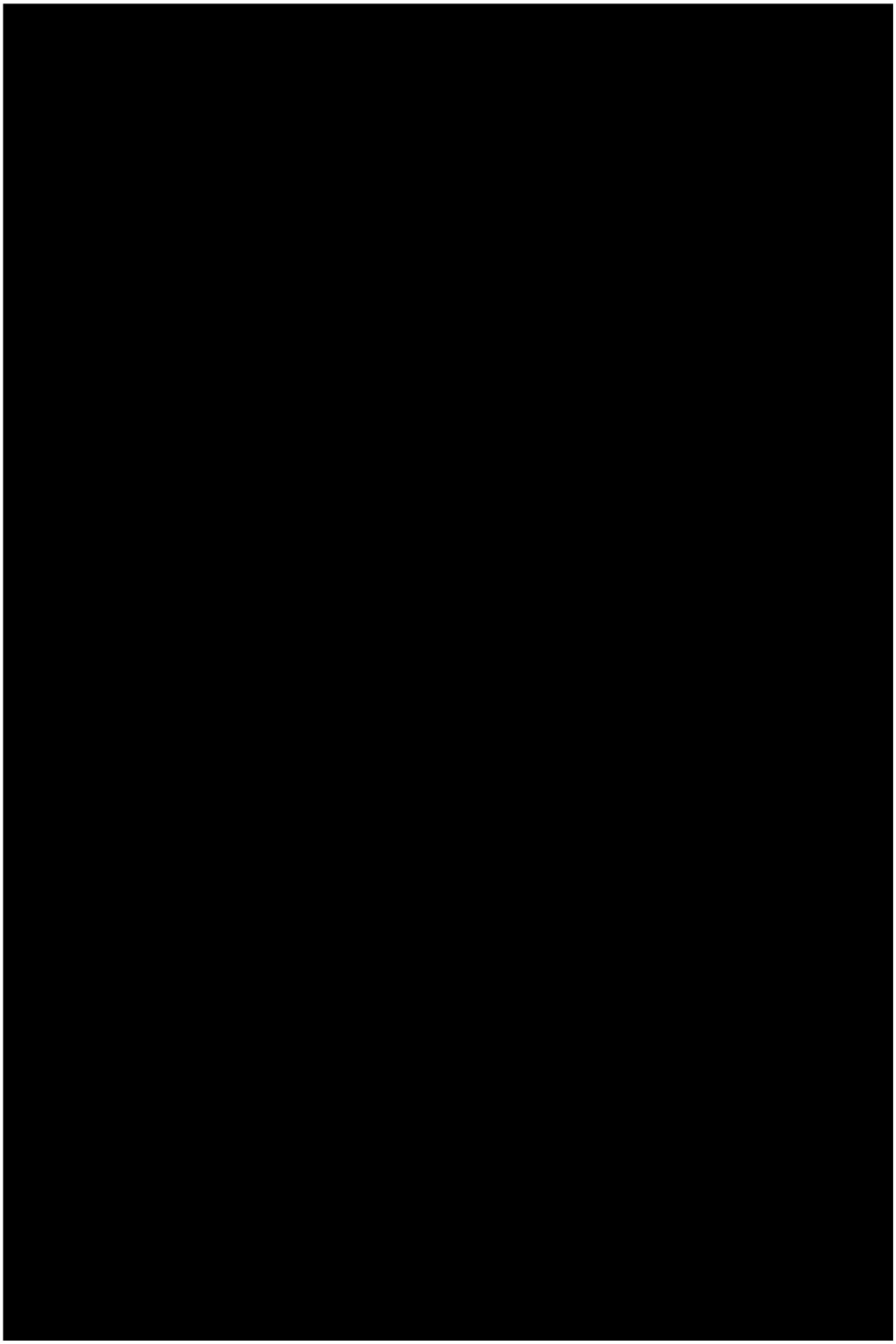

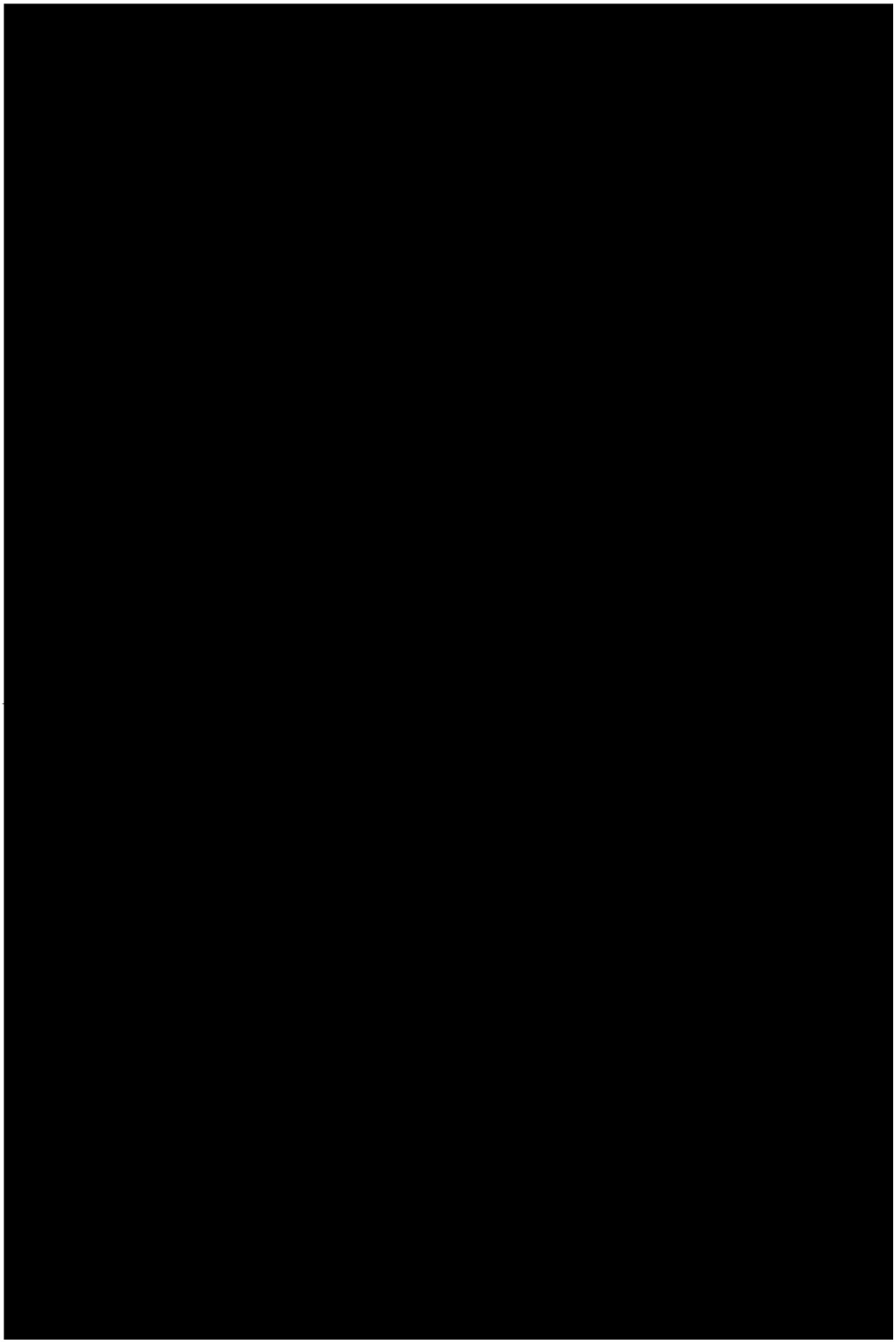

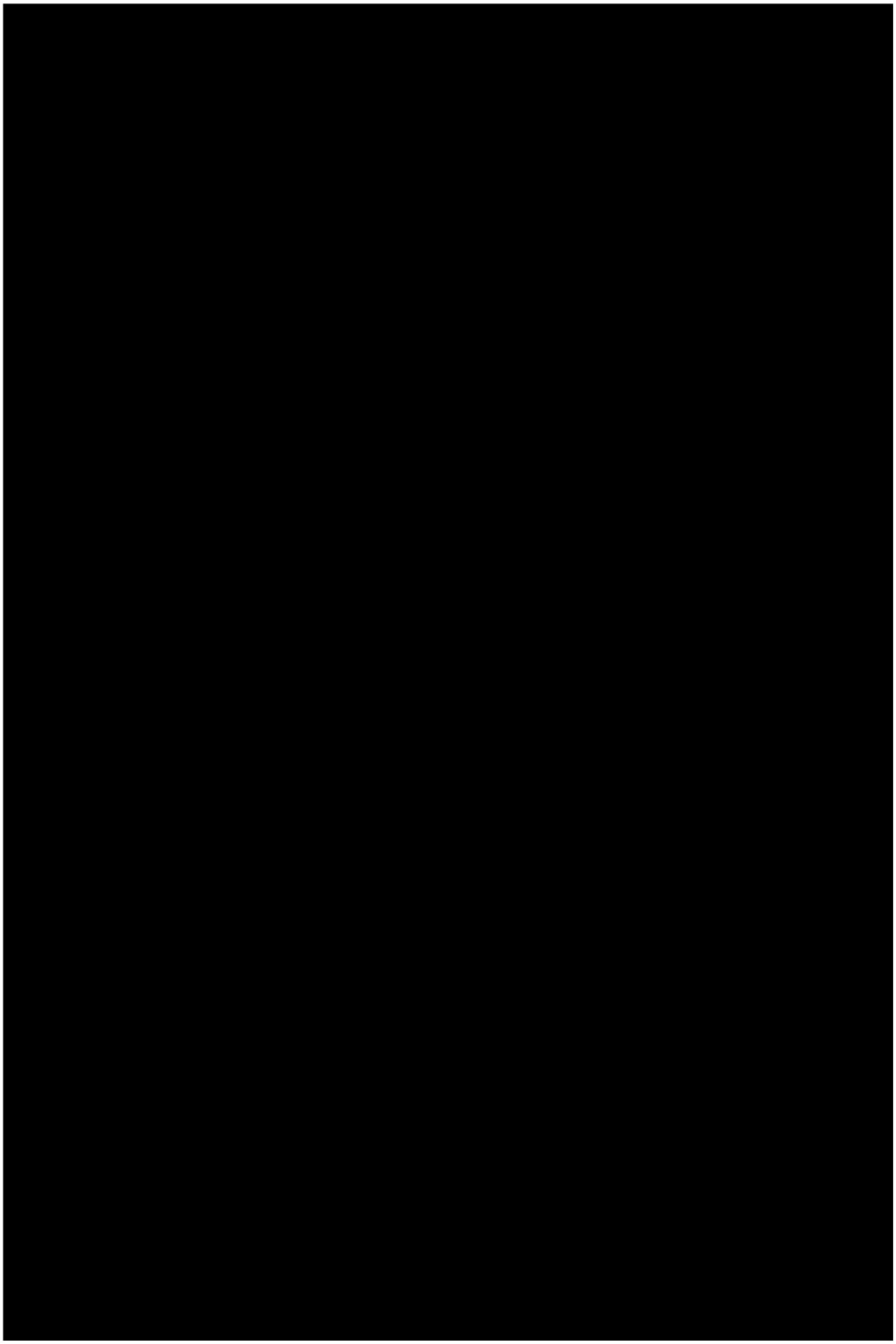

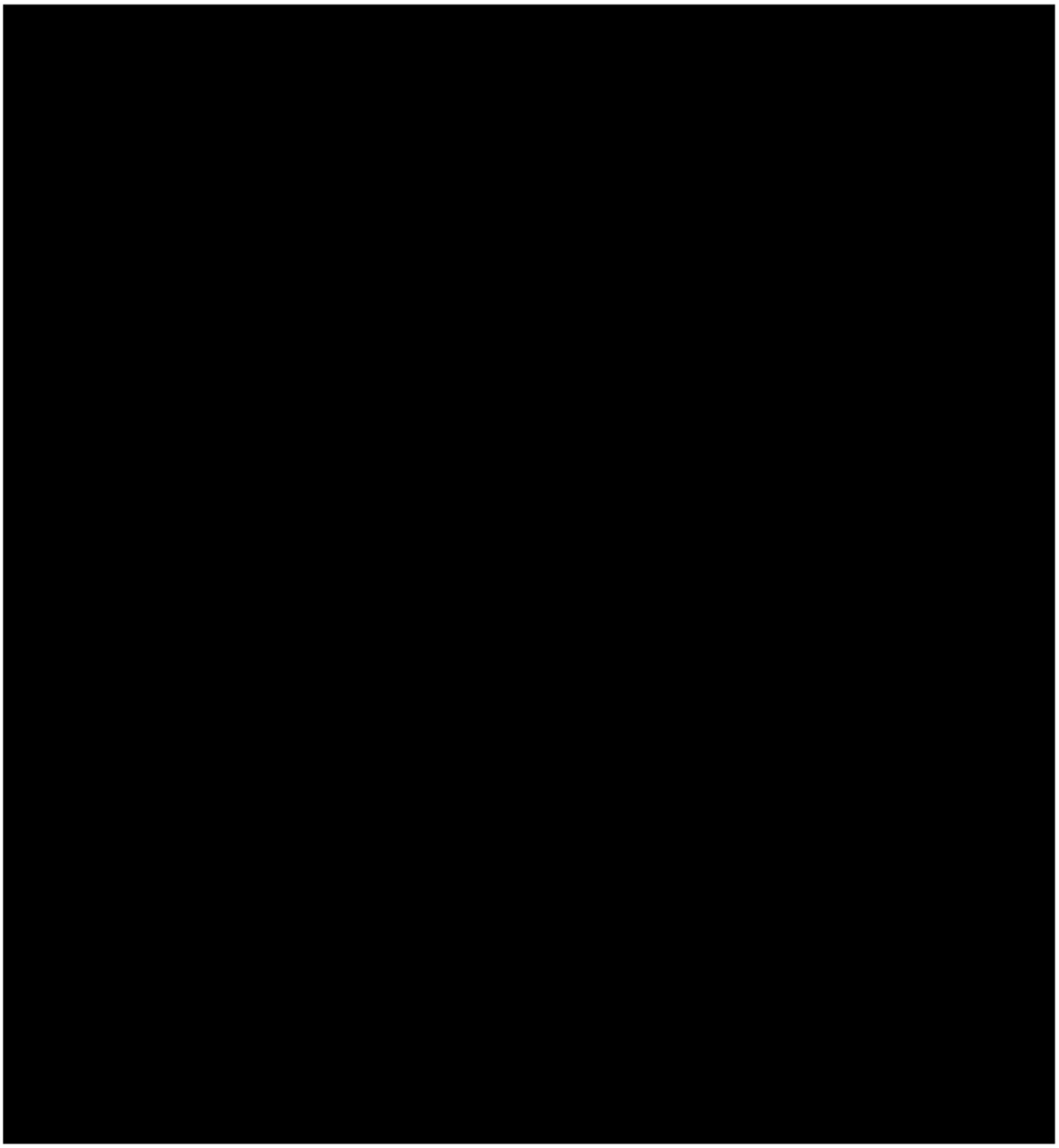

4.6 Discussion of the temperature jump phenomenon

In this chapter, a large number of tests on UHTCMC materials in atmospheric re-entry environment has been presented. A specific interest has been dedicated to the aero-thermal behaviour of UHTCMCs and UHTCs based on ZrB_2, for which several phenomena have been observed during samples exposure to arc-jet supersonic plasma flow. A comprehensive interpretation could be proposed, combining the results of the

different test campaigns and relating the experimental observations to the phase changes occurred on the samples surfaces due to ultra-high-temperature oxidation.

Common features and general observations are the following:

- All ZrB_2-based samples appeared to be completely oxidized on the exposed surface, but kept an almost null erosion rate with respect to other materials formulations.
- Infrared and optical videos of the tests showed in most cases the apparent presence of a liquid phase on the surface, in the form of an unsteady variation of the surface radiance (Fig. 4.18, 4.35, 4.58), or even bubble and droplets nucleation (Fig. 4.11, 4.17, 4.42, 4.46). This phenomenon has been labelled as *waves of radiance*, and occurs when the sample temperature is in the range 2100-2300 K.
- Most samples have experienced a *spontaneous temperature jump*, a sudden rise in temperature of 4-500 K, at constant flow conditions, starting in a temperature range from 2000 to 2300 K.
- The spectral emissivity in the Near-Infrared wavelength band (Fig. 4.21, 4.36a, 4.43, 4.57) has a trend with temperature that is qualitatively similar for all the samples, with values depending mainly on the SiC content (Fig. 4.36a). Specifically, it increases up to values around 0.8 at temperatures of 1700-1800 K, then decreases to values down to 0.4-0.5 for temperatures of 2000-2200 K, for the samples containing the minimum amount of SiC (5 vol% in the matrix). Samples exceeding those temperatures, with or without a *TJ*, experience a further increase in ε_λ. The only exception is test sequence 2b on samples with varying SiC content (Fig. 4.43 in section 4.3.3), where the spectral emissivity constantly increases with time and temperature. This trend is actually comparable to that of the ZC-LF samples, based on ZrB_2-PyC matrix, whose data were reported in section 0.

Specific features of the *temperature jump* are:

- It only occurs when the flow specific total enthalpy exceeded 18 MJ/kg.

- A porous zirconia layer is found on the front surface of the samples after test.
- The *temperature jump* takes place only on the front surface of the sample, whereas the rear part of the material keeps a relatively low temperature (as shown by Fig. 4.19, 4.34, 4.41, 4.45, 4.49).
- The *TJ* appears to be favoured by a low SiC amount, as explicitly verified in section 4.3, but it was demonstrated that it can occur even for higher SiC content (up to at least 15 vol%) if exposure time at a sufficient enthalpy level is long enough. It is also interesting to notice that samples containing ZrB_2 but no SiC (sample ZS0-LF, section 4.2.3.1, and samples densified by RF-CVI, sections 0 and 4.5, for small- and large-scale tests respectively), do not experience the *jump*, but rather a steep increase in the temperature already at the earliest stages of the tests, sharing the feature of having this increase localized on the front exposed surface.
- The *TJ* features are affected by the atmospheric composition, as analysed in section 4.4: when the oxygen partial pressure is extremely low (as for test in nitrogen), the *TJ* occurs at lower temperatures, is very steep and destructive for the material; on the other hand, in presence of oxygen, the *jump* is retarded and more gradual, with less dramatic effects on the structural resistance of the oxide layer.
- The surface NIR spectral emissivity after the *jump* is higher than before the *jump.*

Before proposing a correlation among all these experimental observations, it could be useful to recap the oxidation process of ZrB_2-SiC-based UHTCs. As a reference, Fig. 4.59 shows a sketch of the different stages of the process for a long-fibre-reinforced UHTCMC, as those presented in section 4.2.2. The presence of fibres is supposed not to affect the ultra-high-temperature aero-thermal behaviour, since the exposed surface had no protective coating, so that surficial carbon fibres vaporized at relatively low temperature [114], leaving a rough ZrB_2-SiC surface. In agreement with ZrB_2-SiC oxidation mechanism [27,115], at temperatures below 1400 K, the sample surface is covered by a boron-oxide glassy phase, as relevant SiC oxidation has not

been triggered yet. Between 1500 and 1600 K, SiC undergoes passive oxidation and the formation of a stable borosilicate glass (BSG) provided the highest oxidation protection to the UHTC matrix, Fig. 4.59a. The maximum emissivity of around 0.75-0.8 in the different cases is reached at temperatures between 1600 and 1700 K, when consistent B_2O_3 vaporization occurs and the glass is mostly composed of SiO_2. In the 2100-2300 K temperature range, which are the maximum temperatures reached before the occurrence of the *temperature jump* for all the samples, emissivity is then minimum, around 0.5. This is also the temperature range in which the *waves of radiance* phenomenon occurs, right before the *temperature jump*. Since at those temperatures the BSG layer is supposed to be mainly composed of silica, which has a melting point around 2000 K [116], it is reasonable to speculate that the oxide is completely liquid and therefore, in agreement with the discussion by Monteverde et al. [50], the *waves* phenomenon is associated to the shear-induced transportation of the glass along the specimen side surface. It is largely accepted that more SiC promotes a better physical barrier against oxidation thanks to a higher amount of borosilicate glass [26,27,117,118]. A combination of shear transportation and volatilization of the glassy phase can leave the underneath skeleton unprotected, exposing the ZrO_2 grains directly to the supersonic flow [27]. Meanwhile, if the residual liquid phase being generated in the sub-scales is not capable to prevent massive volatilization of the gaseous products of SiC and carbon fibres oxidation (SiO, CO_2, CO), whose vapour pressure lead to unsteady protrusion and bursting of liquid bubbles, Fig. 4.59b,c only porous zirconia remains in the outer oxide layer.

More precisely, the "durability" of the BSG, i.e. its capacity to remain not only adherent to the external surface but to survive also inside the oxide scale, is vital to continue have an effective barrier to oxidation. Due to the temperatures reached during the present test campaigns, on the front surface of the buttons, the BSG got lost. In fact, according to the different post-test analysis by SEM-EDS, the exposed surfaces showed sparse residual glassy pools, unable alone to protect effectively from the oxidation attack. Part of the BSG survived instead inside the oxide scale, in larger quantities for more SiC available in the starting composition. If the outermost glassy layer was basically lost during the most stressful stages of the test sequences, the

underlying oxide scale was able to hold more and more BSG as long as the thermal insulation of the oxide scale worked in an effective manner.

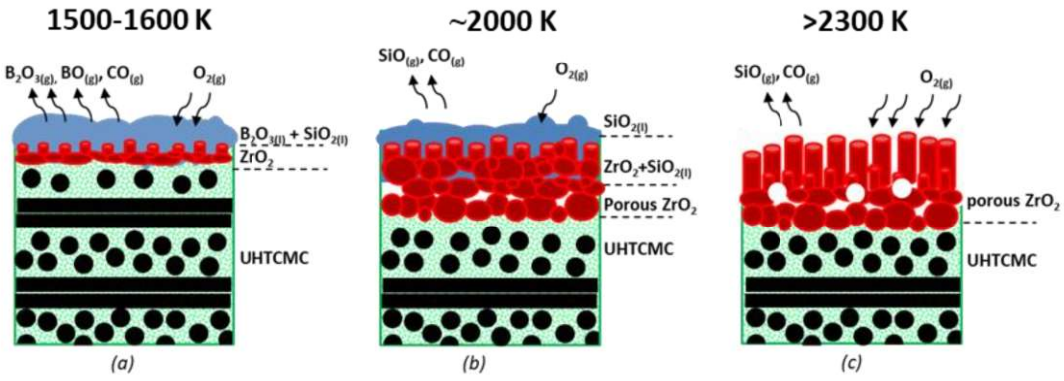

Fig. 4.59. Sketch of LF UHTCMCs oxidation highlighting three different stages, a) formation of borosilicate glass and compact ZrO_2 layer, b) glass bubbling, development of columnar ZrO_2 outer scale and progressive silica migration outwards from the subscale, c) exposed porous ZrO_2 layer after complete silica shear removal.

Referring to tests for varying SiC content, in Fig. 4.37 and 4.38, the concentration profile of Si reflects that of the residual BSG in buttons ZSY-05 and ZSY-18: larger quantities of BSG survived in the oxide scale of the SiC richest composition. Nevertheless, the lack of BSG noticed inside the Si-free strip lying above the oxide/bulk interface (see Fig. 4.38) was interpreted in this manner. SiO(g), and not liquid BSG, forms at the oxidation front, diffuses through the open channels outward, leaving voids and porosities behind. If such physical discontinuities were continuously replenished by fresh BSG rising up from the interior and re-condensing for the increased oxygen partial pressure, the oxide scale is still able to afford protection against oxidation and draw heat away from the stagnation points. The concentration profile of the residual Si in the ZSY-18 specimen tells us that, for the duration of the test, the replenishment seamlessly worked so that the feeding of protective BSG never stopped. This is more evident along the lateral walls of the button which were affected by less harsh conditions of heat flux and temperature compared to the front one. In fact, the SEM-EDS mapping revealed the presence of residual BSG close to the

deepest oxidation front, with increasing residual amount of the same moving toward the exterior.

Such a feeding mechanism of BSG was not effective in specimen ZSY-05, as well as in the fibre-reinforced samples of section 4.2.2 and in the ZSW samples whose test are described in section 4.4, and also in specimens ZSY-10 and ZSY-15 after repeated, long-duration plasma exposures. This was due to a native lack of Si, drastically shrinking the "incubation" time necessary to deprive the oxide scale of the residual BSG. The concept of an incubation time preceding a *TJ* was already mentioned by other authors which correlated this phenomenon to the rapid loss of protection no more afforded by external protective glasses [52]. The depletion of BSG inside *and* outside the zirconia oxide scale was pre-condition to push those button to interact differently with the flow-field, disclosing in a measurable manner a new energy balance through a rapid spontaneous rise of the front surface temperature, e.g *TJ*.

Moreover, of course, the protection from oxidation was not present in the cases in which the BSG had not the opportunity to form at all. These are the cases of the samples without SiC (again, sample ZS0-LF, ZC-LF-1 and 2 in SPES tests, and RF-CVI samples in L3K tests), and in the ZSW-N test, in which the missing reactant for the formation of a sufficient amount of SiO_2 was the oxygen in the atmosphere. In the former case (presence of oxygen, absence of SiC), the result was likely the formation of ZrO_2 on the surface at lower-temperatures with respect to SiC-containing samples, and so a behaviour similar to that of the other samples after the *TJ* (rapid temperature increase limited to the outer front layers). In the latter case, despite the presence of SiC, the very limited amount of atmospheric oxygen, with partial pressures in the order of tens of Pa, is not able to trigger this healing mechanism by formation of glassy borosilicate. This is responsible for a more violent oxidation process, which could be associated to a volcano eruption. Due to the unhampered diffusion of oxygen from the gas flow to the bulk material, the gas oxides generated by evaporation in the sample reach a relatively high partial pressure, until they get super-heated, and become an explosive gas mixture breaking the surface solid scale (as shown by the microstructures of Fig. 4.53).

At this point, it is possible to propose an interpretation for the *temperature jump*. It is important to underline that, whatever the reason behind the considerable temperature increase, this was not just a transitory phase, but led to a new condition which persisted for all the remaining test duration. Indeed, all the experimental plots of surface temperature presented in the previous sections demonstrate that a steady-state radiative equilibrium temperature was achieved, not only during the maximum enthalpy step, but even during the cooling procedure, in which the torch arc power is stepwise decreased. In the cooling phase, the surface temperature measured by the ISQ5 pyrometer was always higher than during the heating sequence, at all the enthalpy levels. Therefore, after the unsteady evolution corresponding to the trigger of the *temperature jump*, a new stable equilibrium condition of the heat balance through the exposed surface of the sample must have been established, related to variations of the heat flux contributions at the solid/fluid interface.

One possible trigger could be a reduced capability of the material to dissipate the incoming heat flux by radiation. However, in the assumption that, especially at the very high temperatures reached after the jump, the estimated value of spectral emissivity is representative of the total emissivity along the whole wavelength spectrum (as most of the power is irradiated in the wavelength band around 1 μm, where the value of ε_λ was calculated [69]), it could be argued that the observed increase in the emissivity after the *jump* should even favour an improved radiative heat dispersion. On the other hand, the general estimated emissivity trend is in agreement with the total emissivity measurements presented by Scatteia et al. [119], while the increase in spectral emissivity with temperature, observed after the occurrence of the *jump*, is coherent with available data related to total emittance of ZrO_2 at ultra-high-temperature [120], so a different reason is most likely to be searched.

Another possibility could be the release of extra heat due to the energy balance in surface oxidation reactions. It should be reminded that reactions (1) and (2), which where defined in section 4.3.1 and are here reported again for the reader's convenience:

$$ZrB_2(s) + 5/2\ O_2(g) = ZrO_2(s) + B_2O_3(l,g) \quad (1)$$

$$SiC(s) + 3/2\ O_2(g) = SiO_2(s,l) + CO(g) \quad (2)$$

never stop happening until oxygen diffuses inward and reaches the un-oxidized bulk: they are exothermic and in this sense they continue to release extra heat to the system. On the contrary, the loss of the BSG implies endothermic vaporization reactions, with a reaction enthalpy ΔH_R in the range of 600-700 kJ/mol. When the surface gets depleted of BSG, a part of the incoming heat flux, till now trapped to feed the BSG volatilization, returns available to provide an extra heating. Actually, the overall amount of the consumed SiC, i.e. that formerly present in the volume occupied by the oxide scale in the different tests, is on the order of $5 \cdot 10^{-4}$ mol, but so limited that any extra heat eventually released to the system (only a few W) has to be considered of marginal entity.

It is more likely that the *TJ* is related to a decay of the capability of the oxide scale to conduct heat. BSG also plays a function as "filler" to keep glued the zirconia grains of the oxide scale, retarding the onset of defects such as voids or even detachments. This is particularly evident in samples not containing SiC, which have a brittle and poorly "glued" oxide layer after test. Moreover, porosity is a characteristic feature of all the microstructures shown in the previous sections, and in some particular cases, such as sample ZSW-N (tested in nitrogen, Fig. 4.53) and ZSY-05 (in the test campaign for varying SiC content, Fig. 4.33a), evident detachments of the oxide from the bulk substrate can be observed. Actually, aero-heating of ZSY-05 specimen was not stopped but proceeded through the most stressful last step. It follows that many microstructure features, more pertinent to the scenario above described, may have been irreparably changed. In fact, after the *TJ*, the IR-TC outputs confirmed that some front areas of the ZSY-05 button reached temperatures so high to induce a partial melting of the zirconia oxide scale directly exposed to the harshest heat flux condition: the IR frames of Fig. 4.34 suggest that the area which underwent the oxide detachment corresponds to the spot of the further temperature increase measured by the IR-TC in the second half of step #8. Moreover, even the ZSY-15 button (richer in SiC compared to ZSY-05) presents a longitudinal subtle opening of the oxide scale (see Fig. 4.33c), although no apparent *TJ*s have been measured and no catastrophic damage to the oxide layer was observed. However, the temperature axial profiles along the four samples with varying SiC content, depicted in Fig. 4.36b, make possible to infer that the ability

of the materials outer (oxide) layers to conduct heat during the most stressful test stage was reduced accordingly with the capability of retaining BSG, thanks to the presence of higher SiC concentration in the initial composition. This interpretation finds consensus with the relevant literature investigating the ultra-high-temperature heat transfer of HfB_2- and ZrB_2-based UHTCs [121,122], where porous zirconia layers were even proposed as effective insulating thermal barrier coatings for high-temperature aerospace components [123,124].

Indeed, the effective thermal conductivity of the oxide scale can substantially affect the distribution of the incoming convective heat flux among the conductive and radiative contributions, resulting in highly different radiative equilibrium temperatures on the exposed surface. Referring to the conditions measured on sample ZSY-05 during step #7 of test sequence 1, a front surface temperature of 2200 K before *TJ* and of 2600 K after *TJ* were here assumed. By numerical models described above, the distribution of the oncoming convective hot wall heat flux among its radiative and conductive components has been estimated. Fig. 4.60 shows the effect of a 300-μm thick oxide scale thermal conductivity (in the range 0.1-2.5 W/m·K) on the conductive heat flux, together with horizontal lines corresponding to the values of radiative heat flux before and after *TJ* (for a fixed surface emissivity). It can be seen that, to ensure global equilibrium, the substantially increased surface radiation due to the higher surface temperature can be balanced by a reduced capability to dissipate heat by conduction. Specifically, it has been estimated that, in the conditions before *TJ*, assuming the presence of an oxide layer with a thermal conductivity of 2.5 W/m·K (reasonable for a zirconia scale whose internal voids and porosities are filled by liquid silica-based glass [125,126]), the total hot-wall convective heat flux consists of 35% radiative dissipation towards the environment and 65% conduction to the inner layers of the material. Considering, for the conditions after *TJ*, a drastically reduced effective thermal conductivity of 0.1 W/m·K (resulting from the interruption of the BSG replenishment and the corresponding creation of voids, porosities [127,128] or even a detachment), the total heat flux redistributes to 70% radiation and 30% conduction.

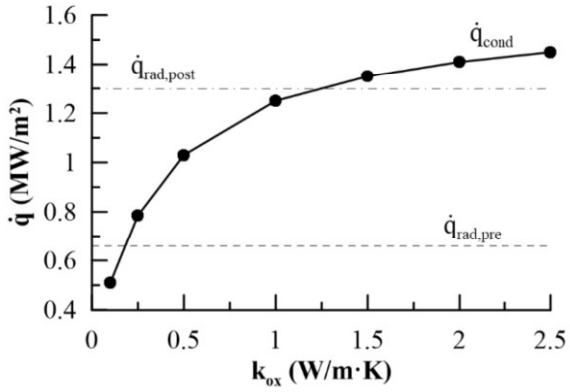

Fig. 4.60. Variation of the conductive heat flux ($\dot{q}_{cond}$) versus the thermal conductivity of the oxide scale (k_{ox}), calculated by CFD. Horizontal lines corresponding to the values of the radiative heat flux before and after *TJ* ($\dot{q}_{rad,pre}$ and $\dot{q}_{rad,post}$, corresponding to a surface temperature of 2200 K and 2600 K respectively and an emissivity ε = 0.8) are also shown.

The last effect that needs to be taken into account is the interaction of the surface with the flow, which changes when the BSG is finally lost and the ZrO_2 gets exposed. Specifically, an increased catalytic recombination efficiency may need to be considered, due to a transition from an oxide layer mainly covered by glassy silica (relatively low γ_w [34,129]) to a scale primarily based on zirconia (relatively high γ_w [130]).

To sum up, all the experimental evidence and the considerations made above suggest that a twofold mechanism could be taken into account to justify the *temperature jump*:

- a substantial reduction of the thermal conductivity in the oxide layer;
- an increased catalytic recombination efficiency.

In order to quantitatively support this interpretation, Computational Fluid Dynamic simulations were carried out and their results were compared with the experimental data. Specifically, the last step of the test on the long-fibre reinforced UHTCMC sample ZSY-LF-2 was selected as a reference case. First, the thermo-fluid-dynamic and chemical field was simulated, employing the numerical models described in section 3.1. One should remind that, as already pointed out in section 4.1, the level of dissociation of molecular species is considerably high, condition that, as discussed

below, results in a relevant effect of surface catalycity on the heat fluxes. Fig. 4.61 shows in fact the profiles of the cold wall heat flux on the front surface of the sample, for both non-catalytic (NC) and fully catalytic (FC) conditions. It is evident that the heat flux is more than double in the FC condition with respect to the NC, reaching values around 5 MW/m^2.

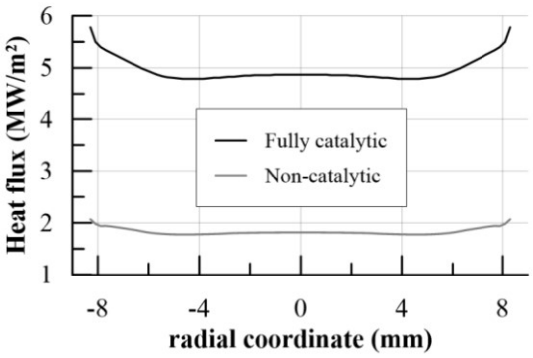

Fig. 4.61. Non-catalytic and fully catalytic cold wall heat flux profiles on the front surface of the samples, conditions corresponding to step #7 (H_0 = 18 MJ/kg), calculated by CFD simulation of the fluid flow in SPES tests.

The aero-thermo-chemical field was then coupled to the thermal analysis of the sample, performing steady-state simulations to match the temperature distribution evaluated by the thermo-camera before and after the *temperature jump*. The sample density was set to 4300 kg/m^3. The surface emissivity, based on the estimation presented in section 4.2.2, was set to 0.5 before the jump, and to 0.8 after the jump. In order to match the temperature axial profile before the *jump*, and based on experimental measurements performed within the frame of the project, a temperature dependent thermal conductivity was considered, varying between 49 W/ m·K at room temperature to 47 W/m·K over 2273 K. Even before the occurrence of the temperature jump, a certain amount of catalytic recombination needed to be taken into account, with a catalytic efficiency $\gamma_w = 4 \cdot 10^{-3}$. This value is representative of SiO_2 [129], which is supposed to be the component with the highest concentration in the BSG phase before the *jump*. As discussed above, at the earliest stages of the temperature jump phenomenon, a liquid phase is transported downstream by the supersonic flow, generating the *waves of radiance* phenomenon. It is opinion of the author that this is

the trigger for an unsteady variation of the surface chemistry, resulting in a complete removal of SiO_2 and carbon fibres from the sub-scale layer of the oxide phase, which proceeds until a new radiative equilibrium condition is reached, corresponding to the exposure of a highly porous ZrO_2 scale (see Fig. 4.22). As anticipated above, to justify the rise in temperature associated to the *jump*, and localized in the front part of the sample, a double effect was considered: an increase in catalytic activity (γ_w), and a dramatic decrease in thermal conductivity in the oxidized region (k_{ox}). An excellent agreement between numerical and experimental results was obtained assuming $\gamma_w = 7 \cdot 10^{-2}$ (more than one order of magnitude higher than before the jump) and $k_{ox} = 1$ W/m·K, and considering an oxide thickness of 400 μm (based on the estimations made by the microstructural analyses presented in section 4.2.2). The comparison between numerical and experimental temperature axial profiles is shown in Fig. 4.62.

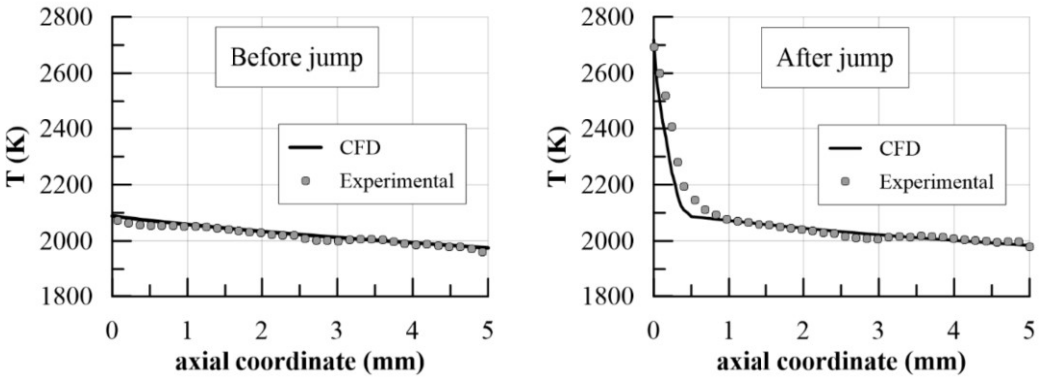

Fig. 4.62. Comparison between numerical and experimental temperature axial profiles, before (left) and after (right) temperature jump, for sample ZSY-LF-2.

The results of these CFD simulations support the proposed interpretation for the temperature jump, demonstrating that, with reasonable assumptions about the involved physical parameters, it is possible to accurately reproduce the experimental behaviour of the UHTCs and UHTCMCs, providing a sufficiently solid explanation of the *temperature jump* phenomenon. To recap, the new thermal status just after a *TJ* reflects the energy re-balancing of the system exposed to the same freestream energy input but affected by an increase in the chemical contribution (which was "trapped" into

enthalpy of dissociation of molecular species, and gets released thanks to the catalytic activity of the zirconia surface) and a modified capability to drain away heat in excess from the stagnation points and thus to re-radiate it: the system "*spontaneously*" equilibrates a new status where the radiative temperature is globally higher.

CHAPTER 5. RESULTS IN ROCKET PROPULSION ENVIRONMENT

This chapter presents and discusses the results obtained for the characterization of innovative materials for rocket nozzles, combining numerical and experimental results to fully characterize the test conditions and identify the parameters that mainly affect the materials performance in relevant combustion environment. Tests were carried out in the Aerospace Propulsion Laboratory of the University of Naples "Federico II", by means of the different experimental configurations described in section 2.3.

The content is structured as follows. Section 5.1 presents the test conditions in the different set-ups, with the support of numerical simulations. Section 5.2 describes the results of tests carried out in the free-jet configuration. Section 5.3 presents the outcomes of tests on combustion chamber inserts. Section 5.4 summarizes the main results of nozzle throat insert testing. Section 5.5 presents all the results of tests on complete subscale nozzles, with some additional numerical analyses for a better understanding of experimental results. Finally, section 5.6 summarizes the main conclusions that can be derived from the overall test campaign.

5.1 Characterization of flow field and test conditions

This section presents the results of the simulations of the flow field in the different test configurations considered for the characterization of UHTCMC materials for rocket propulsion. The CFD simulations allowed characterizing the test conditions encountered by materials samples.

5.1.1 Free-jet test

For free-jet tests, three different test conditions, which differ for the oxidizer mass flow rates and the nozzle throat diameter and area ratio, have been selected, to evaluate the materials performance in different aero-thermo-chemical environments. All tests

had a nominal duration of 10 s. Cylindrical 220mm-long HDPE grains were employed as fuel and gaseous oxygen as oxidizer. Table 5.1 summarizes the main nominal operating parameters of the test conditions, as estimated by means of the one-dimensional tool described in Section 3.2.1.

Table 5.1. Nominal test conditions for free jet tests.

	Test condition 1FJ	**Test condition 2FJ**	**Test condition 3FJ**
Oxidizer mass flow rate [g/s]	25	30	40
Oxidizer-to-Fuel ratio	5.13	5.63	6.50
Chamber pressure [bar]	6.49	6.43	5.65
Combustion temperature [K]	~ 3200	~ 3200	~ 3200
Nozzle exit pressure [bar]	0.42	0.55	0.46
Nozzle exit temperature [K]	~ 2200	~ 2300	~ 2200
Nozzle exit Mach number	2.4	2.22	2.25
Nozzle exit CO_2 mass fraction	0.36	0.35	0.34
Nozzle exit H_2O mass fraction	0.17	0.16	0.14
Nozzle exit O_2 mass fraction	0.30	0.34	0.41

Test conditions 1FJ and 2FJ have been estimated considering the employment of a nozzle with a throat diameter equal to 9.6 mm. On the other side, for Test condition 3FJ nozzle with a throat diameter equal to 12.5 mm has been employed in order to have similar values of the chamber pressure with respect to Test conditions 1FJ, with a higher average oxidizer-to-fuel ratio, i.e. a more oxidizing chemical environment, with respect to the former two conditions.

Additional significant information on the operating conditions around the samples can be obtained from the CFD simulations carried out with the models described in Section 3.2.2. Fig. 5.1, 5.2 and 5.3 show the distributions of temperature, pressure and molecular oxygen mass fraction, respectively, in the flow field of the free jet test, for the three considered test conditions (for a better comparison, the contours of the same quantities are plotted in the same scale for the three conditions). In particular, comparison between Fig. 5.1a, b and c verify that the test conditions do not differ significantly in terms of temperature distribution, as expectable due to the similar values of combustion chamber temperatures evaluated by means of the chemical equilibrium software. On the contrary, major differences are noticeable in the static pressure field, displayed in Fig. 5.2. Downstream a sequence of shock/expansion

oblique waves, the peak static pressure at sample locations is slightly higher than 2.5 bar in test condition 1FJ, almost 4 bar in test condition 2FJ and more than 3 bar in test condition 3FJ. Furthermore, Fig. 5.3 shows the distribution of O_2 mass fraction, whose average value at sample location is 0.26, 0.31 and 0.37, for test conditions 1FJ, 2 FJ and 3FJ respectively.

The thermo-fluid-dynamic and chemical flow fields produce the conditions at sample location summarized in Table 5.2. In summary, it can be seen that test condition 2FJ is the harshest in terms of heat flux and pressure, but test condition 3FJ is more oxidizing. As an example, the cold-wall heat flux, static pressure profile and oxygen mass fraction on the sample front surface are shown in Fig. 5.4. The peak heat flux is 16 MW/m^2, which is a value representative of the actual loads that might be expected on a hybrid rocket nozzle throat surface, as reported in section 1.5. Moreover, it is possible to see that heat flux, pressures and oxygen concentration are maximum on the symmetry axis. As it will be extensively discussed in section 5.2, this is the location where a *temperature jump* phenomenon can be triggered, associated to a consistent local sample erosion.

Table 5.2. Conditions at sample location estimated with the CFD simulations of the free-jet test.

	Test condition 1FJ	**Test condition 2FJ**	**Test condition 3FJ**
Stagnation point pressure [bar]	2.6	3.8	3.2
Average CO_2 mass fraction	0.27	0.29	0.29
Average H_2O mass fraction	0.11	0.12	0.12
Average O_2 mass fraction	0.26	0.31	0.37
Average cold-wall surface heat flux [MW/m^2]	10.8	12.9	12.4
Peak Cold-wall surface heat flux [MW/m^2]	12.4	16.0	14.0

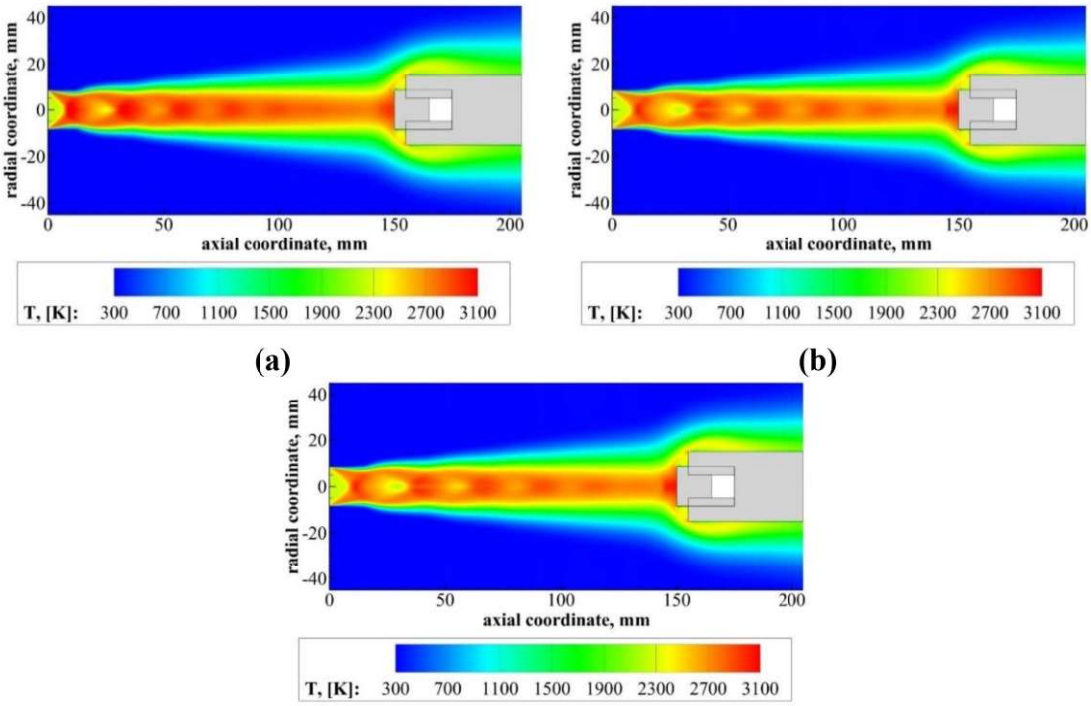

Fig. 5.1. Temperature distribution around the sample (a) for test condition 1FJ, (b) for test condition 2FJ and (c) for test condition 3FJ.

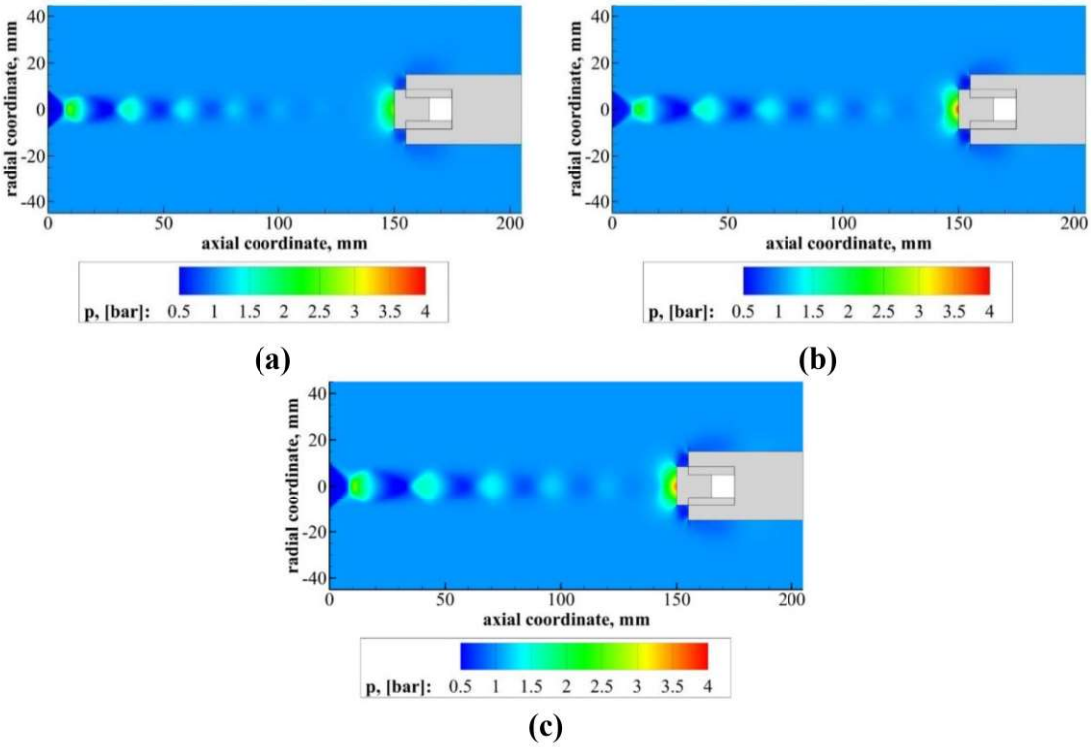

Fig. 5.2. Static pressure distribution around the sample (a) for test condition 1FJ, (b) for test condition 2FJ and (c) for test condition 3FJ.

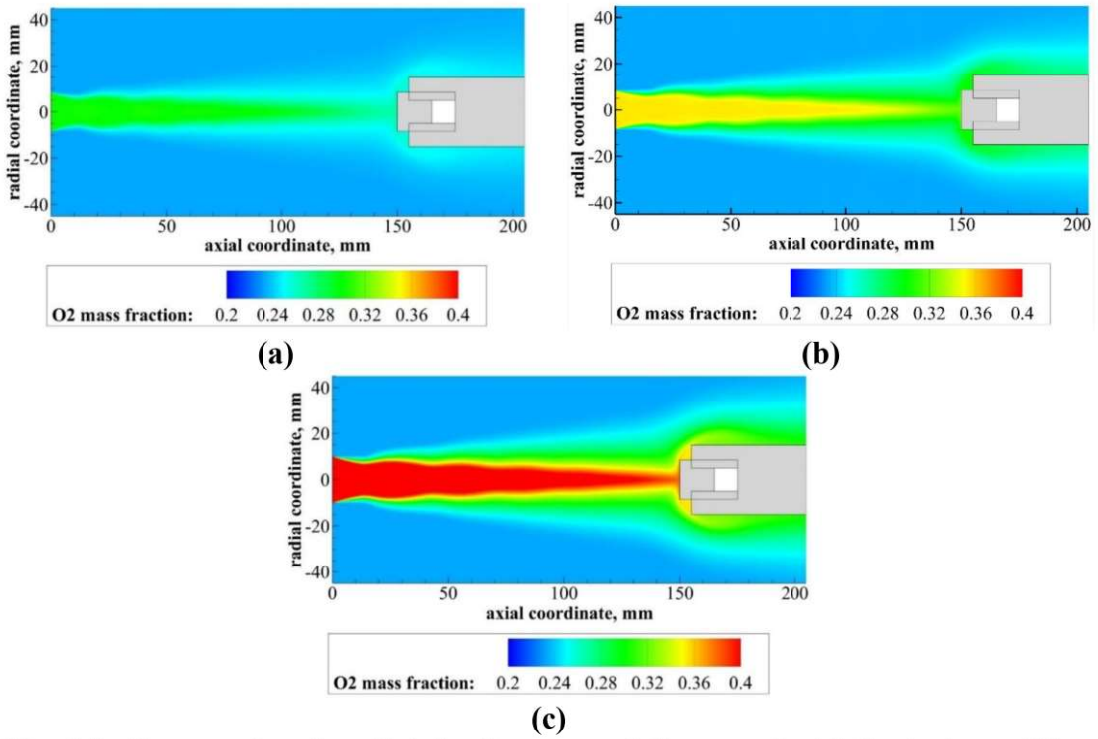

Fig. 5.3. O_2 mass fraction distribution around the sample (a) for test condition 1FJ, (b) for test condition 2FJ and (c) for test condition 3FJ.

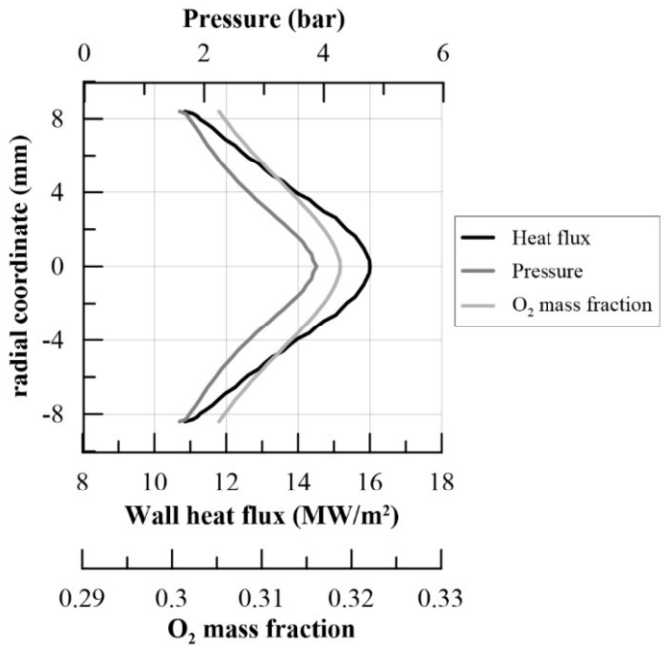

Fig. 5.4. Cold-wall total surface heat flux, static pressure and O_2 mass fraction on free-jet sample front surface, calculated by CFD in condition 3FJ.

5.1.2 Chamber inserts test

Also in this case different test conditions, which differ for the oxidizer mass flow rates, have been selected. In particular, two different sets of test conditions have been considered for testing of chamber inserts. The main conditions in the combustion chamber, estimated by means of the 1D model presented in section 3.2.1, are summarized in Table 5.3.

Table 5.3. Nominal test conditions in chamber inserts tests.

	Test condition 1CI	**Test condition 2CI**
Oxidizer mass flow rate [g/s]	25	40
Oxidizer-to-Fuel ratio	5.13	6.50
Chamber pressure [bar]	6.49	8.2
Combustion temperature [K]	~ 3200	~ 3200
Combustion chamber CO_2 mass fraction	0.32	0.32
Combustion chamber H_2O mass fraction	0.16	0.14
Combustion chamber O_2 mass fraction	0.30	0.41

In order to estimate the operating conditions to which the chamber inserts were subjected during the test, the CFD model for the simulation of hybrid rocket internal ballistics described in section 3.2.3 was employed. Details are only reported for test condition 2CI.

Fig. 5.5 shows the plot of the calculated temperature contour with the streamlines overlapped on the top half, and the fuel mass-fraction in the unburned mixture isolines drawn on the bottom half, in the region surrounding the chamber insert, located, as mentioned before, between the fuel grain and the post-chamber. From this picture, all the main features of the internal flow field can be unveiled. For example, it should be noted that the inclusion of the chamber insert and the corresponding geometrical discontinuity determined a slight change in the fluid behaviour, which, as also pointed out in the literature [131], further promoted the propellant mixing and the combustion efficiency in the post-chamber.

Table 5.4 summarizes the average operating conditions estimated in the transversal section corresponding to the chamber insert location, which are in good

agreement with the values obtained with the one-dimensional model (see Table 5.3). Finally, Table 5.5 reports the conditions on the sample surface, on which a cold-wall average heat flux equal to 4.3 and 5.8 MW/m^2 is experienced, with a peak value of 5.7 and 7.8 MW/m^2, respectively for conditions 1CI and 2CI. Since in the typical chemical field of hybrid rockets the oxidizer is mainly concentrated in the core flow, the oxidizing species interacting with the insert surface were prevalently combustion products like CO_2 and H_2O [132] rather than O_2.

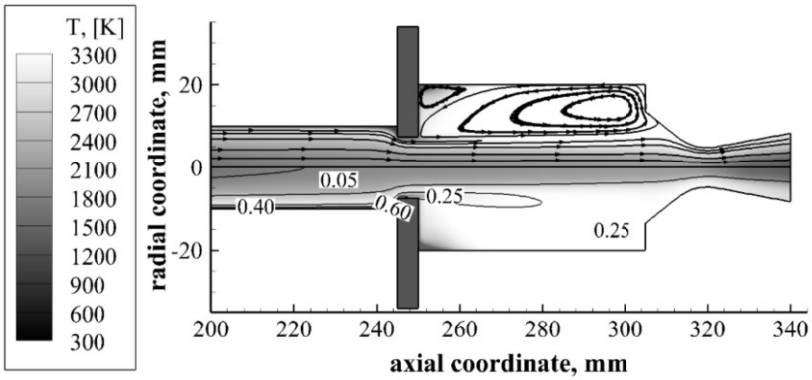

Fig. 5.5. CFD results around the chamber insert: temperature contour plot with overlapped streamlines (top half) and mixture-fraction isolines (bottom half).

Table 5.4. Average operating conditions in the rocket post-chamber.

	Test condition 1CI	**Test condition 2CI**
Total Pressure [bar]	6.20	7.90
Average Oxidizer-to-Fuel ratio	4.34	6.15
Average Total Temperature [K]	2930	2900

Table 5.5. Summary of conditions on the chamber insert surface.

	Test condition 1CI	**Test condition 2CI**
Average CO_2 mass fraction	0.51	0.58
Average H_2O mass fraction	0.25	0.25
Average Cold-wall surface heat flux [MW/m^2]	4.3	5.8
Peak Cold-wall surface heat flux [MW/m^2]	5.7	7.8

5.1.3 Nozzle inserts and complete nozzles test

For the experimental characterization of the nozzle throat inserts and complete subscale nozzles, two test conditions have been selected, with increasing mass flow rate. Tests had a nominal duration of 10 s. Cylindrical 220mm-long HDPE grains were employed as fuel and gaseous oxygen as oxidizer. In this case, for the estimation of the nominal test conditions the nominal value of the throat diameter, equal to 9.6 mm, has been considered in all cases, so in this case the most severe test condition foresees also a higher value of the chamber pressure. Table 5.6 summarizes the main nominal operating parameters, as estimated by means of the one-dimensional tool described in section 3.2.1.

Repeatability tests have been also considered for some of the complete subscale nozzle prototypes, in test condition 2N, with a nominal duration of 15 s.

Table 5.6. Nominal test conditions for nozzle throat inserts and complete nozzles testing.

	Test condition 1N	**Test condition 2N**
Oxidizer mass flow rate [g/s]	25	40
Oxidizer-to-Fuel ratio	5.13	6.50
Chamber pressure [bar]	6.49	9.63
Combustion temperature [K]	~ 3200	~ 3200
Nozzle inlet CO_2 mass fraction	0.32	0.32
Nozzle inlet H_2O mass fraction	0.16	0.14
Nozzle inlet O_2 mass fraction	0.30	0.41

Also in this case, CFD simulations of the flow field through the nozzle have been performed to collect additional significant information on the operating conditions around the prototypes.

As an example, Fig. 5.6 shows the distributions of temperature, pressure and molecular oxygen mass fraction in the flow field through the rocket nozzle, for condition 2N. Throughout the nozzle, the combusting flow undergoes an expansion to supersonic conditions, with a corresponding decrease in temperature and pressure and keeps reacting burning some residual oxygen. Remarkably, the temperature is still in

the order of 3000 K and pressure is on the order of 5 bar in the throat region, where the cold-wall heat flux achieves its peak value.

Finally, Table 5.7 summarizes the other significant quantities which characterize the test conditions at the throat section as estimated by the CFD simulations shown above.

Table 5.7. Conditions at nozzle throat estimated with the CFD simulations.

	Test condition 1N	**Test condition 2N**
Pressure [bar]	3.2	4.8
Shear stress [hPa]	24.3	34.1
Average CO_2 mass fraction	0.35	0.33
Average H_2O mass fraction	0.17	0.14
Average O_2 mass fraction	0.30	0.41
Maximum cold-wall surface heat flux [MW/m^2]	11.0	13.0

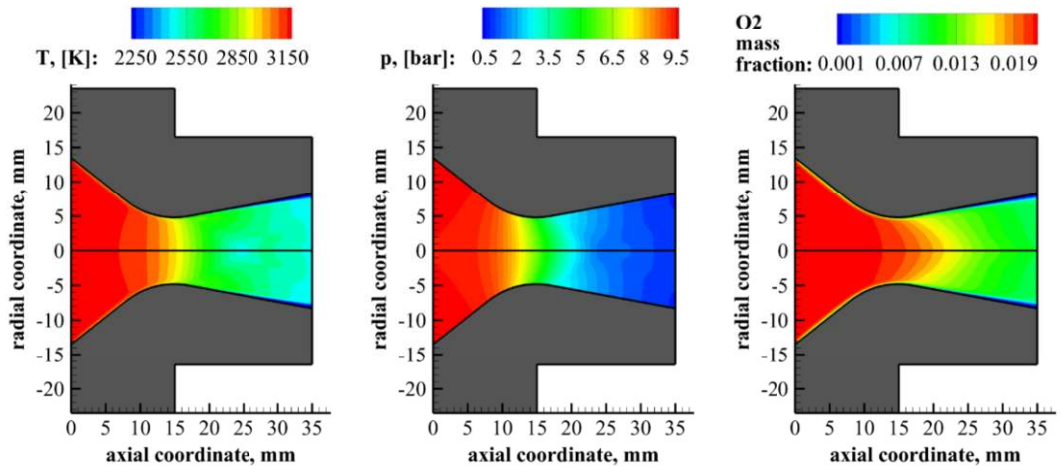

Fig. 5.6. Distributions of static temperature, static pressure and molecular oxygen mass fractions in test condition 2N.

5.2 Experimental characterization of UHTCMC samples in free jet conditions

As explained before, the first step of the characterization of the new UHTCMC materials foresees testing of small samples exposed to the free jet of the exhaust gases coming from the hybrid rocket nozzle. In this section, first the samples tested in this experimental campaign will be presented, then the test conditions will be described and finally the experimental results, in terms of the erosion behaviour and of the samples thermal histories, will be discussed.

5.2.1 UHTCMC samples

Eight sintered UHTCMC samples were manufactured and tested, which are summarized in Table 5.8. The samples differed for the matrix and the carbon fibres architecture. In particular, two samples, manufactured by TECNALIA, had a Ti_3SiC_2 matrix with short (chopped, up to 500 μm length) carbon fibres, uniformly dispersed into the matrix, and are labelled TSC-SF. SPS was used as the densification process. The other samples had the matrix based on ZrB_2 as major component and SiC as a minority phase. Three of them had long continuous pitch-based carbon fibres, with a 0°/90° plies architecture, while the others had chopped fibres uniformly dispersed into the matrix.

Table 5.8. UHTCMC samples for free jet test.

Sample ID	Matrix	Carbon fibres	FVC	Densification	Test condition
TSC-SF-1	Ti_3SiC_2	Short	40	SPS	1FJ
TSC-SF-2	Ti_3SiC_2	Short	40	SPS	3FJ
ZS-LF-1	ZrB_2-SiC	Long UD 0°/90°	40	HP	1FJ
ZS-LF-2	ZrB_2-SiC	Long UD 0°/90°	45	SPS	2FJ
ZS-LF-3	ZrB_2-SiC	Long UD 0°/90°	45	HP	2FJ
ZS-LF-4	ZrB_2-SiC	Long UD 0°/90°	40	HP	3FJ
ZS-SF-1	ZrB_2-SiC	Short	40	SPS	2FJ
ZS-SF-2	ZrB_2-SiC	Short	40	SPS	3FJ

5.2.2 Tests in condition 1FJ

First, two tests were carried out in test condition 1FJ (Table 5.1), in order to compare the response of materials with very different compositions. A long fibres ZrB_2-SiC-based sample (ZS-LF-1) and the chopped fibres Ti_3SiC_2-based sample (TSC-SF-1) were exposed to the exhaust plume of the hybrid rocket, injecting a gaseous oxygen mass flow rate of 25 g/s. The time profile of the maximum surface temperature for the two samples is shown in Fig. 5.7. The thermal histories practically overlap for the first 4-5 s, then, when T approaches 1900 K, the TSC-SF sample experiences a sudden rise in temperature, which at the end of the test exceeds 2800 K.

The sudden temperature jump was associated to a change in the shape of the flame surrounding the sample, as clearly shown in Fig. 5.8, which depicts images taken at the beginning and at the end of the test on TSC-SF-1. Starting from the instant corresponding to the jump, a very bright halo developed in front of the TSC-SF1 sample, from which a considerable amount of material was removed, probably due to the extremely high shear stresses. This resulted in a consistent erosion, estimated to be 0.204 mm/s, based on mass measurements. On the contrary, the stable behaviour exhibited by sample ZBSC-LF-1 was associated to a near-zero erosion rate ($4.3 \cdot 10^{-4}$ mm/s). Erosion data for the two samples are reported in Table 5.9.

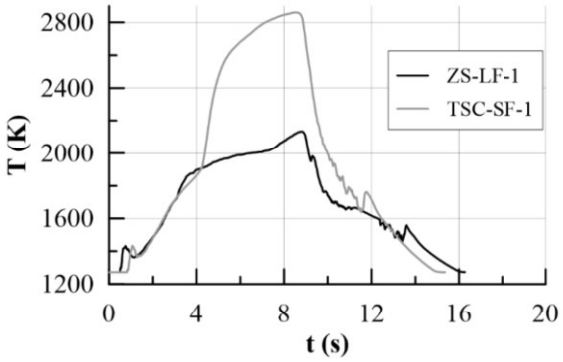

Fig. 5.7. Thermal histories of the two samples tested in test condition 1FJ.

Fig. 5.9a shows four pictures taken by the infrared thermo-camera before and after the temperature jump occurred on sample TSC-SF-1 (the correct value of the NIR spectral emissivity was set using the procedure described in section 2.1). Immediately

before the jump, the temperature on the front surface of the sample was relatively uniform. The temperature jump corresponds to a steep increase in temperature by almost 300 K in 0.5 s, localized in the central region of the surface. This also appears in Fig. 5.9b, showing the temperature radial profiles on the sample surface at different time instants. As already pointed out by numerical simulations, this is the area where the heat flux is most intense and the concentration of molecular oxygen is expected to be higher, so the jump might be associated to triggering, at high temperature, of chemical reactions involving the species contained in the ceramic matrix and/or the carbon fibres; the exothermic release of gaseous products might also justify the change in shape and brightness of the flame surrounding the sample, which was also detected by the thermo-camera, as noticeable in the last two pictures of Fig. 5.9.

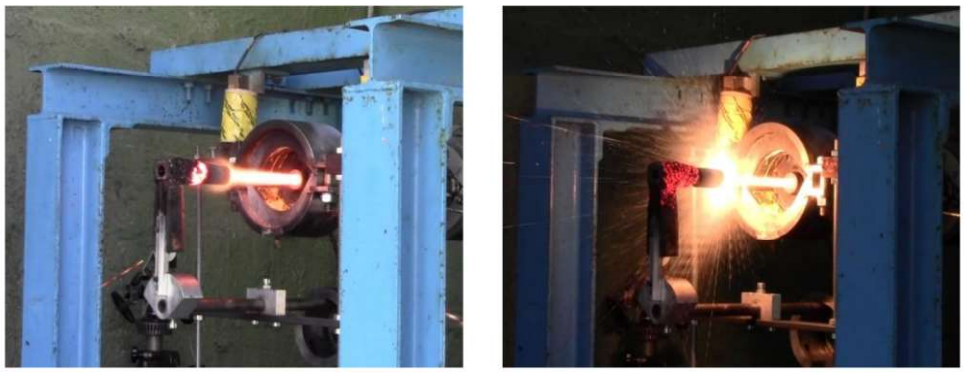

Fig. 5.8. Pictures of test on TSC-SF-1 sample, at beginning (left) and end (right) of the test (test condition 1FJ).

Table 5.9. Mass data before and after the test for samples characterized in test condition 1FJ.

Sample ID	Initial mass	Final mass	Average erosion rate (mass)
ZS-LF-1	7.512 g	7.508 g	$4.3 \cdot 10^{-4}$ mm/s
TSC-SF-1	6.854 g	5.345 g	0.204 mm/s

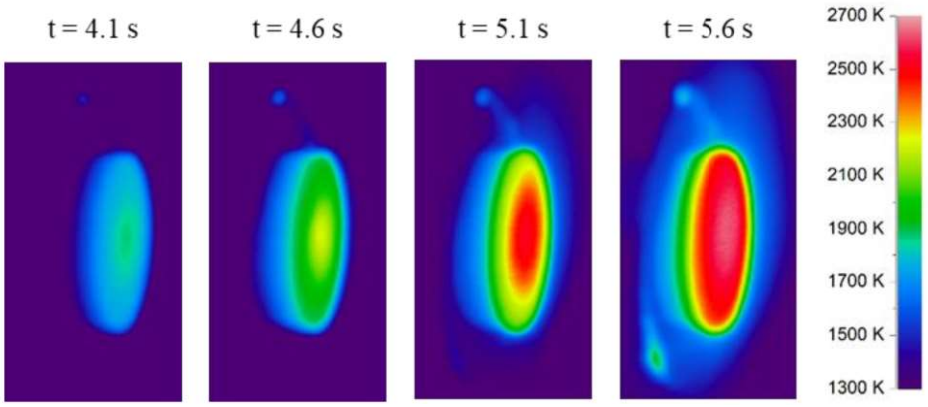

(a)

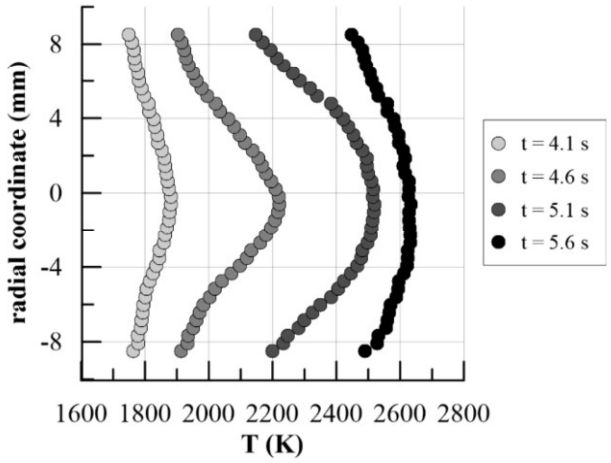

(b)

Fig. 5.9. (a) IR Thermal images of sample TSC-SF-1 at different time instants, around the moment in which the abrupt temperature rise occurred, and (b) corresponding temperature radial profiles.

Finally, Fig. 5.10 and 5.11 show pictures of the two samples before (top) and after (bottom) test, taken by a CCD camera and the optical microscope described in section 2.3. In the pictures taken before the test, the continuous fibre structure of the ZS-LF-1 sample is observable. It is clear that the ZrB_2-SiC-based sample preserved its original shape with no erosion. However, the microscopic observation of the surface revealed the presence of a thin, irregular white layer, after the test, presumably associated to oxidation of zirconium contained in the sample matrix. The titanium silicocarbide-

based sample, on the contrary, eroded significantly, and the exposed surface appears to be almost completely oxidized.

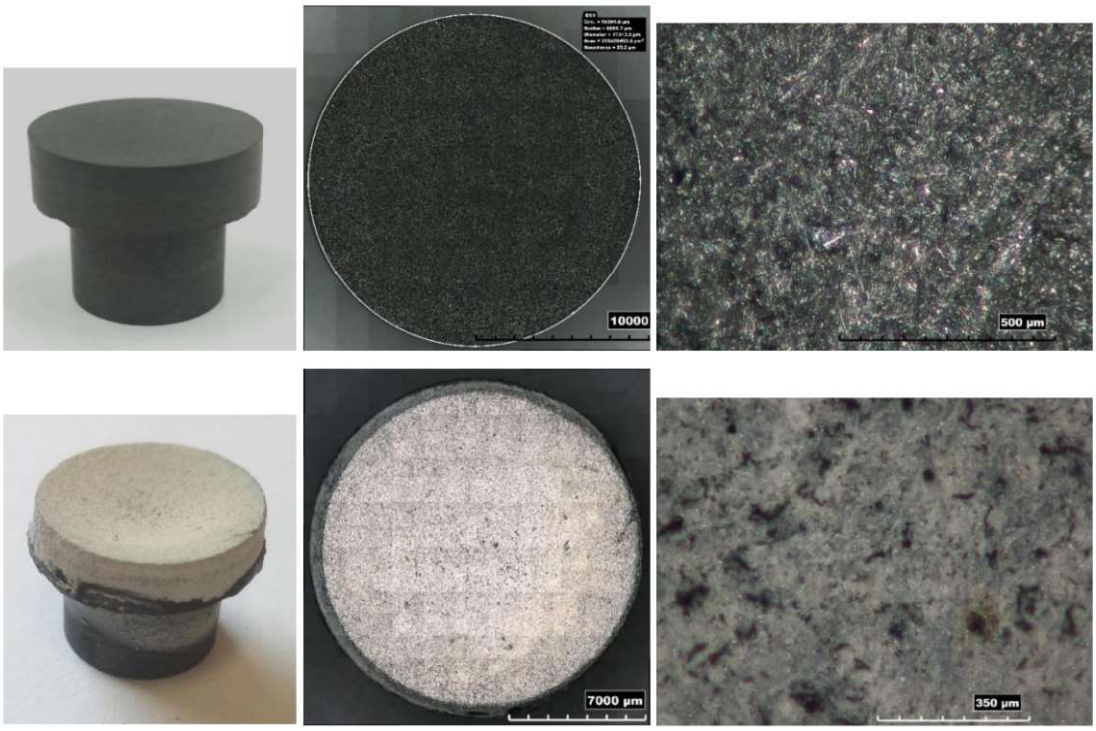

Fig. 5.10. Pictures of sample TSC-SF-1 before (top) and after (bottom) the test.

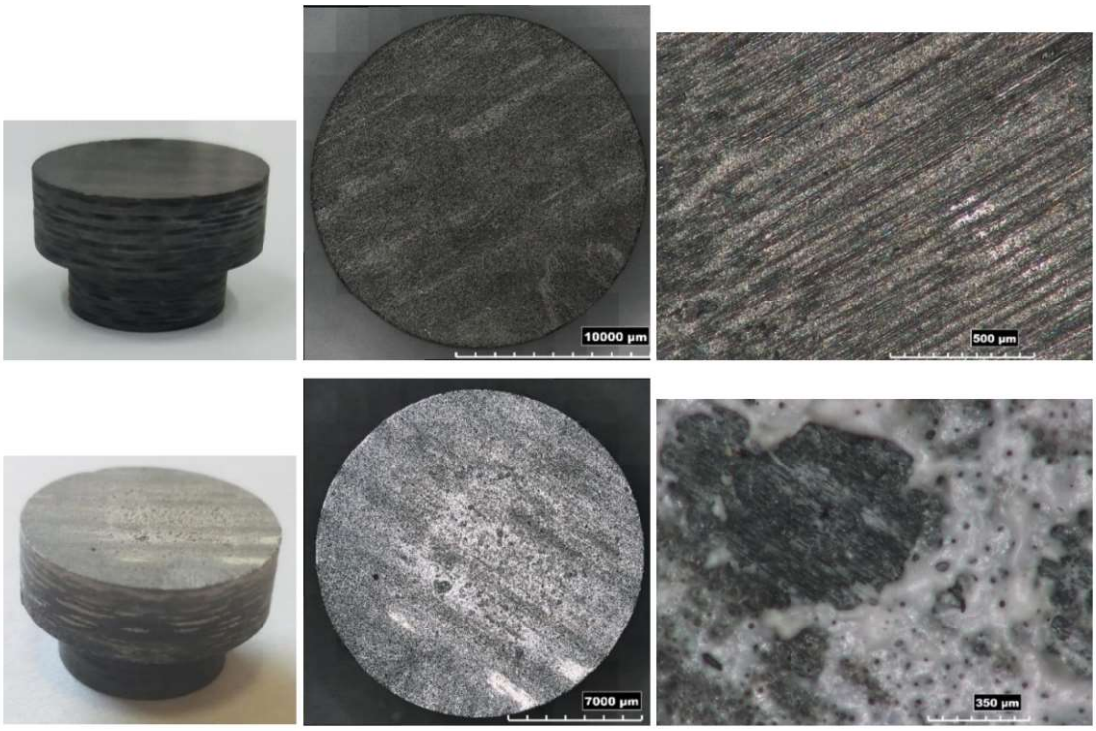

Fig. 5.11. Pictures of sample ZS-LF-1 before (top) and after (bottom) the test.

As a validation of the numerical models used for the simulation of the test conditions, the flow field solution presented in section 5.1.1 has been coupled to the thermal analysis of the sample, assuming as a reference test case that of specimen ZS-LF-1, which exhibited both stable dimensions and almost null oxidation. A mesh of the solid components was realized and the transient solution of the energy equation inside the solid domain was calculated, coupling it to the evolving solution of the fluid field by imposing temperature and heat flux continuities at the interfaces, as described in section 3.3. The density of the sample was set to 4300 kg/m^3, based on mass and volume measurements. The specific heat was set to 1100 J/(kg·K), according to a rule of mixture also employed in [30] for the numerical simulation of the thermal behaviour of a nozzle-throat insert with a similar composition. The thermal conductivity was set to 20 W/(m·K) and the surface emissivity was 0.85. The time history of the maximum surface temperature calculated by CFD is shown in Fig. 5.12, where the very good agreement with the experimental measurement made by ISQ5 pyrometer is observable.

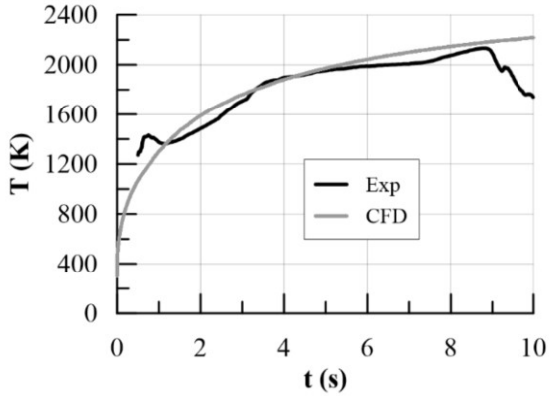

Fig. 5.12. Temperature history of maximum surface temperature of sample ZS-LF-1, comparison between experimental and numerical results.

5.2.3 Tests in condition 2FJ

Three tests were carried out in condition 2FJ. All samples had a ZrB_2-SiC matrix. Two of them (ZS-LF-2 and ZS-LF-3) had a long-fibre architecture and the other one (ZS-SF-1) a short-fibre architecture. Measured oxidizer mass flow rate was 31 g/s in all the test, whereas the time-averaged combustion chamber pressure was about 6.5 bar. Fig. 5.13 shows the time history of the maximum temperature reached by the

samples, detected by the ISQ5 pyrometer, operated in two-colour mode. Although the test conditions were the same, the final temperature reached by the sample ZS-LF-3 was over 400 K lower than that reached by the other two samples. In fact, after 4-5 s, the temperature of ZS-LF-2 and ZS-SF-1 started rising more rapidly, reaching in the end values over 2800 or even 2900 K. In the final part of the test, after the sudden temperature jump, solid fragments were wiped off the samples surfaces by the oncoming supersonic flow, as visible in Fig. 5.14, showing, as an example, pictures recorded by the optical camera at the beginning and at the end of test on sample ZS-LF-2. A similar phenomenon was observed for the short-fibres sample, whereas no instability was detected in the case of ZS-LF-3, which preserved stable mass and dimensions. The erosion data, based on mass measurements before and after test, are summarized in Table 5.10.

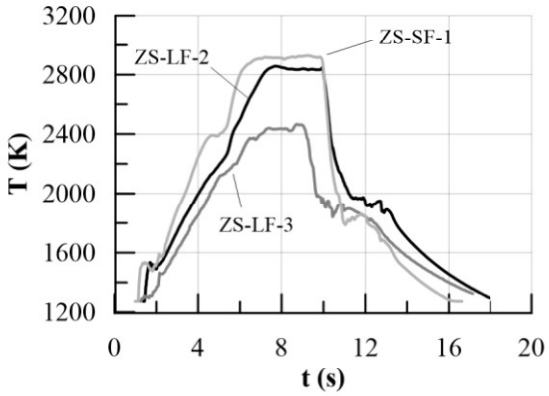

Fig. 5.13. Thermal histories of the free-jet samples tested in condition 2FJ, recorded by the ISQ5 pyrometer.

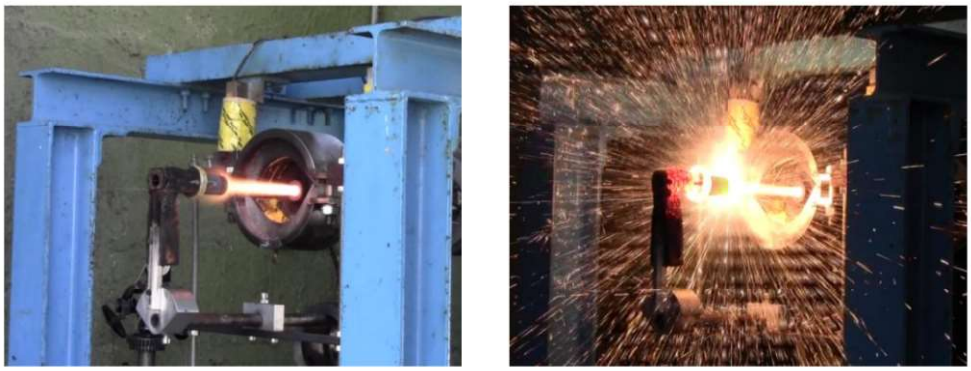

Fig. 5.14. Pictures of test on ZS-LF-2 sample, before (left) and after (right) the temperature jump.

Table 5.10. Mass data before and after the test for samples characterized in test condition 2FJ.

Sample ID	Initial mass	Final mass	Average erosion rate (mass)
ZS-LF-2	7.130 g	5.784 g	$2.3 \cdot 10^{-4}$ mm/s
ZS-LF-3	7.429 g	7.427 g	0.154 mm/s
ZS-SF-1	7.928 g	6.523 g	0.180 mm/s

(a) ZS-LF-2 **(b) ZS-LF-3**

(c) ZS-SF-1

Fig. 5.15. Pictures of samples (a) ZS-LF-2, (b) ZS-LF-3 and (c) ZS-SF-1 before (top) and after (bottom) the test.

Fig. 5.15 shows pictures of the three samples before (top) and after (bottom) the test. All of them appeared oxidized after exposure to the supersonic flame, but, whereas the oxide layer of ZS-LF-3 survived the thermo-mechanical load, preserving structural integrity, the ZS-LF-2 and ZS-SF-1 underwent notable shear stresses and their shape was consistently modified upon achieving temperature peaks of 2860 and 2930 K, respectively. A valley formed in the ZS-LF-2, Fig. 5.15a, whilst the FJ-SF-1 ended with a lateral squashing, Fig. 5.15c, possibly due to a slight misalignment that resulted fatal under the high thermo-mechanical loads.

A detailed analysis of the thermographic images was carried out for sample FJ-LF-1, to better understand the mechanism observed during the jump, which led to the high erosion rate. First, the sample spectral emissivity had to be estimated. The result is presented in Fig. 5.16, where it is shown that in the earliest stages of the test, the emissivity had a steep increase to values up to 0.9, then slightly decreased to 0.8, and finally, when the jump was triggered, it appeared to increase again, keeping, in the final part of the test, values close to a black body radiator. Applying the corresponding correct values of ε_λ, some images were extracted from the IR-TC. Specifically, Fig. 5.17a shows the temperature distribution over the sample surface at different time instants, around the moment in which the abrupt temperature rise occurred, and Fig. 5.17b reports the corresponding temperature radial profiles.

The figure highlights that the temperature started rising suddenly in a localized region in the centre of the surface, progressively spreading its area. As already stated in the previous section, and as highlighted above by numerical simulations, this is the area where the heat flux was most intense and the concentration of molecular oxygen was expected to be higher, so the jump might be associated to triggering, at high temperature, of a consistent sample oxidation; the porosity left by depletion of carbon fibres and the characteristic low thermal conductivity of oxidized phases such as ZrO_2 [128,133] (whose presence was highlighted by post-test SEM analysis carried out at CNR-ISTEC, not shown for the sake of brevity), together with the peaked distribution of heat flux along the surface, might have favoured the steep increase in temperature in the central area, therefore fostering considerable thermo-mechanical erosion. The corresponding increase in the spectral emissivity could be therefore associated to the

formation of a cavity, whose radiative properties might have got closer to those of a perfect black body.

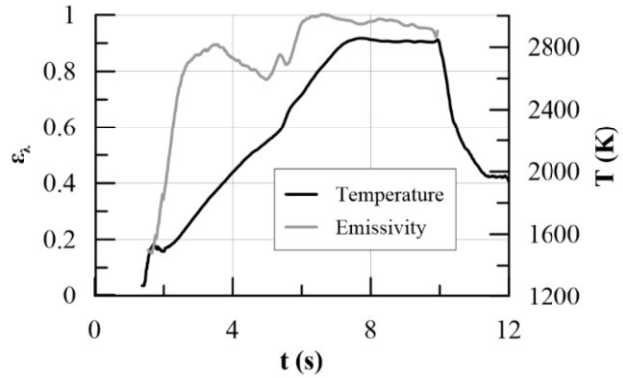

Fig. 5.16. Near-infrared spectral emissivity of sample ZS-LF-2 during the heating phase of the test, compared with the temperature measured by the ISQ5 pyrometer.

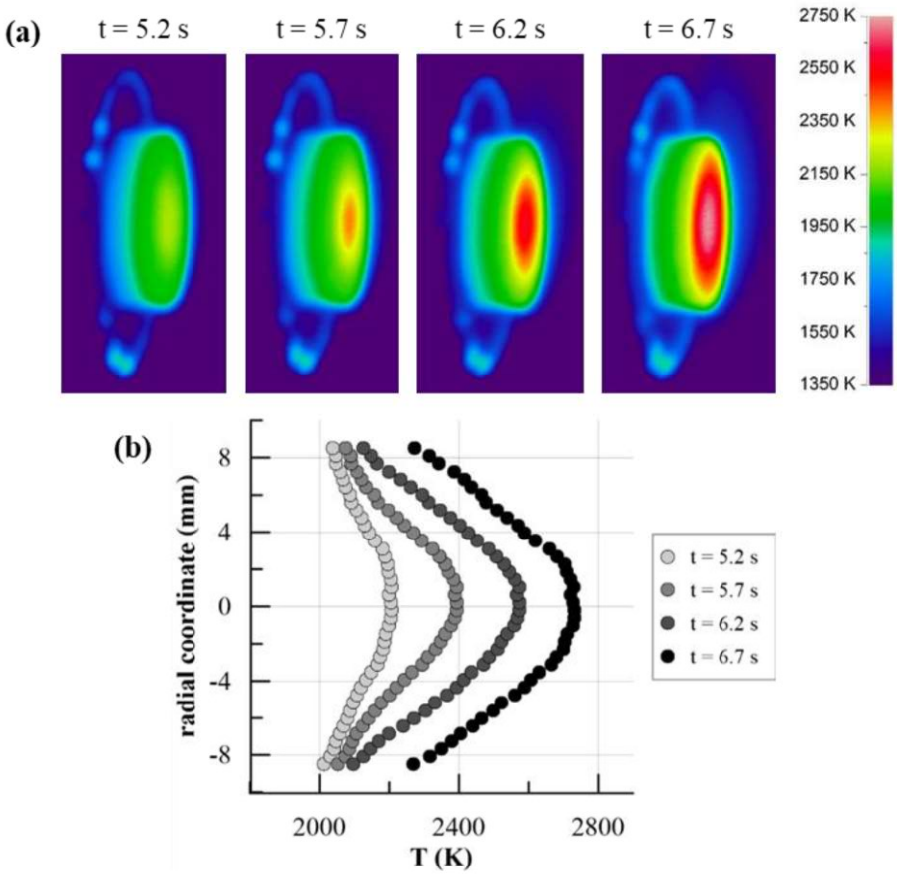

Fig. 5.17. (a) IR Thermal images of sample ZS-LF-2 at different time instants, around the moment in which the abrupt temperature rise occurred, and (b) corresponding temperature radial profiles.

5.2.4 Tests in condition 3FJ

Finally, in this section the tests performed in condition 3FJ are presented. The three samples (TSC-SF-2, ZS-LF-4 and ZS-SF-2) had different matrix compositions and fibre architectures. Fig. 5.18 shows the time history of the maximum temperature reached by samples, which all exhibited the thermal jump reaching a maximum temperature around 2900 K.

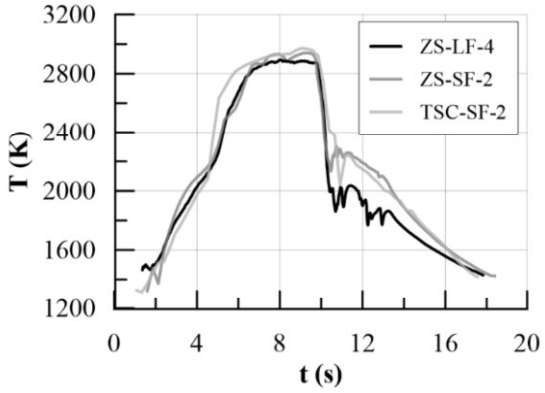

Fig. 5.18. Thermal histories of the free-jet samples tested in condition 3FJ.

As it can be seen from Table 5.11, where the mass data before and after the tests and the corresponding average erosion rates are summarized, again the thermal jump was associated to a significant sample erosion. Anyway the ZrB_2-based samples showed a better behaviour, with erosion rates significantly lower than that of the Ti_3SiC_2-based sample. This is evident also from Fig. 5.19 and 5.20, which show CCD and microscope pictures of TSC-SF-2 and ZS-LF-4 samples after the test.

Table 5.11. Mass data before and after the test for samples characterized in test condition 3FJ.

Sample ID	Initial mass	Final mass	Average erosion rate (mass)
ZS-LF-4	7.398 g	5.710 g	0.183 mm/s
ZS-SF-2	8.262 g	6.986 g	0.166 mm/s
TSC-SF-2	6.951 g	4.281 g	0.360 mm/s

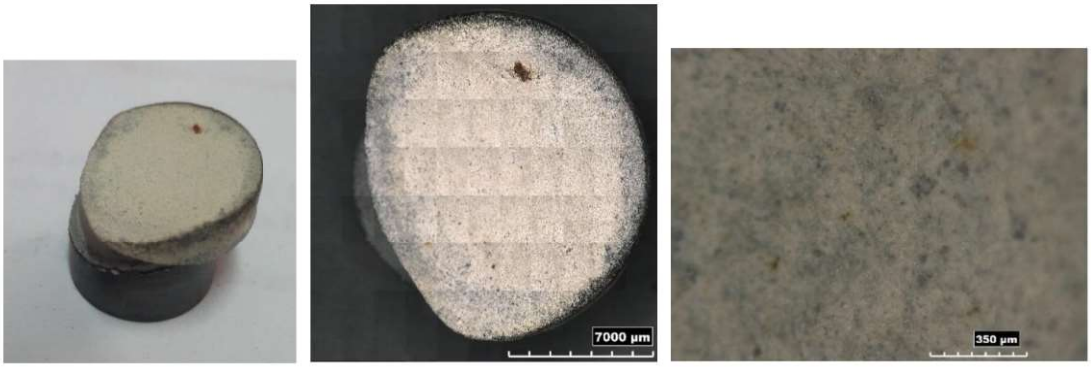

Fig. 5.19. Pictures of sample TSC-SF-2 after the test.

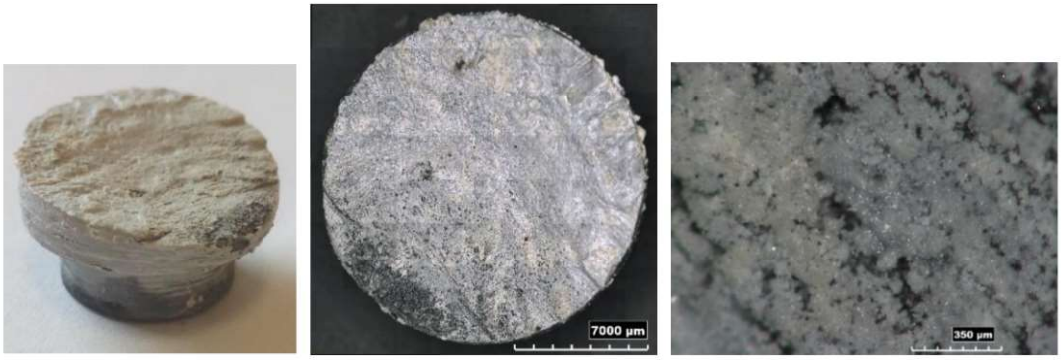

Fig. 5.20. Pictures of sample ZS-LF-4 after the test.

5.2.5 Conclusions of free-jet tests

Fig. 5.21 shows the samples equivalent average erosion rates, evaluated by means of mass measurements before and after test. Data are also compared to that related to the test of a graphite sample, used as a reference material, and tested in a condition similar to 2FJ.

It appears that all the UHTCMC samples have a better erosion resistance with respect to a classical graphite material. Anyway, the Ti_3SiC_2-based CMCs showed unacceptable rates of erosion while the formulations based on ZrB_2-SiC matrix showed significantly higher performance. Moreover, two samples among those based n ZrB_2-SiC matrix, specifically having long fibres and having being sintered by HP, were the best, being the only ones which were not subjected to significant erosion in test conditions 1FJ and 2FJ.

Finally, it was observed that when significant erosion occurred on UHTCMC samples, the material experienced also a sudden rise in temperature (temperature jump) of several hundred degrees, reaching temperatures up to 2800-2900 K, and solid fragments wiped off the surface of the samples by the oncoming supersonic flow. The jump has been associated to the formation of a poorly conductive oxide phase (which prevents an effective distribution of the incoming heat to the whole sample volume), exhibiting moreover poor structural performance, resulting in the high erosion under the significant aerothermodynamic loads.

It needs however to be remarked that also the ablation rate of the ZrB_2-SiC-based samples that underwent erosion was over 2 times lower than that of graphite, increasing the confidence in the fact that an optimized formulation of ZrB_2-SiC-based materials, with a manufacturing process able to provide the ceramic with sufficient mechanical properties even upon oxidation, could be a significant improvement with respect to state-of-art materials.

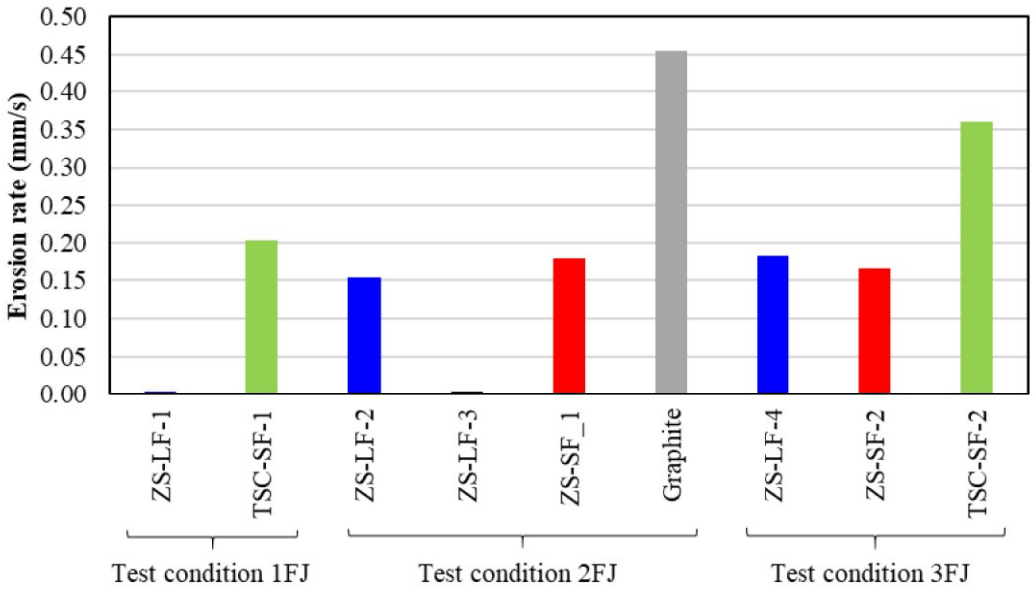

Fig. 5.21. Erosion rates of free-jet test samples.

5.3 Experimental results in chamber insert configuration

5.3.1 UHTCMC samples

This section summarizes the results of the tests performed on chamber inserts. Four prototypes, with different matrices and carbon fibres architectures, were provided by the C^{3}HARME project partners.

AIRBUS CRT provided a non-coated, flat plate made of C/SiC, which was processed using the Polymer-Infiltration-Pyrolysis (PIP) process without further re-infiltration. It was machined by UNINA to obtain the flat disk sample and tested as a reference material without specific modifications to improve the oxidation resistance.

CNR provided samples based on ZrB_2-SiC matrix (in a volume ratio of 90/10%), with different carbon fibres architectures, sintered either by HP or SPS, the latter manufactured in collaboration with the Spanish company NANOKER.

Table 5.12 summarizes the most important information about all the samples tested, including their composition, manufacturing process, porosity and the test conditions experienced in the combustion chamber of the hybrid rocket.

Samples surfaces were observed before and after test by the digital microscope described before, while a precision calliper (0.01 mm accuracy) was used to measure the initial and final diameters of the insert transversal section and calculate the average erosion rate.

Table 5.12. Samples for chamber insert test.

Sample ID	Matrix	Carbon fibres	FVC	Densif.	Porosity	Test condition
C-SiC	SiC	Long	33	PIP	25%	1CI (Test 1) 2CI (Test 2)
ZS-LF-1	ZrB_2-SiC	Long UD 0°/45°/90°	45	SPS	<1%	1CI
ZS-LF-2	ZrB_2-SiC	Long UD 0°/45°/90°	45	HP	15%	2CI
ZS-SF	ZrB_2-SiC	Short	45	SPS	<1%	2CI

5.3.2 Test results

Five tests were carried out, either in condition 1CI or 2CI: the measured oxidizer mass flow rates were 25.3 g/s and 40.4 g/s, whereas the time-averaged combustion chamber pressures were about 6.3 bar and 8.6 bar, respectively.

Starting from the C/SiC chamber insert, it was tested twice, first in condition 1CI and then in condition 2CI. Fig. 5.22 shows the pictures of the sample before and after each test, where the surface exposed to the flame is clearly observable, as well as the enlargement of the transversal section, whose diameter increased from the initial value of 15 mm to a final value of around 20.6 mm after the tests, Fig. 5.22d. Moreover, also for what concerns the structural resistance, although no cracks were detected, a delamination of parts of the first layer was found, as it can be seen from Fig. 5.22b. The low value of interlaminar shear strength of these CMCs is well known in the literature [11].

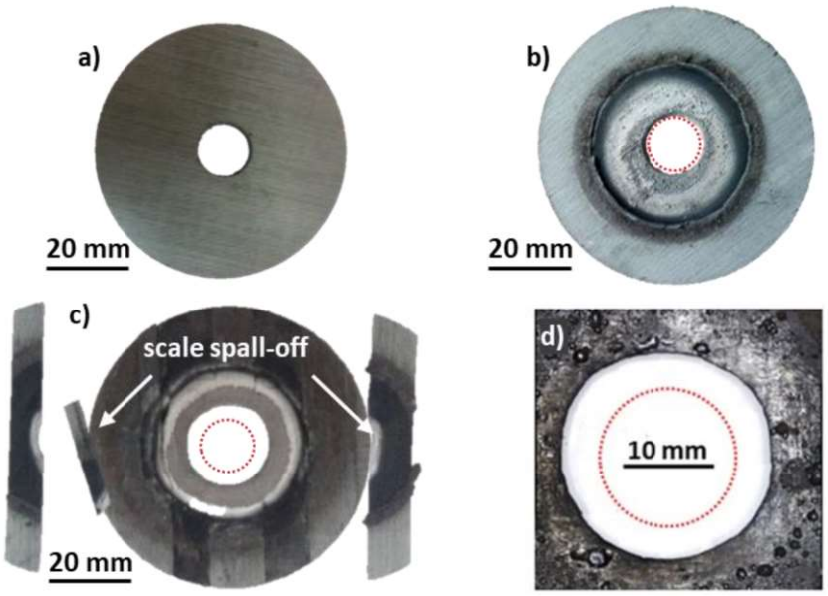

Fig. 5.22. Pictures of a chamber insert made of conventional C/SiC: a) before test; b) after test 1 (condition 1CI); c) after test 2 (condition 2CI), showing oxide spall-off; d) zoom of the central throat. The dotted line in b), c) and d) marks the original throat diameter.

For what concerns the UHTCMC chamber inserts, Fig. 5.23, 5.24 and 5.25 show respectively pictures of ZS-LF-1, ZS-LF-2 and ZS-SF chamber inserts before and after

test. After the test the ZS-LF-2 chamber insert presented visible oxidation on the surface exposed to the reacting flow, whilst the internal hole surface did show neither significant material erosion, nor structural failures, but only little deposit and surface roughening, Fig. 5.24b&c. On the other side, ZS-LF-1 and ZS-SF samples were subjected to structural cracks, which in the latter case, corresponding to the harshest test conditions, led to leakage of the combusting gases determining critical damages also to the engine, Fig. 5.25. Anyway, it is worth to note that, besides the zones around the crack, the internal surfaces of the hole did not show significant material erosion for both samples.

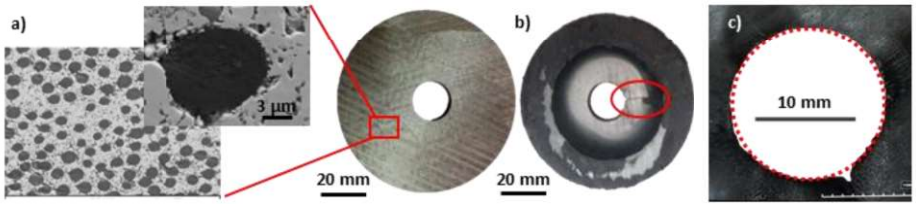

Fig. 5.23. Pictures of the ZS-LF-1 chamber insert a) before and b), c) after test (condition 1CI) showing no erosion of the central throat. Microstructural details of the pristine material are shown in a).

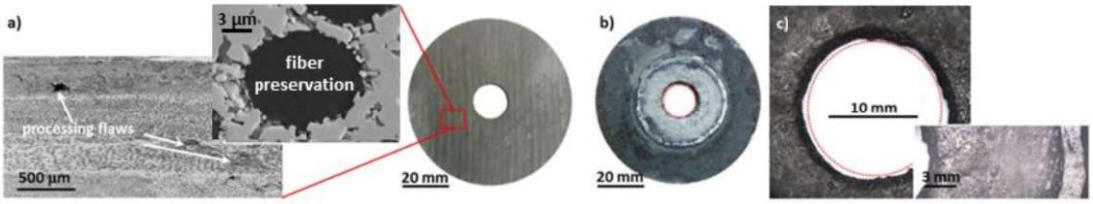

Fig. 5.24. Pictures of the ZS-LF-2 chamber insert a) before and b), c) after test (condition 2CI) showing no erosion of the central throat. Microstructural details of the pristine material are shown in a).

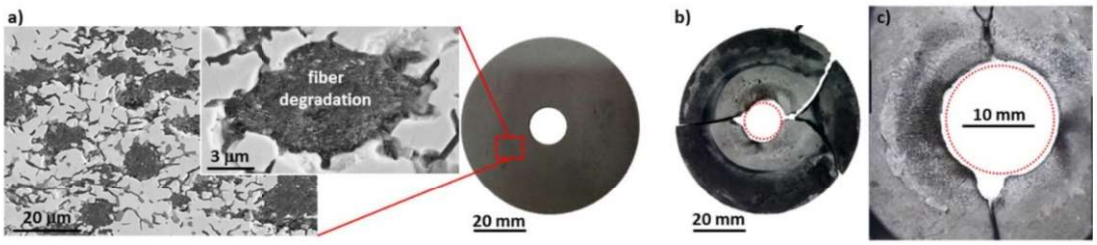

Fig. 5.25. Pictures of the ZS-SF chamber insert a) before and b), c) after test (condition 2CI). Microstructural details of the pristine material are shown in a).

The diverse behaviour of the chamber inserts can be ascribed to the thermal shock resistance of the starting material, i.e. in the case of the long-fibre samples, only when about 15% porosity was left after sintering no structural damage occurred. Accordingly, the material with short fibres (which provide weaker mechanical reinforcement), having a fully dense matrix and whose fibres integrity had been compromised during sintering, behaved as a brittle ceramic and shattered.

Therefore, the results described above confirm the fact that the ZrB_2-SiC-based UHTCMC are characterized by outstanding erosion resistance, provided that sufficient porosity is left to guarantee enough thermal shock tolerance.

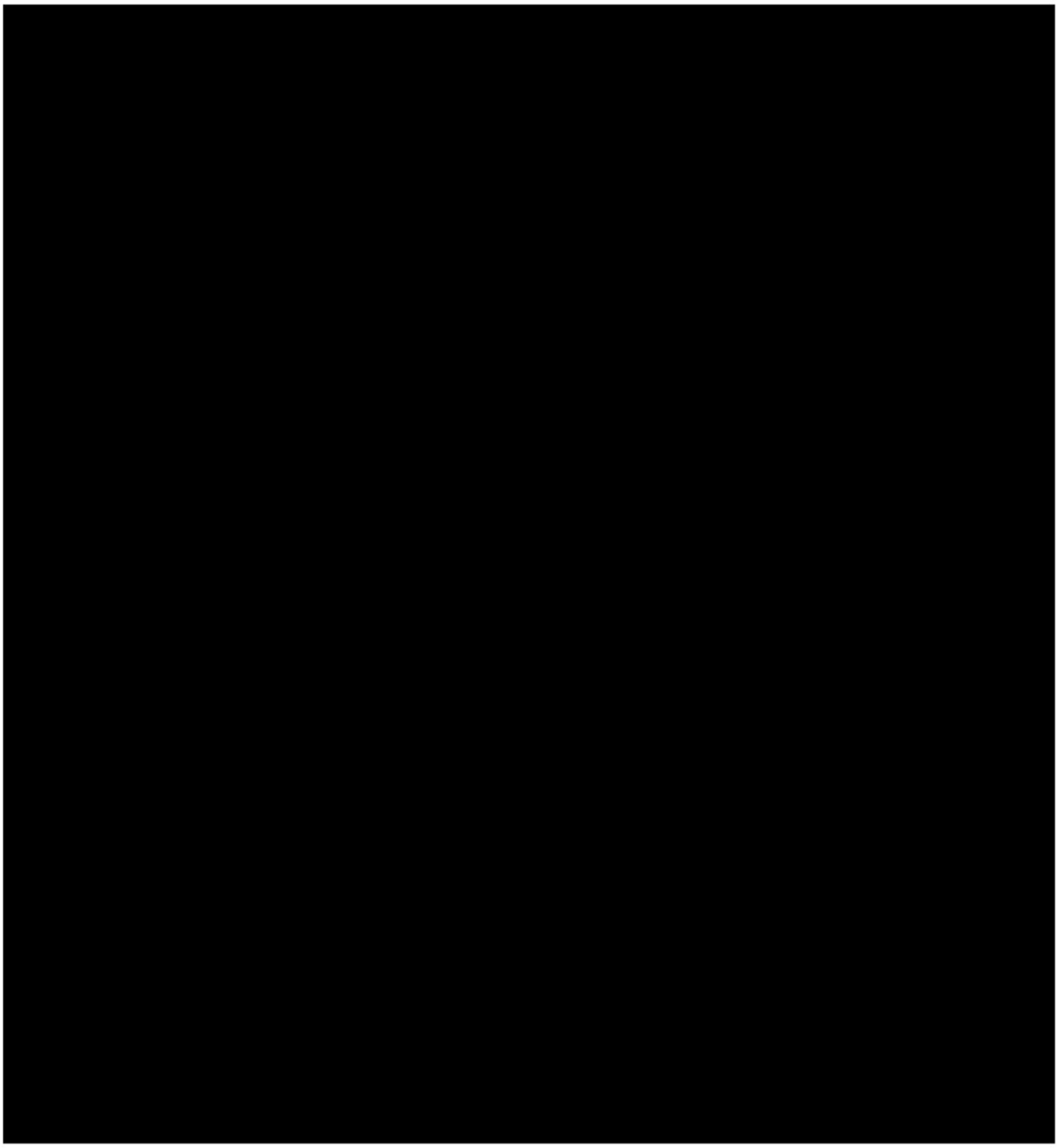

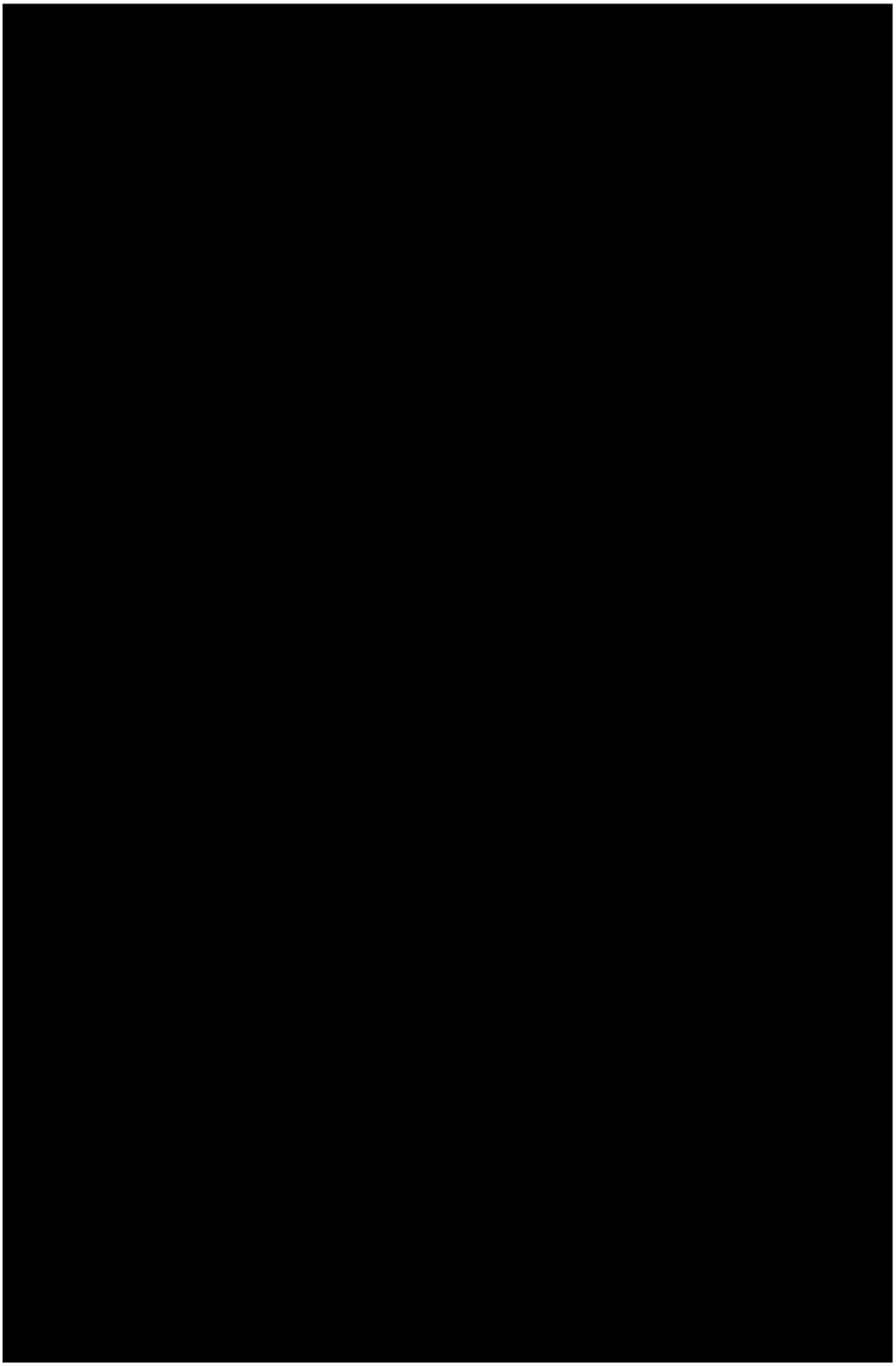

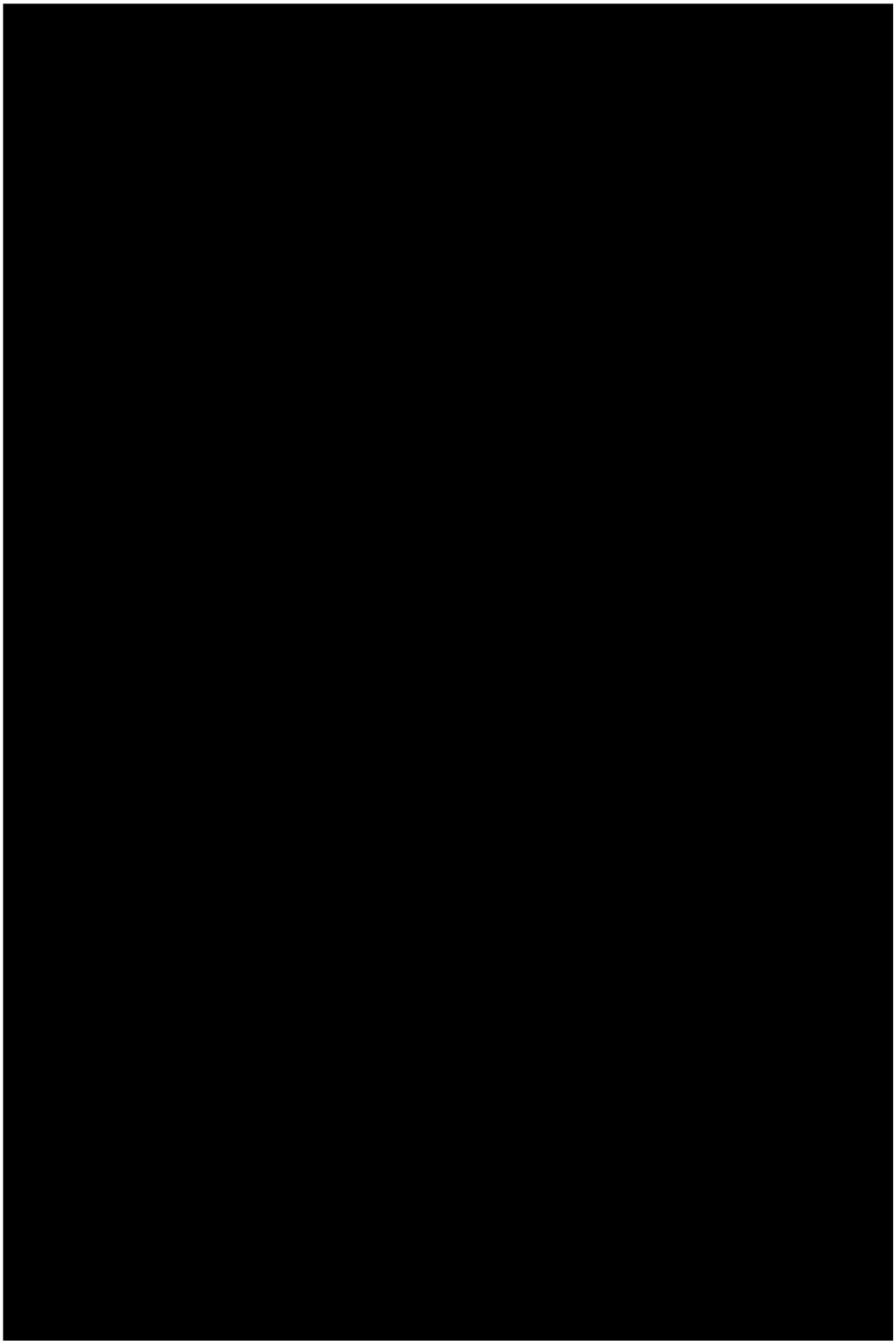

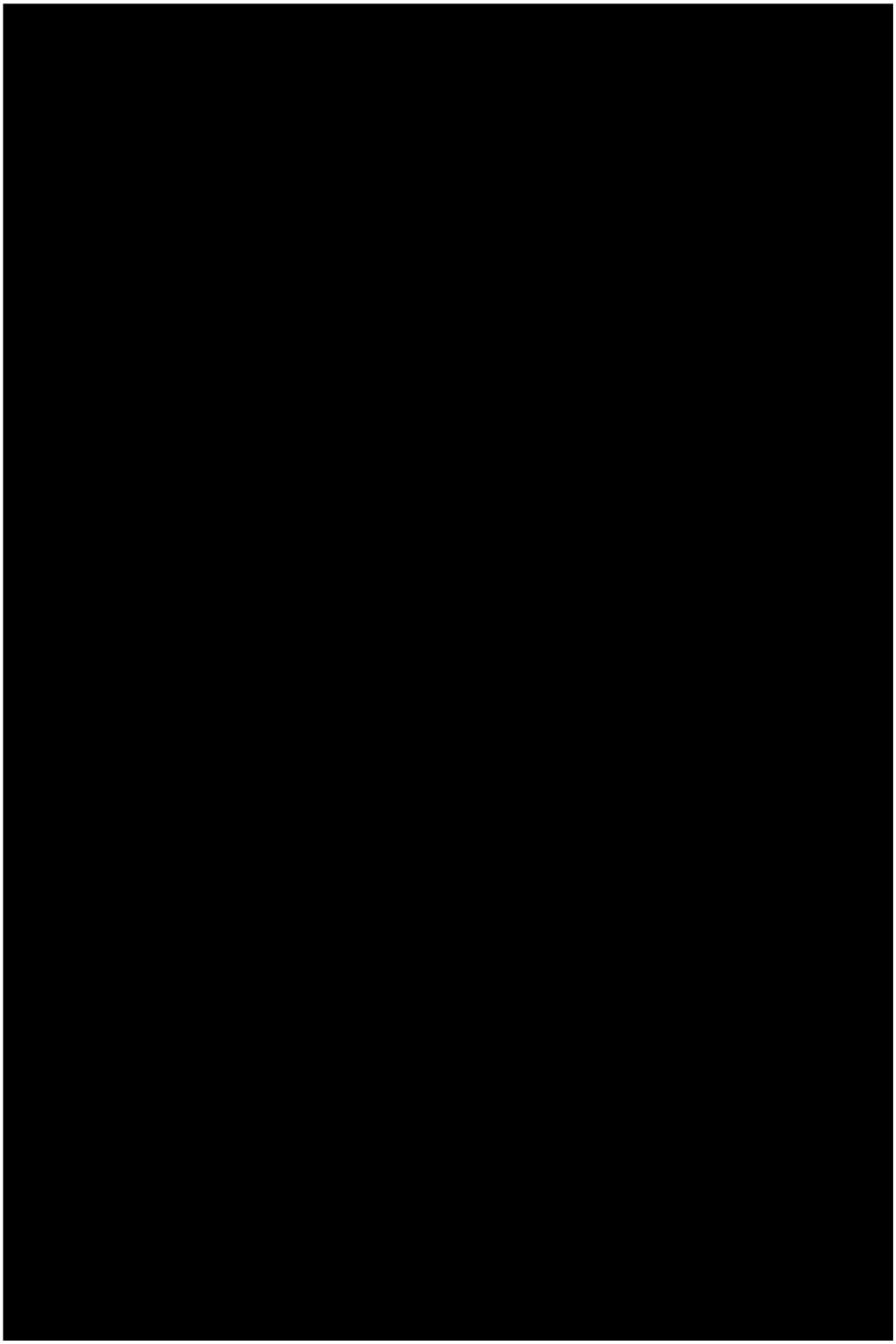

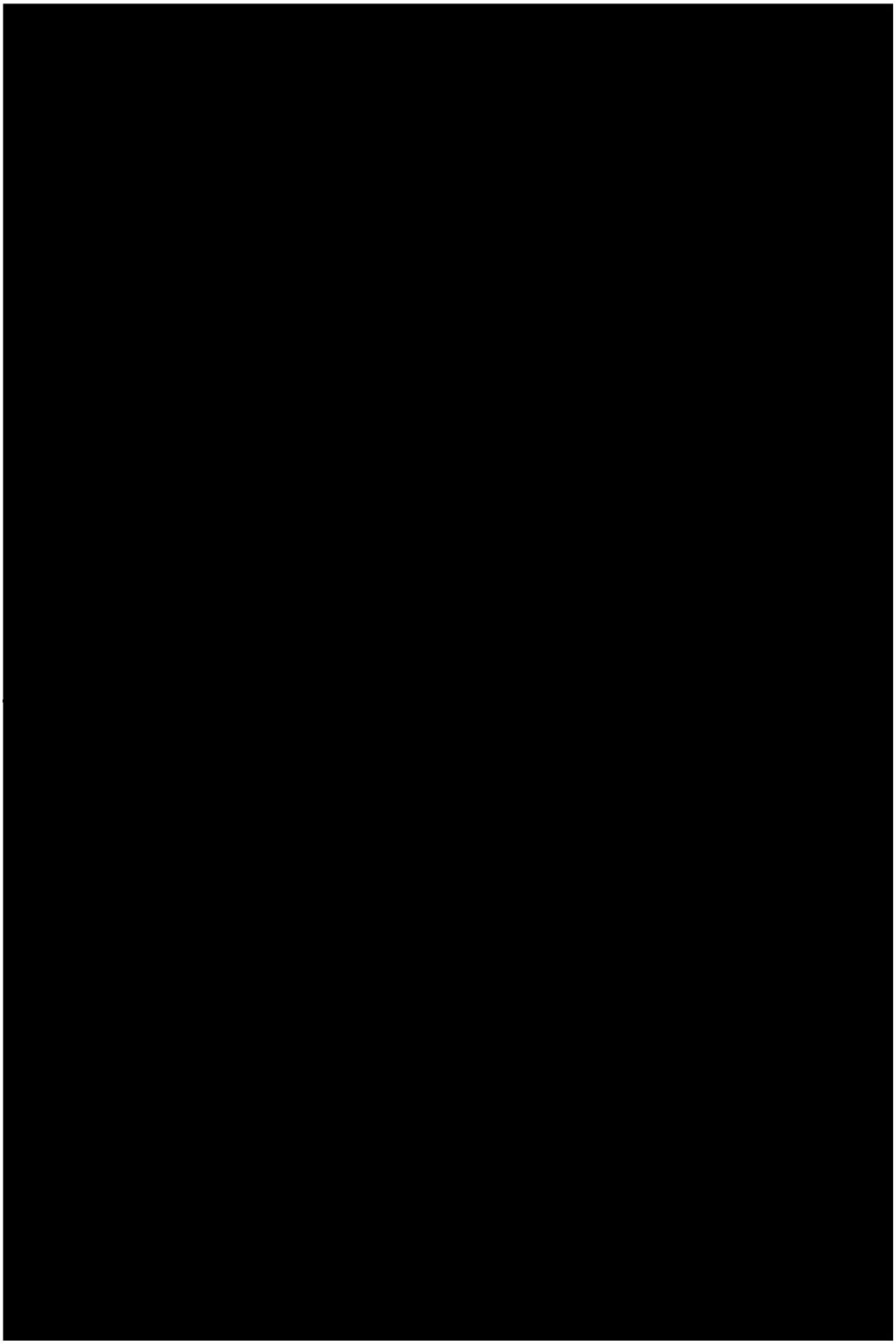

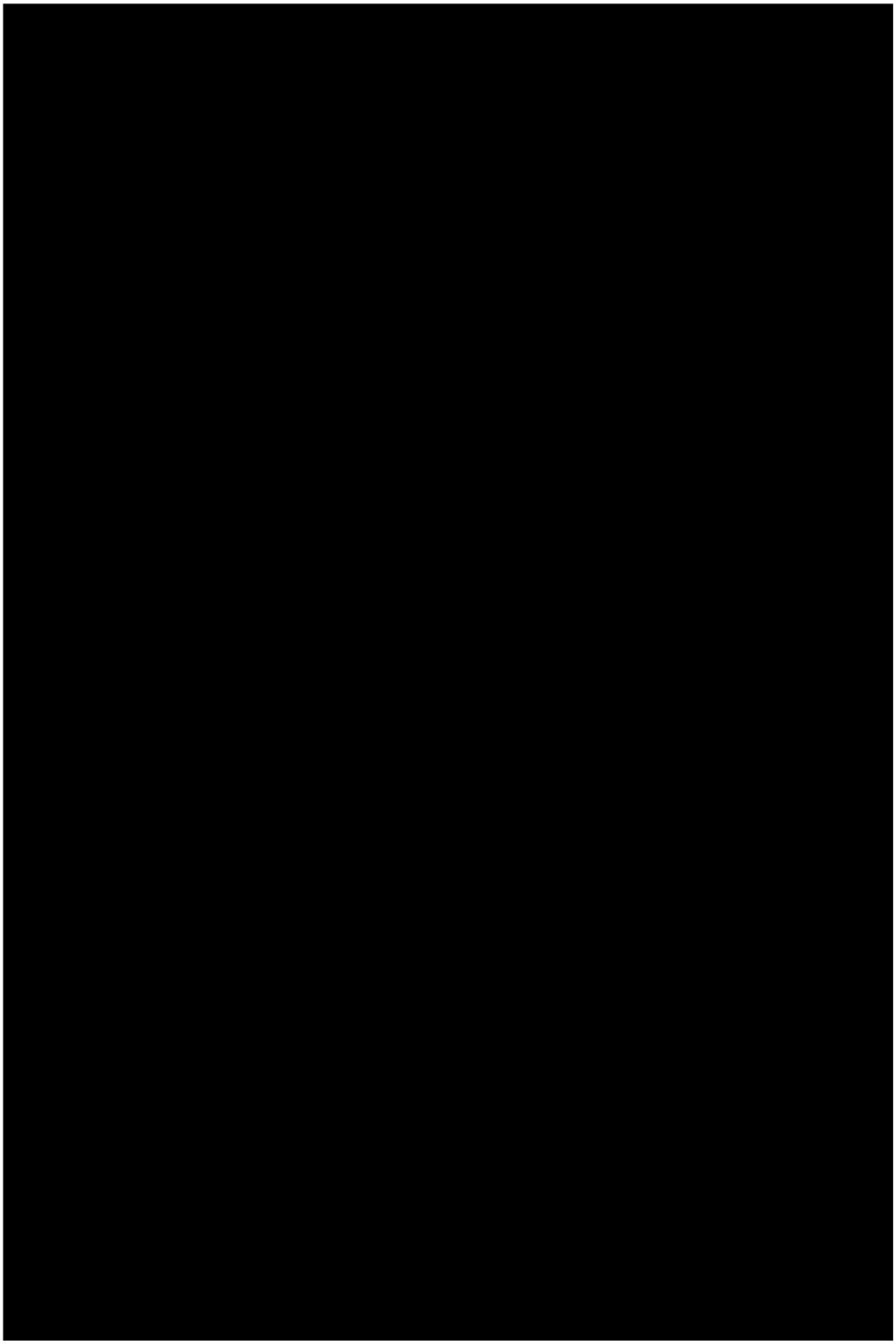

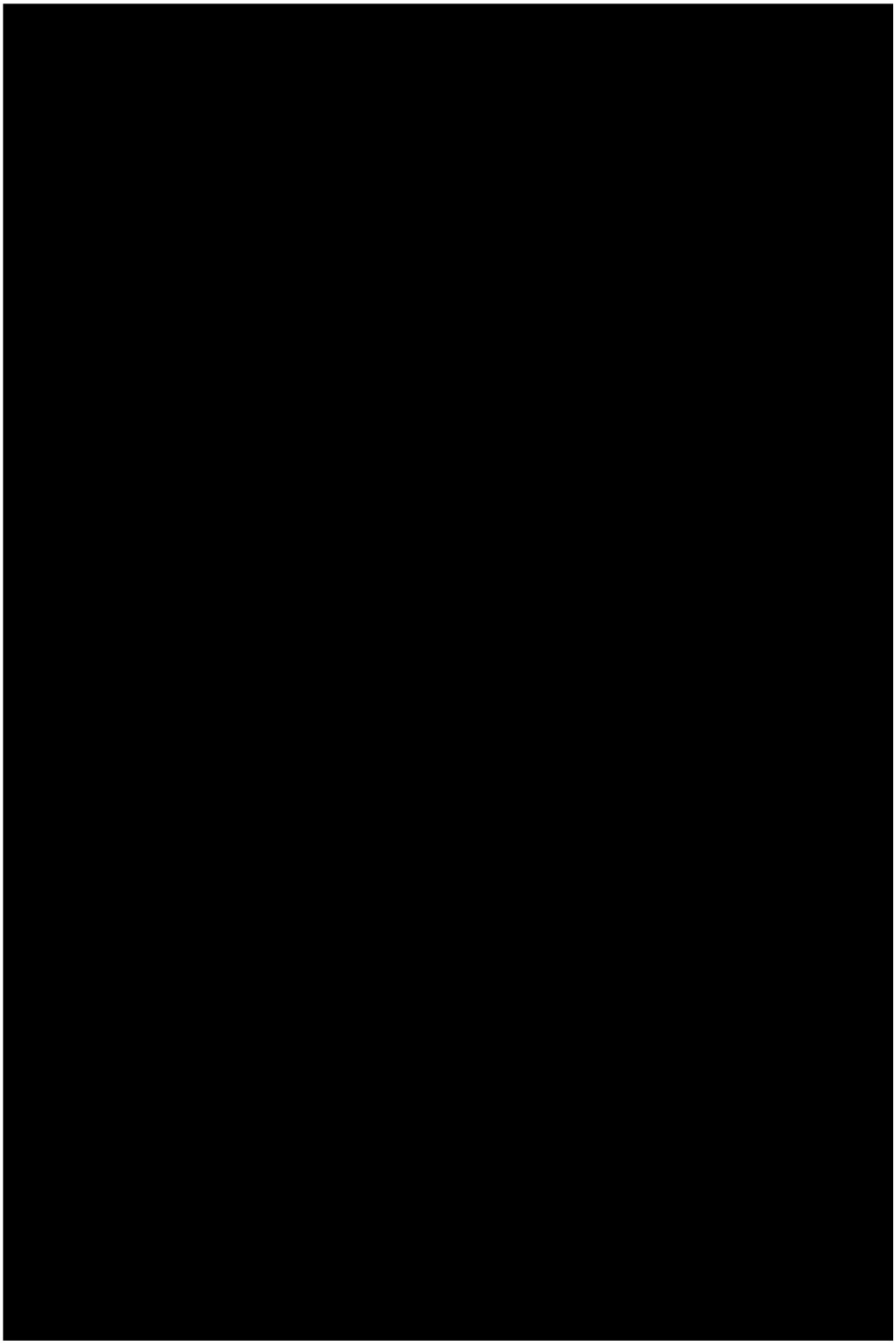

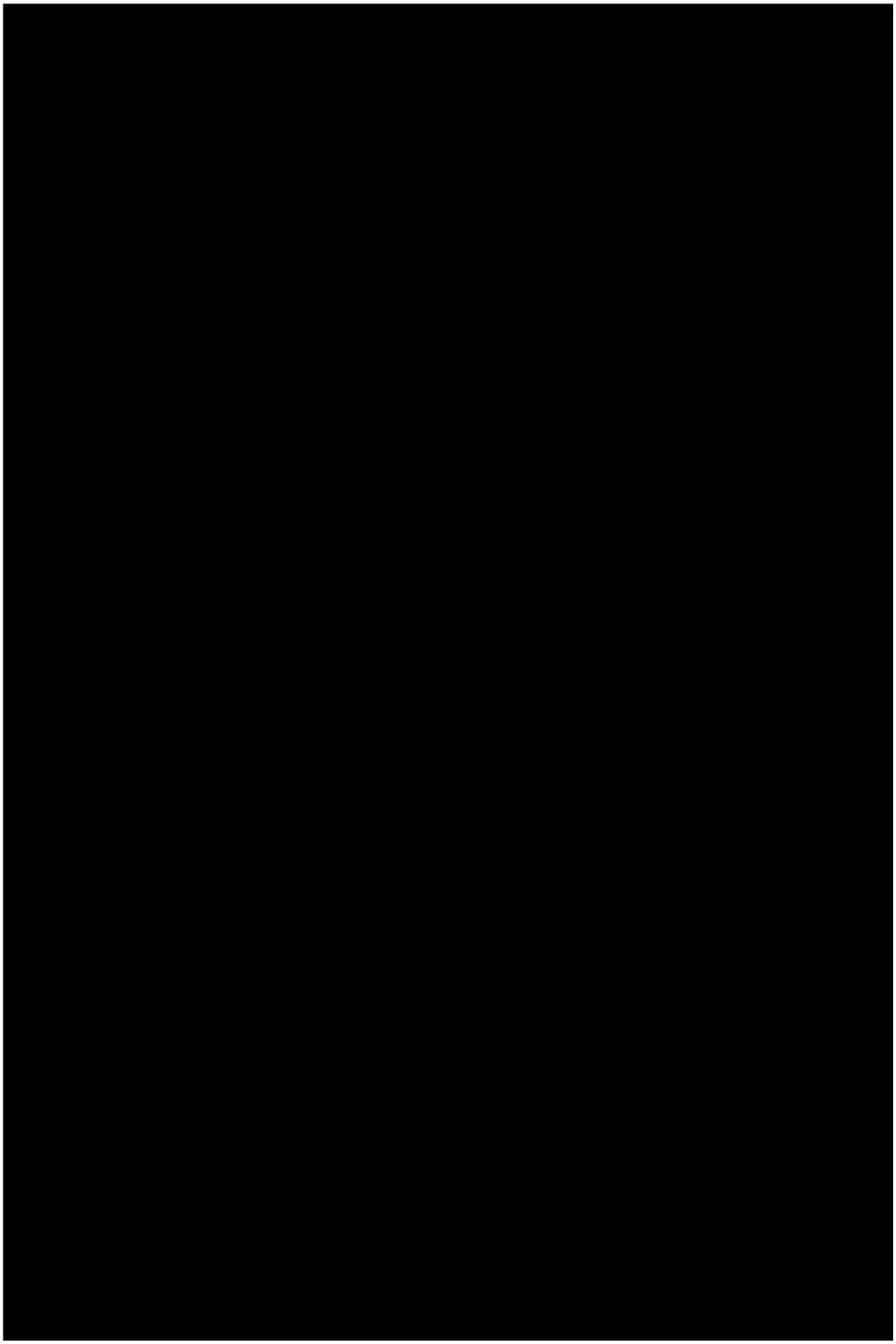

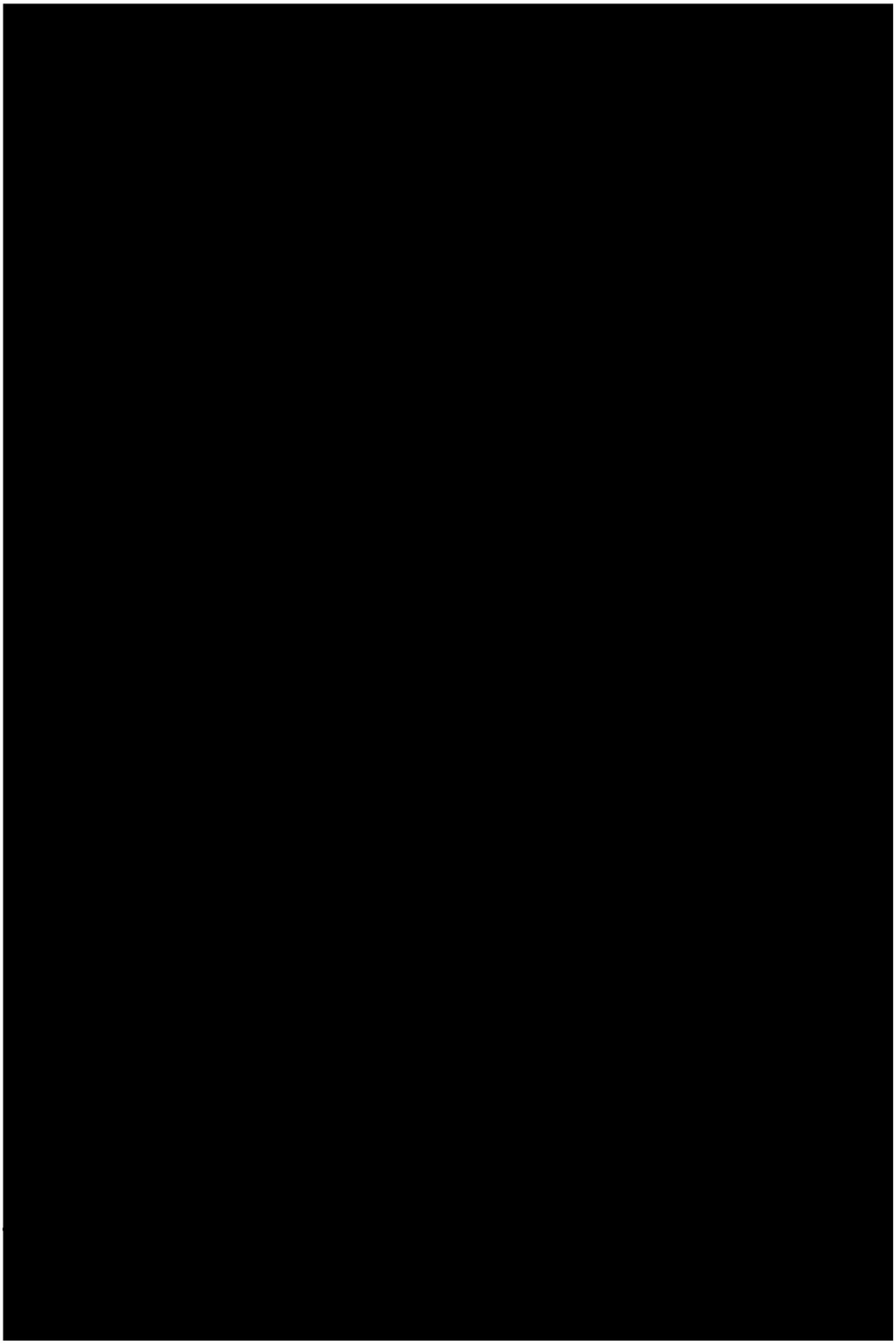

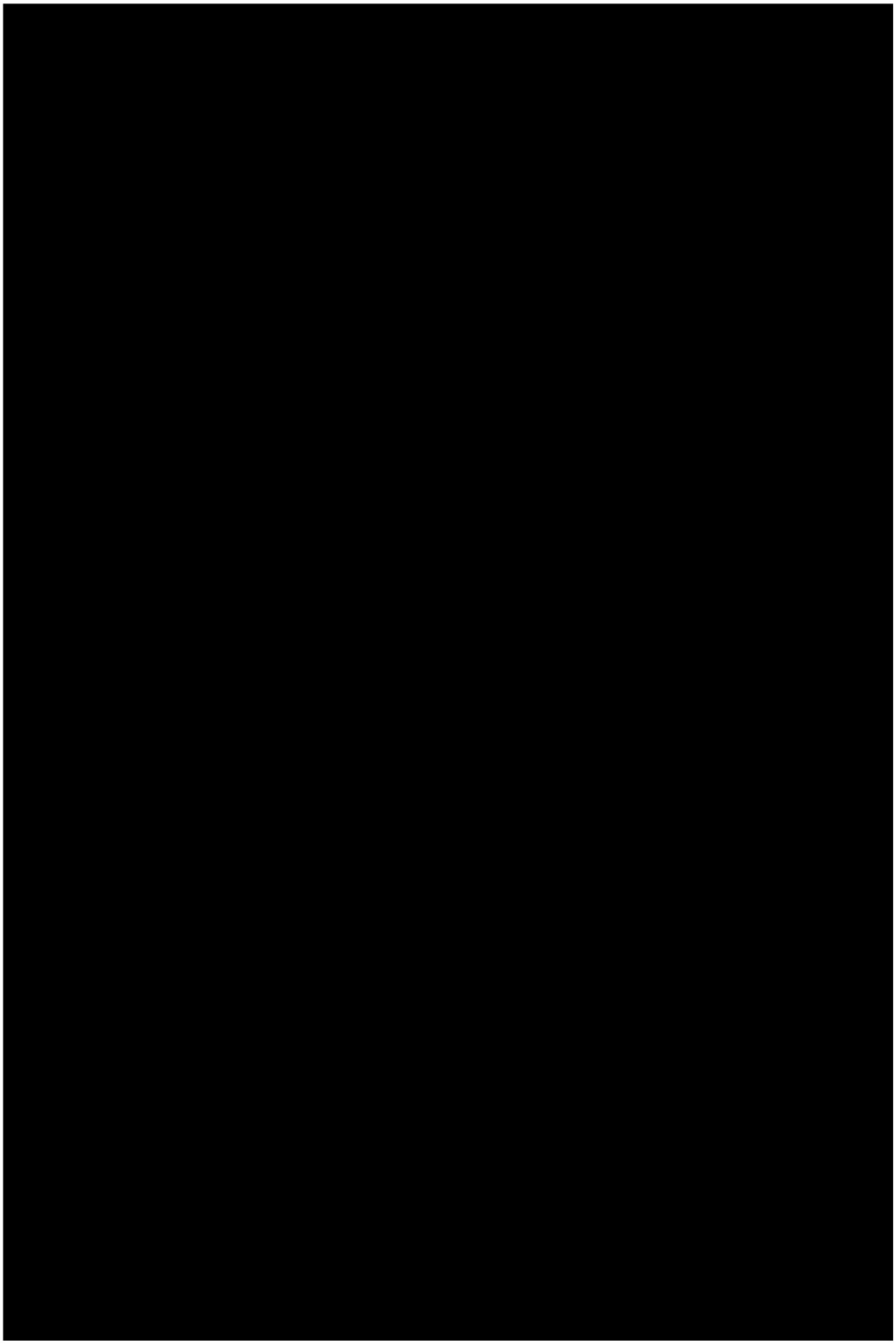

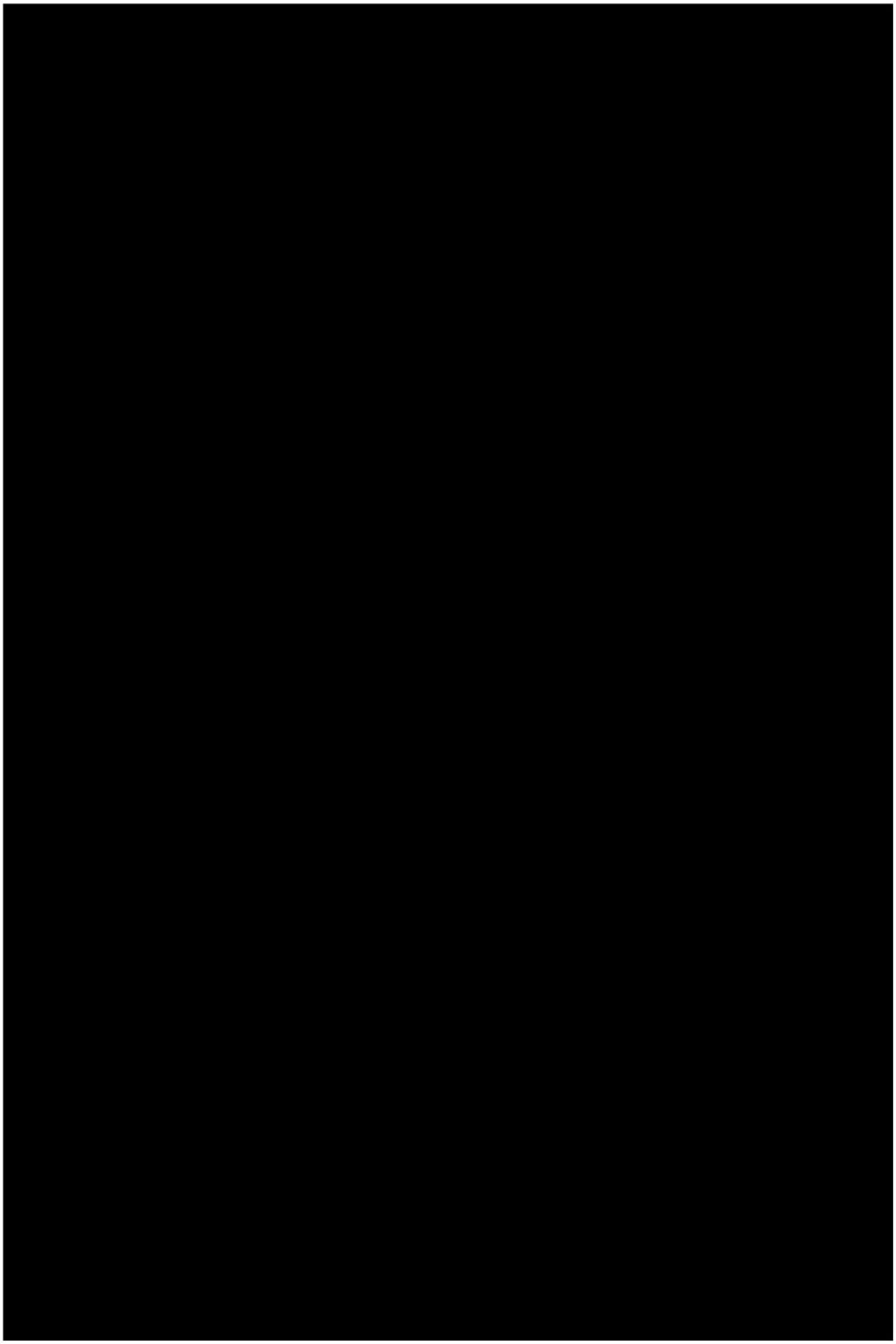

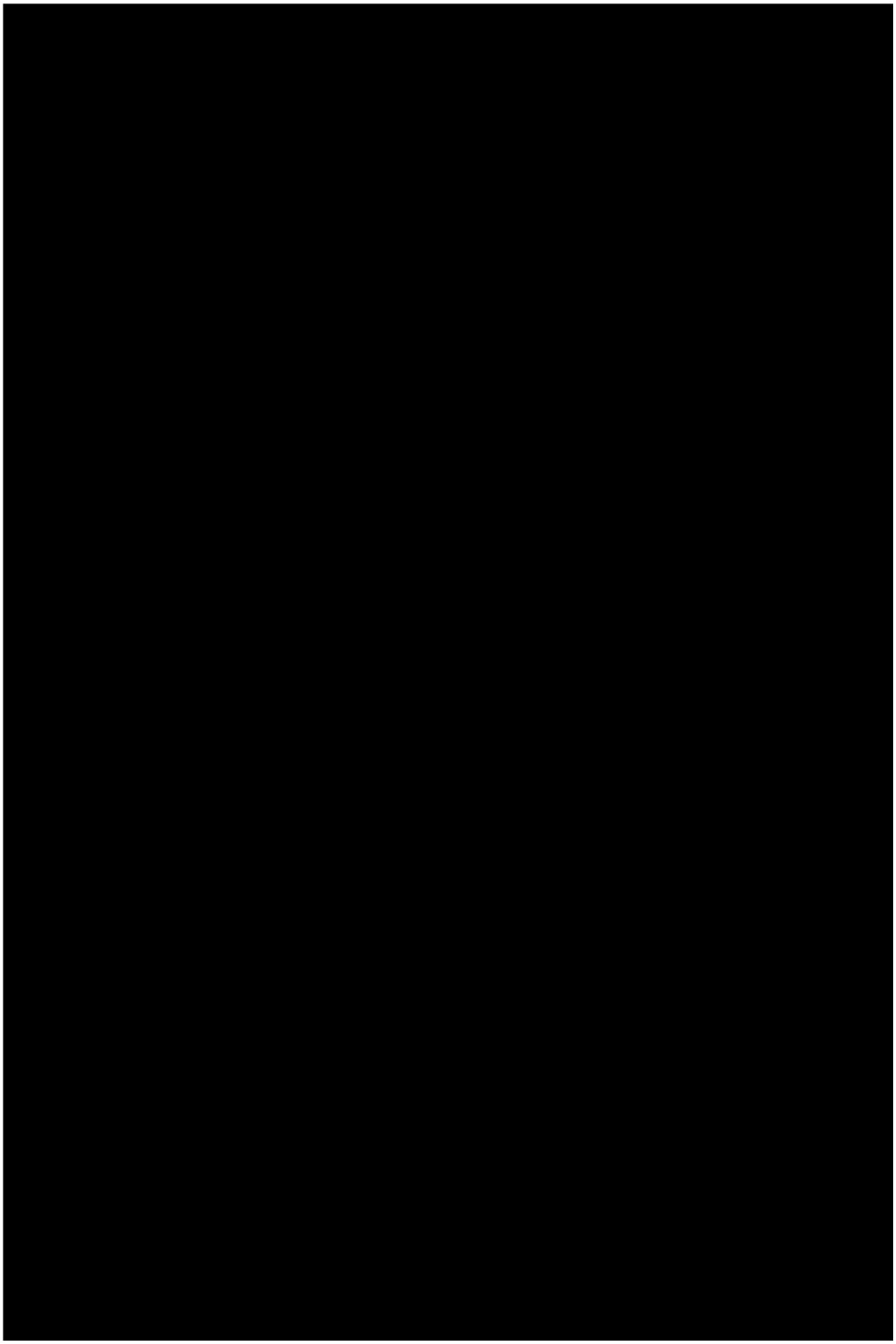

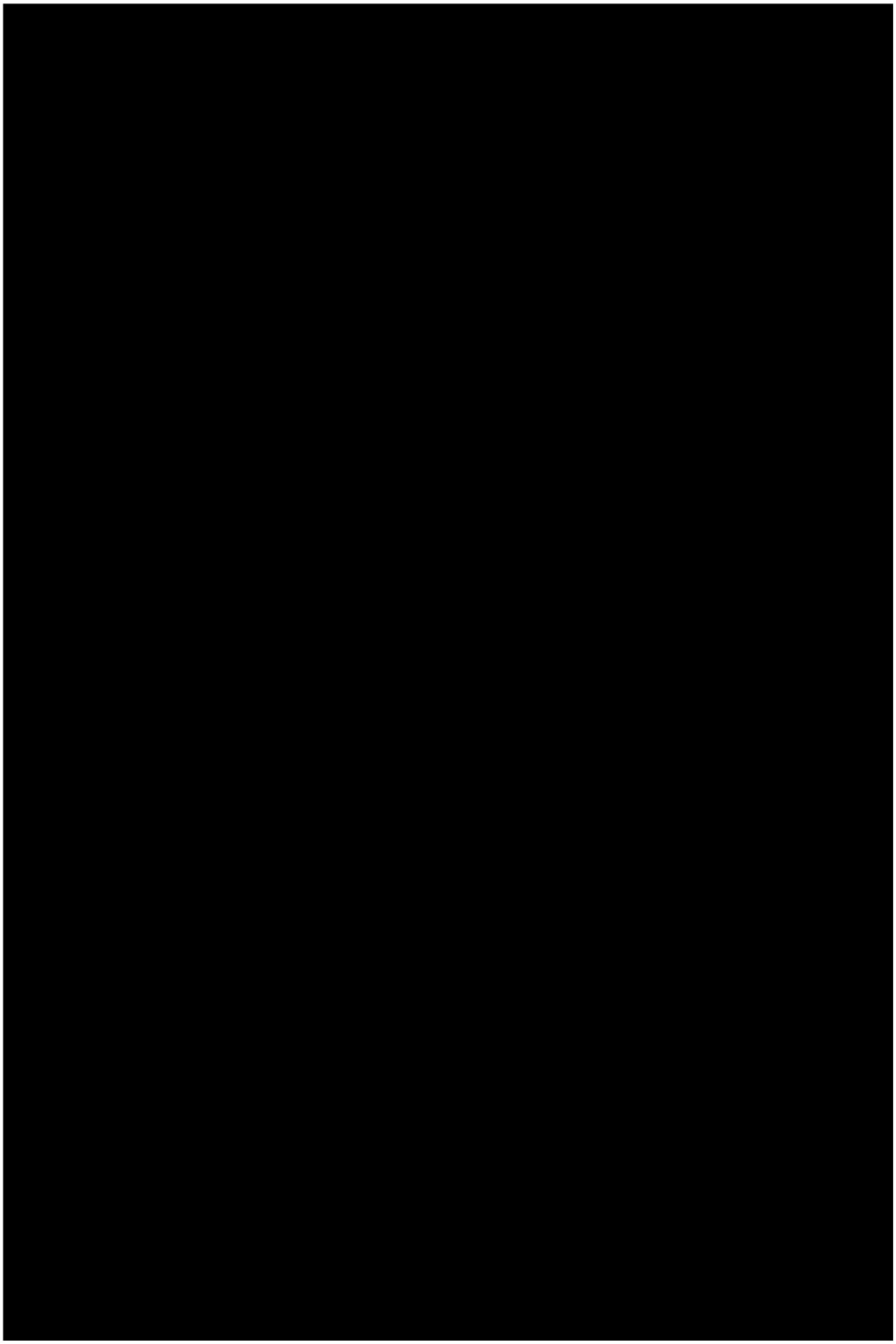

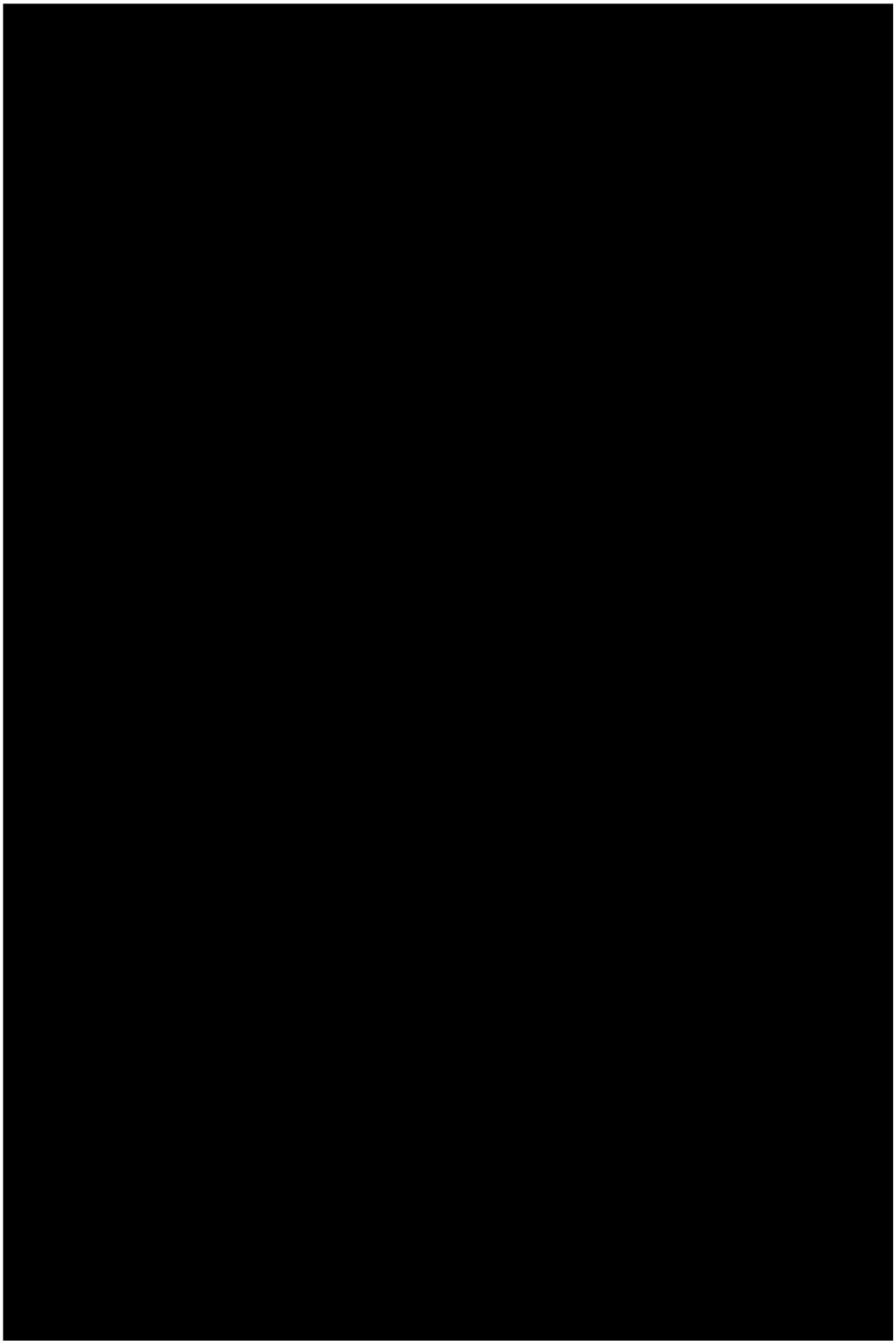

CONCLUSIONS

The present thesis was focused on the aero-thermo-dynamic characterization, in relevant environments, of UHTC and UHTCMC materials able to withstand the extreme conditions of the most demanding aerospace applications, therefore exploitable as structural materials for thermal protection systems of hypersonic re-entry vehicles and for reusable rocket nozzles. For this purpose, combined experimental and numerical activities have been carried out.

For the characterization of materials for TPS applications, several experimental campaigns were carried out by means of two supersonic arc-jet plasma wind tunnels, allowing test on small and medium scale materials samples in stagnation point configuration, in which conditions typical of atmospheric re-entry are reproduced, in terms of aero-thermo-dynamic loads on the specimens and chemical environment. Samples surface temperatures were monitored by means of non-intrusive diagnostic techniques (infrared pyrometers and thermo-cameras). First, different UIITCMC formulations have been compared, highlighting the excellent ablation resistance of short- and long-carbon-fibre reinforced UHTCs with a matrix based on ZrB_2-SiC, with respect to other compositions and most of all to conventional materials such as graphite or C/SiC. Several interesting phenomena have been observed on these materials during plasma exposure, including a *spontaneous temperature jump*, typically reported in literature, consisting in a rapid increase in the materials surface temperature, by 4-500 K, under constant flow conditions. To further investigate the ultra-high-temperature aero-thermal response of ZrB_2-SiC-based materials, dedicated test campaigns were also carried out to study the effect of SiC content in the initial composition and of the atmospheric chemical composition (in terms of oxygen partial pressure). It was highlighted that the *temperature jump* appears to be favoured by a lower SiC amount and that a very limited amount of oxygen in the plasma flow favours its occurrence at lower temperatures and in a more disruptive manner. Test on larger scale sample confirmed the results of small-scale campaigns.

Combining the results of all the experimental campaigns, including post-test microstructural analyses, and with the support of dedicated CFD simulations, a comprehensive interpretation of all the observed phenomena has been provided. In particular, the *spontaneous temperature jump* has been correlated to the durability of the protective borosilicate glass forming during high-temperature oxidation of ZrB_2-SiC UHTCs, not only on the exposed surface but also inside the oxide scale. A twofold mechanism has been proposed to explain the *jump*, related to the massive removal of the liquid BSG and the consequent exposure of a porous ZrO_2 layer: a dramatic reduction in the oxide thermal conductivity and a significantly increased catalytic recombination efficiency of the surface. An excellent agreement has been found between experimental and numerical results, in the reproduction of samples temperature axial distribution.

Moving to the characterization of UHTCMCs for near-zero erosion rocket nozzles, tests have been carried out in four different configurations, with increasing size and complexity. First, small samples have been exposed to the supersonic flame of a 200 N-class hybrid rocket engine, measuring their temperatures by means of the infrared equipment also used in arc-jet testing, and comparing the erosion rates of different material formulations. Then, larger prototypes, in the shape of flat annular inserts, have been placed inside the combustion chamber of the rocket, to test the capability of the materials to withstand considerable mechanical stresses under a representative thermo-chemical environment. As a third step, nozzle throat inserts were tested, assembled with a converging and a diverging nozzle parts made of graphite. Finally, complete nozzles entirely made of UHTCMC were subjected to repeated test sequences to compare different technologies and formulations and increase the TRL up to 5/6. Again, experimental activities were supported by numerical simulations, used not only for the rebuilding of the flow field around test articles, but also to reproduce the materials ultra-high-temperature behaviour.

These extensive test campaigns highlighted the outstanding erosion resistance of sintered ZrB_2-SiC-based UHTCMCs, with respect to other matrix formulations and to conventional materials (e.g. graphite and C/SiC). Moreover, it was verified that long-fibre-reinforced UHTCs offer an excellent structural performance, and their reusability

has been demonstrated up to at least 30 s. Finally, it was observed that even short-fibre-reinforced materials can provide a good mechanical resistance if their fibre volume content and porosity are adequately tuned.

Overall, the work carried out in the framework of this PhD was meant to provide a connection among different scientific and technological fields, and between industrial and research environments, in order to improve the understanding about UHTCs and UHTCMCs behaviour in relevant aero-thermo-dynamic environments. The collected data and the performed analyses contributed to the achievement of the goals of the C^{3}HARME project, which was successfully concluded, with a combined effort of the whole consortium, with the development and test of high-TRL large-scale prototypes (a complete TPS assembly tested in L3K and a large-scale solid rocket nozzle tested in AVIO test bench motors). The final objective of future research activities will need to include further increase of the TRL for the best performing materials, by a higher level of geometrical complexity, dimensions (up to full scale), system integration, and by all the necessary mechanical and environmental qualification assessments required by the space agencies for flight-ready space components.

In addition to the applications considered in the framework of C^{3}HARME, future research efforts could be interestingly devoted to assess and improve the performance of UHTCMCs in sharp TPS components, which would allow developing aerodynamically efficient wing leading edges for new-generation high-lift spaceplanes, able to perform controlled manoeuvres in extreme aero-thermo-dynamic conditions. Also, other applications such as TPS for planetary entry in space exploration missions (e.g. for Mars) or power generation (e.g. nuclear fusion plants, combustion chambers, solar panels) in ground- or space-scenarios will be of great interest, and specifically tailored development and testing would be needed.

Finally, several interesting developments may be considered from the modelling point of view, including more detailed rebuilding of thermal responses, taking into account the intrinsic anisotropy of composite materials, and possibly the dynamic simulation of oxidation and ablation processes.

ACKNOWLEDGMENTS

A significant part of the PhD research activities has been supported by the European Commission, through the C^{3}HARME research project, which has received funding in the framework of Horizon2020 research and innovation programme under the Grant Agreement n. 685594.

The experimental activities and the firing tests carried out at the Aerospace Propulsion Laboratory located in the military airport "F. Baracca" of Grazzanise (CE) have been possible thanks to the cooperation agreement between the University of Naples "Federico II" and the Italian Air Force.

The optical microscopic pictures presented in this work have been realized thanks to the courtesy of CIRTIBS Research Centre.

I would like to express my gratitude for all the people that walked next to me along this path that so deeply influenced the past few years of my life.

I want to start with a sincere acknowledgement to my PhD supervisor, prof. Raffaele Savino, who has always been present as a mentor and a guide, accompanying me through the exploration of scientific fields that were completely unknown to me just a few years ago.

I need to thank all the people that I met during the C^{3}HARME project, especially those who provided the materials samples for the experiments presented in this work and supported all my studies with post-test microstructural analyses. Among them, a special thank goes to the people from CNR-ISTEC, Luca Zoli, Laura Silvestroni, Antonio Vinci, Diletta Sciti, Frédéric Monteverde, with whom I had the most active collaboration and forged relationships that go beyond the professional sphere.

Also, I would like to express deep gratitude to Dr. Burkard Esser, who was my tutor during my research period at DLR, and continuously demonstrated being a wonderful person, besides an excellent researcher.

Another special thought is due to Giuseppe Di Martino, who started this adventure with me as a colleague, and ended it as a friend, and Giuseppe Gallo, who arrived a

little bit later, but shared with me an important part of the journey I am about to conclude. I also thank all the other people who I worked with, especially Anselmo, Giandomenico, Dr. Antonio Esposito, and all the professors, researchers and University staff who supported me during these years.

Of course, to conclude, I have to say thanks, with all my heart, to my family, who has always been there, even in the darkest moments, and my friends, who will always be my greatest supporters in my growth as a human and as an engineer. And, finally, thanks to my "cum-vivente" Carmela, who has been right here for all this time, close to me with all herself, with her ability to look deep inside my soul, through her wonderful eyes, and fill my life with the joy of the purest love. The crazy latest weeks have been really tough, but I am happy and proud to have faced them with her at my side, now closer than ever, taking care of each other. I hope we will soon be able to start again exploring together the world, the universe and "beyond".

BIBLIOGRAPHY

[1] J.D. Anderson, Hypersonic and High-Temperature Gas Dynamics, Third Edition, 2019. https://doi.org/10.2514/4.105142.

[2] A. Di Maso, Plasma Wind Tunnel Testing of Ultra High Temperature Ceramics: Experiments And Numerical Correlation, Università degli Studi di Napoli "Federico II," 2009. http://www.fedoa.unina.it/3832/.

[3] I.D. Boyd, G. V. Candler, Hypersonic Educational Initiative - Section 1, (2007).

[4] W.G. Fahrenholtz, G.E. Hilmas, Ultra-high temperature ceramics: Materials for extreme environments, Scr. Mater. 129 (2017) 94–99. https://doi.org/10.1016/j.scriptamat.2016.10.018.

[5] E. Wuchina, E. Opila, M. Opeka, W. Fahrenholtz, I. Talmy, UHTCs: Ultra-High Temperature Ceramic materials for extreme environment applications, in: Electrochem. Soc. Interface, 2007: pp. 30–36.

[6] O. Uyanna, H. Najafi, Thermal protection systems for space vehicles: A review on technology development, current challenges and future prospects, Acta Astronaut. 176 (2020) 341–356. https://doi.org/10.1016/j.actaastro.2020.06.047.

[7] K.Z. Li, X.T. Shen, H.J. Li, S.Y. Zhang, T. Feng, L.L. Zhang, Ablation of the carbon/carbon composite nozzle-throats in a small solid rocket motor, Carbon N. Y. 49 (2011) 1208–1215. https://doi.org/10.1016/j.carbon.2010.11.037.

[8] G. Sutton, O. Biblarz, Rocket Propulsion Elements 7th., 2001.

[9] P. Lemieux, Nitrous oxide cooling in hybrid rocket nozzles, Prog. Aerosp. Sci. 46 (2010) 106–115. https://doi.org/10.1016/j.paerosci.2009.12.001.

[10] R. Savino, G. Festa, A. Cecere, L. Pienti, D. Sciti, Experimental set up for characterization of carbide-based materials in propulsion environment, J. Eur. Ceram. Soc. 35 (2015) 1715–1723. https://doi.org/10.1016/j.jeurceramsoc.2014.12.032.

[11] W. Krenkel, Ceramic Matrix Composites: Fiber Reinforced Ceramics and their Applications, Wiley, 2008. https://doi.org/10.1002/9783527622412.

[12] P. Sanoj, B. Kandasubramanian, Hybrid Carbon-Carbon Ablative Composites for Thermal Protection in Aerospace, J. Compos. 2014 (2014). https://doi.org/10.1155/2014/825607.

[13] J.H. Zheng, H. Cui, H.J. Li, Y.H. Li, D.M. Yao, Z.Y. Ying, H.L. Deng, Mechanical and ablative properties of C/C composites modified by SiC using liquid silicon infiltration method, in: Proc. Int. Astronaut. Congr. IAC, 2017.

[14] Y. Wang, Z. Chen, S. Yu, Ablation behavior and mechanism analysis of C/SiC composites, J. Mater. Res. Technol. 5 (2016) 170–182. https://doi.org/10.1016/j.jmrt.2015.10.004.

[15] R.R. Hickman, T.N. Mckechnie, A. Agarwal, Net shape fabrication of high temperature materials for rocket engine components, in: 37th Jt. Propuls. Conf. Exhib., American Institute of Aeronautics and Astronautics, Reston, Virigina, 2001. https://doi.org/10.2514/6.2001-3435.

[16] J.R. Johnston, R.A. Signorelli, J.C. Freche, Performance of Rocket Nozzle Materials With Several Solid Propellants, NASA Tech. Notes. (1966).

[17] N.P. Padture, Advanced structural ceramics in aerospace propulsion, Nat. Mater. 15 (2016) 804–809. https://doi.org/10.1038/nmat4687.

[18] P. Thakre, V. Yang, Chemical erosion of carbon-carbon/graphite nozzles in solid-propellant rocket motors, J. Propuls. Power. 24 (2008). https://doi.org/10.2514/1.34946.

[19] J.P. Murugan, T. Kurian, J. Jayaprakash, T. Jayachandran, Design and thermo-structural analysis of the interface between subscale versions of carbon-carbon (C-C) nozzle divergent to metallic flange hardware for a ground simulation test, in: Proc. Int. Astronaut. Congr. IAC, 2017.

[20] L. Kamps, S. Hirai, Y. Ahmimache, R. Guan, H. Nagata, Investigation of graphite nozzle-throat-erosion in a laboratory-scale hybrid rocket using GOX and HDPE, in: 53rd AIAA/SAE/ASEE Jt. Propuls. Conf. 2017, 2017. https://doi.org/10.2514/6.2017-4736.

[21] G.J.K. Harrington, G.E. Hilmas, Thermal Conductivity of ZrB2 and HfB2, in: Ultra-High Temp. Ceram. Mater. Extrem. Environ. Appl., 2014. https://doi.org/10.1002/9781118700853.ch9.

[22] E.P. Simonenko, D. V. Sevast'Yanov, N.P. Simonenko, V.G. Sevast'Yanov, N.T. Kuznetsov, Promising ultra-high-temperature ceramic materials for aerospace applications, Russ. J. Inorg. Chem. 58 (2013) 1669–1693. https://doi.org/10.1134/S0036023613140039.

[23] B.R. Golla, A. Mukhopadhyay, B. Basu, S.K. Thimmappa, Review on ultra-high temperature boride ceramics, Prog. Mater. Sci. 111 (2020) 100651. https://doi.org/10.1016/j.pmatsci.2020.100651.

[24] T.A. Parthasarathy, M.D. Petry, M.K. Cinibulk, T. Mathur, M.R. Gruber, Thermal and oxidation response of UHTC leading edge samples exposed to simulated hypersonic flight conditions, J. Am. Ceram. Soc. 96 (2013) 907–915. https://doi.org/10.1111/jace.12180.

[25] S. Tang, C. Hu, Design, Preparation and Properties of Carbon Fiber Reinforced Ultra-High Temperature Ceramic Composites for Aerospace Applications: A Review, J. Mater. Sci. Technol. 33 (2017) 117–130. https://doi.org/10.1016/j.jmst.2016.08.004.

[26] F. Monteverde, The thermal stability in air of hot-pressed diboride matrix composites for uses at ultra-high temperatures, Corros. Sci. 47 (2005) 2020–2033. https://doi.org/10.1016/j.corsci.2004.09.019.

[27] T.A. Parthasarathy, R.A. Rapp, M. Opeka, M.K. Cinibulk, Modeling oxidation kinetics of SiC -containing refractory diborides, J. Am. Ceram. Soc. 95 (2012) 338–349. https://doi.org/10.1111/j.1551-2916.2011.04927.x.

[28] F. Monteverde, R. Savino, Stability of ultra-high-temperature ZrB2-SiC ceramics under simulated atmospheric re-entry conditions, J. Eur. Ceram. Soc. 27 (2007) 4797–4805. https://doi.org/10.1016/j.jeurceramsoc.2007.02.201.

[29] D. Alfano, R. Gardi, L. Scatteia, A. Del Vecchio, UHTC-Based Hot Structures: Characterization, Design, and On-Ground/In-Flight Testing, in: Ultra-High Temp. Ceram. Mater. Extrem. Environ. Appl., John Wiley & Sons, Inc, Hoboken, NJ, 2014: pp. 416–436. https://doi.org/10.1002/9781118700853.ch16.

[30] D. Sciti, L. Zoli, L. Silvestroni, A. Cecere, G.D. Di Martino, R. Savino, Design, fabrication and high velocity oxy-fuel torch tests of a Cf-ZrB2- fiber nozzle to

evaluate its potential in rocket motors, Mater. Des. 109 (2016) 709–717. https://doi.org/10.1016/j.matdes.2016.07.090.

[31] L. Zoli, D. Sciti, Efficacy of a ZrB2–SiC matrix in protecting C fibres from oxidation in novel UHTCMC materials, Mater. Des. 113 (2017) 207–213. https://doi.org/10.1016/j.matdes.2016.09.104.

[32] A. Vinci, L. Zoli, D. Sciti, J. Watts, G.E. Hilmas, W.G. Fahrenholtz, Influence of fibre content on the strength of carbon fibre reinforced HfC/SiC composites up to 2100 °C, J. Eur. Ceram. Soc. 39 (2019). https://doi.org/10.1016/j.jeurceramsoc.2019.04.049.

[33] A. Vinci, L. Zoli, D. Sciti, J. Watts, G.E. Hilmas, W.G. Fahrenholtz, Mechanical behaviour of carbon fibre reinforced TaC/SiC and ZrC/SiC composites up to 2100°C, J. Eur. Ceram. Soc. 39 (2019). https://doi.org/10.1016/j.jeurceramsoc.2018.11.017.

[34] Y. Yang, I. Kim, G. Park, Experimental and numerical study of oxygen catalytic recombination of SiC-coated material, Int. J. Heat Mass Transf. 143 (2019) 118510. https://doi.org/10.1016/j.ijheatmasstransfer.2019.118510.

[35] L. Zoli, A. Vinci, P. Galizia, C. Melandri, D. Sciti, On the thermal shock resistance and mechanical properties of novel unidirectional UHTCMCs for extreme environments, Sci. Rep. 8 (2018) 9148. https://doi.org/10.1038/s41598-018-27328-x.

[36] D. Zhang, J. Feng, P. Hu, L. Xun, M. Liu, S. Dong, X. Zhang, Enhanced mechanical properties and thermal shock resistance of Cf/ZrB2-SiC composite via an efficient slurry injection combined with vibration-assisted vacuum infiltration, J. Eur. Ceram. Soc. 40 (2020) 5059–5066. https://doi.org/10.1016/j.jeurceramsoc.2020.07.003.

[37] F. Monteverde, J.M. Cordoba, R. Savino, A. Cecere, S. Genna, C. Leone, Thermal stability under laser heating of hot-pressed (Hf1-X ZrX)B2/SiC powder mixtures obtained by mechano-synthesis, J. Eur. Ceram. Soc. 39 (2019) 4575–4587. https://doi.org/10.1016/j.jeurceramsoc.2019.06.050.

[38] Z. Yan, Z. Ma, S. Zhu, L. Liu, Q. Xu, Reflectivity and laser ablation of ZrB 2 /Cu ultra high temperature ceramic , in: 2nd Int. Symp. Laser Interact. with

Matter (LIMIS 2012), 2013. https://doi.org/10.1117/12.2011293.

[39] N.K. Gopinath, G. Jagadeesh, B. Basu, Shock wave-material interaction in ZrB2–SiC based ultra high temperature ceramics for hypersonic applications, J. Am. Ceram. Soc. 102 (2019). https://doi.org/10.1111/jace.16548.

[40] L. Scatteia, D. Alfano, S. Cantoni, F. Monteverde, M. De Stefano Fumo, A. Di Maso, Plasma torch test of an ultra-high-temperature ceramics nose cone demonstrator, J. Spacecr. Rockets. 47 (2010) 271–279. https://doi.org/10.2514/1.42834.

[41] R.K. Chinnaraj, S.M. Hong, H.S. Kim, P.Y. Oh, S.M. Choi, Ablation Experiments of Ultra-High-Temperature Ceramic Coating on Carbon–Carbon Composite Using ICP Plasma Wind Tunnel, Int. J. Aeronaut. Sp. Sci. 21 (2020). https://doi.org/10.1007/s42405-020-00267-6.

[42] A. Paul, J.G.P. Binner, B. Vaidhyanathan, A.C.J. Heaton, P.M. Brown, Oxyacetylene torch testing and microstructural characterization of tantalum carbide, J. Microsc. 250 (2013). https://doi.org/10.1111/jmi.12028.

[43] M. Natali, M. Monti, J.M. Kenny, L. Torre, A nanostructured ablative bulk molding compound: Development and characterization, Compos. Part A Appl. Sci. Manuf. 42 (2011) 1197–1204. https://doi.org/10.1016/j.compositesa.2011.04.022.

[44] S. Lee, G. Park, J.G. Kim, J.G. Paik, Evaluation System for Ablative Material in a High-Temperature Torch, Int. J. Aeronaut. Sp. Sci. 20 (2019). https://doi.org/10.1007/s42405-019-00185-2.

[45] L. Silvestroni, A. Vinci, S. Failla, L. Zoli, V. Rubio, J. Binner, D. Sciti, Ablation behaviour of ultra-high temperature ceramic matrix composites: Role of MeSi 2 addition, J. Eur. Ceram. Soc. 39 (2019) 2771–2781. https://doi.org/10.1016/j.jeurceramsoc.2019.03.031.

[46] T.A. Parthasarathy, M.K. Cinibulk, M. Opeka, Modeling and evaluating the environmental degradation of UHTCs under hypersonic flow, in: Y.Z. W. Fahrenholtz, E. Wuchina, W. Lee (Ed.), Ultra-High Temp. Ceram. Mater. Extrem. Environ. Appl., First ed, John Wiley & Sons, Inc., Hoboken, New Jersey, 2014: pp. 268–290.

[47] A. Purwar, V. Thiruvenkatam, B. Basu, Experimental and computational analysis of thermo-oxidative-structural stability of ZrB 2 -SiC-Ti during arc-jet testing, J. Am. Ceram. Soc. 100 (2017) 4860–4873. https://doi.org/10.1111/jace.15001.

[48] P. Patrick Ritt, P.A. Williams, J.H. Splinter, J.H. Perepezko, Arc jet testing and evaluation of Mo–Si–B coated Mo and SiC–ZrB2 ceramics, J. Eur. Ceram. Soc. 34 (2014) 3521–3533.

[49] K.S. Kim, S.H. Lee, V.Q. Nguyen, Y. Yun, S. Kwon, Ablation characteristics of rocket nozzle using HfC-SiC refractory ceramic composite, Acta Astronaut. 173 (2020) 31–44. https://doi.org/10.1016/j.actaastro.2020.03.050.

[50] F. Monteverde, A. Cecere, R. Savino, Thermo-chemical surface instabilities of SiC-ZrB2 ceramics in high enthalpy dissociated supersonic airflows, J. Eur. Ceram. Soc. 37 (2017) 2325–2341. https://doi.org/10.1016/j.jeurceramsoc.2017.01.018.

[51] M.J.H. Balat, Determination of the Active-to-Passive Transition in the Oxidation of Silicon Carbide in Standard and Microwave-Excited Air, J. Eur. Ceram. Soc. 16 (1996). https://doi.org/10.1016/0955-2219(95)00104-2.

[52] J. Marschall, D.A. Pejaković, W.G. Fahrenholtz, G.E. Hilmas, F. Panerai, O. Chazot, Temperature jump phenomenon during plasmatron testing of ZrB 2-SiC ultrahigh-temperature ceramics, J. Thermophys. Heat Transf. 26 (2012) 559–572. https://doi.org/10.2514/1.T3798.

[53] S. Zhou, W. Li, P. Hu, C. Hong, L. Weng, Ablation behavior of ZrB2-SiC-ZrO2 ceramic composites by means of the oxyacetylene torch, Corros. Sci. 51 (2009) 2071–2079. https://doi.org/10.1016/j.corsci.2009.05.035.

[54] I. Sakraker, C.O. Asma, Experimental investigation of passive/active oxidation behavior of SiC based ceramic thermal protection materials exposed to high enthalpy plasma, J. Eur. Ceram. Soc. (2013). https://doi.org/10.1016/j.jeurceramsoc.2012.09.002.

[55] M. Balat-Pichelin, L. Charpentier, F. Panerai, O. Chazot, B. Helber, K. Nickel, Passive/active oxidation transition for CMC structural materials designed for the IXV vehicle re-entry phase, J. Eur. Ceram. Soc. 35 (2015) 487–502.

https://doi.org/10.1016/j.jeurceramsoc.2014.09.026.

[56] H. Hald, Operational limits for reusable space transportation systems due to physical boundaries of C/SiC materials, Aerosp. Sci. Technol. 7 (2003) 551–559. https://doi.org/10.1016/S1270-9638(03)00054-3.

[57] G. Herdrich, M. Fertig, S. Löhle, S. Pidan, M. Auweter-Kurtz, T. Laux, Oxidation behavior of silicon car bide-based materials by using new probe techniques, J. Spacecr. Rockets. 42 (2005) 817–824. https://doi.org/10.2514/1.12265.

[58] E.P. Simonenko, N.P. Simonenko, A.N. Gordeev, A.F. Kolesnikov, A.S. Lysenkov, I.A. Nagornov, V.G. Sevastyanov, N.T. Kuznetsov, The effects of subsonic and supersonic dissociated air flow on the surface of ultra-high-temperature HfB2-30 vol% SiC ceramics obtained using the sol-gel method, J. Eur. Ceram. Soc. 40 (2020) 1093–1102. https://doi.org/10.1016/j.jeurceramsoc.2019.11.023.

[59] L. Duan, L. Luo, L. Liu, Y. Wang, Ablation of C/SiC-HfC composite prepared by precursor infiltration and pyrolysis in plasma wind tunnel, J. Adv. Ceram. 9 (2020). https://doi.org/10.1007/s40145-020-0379-4.

[60] A. Gülhan, B. Esser, U. Koch, M. Fischer, E. Magens, V. Hannemann, Characterization of high-enthalpy-flow environment for ablation material tests using advanced diagnostics, AIAA J. 56 (2018) 1072–1084. https://doi.org/10.2514/1.J056312.

[61] A. Coronetti, W.A. Sirignano, Numerical analysis of hybrid rocket combustion, J. Propuls. Power. 29 (2013). https://doi.org/10.2514/1.B34760.

[62] A. Cecere, R. Savino, C. Allouis, F. Monteverde, Heat transfer in ultra-high temperature advanced ceramics under high enthalpy arc-jet conditions, Int. J. Heat Mass Transf. 91 (2015). https://doi.org/10.1016/j.ijheatmasstransfer.2015.08.029.

[63] H.K. Chelliah, A. Makino, I. Kato, N. Araki, C.K. Law, Modeling of graphite oxidation in a stagnation-point flow field using detailed homogeneous and semiglobal heterogeneous mechanisms with comparisons to experiments, Combust. Flame. 104 (1996). https://doi.org/10.1016/0010-2180(95)00151-4.

[64] L. Liu, Y. Wang, G.L. Wang, H. Ma, J. Luo, Experiments to determine surface catalytic recombination coefficients of ultra high temperature ceramics in high temperature dissociated flows, in: 21st AIAA Int. Sp. Planes Hypersonics Technol. Conf. Hypersonics 2017, 2017. https://doi.org/10.2514/6.2017-2153.

[65] B. Massuti-Ballester, S. Pidan, G. Herdrich, M. Fertig, Recent catalysis measurements at IRS, Adv. Sp. Res. 56 (2015). https://doi.org/10.1016/j.asr.2015.04.028.

[66] D.G. Fletcher, J.M. Meyers, Surface catalyzed reaction efficiencies in oxygen plasmas from laser-induced fluorescence measurements, J. Thermophys. Heat Transf. 31 (2017). https://doi.org/10.2514/1.T4923.

[67] J.M. Meyers, D.G. Fletcher, Nitrogen surface catalyzed recombination efficiency from two-photon laser induced fluorescence measurements, J. Thermophys. Heat Transf. 33 (2019). https://doi.org/10.2514/1.T5455.

[68] A. Nawaz, D.M. Driver, I. Terrazas-Salinas, S. Sepka, Surface catalysis and oxidation on stagnation point heat flux measurements in high enthalpy arc jets, in: 44th AIAA Thermophys. Conf., 2013. https://doi.org/10.2514/6.2013-3138.

[69] J.R. Howell, M.P. Mengüç, R. Siegel, Thermal radiation heat transfer, sixth edition, 2015.

[70] A. Gülhan, B. Esser, Arc-Heated Facilities as a Tool to Study Aerothermodynamic Problems of Reentry Vehicles, in: Adv. Hypersonic Test Facil., American Institute of Aeronautics and Astronautics, Reston ,VA, 2002: pp. 375–403. https://doi.org/10.2514/5.9781600866678.0375.0403.

[71] A. Gülhan, B. Esser, U. Koch, Experimental investigation of reentry vehicle aerothermodynamic problems in arc-heated facilities, J. Spacecr. Rockets. 38 (2001) 199–206. https://doi.org/10.2514/2.3670.

[72] C. Carmicino, F. Scaramuzzino, A. Russo Sorge, Trade-off between paraffin-based and aluminium-loaded HTPB fuels to improve performance of hybrid rocket fed with N2O, Aerosp. Sci. Technol. 37 (2014) 81–92. https://doi.org/10.1016/j.ast.2014.05.010.

[73] C. Carmicino, Acoustics, vortex shedding, and low-frequency dynamics interaction in an unstable hybrid rocket, J. Propuls. Power. 25 (2009) 1322–

1335. https://doi.org/10.2514/1.42869.

[74] A. Russo Sorge, C. Carmicino, A. Nocito, Design of a lab-scale cooled two-dimensional plug nozzle for experimental tests, in: 38th AIAA/ASME/SAE/ASEE Jt. Propuls. Conf. Exhib., American Institute of Aeronautics and Astronautics, Reston, Virigina, 2002. https://doi.org/10.2514/6.2002-4039.

[75] S. Bonifacio, G. Festa, A. Russo Sorge, Novel structured catalysts for hydrogen peroxide decomposition in monopropellant and hybrid rockets, J. Propuls. Power. 29 (2013) 1130–1137. https://doi.org/10.2514/1.B34864.

[76] G. Gallo, G.D. Di Martino, G. Festa, R. Savino, Experimental investigation of N2O decomposition with pd⁄al2 o3 cylindrical pellets catalyst, J. Spacecr. Rockets. 57 (2020) 720–727. https://doi.org/10.2514/1.A34700.

[77] L. Galfetti, F. Nasuti, D. Pastrone, A.M. Russo, An Italian network to improve hybrid rocket performance: Strategy and results, Acta Astronaut. 96 (2014) 246–260. https://doi.org/10.1016/j.actaastro.2013.11.036.

[78] G.D. Di Martino, S. Mungiguerra, C. Carmicino, R. Savino, D. Cardillo, F. Battista, M. Invigorito, G. Elia, Two-hundred-Newton laboratory-scale hybrid rocket testing for paraffin fuel-performance characterization, J. Propuls. Power. 35 (2019). https://doi.org/10.2514/1.B37017.

[79] C. Carmicino, A.R. Sorge, Experimental investigation into the effect of solid-fuel additives on hybrid rocket performance, J. Propuls. Power. 31 (2015) 699–713. https://doi.org/10.2514/1.B35383.

[80] T. Cebeci, Analysis of Turbulent Flows, 2nd ed., Elsevier, Ltd., 2004. https://www.sciencedirect.com/book/9780080443508/analysis-of-turbulent-flows.

[81] A.J. Chorin, Numerical Solution of the Navier-Stokes Equations, Math. Comput. 22 (1968) 745. https://doi.org/10.2307/2004575.

[82] B. Launder, D. Spalding, Lectures in Mathematical Models of Turbulence, Academic Press, London, UK, 1972.

[83] S. Sarkar, B. Lakshmanan, Application of a Reynolds stress turbulence model to the compressible shear layer, AIAA J. 29 (1991) 743–749.

https://doi.org/10.2514/3.10649.

[84] A. Fluent, Ansys Fluent Theory Guide, ANSYS Inc., USA. 15317 (2013).

[85] S. Gordon, B.J. McBride, Computer Program for Calculation of Complex Chemical Equilibrium, NASA Ref. Publ. 1311. (1994).

[86] M.G. Dunn, S.W. Kang, Theoretical and Experimental Studies of Re-entry Plasmas, NASA Contract. Rep. 2232. (1973).

[87] G.P. Russo, G. Zuppardi, A. Esposito, Computed versus measured force coefficients on a cone in a small arc facility, Proc. Inst. Mech. Eng. Part G J. Aerosp. Eng. 222 (2008) 403–409. https://doi.org/10.1243/09544100JAERO252.

[88] R.H. Oppermann, Gaseous conductors, theory and engineering applications, J. Franklin Inst. 233 (1942). https://doi.org/10.1016/s0016-0032(42)90330-2.

[89] O.N. Suslov, G.A. Tirskiy, The kinetics of the recombination of nitrogen atoms on high temperature reusable surface insulation in hypersonic thermo-chemical non-equilibrium flow, in: J.J. Hunt (Ed.), Aerothermodyn. Sp. Veh. Proc. 2nd Eur. Symp. Held ESTEC, European Space Agency, Noordwijk, The Netherlands, 1994.

[90] S.M. Scala, Hypersonic Heat Transfer to Catalytic Surfaces, J. Aerosp. Sci. 25 (1958) 273–275. https://doi.org/10.2514/8.7621.

[91] M.A. Karabeyoglu, B.J. Cantwell, G. Zilliac, Development of scalable space-time averaged regression rate expressions for hybrid rockets, J. Propuls. Power. 23 (2007). https://doi.org/10.2514/1.19226.

[92] F.R. Menter, Two-equation eddy-viscosity turbulence models for engineering applications, AIAA J. 32 (1994). https://doi.org/10.2514/3.12149.

[93] B. Magnussen, On the structure of turbulence and a generalized eddy dissipation concept for chemical reaction in turbulent flow, in: 1981. https://doi.org/10.2514/6.1981-42.

[94] D.J. Singh, C.J. Jachimowski, Quasiglobal reaction model for ethylene combustion, AIAA J. 32 (1994) 213–216. https://doi.org/10.2514/3.11972.

[95] M.F. Modest, Radiative heat transfer, 2nd edition, 2003. https://doi.org/10.1016/B978-0-12-503163-9.X5000-0.

[96] G.D. Di Martino, C. Carmicino, S. Mungiguerra, R. Savino, The Application of Computational Thermo-Fluid-Dynamics to the Simulation of Hybrid Rocket Internal Ballistics with Classical or Liquefying Fuels: A Review, Aerospace. 6 (2019) 56. https://doi.org/10.3390/aerospace6050056.

[97] G.D. Di Martino, S. Mungiguerra, C. Carmicino, R. Savino, Computational fluid-dynamic simulations of hybrid rocket internal flow including discharge nozzle, in: 53rd AIAA/SAE/ASEE Jt. Propuls. Conf. 2017, 2017. https://doi.org/10.2514/6.2017-5045.

[98] G.D. Di Martino, C. Carmicino, R. Savino, Transient Computational Thermofluid-Dynamic Simulation of Hybrid Rocket Internal Ballistics, J. Propuls. Power. 33 (2017) 1395–1409. https://doi.org/10.2514/1.B36425.

[99] Y.R. Sivathanu, G.M. Faeth, Generalized state relationships for scalar properties in nonpremixed hydrocarbon/air flames, Combust. Flame. 82 (1990) 211–230. https://doi.org/10.1016/0010-2180(90)90099-D.

[100] J. Binner, M. Porter, B. Baker, J. Zou, V. Venkatachalam, V.R. Diaz, A. D'Angio, P. Ramanujam, T. Zhang, T.S.R.C. Murthy, Selection, processing, properties and applications of ultra-high temperature ceramic matrix composites, UHTCMCs – a review, Int. Mater. Rev. (2019) 1–56. https://doi.org/10.1080/09506608.2019.1652006.

[101] M. Balat-Pichelin, E. Bêche, D. Sciti, D. Alfano, Emissivity, catalycity and microstructural characterization of ZrB 2-SiCfiber based UHTC at high temperature in a non-equilibrium air plasma flow, Ceram. Int. 40 (2014). https://doi.org/10.1016/j.ceramint.2014.02.059.

[102] Y.S. Touloukian, D.P. DeWitt, Thermophysical properties of matter - the TPRC data series. Volume 8. Thermal radiative properties - nonmetallic solids, IFI/Plenum, New York – Washington, 1972.

[103] G.T. Van Laningham, Oxidation resistance, thermal conductivity, and spectral emittance of fully dense zirconium diboride with silicon carbide and tantalum diboride additives, Georgia Institute of Technology, 2012.

[104] D. Sciti, R. Savino, L. Silvestroni, Aerothermal behaviour of a SiC fibre-reinforced ZrB 2 sharp component in supersonic regime, J. Eur. Ceram. Soc. 32

(2012) 1837–1845. https://doi.org/10.1016/j.jeurceramsoc.2012.01.019.

[105] C.D. Scott, CATALYTIC RECOMBINATION OF NITROGEN AND OXYGEN ON HIGH-TEMPERATURE REUSABLE SURFACE INSULATION., in: AIAA Pap., 1980.

[106] R. GOULARD, On Catalytic Recombination Rates in Hypersonic Stagnation Heat Transfer, J. Jet Propuls. 28 (1958). https://doi.org/10.2514/8.7444.

[107] J. Marschall, D. Pejakovic, W.G. Fahrenholtz, G.E. Hilmas, F. Panerai, O. Chazot, Temperature Jump Phenomenon During Plasmatron Testing of ZrB2-SiC Ultrahigh-Temperature Ceramics, J. Thermophys. Heat Transf. 26 (2012) 559–572.

[108] L. Silvestroni, C. Melandri, V. Venkatachalam, J. Binner, D. Sciti, Merging toughness and oxidation resistance in a light ZrB2 composite, Mater. Des. 183 (2019). https://doi.org/10.1016/j.matdes.2019.108078.

[109] J. Zeng, S. Ren, J. Lu, Phase evolution of Ti3SiC2 annealing in vacuum at elevated temperatures, Int. J. Appl. Ceram. Technol. 10 (2013). https://doi.org/10.1111/j.1744-7402.2012.02760.x.

[110] P. Hu, K. Gui, Y. Yang, S. Dong, X. Zhang, Effect of SiC Content on the Ablation and Oxidation Behavior of ZrB2-Based Ultra High Temperature Ceramic Composites, Materials (Basel). 6 (2013) 1730–1744. https://doi.org/10.3390/ma6051730.

[111] F. Monteverde, D. Alfano, R. Savino, Effects of LaB6 addition on arc-jet convectively heated SiC-containing ZrB2-based ultra-high temperature ceramics in high enthalpy supersonic airflows, Corros. Sci. 75 (2013) 443–453. https://doi.org/10.1016/j.corsci.2013.06.029.

[112] F. Monteverde, L. Silvestroni, Combined effects of WC and SiC on densification and thermo-mechanical stability of ZrB2 ceramics, Mater. Des. 109 (2016) 396–407. https://doi.org/10.1016/j.matdes.2016.06.114.

[113] M. Weil, W.D. Schubert, The Beautiful Colours of Tungsten Oxides, Tungsten - Newsl. (2013) 1–12.

[114] A. Vinci, L. Zoli, D. Sciti, Influence of SiC content on the oxidation of carbon fibre reinforced ZrB2/SiC composites at 1500 and 1650 °C in air, J. Eur. Ceram.

Soc. 38 (2018) 3767–3776. https://doi.org/10.1016/j.jeurceramsoc.2018.04.064.

[115] P. Hu, W. Guolin, Z. Wang, Oxidation mechanism and resistance of ZrB2–SiC composites, Corros. Sci. 51 (2009) 2724–2732.

[116] W.M. Haynes, CRC Handbook Chemistry and Physics, CRC Press. (2016).

[117] K. Shugart, S. Liu, F. Craven, E. Opila, Determination of Retained B 2 O 3 Content in ZrB 2 -30 vol% SiC Oxide Scales, J. Am. Ceram. Soc. 98 (2015) 287–295. https://doi.org/10.1111/jace.13236.

[118] S. Gangireddy, S.N. Karlsdottir, J.W. Halloran, Liquid oxide flow during oxidation of zirconium diboride-silicon carbide ultra high temperature ceramics, in: Key Eng. Mater., 2010. https://doi.org/10.4028/www.scientific.net/KEM.434-435.144.

[119] L. Scatteia, D. Alfano, F. Monteverde, J.L. Sans, M. Balat-Pichelin, Effect of the machining method on the catalycity and emissivity of ZrB 2 and ZrB2-HfB2-based ceramics, J. Am. Ceram. Soc. 91 (2008) 1461–1468. https://doi.org/10.1111/j.1551-2916.2008.02325.x.

[120] V.A. Petrov, A.Y. Vorobyev, A.P. Chernyshev, Thermal radiation and optical properties of cubic zirconia stabilised with yttria up to the temperature of high rate evaporation, High Temp. - High Press. 34 (2002) 657–668. https://doi.org/10.1068/htjr077.

[121] E.P. Simonenko, A.N. Gordeev, N.P. Simonenko, S.A. Vasilevskii, A.F. Kolesnikov, E.K. Papynov, O.O. Shichalin, V.A. Avramenko, V.G. Sevastyanov, N.T. Kuznetsov, Behavior of HfB2-SiC (10, 15, and 20 vol %) ceramic materials in high-enthalpy air flows, Russ. J. Inorg. Chem. 61 (2016) 1203–1218. https://doi.org/10.1134/S003602361610017X.

[122] E.P. Simonenko, N.P. Simonenko, A.N. Gordeev, A.F. Kolesnikov, A.S. Lysenkov, I.A. Nagornov, V.G. Sevastyanov, N.T. Kuznetsov, The effects of subsonic and supersonic dissociated air flow on the surface of ultra-high-temperature HfB2-30 vol% SiC ceramics obtained using the sol-gel method, J. Eur. Ceram. Soc. 40 (2020) 1093–1102. https://doi.org/10.1016/j.jeurceramsoc.2019.11.023.

[123] E.H. Jordan, C. Jiang, J. Roth, M. Gell, Low thermal conductivity yttria-stabilized zirconia thermal barrier coatings using the solution precursor plasma spray process, J. Therm. Spray Technol. 23 (2014) 849–859. https://doi.org/10.1007/s11666-014-0082-5.

[124] G. Ouyang, M.F. Besser, M.J. Kramer, M. Akinc, P.K. Ray, Designing oxidation resistant ultra-high temperature ceramics through the development of an adherent native thermal barrier, J. Alloys Compd. 790 (2019) 1119–1126. https://doi.org/10.1016/j.jallcom.2019.03.250.

[125] S. Elhadj, S.T. Yang, M.J. Matthews, D.J. Cooke, J.D. Bude, M. Johnson, M. Feit, V. Draggoo, S.E. Bisson, High temperature thermographic measurements of laser heated silica, in: G.J. Exarhos, V.E. Gruzdev, D. Ristau, M.J. Soileau, C.J. Stolz (Eds.), 2009: p. 750419. https://doi.org/10.1117/12.836985.

[126] S. Kasap, J. Málek, R. Svoboda, Thermal Properties and Thermal Analysis: Fundamentals, Experimental Techniques and Applications, in: Springer Handb. Electron. Photonic Mater., Springer International Publishing, Cham, 2017: pp. 1–1. https://doi.org/10.1007/978-3-319-48933-9_19.

[127] B. Nait-Ali, K. Haberko, H. Vesteghem, J. Absi, D.S. Smith, Thermal conductivity of highly porous zirconia, J. Eur. Ceram. Soc. 26 (2006) 3567–3574. https://doi.org/10.1016/j.jeurceramsoc.2005.11.011.

[128] K.W. Schlichting, N.P. Padture, P.G. Klemens, Thermal conductivity of dense and porous yttria-stabilized zirconia, J. Mater. Sci. 36 (2001). https://doi.org/10.1023/A:1017970924312.

[129] L. Bedra, M.J.H. Balat-Pichelin, Comparative modeling study and experimental results of atomic oxygen recombination on silica-based surfaces at high temperature, Aerosp. Sci. Technol. 9 (2005) 318–328. https://doi.org/10.1016/j.ast.2005.01.011.

[130] M. Balat-Pichelin, M. Passarelli, A. Vesel, Recombination of atomic oxygen on sintered zirconia at high temperature in non-equilibrium air plasma, Mater. Chem. Phys. (2010). https://doi.org/10.1016/j.matchemphys.2010.03.059.

[131] X. Sun, H. Tian, G. Cai, Diameter and position effect determination of diaphragm on hybrid rocket motor, Acta Astronaut. 126 (2016).

https://doi.org/10.1016/j.actaastro.2016.04.029.

[132] D. Bianchi, F. Nasuti, Carbon-carbon nozzle erosion and shape change in full-scale solid-rocket motors, J. Propuls. Power. 28 (2012). https://doi.org/10.2514/1.B34267.

[133] Z.Y. Deng, J.M.F. Ferreira, Y. Tanaka, Y. Isoda, Microstructure and thermal conductivity of porous ZrO2 ceramics, Acta Mater. 55 (2007). https://doi.org/10.1016/j.actamat.2007.02.014.